# Modeling and experimental analysis of cable-in-conduit superconductor joints for fusion magnets

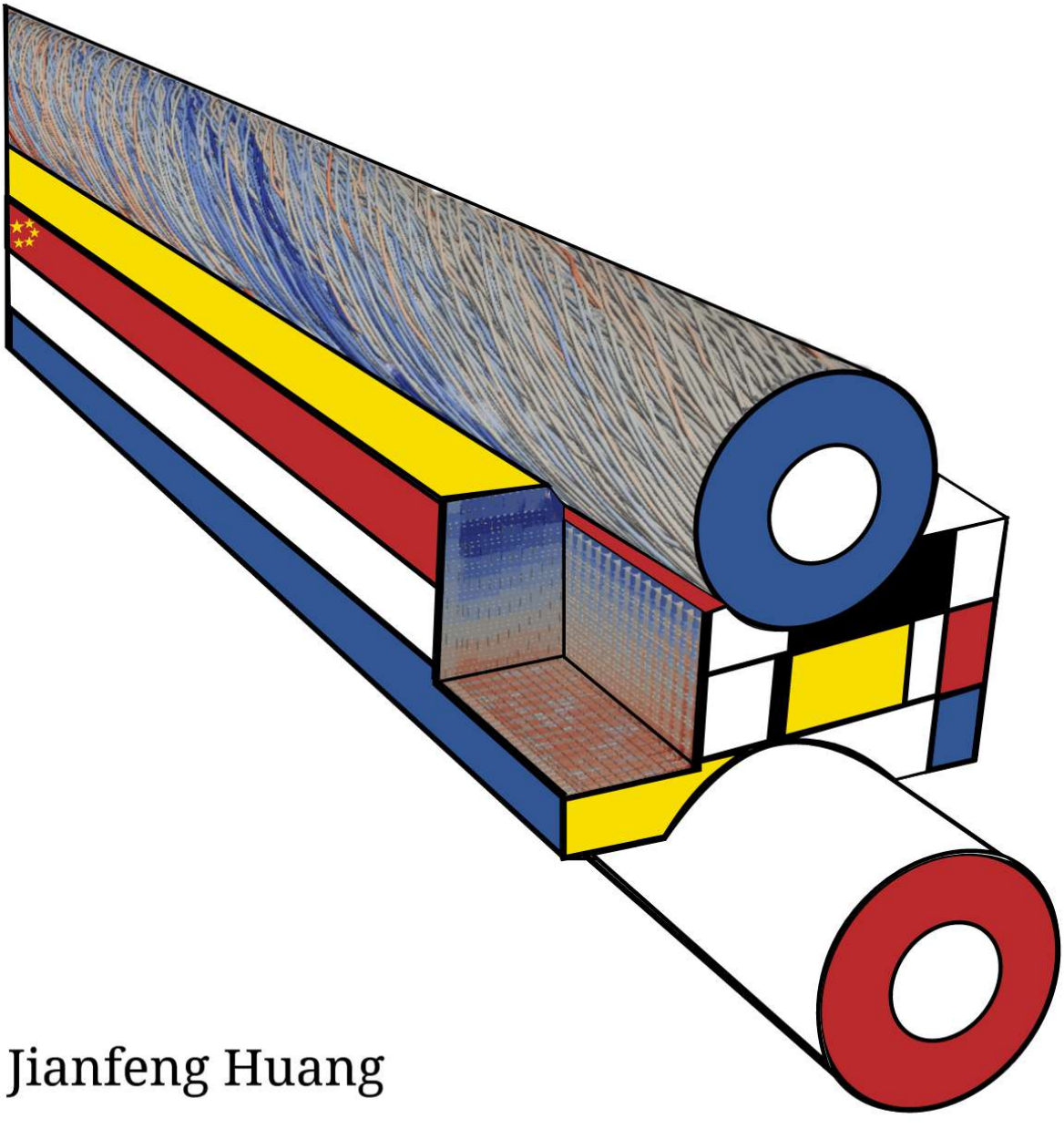

Jianfeng Huang

# MODELING AND EXPERIMENTAL ANALYSIS OF CABLE-IN-CONDUIT SUPERCONDUCTOR JOINTS FOR FUSION MAGNETS

Jianfeng Huang

# MODELING AND EXPERIMENTAL ANALYSIS OF CABLE-IN-CONDUIT SUPERCONDUCTOR JOINTS FOR FUSION MAGNETS

DISSERTATION

to obtain
the degree of doctor at the University of Twente,
on the authority of the rector magnificus,
Prof. dr. ir. A. Veldkamp,
on account of the decision of the Doctorate Board,
to be publicly defended
on Thursday June 20, 2024 at 16:45

by

**Jianfeng Huang**

born on August 30, 1986
in Changsha, China

This thesis has been approved by:
Promotors
Prof. dr. ir. H. H. J. ten Kate
Prof. dr. ir. H. J. M. ter Brake

Co-promotor
Dr. ing. A. Nijhuis

The research described in this thesis was carried out at the University of Twente.

JackPot-AC/DC ©Arend Nijhuis, University of Twente, Enschede. All rights reserved.

Modeling and experimental analysis of cable-in-conduit superconductor joints for fusion magnets
J. Huang
Ph.D. thesis, University of Twente, The Netherlands
ISBN: 978-90-365-6146-4
Printed by Ipskamp Printing, Enschede, The Netherlands
Cover by J. Huang
©J. Huang, Enschede, 2024.

PhD Graduation Committee:

| | | |
|---|---|---|
| Chairman | : Prof. dr. ir. A. Veldkamp | University of Twente |
| Supervisor 1 | : Prof. dr. ir. H. H. J. ten Kate | University of Twente |
| Supervisor 2 | : Prof. dr. ir. H. J. M. ter Brake | University of Twente |
| Co-supervisor | : Dr. ing. A. Nijhuis | University of Twente |
| Referee | : Dr. Y. Ilyin | ITER Organization |
| Members | : Prof. dr. M. R. De Baar | Eindhoven University of Technology & DIFFER |
| | : Prof. dr. F. Grilli | Karlsruhe Institute of Technology |
| | : Prof. dr. ir. R. Akkerman | University of Twente |
| | : Prof. dr. ir. J. M. van Oort | University of Twente |

# Summary

Thermonuclear fusion stands as a highly promising solution for the foreseeable future, offering a nearly limitless source of energy. At the forefront of experimental tokamak-type fusion reactors, ITER employs a complex magnetic field configuration to heat, control and shape the intense plasma. The magnet system of ITER comprising toroidal field coils, poloidal field coils, a central solenoid and various correction coils, relies on advanced NbTi and $Nb_3Sn$ Cable-In-Conduit (CIC) superconductors. Given the substantial dimensions of the magnet coils and the constrained production length of conductors, electrical joints become imperative to establish connections between unit lengths of conductors. Functioning as a critical interface comprising a transition from superconducting to non-superconducting materials, the joint plays a pivotal role in maintaining the stability of the magnet and achieving reliable magnet operation.

Stringent design and qualification tests, encompassing DC, AC, and stability evaluations mirroring ITER operational conditions, are mandatory for all CIC superconductors and joints. The majority of the tests are conducted at the SULTAN facility at the Swiss Plasma Center, and some complementary tests are performed at the University of Twente. Considering the high associated cost and limitations in test conditions such as ITER relevant magnetic field conditions, necessitate assessments based on extensive numerical simulations. To this end, the numerical simulation model JackPot-AC/DC, developed at the University of Twente, is employed for a meticulous analysis of the electromagnetic and thermal behaviors of superconductors and joints with a strand-level precision.

For a comprehensive exploration of the stability aspects of ITER coils, a profound understanding of the inherent characteristics of NbTi and $Nb_3Sn$ strands is indispensable. Notably, two key challenges are encountered during the research and development and qualification procedures. Firstly, the establishment of a practical scaling law for all $Nb_3Sn$ strands proved to be crucial. The existing scaling laws for ITER $Nb_3Sn$ strands, derived from measurements conducted in relatively high magnetic field beyond 7 T, have demonstrated inaccuracies since most strands typically operate in a relatively low magnetic field region of less than 4 T. An effective scaling law, derived by measuring critical current

and magnetization in different field ranges, addressing this disparity, was developed and adopted by the ITER organization. Secondly, the angular dependence of hysteresis loss in complex cables on the applied magnetic field poses another challenge. An accurate assessment method for estimating the hysteresis and coupling losses of CICCs and joints was derived by measuring hysteresis loss in a strand sample with respect to magnetic fields in different directions.

Qualification tests stand as imperative phase of the ITER magnet research and development program. A comprehensive campaign of Poloidal Field (PF) joint qualification measurements, encompassing DC, AC, and stability evaluations, was executed at the SULTAN facility. Following the SULTAN tests, an ITER PF5 joint sample, PFJEU6, underwent extensive testing at the University of Twente for measuring joint internal contact resistances, and AC losses, complemented with numerical simulation and analysis. This marks a significant milestone, as it has been the first time that these strand level resistances of a full-size ITER joint were measured. Notably, the critical input parameters of contact resistivities in the JackPot-AC/DC model were derived from these tests, enabling a precise quantitative analysis. Furthermore, a parametric sensitivity analysis, considering contact resistivities, solder parameters, void fraction, and external magnetic field configurations, has been meticulously performed.

The so-called twin-box lap-type joint, a critical yet delicate component in the coil assembly, is crafted by tightly compressing two conductors with a copper sole, employing specific solders such as AgSn and PbSn, and use of explosive bonding technology. Given the distinct electric, thermal, and mechanical properties of the constituents, the joint assumes a pivotal role in the functioning of the coil. Rigorous testing is imperative throughout the design, manufacturing, and qualification phases. In the preliminary qualification measurements of ITER PF joint samples (PFJEU2 and PFJEU3), unexpected nonlinear voltage-current characteristics surfaced in the DC tests. The observed resistance variation reaches $3.5$ n$\Omega$ on top of the $5.0$ n$\Omega$ resistance, as transport current and background magnetic field increase. Despite the apparent influence of the transport current and magnetic field, as corroborated by numerical calculations incorporating the copper sole and the strands' magneto-resistance, the magnitude of their influence on the joint resistance appeared relatively limited. Similar phenomena were noted in other joint samples, yet definitive reasons remained elusive.

This study introduces models founded on non-homogeneous contact resistances between the two cable ends and the intermediate copper sole. By adjusting contact conditions at diverse interfaces, the overall joint resistance is calculated and compared to measured data. The investigation reveals that a defective connection between the copper sole and shim, caused by electromagnetic force, is the most probable cause for the nonlinear voltage-current behavior. The conclusion of the modeling finds validation through post-mortem examination, employing microscopy (SEM) and energy-dispersive X-ray spectroscopy (EDX). Additionally, a detailed analysis of local power dissipation and current distribution under non-homogeneous contact resistance conditions was conducted. The developed model not only addresses the encountered problem of nonlinear voltage-current characteristics but also furnishes a non-destructive detection method for joint manufacturing and testing.

The advantage of the tokamak heavily relies on robust magnetic confinement of the burning plasma. In the case of PF coils operating in pulsed mode, rapidly varying cur-

rents cause a relatively high AC loss, primarily attributed to ohmic dissipation due to induced coupling currents. The distribution of coupling and transport currents within the conductors can exhibit significant non-uniformity, influenced by resistive variations in strand contacts at joints and inductive coupling variations along the cable. While current non-uniformity may not be inherently problematic, in fast-pulsed coils, it can lead to reduced critical current, particularly in the case of PF conductor cables with NbTi strands characterized by a relatively low temperature margin and high $'n'$ value. Additionally, large NbTi CICCs operating at high currents exhibit very low take-off voltages due to the substantial gradient in self-field. In critical areas of operation, local quenches may occur before sufficient inter-strand current redistribution transpires.

This study explores a method to mitigate current non-uniformity by applying high-resistive polyimide layers (referred to as masks) to block petal current paths leading to a high coupling loss. The impact of masks on current distribution, power dissipation, and thermal evolution is quantitatively evaluated using the JackPot-AC/DC model. The study reveals that while the implementation of masks causes an increase of total heat dissipation in some petals, it renders the heat distribution more uniform along the joint compared to the concentrated heat observed in joints without masks. This contributes positively to temperature profiles along the joint box by smoothing temperature peaks in the petals, thereby enhancing the stability and working conditions of the joints and so coils.

A more thorough and comprehensive analysis of joint stability in both steady and transient states was undertaken, encompassing assessments of the current sharing temperature $T_{cs}$ in stationary current conditions and AC losses, as well as the Minimum Quench Energy (MQE) in AC conditions. Given the limitations of test conditions in the SULTAN facility, replicating actual ITER operations poses challenges. Leveraging both experimental tests and numerical simulations addresses this limitation. While tests in the SULTAN facility offer valuable insights, they cannot precisely emulate the intricacies of ITER's operational environment. In contrast, the numerical model not only aligns well with SULTAN qualification tests but also extends to simulate ITER operating conditions. Consequently, the performance evaluation for future operations becomes accurate and comprehensive. Taking the current sharing temperature $T_{cs}$ in DC condition as an illustration, the analysis not only reveals a lower $T_{cs}$ in the ITER operating magnetic field configuration but also elucidates the specific evolution of the current sharing and quench procedures precisely.

Regarding thermal stability, we propose a novel method utilizing the electromagnetic and thermal routines embedded in the JackPot-AC/DC code. This approach involves determining the temperature evolution and establishing an equilibrium between generated and deposited energies. Systematic numerical tests are conducted on joints under various magnetic field and cooling parameters, such as helium inlet temperature and mass flow rate. The numerical outcomes exhibit excellent agreement with SULTAN measurement results, thereby validating the efficacy of this new method. In comparison to combined models, our proposed method offers a relatively effective and straightforward means to investigate the electromagnetic and thermal stability of joints. Moreover, it facilitates the determination of quench initiation and propagation on a macroscopic scale.

Notably, when complemented with analyses of joints in DC condition, a comprehensive understanding of joint stability has been achieved. The combined approach ensures a comprehensive understanding of the joint's performance, facilitating informed decisions for optimizing safety and functionality during ITER operations and providing valuable

considerations for the design of future CICC-based joints, ultimately contributing to the safe and reliable operation of the magnets when exposed to the various ITER plasma scenarios.

# Samenvatting (summary in Dutch)

Kernfusie staat bekend als een veelbelovende oplossing voor de voorzienbare toekomst, met een bijna onbeperkte bron van energie als resultaat. Als vooroplopende experimentele tokamak-type fusiereactor maakt ITER gebruik van een krachtig magneetveld om het intense plasma te beheersen en vorm te geven. Het magneetsysteem van ITER is gebaseerd op geavanceerde NbTi en $Nb_3Sn$ kabel-in-buis-supergeleiders. Gezien de aanzienlijke afmetingen van de magneetspoelen en de beperkte productielengtes van de geleiders zijn elektrische verbindingen tussen de geleiders essentieel. Deze verbindingen vormen een cruciale overgang van supergeleidend naar niet-supergeleidend materiaal en spelen daarom een doorslaggevende rol bij het garanderen van de stabiliteit van de magneet. Strikte kwalificatietests, waaronder DC-, AC- en stabiliteitsevaluaties die de operationele omstandigheden van ITER weerspiegelen, zijn noodzakelijk voor alle supergeleiders en verbindingen. Het merendeel van de tests wordt uitgevoerd in de SULTAN-faciliteit bij het Swiss Plasma Center, en enkele aanvullende tests worden uitgevoerd bij de Universiteit Twente. Gezien de hoge kosten en beperkingen in de testomstandigheden vooral wat het magneetveld betreft, zijn beoordelingen op basis van numerieke simulaties noodzakelijk. Met dit doel is aan de Universiteit Twente het numerieke model JackPot-AC/DC ontwikkeld voor een nauwkeurige analyse van het elektromagnetische en thermische gedrag van de supergeleiders en de verbindingen met een nauwkeurigheid tot op de schaal van een individuele draad.

Voor een grondige verkenning van de stabiliteitsaspecten van ITER-spoelen is een diepgaand begrip van de basiskenmerken van NbTi- en $Nb_3Sn$ draden onmisbaar. Twee belangrijke uitdagingen zijn relevant voor ontwikkeling en kwalificatie. Ten eerste is een praktische schalingswet die de $Nb_3Sn$ draden kan beschrijven cruciaal. De bestaande schalingswetten voor ITER $Nb_3Sn$ draden, afgeleid van metingen uitgevoerd in relatief hoge magneetvelden van meer dan 7 T, blijken niet nauwkeurig genoeg voor magneetvelden van minder dan 4 T, terwijl zulke lagere veldsterkes wel door omvangrijke delen van de magneet gezien worden. Een effectieve schalingswet is daarom opgezet, afgeleid door de kritieke stroom en magnetisatie te meten over een breder magneetveldbereik. Deze

nieuwe schalingswet wordt nu gebruikt door ITER. Ten tweede is de hoekafhankelijkheid van het hysterese-verlies ten opzichte van het toegepaste magneetveld van belang. Een nauwkeurige methode voor het schatten van de hysterese- en koppelingsverliezen van de supergeleider en zijn verbindingen is opgesteld door het verrichten van experimenteel onderzoek.

Kwalificatietests zijn essentieel voor de magneten van ITER. Een uitgebreide campagne van kwalificatiemetingen voor Poloidal Field (PF) verbindingen is uitgevoerd bij de SULTAN-faciliteit. Hiermee kunnen DC-, AC- en stabiliteitscriteria worden geëvalueerd. Na SULTAN-tests is een ITER PF5 testverbinding, PFJEU6, uitgebreid getest bij de Universiteit Twente om contactweerstanden en AC-verliezen te meten, en voor numerieke analyse. Dit markeert een significante mijlpaal, aangezien het de eerste keer is dat deze strengniveaumweerstanden van een ITER-verbinding op ware grootte zijn gemeten. Met name de contactweerstanden, cruciale invoerparameters voor het JackPot-AC/DC-model, zijn afgeleid uit deze tests, waardoor een nauwkeurige kwantitatieve analyse mogelijk is geworden. Verder is een parametrische gevoeligheidsanalyse, betreffende zowel de contactweerstanden, soldeerparameters, de invloed van de fractie lege ruimte als ook externe magneetveldconfiguraties, zorgvuldig uitgevoerd.

De zogenaamde twin-box lap-type verbinding, een kritiek en delicaat onderdeel in de spoelconstructie, wordt vervaardigd door twee geleiders samen te persen op een tussenliggende koperen zool. Hierbij worden bepaalde solderen zoals AgSn en PbSn alsmede explosie-verbindingstechnologie toegepast. Gelet op de verschillende elektrische, thermische en mechanische eigenschappen van de componenten, is de verbinding van cruciaal belang voor het goed functioneren van de spoel. Rigoureuze tests zijn van vitaal belang gedurende de ontwerp-, productie- en kwalificatieprocessen. Tijdens de initiële kwalificatiemetingen van ITER PF testverbindingen (PFJEU2 en PFJEU3) werden onverwachte niet-lineaire spanning-stroomkarakteristieken gemeten in de DC-tests. De gemeten weerstand rijkt van $5.0$ nΩ bij lage transportstromen en lage achtergrondmagneetvelden tot $8.5$ nΩ bij belastendere scenarios. Deze gemeten weerstandswaarde is gereproduceerd door numerieke berekeningen waarbij het magneto-weerstandseffect van de koperen zool en de draden in de kabel zijn meegenomen. Soortgelijke verschijnselen zijn opgemerkt in andere testverbindingen.

Deze studie introduceert een model gebaseerd op niet-homogene contactweerstand tussen de componenten van twee kabels en de koperen zool. Door de parameters aan te passen voor de diverse soorten contact, is de weerstand van de verbinding berekend en vergeleken met gemeten gegevens. Het model laat zien dat een defecte verbinding tussen de koperen zool en de shim, ontstaan door elektromagnetische krachten, de meest waarschijnlijke oorzaak is van het niet-lineaire spannings-stroomgedrag. Deze conclusie wordt bevestigd door post-mortem onderzoek, waarbij gebruik is gemaakt van microscopie (SEM) en energie-dispersieve röntgenspectroscopie (EDX). Bovendien is een gedetailleerde analyse van de lokale vermogensdissipatie en stroomverdeling onder invloed van niet-homogene contactweerstandsomstandigheden uitgevoerd. Het ontwikkelde model laat niet alleen het geconstateerde probleem van niet-lineaire spannings-stroomkarakteristieken zien, maar is ook een niet-destructieve testmethode voor de productie en test van de verbinding.

De prestaties van de tokamak zijn sterk afhankelijk van de robuustheid van de magnetische opsluiting van het brandende plasma. In het geval van PF-spoelen veroorzaken snel

variërende stromen relatief hoge AC-verliezen, voornamelijk toe te schrijven aan koppelingsstromen. De verdeling van koppelings- en transportstromen binnen de geleiders kan grote verschillen vertonen, door variaties in de contactweerstanden tussen de draden in de verbinding en door inductieve koppelingen langs de kabel. Hoewel een ongelijke stroomverdeling op zichzelf niet perse problematisch hoeft te zijn, kan het in snelgepulste spoelen leiden tot degradatie van de kritieke stroom, met name voor PF-geleiders verkabeld met NbTi draad met een relatief lage temperatuurmarge en hoge $'n'$-waarde. Bovendien vertonen dikke NbTi kabels voor hoge stromen al bij relatief lage stroom elektrische spanning als gevolg van de aanzienlijke eigen veldgradiënt. Onder kritieke werkomstandigheden kunnen lokale quenches optreden voordat er voldoende herverdeling van de stroom in de kabel plaatsvindt.

In deze studie is een methode onderzocht om stroomongelijkheid te verminderen door isolerende polyimide lagen (aangeduid als maskers) aan te brengen om bepaalde stroompaden die hoge koppelingsverliezen veroorzaken, te onderbreken. De invloed van maskers op de stroomverdeling, vermogensdissipatie en temperatuur is kwantitatief onderzocht met het JackPot-AC/DC-model. De studie onthult dat, hoewel de implementatie van maskers de totale warmteafgifte in sommige secties verhoogt, het de warmteverdeling langs de verbinding meer uniform maakt in vergelijking met de geconcentreerde warmtedepositie die wordt waargenomen in verbindingen zonder maskers. Dit draagt positief bij aan het temperatuurprofiel langs de verbinding doordat pieken in de temperatuur worden gladgestreken. Hierdoor verbeteren de stabiliteit en operationele omstandigheden van de verbindingen en de spoelen.

Een uitgebreide en grondige analyse van de stabiliteit van de verbinding onder zowel stationaire als niet-stationaire omstandigheden is uitgevoerd, waarbij voor het geval van een DC stroom de karakteristieke temperatuur $T_{cs}$ wordt afgeschat, en onder AC-condities de AC-verliezen, en Minimum Quench Energy (MQE). Gezien de beperkingen van de testomstandigheden in de SULTAN-faciliteit is het repliceren van de daadwerkelijke ITER operationele omstandigheden moeilijk. Het benutten van zowel experimentele tests als numerieke simulaties is een oplossing voor deze beperking. Hoewel experimentele tests in de SULTAN-faciliteit waardevolle inzichten bieden, kunnen ze de complexiteit van de operationele omstandigheden van ITER niet nauwkeurig nabootsen. Het numerieke model sluit niet alleen goed aan bij de SULTAN-kwalificatietests, maar maakt het ook mogelijk ITER-operationele omstandigheden te simuleren. Hierdoor wordt de prestatie-evaluatie voor de werking in de tokamak nauwkeurig en uitgebreid. De analyse onthult niet alleen een relatief lage $T_{cs}$ in omstandigheden die representatief zijn voor ITER, maar laat ook de evolutie van stroomherverdeling en quench-procedures nauwkeurig zien.

Voor de analyze van de thermische stabiliteit is een nieuwe methode ontwikkeld die gebruikmaakt van de elektromagnetische en thermische routines, onderdeel van de JackPot-AC/DC-code. Met deze methode kan de temperatuurevolutie en het evenwicht tussen opgewekte en afgevoerde warmte worden berekend. Systematische numerieke tests zijn uitgevoerd op testverbindingen onder variërende magneetvelden en koelomstandigheden, zoals de inlaattemperatuur en stroomsnelheid van het koelmiddel helium. De numerieke resultaten vertonen een uitstekende overeenkomst met SULTAN meetresultaten, wat de doeltreffendheid van deze nieuwe methode bevestigt. In vergelijking met het combineren van afzonderlijke elektromagnetische en thermische modellen biedt onze voorgestelde gekoppelde methode een relatief effectieve en eenvoudige manier om de stabiliteit van ver-

bindingen te onderzoeken. Bovendien maakt het de bepaling van condities voor quench-initiatie en -propagatie op macroscopische schaal makkelijker.

Opmerkelijk is dat, wanneer aangevuld met analyses van verbindingen in DC-condities, een alomvattend begrip van de stabiliteit van de verbinding wordt bereikt. De gecombineerde aanpak zorgt voor een grondig begrip van de prestaties van de verbinding, hetgeen goede beslissingen mogelijk maakt voor het optimaliseren van veiligheid, functionaliteit en betrouwbaarheid tijdens operatie van ITER en biedt waardevolle overwegingen voor het ontwerpen van toekomstige elektrische verbindingen. Dit draagt uiteindelijk bij aan de veilige werking van magneten in ITER-plasmascenario's.

# Acknowledgements

This thesis marks the culmination of my PhD journey, encapsulating the most significant moments of my academic pursuit within the Energy, Materials, and Systems group at the University of Twente. It has been a voyage filled with joys, surprises, and challenges. Grateful for this experience, I extend my sincere appreciation to those who have played pivotal roles in shaping my academic and personal growth during my time in the Netherlands.

Foremost, my deepest thanks go to my daily supervisor, Arend Nijhuis, for his constant support and patience. His guidance, spanning from the development of projects to the intricacies of paper writing, has played a crucial role in my academic journey. I am truly grateful for the valuable opportunities he provided me, including the chance to pursue a PhD and the involvement in the ITER project.

I extend heartfelt gratitude to my supervisor, Herman ten Kate, whose profound knowledge and scholarly rigor have been a constant source of inspiration in my journey as a researcher. I would have deemed it insurmountable to overcome certain difficulties and obstacles without his indispensable support and assistance.

I express my sincere appreciation to Marcel ter Brake for his invaluable support and encouragement, enabling me to persist in my PhD journey despite encountering obstacles. I also want to acknowledge Marc Dhalle for his enlightening lectures and insightful discussions in our professional field.

The projects presented in this thesis primarily serve the ITER organization, and I extend my gratitude to Yuri Ilyin. His dedication to scientific excellence and wealth of experience have driven me to delve deeply into research problems, and I have greatly benefited from our discussions.

A significant portion of my research revolves around modeling, and I am indebted to Marcel Dijkstra for his selfless assistance. His shared experiences and extensive knowledge have broadened my perspective on scientific computing. Special thanks also go to Tommaso Bagni for introducing me to the remarkable JackPot code and providing valuable insights into modeling.

I reserve special thanks for Sander, whose warm-hearted help and constant support have been invaluable throughout my study and work. Additionally, Jaap deserves heartfelt appreciation for his help since the early days of introducing me to the campus, serving as my swimming teammate, and acting as a reliable consultant whenever problems arose.

I cherish the memories with my EMS colleagues, extending my sincere thanks and greetings to Ruben, Cris, Erik, Srini, Harry, Anne, Goncalo, Anvar, Jeroen, Nando, Sahil, Koen, Wilco, Bas, Izak, Tim, Tiemo, Simon, Michiel and many others, and also to my

Chinese colleagues Chao, Haishan, Peng, Yingzhe, Wei, Keyang and Zhuo. Our time together, both inside and outside the University, has been a source of camaraderie and shared learning experiences.

The indelible journey is enriched by the cherished moments spent with my friends in Enschede. My heartfelt gratitude goes to Bingbing, Yi Wang, Aijie, Yin Tao, Liqun, Xingwu, Yang Cui, Lijie, Shuqin, Chong Wang, Liulin, Xiu, Zhiliang, Guangjiao, Wenlong, Ruilin, Lele, Chuan Li, Dongfang, Linlin, Lantian, Ying Du, Xiaokui, Jinfeng, Tianpei, Zhou Lu, Jinyuan, Can Wang, Wenbo Wang, Siyu, Hao Wei, Zhen Jiao, Qirong, Zhiguo, Ruonan, Qian Li, Jun Luo, Minmin, Yawei, Xiaozhen, Yaxiang Zeng, Song Ma, Jun Wang, Yang Wang, Yan Liu, Youwen, Xingyu, Yuxin, Qin Huang, Binbin Chen, and countless other friends who have shared this remarkable journey with me.

Special acknowledgment is reserved for my family, whose unwavering support has served as my pillar of strength. My heartfelt thanks go to my longtime friends Yanan, Liang, Wei, Laofa, Baocan, Guozheng, and Yulong for their enduring encouragement. I also extend sincere appreciation to the professors at ASIPP, namely Ling Wang, Zhenwei Wu, Yu Wu, Jinggang Qin and Fang Liu, for their invaluable guidance and help. Lastly, I express gratitude to myself for the persistence that paved the way to this accomplishment.

# Contents

# Chapter 1

# Introduction

## 1.1 Nuclear fusion

Nuclear fusion is a reaction in which two lighter atomic nuclei are merged into a heavier nucleus. The total mass of the produced nucleus is less than the reactants, and a large amount of energy is released due to the mass-energy conversion according to Einstein's equation $E = (\Delta m)c^2$. Nuclear fusion reactions power the sun and other stars.

Scientists are seeking a way to harness energy from fusion in machines on earth ever since the theory was understood. In 1920, British astrophysicist Arthur Eddington suggested hydrogen-helium fusion could be the primary source of stellar energy. In 1932, The first man-produced fusion reactions were performed by Ernest Rutherford and his team in Cambridge, UK. They observed not only the fusion of deuterium atoms, but also two new fusion born nuclei, $^3He$ and tritium [1]. In the next few decades, the fusion for military purposes developed rapidly. In comparison, research into developing controlled fusion in fusion reactors has been ongoing since the 1940s, but the technology is still in its development phase [2].

The global energy demand has increased greatly and it is expected to perhaps reach $10$ TW in the second part of this century. Furthermore, a common view on sustainable clean energy for the future is already well-established, by which time the vast majority of energy sources needs to be low-carbon. Fusion could generate four times more energy per kilogram of fuel than fission, which is presently used in nuclear power plants, and nearly four million times more energy than fossil fuel like oil or coal. Thus, fusion is one of the few potential technologies, which can meet the global energy demand. It is estimated that, to make a relevant contribution worldwide, fusion has to generate on average $1$ TW of energy in the long-term. That means at least several hundreds of fusion plants are needed in the 22nd century [3].

Fusion has the potential of providing essentially an inexhaustible energy source for the future, but some strict constraints need to be satisfied. First, the reactants of an energy releasing fusion should have relatively small mass per nucleon and large binding energy. This means the lighter elements, like hydrogen and helium, are generally more suitable. Secondly, to realize a fusion reaction, the nuclei must have enough energy to overcome the repulsive Coulomb force acting between the nuclei. The distance between nuclei must become sufficiently short before the short-range attractive nuclear force becomes dominant. Thirdly, a confining environment, with sufficient temperature, pressure, and confinement time is required to create a plasma that can serve as a basis for fusion. The plasma is a macroscopically neutral collection of ions and unbound electrons. The triple product of these three vital constraints has to reach a certain criterion, which is known as the Lawson criterion [4].

In stars, the most common fuel is hydrogen, and gravity provides optimal confinement conditions that satisfy the criteria for producing fusion energy. For the proposed fusion reactors, researchers are especially interested in the hydrogen isotopes deuterium D and tritium T, in consideration of the large amounts of energy released and relatively low temperature needed. The schematic of the deuterium-tritium DT fusion reaction is shown in Figure 1.1 and Equation 1.1

$$D + T \rightarrow {}^4He + n \quad (Q = 17.6 \text{ MeV}). \tag{1.1}$$

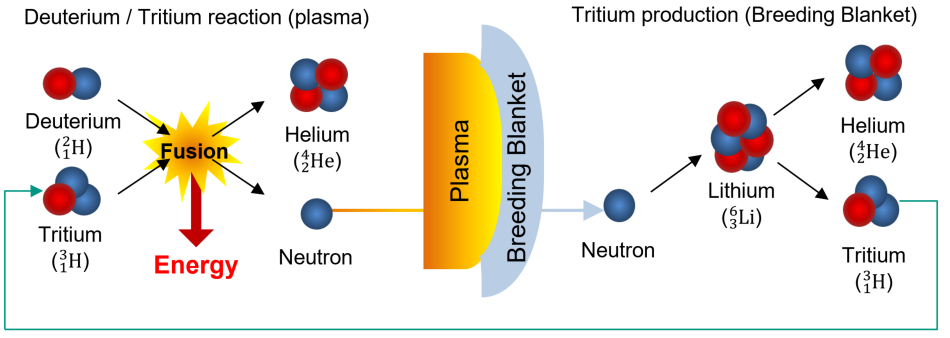


Figure 1.1: Deuterium-tritium fusion reaction and the tritium breeding reaction from lithium 6 (picture courtesy of R. Antunes, KIT-ITeP-TLK).

One advantage of this reaction is that the fuels are plentiful available and easily accessible. Deuterium can be extracted from seawater. Tritium undergoes a beta decay with a half-life of 12.5 year, it rarely exists in nature but can be produced by utilizing neutrons to act with lithium Li. It is notably at this point that, neutrons are exactly one of the products of D-T fusion.

The products of DT fusion are a helium nucleus and a neutron, together with 17.6 MeV of energy in two forms, 14.1 MeV kinetic energy of the neutron and 3.5 MeV of the alpha particle. The alpha particle is confined within the plasma and collides with the ions and electrons. During the process its energy is distributed and eventually clashes with the wall of the reaction chamber in the form of surface heat flux. The neutron escapes from the plasma immediately and transfers its kinetic energy to the surrounding materials, creating heat spots or even radiation damage in the materials. As mentioned previously, the neutrons can be captured in lithium, thereby producing tritium and then possibly sustain the fusion fuel cycle [5]. Lithium is naturally abundantly available and consists of two main isotopes, 7.5% $^6Li$ and 92.5% $^7Li$. The corresponding reactions for the tritium production are

$$n + {}^6Li \rightarrow T + {}^4He, \tag{1.2}$$

$$n + {}^7Li \rightarrow T + {}^4He + n'. \tag{1.3}$$

The first reaction (Equation 1.2) has a large cross section for thermal (slow) neutrons, while the second reaction (Equation 1.3) is more probable with fast neutrons. If the lithium is present close around the fusion chamber, it allows to absorb the runaway neutrons and produce tritium. The so-called ”breeding blanket” of lithium makes it possible to breed new fuel for a fusion reactor. The schematic of the tritium breeding reaction from lithium 6 ($^6Li$) is shown in Figure 1.1 as well.

Besides the sustainable fusion fuel cycle, heating a plasma to favorable thermonuclear temperatures and then confining it sufficiently long so as to establish and maintain a net positive energy balance, are the two premier technical issues that are determining the feasibility of fusion as an energy source.

In order to achieve high power density and a quasi-steady-state mode of operation, various confinement concepts are investigated by fusion scientists. For example, three main

designs of z-pinch, stellarator and magnetic mirror were proposed in the early stage. In recent years, magnetic confinement and inertial confinement (ICF) by lasers have shown an impressive development. The corresponding main representatives are the ITER (International Thermonuclear Experimental Reactor) tokamak in France, and the National Ignition Facility laser in the United States, both are under research at very large scale. Furthermore, there is increasing interest in attractive approaches, like magnetized target fusion, inertial electrostatic confinement, and new variations of the stellarator [5].

Among all the concepts, the most promising one for utilizing fusion energy peacefully, might be magnetic confinement. It is also called tokamak and was first tested in Russia in 1968, although at that moment lacking the capacity for containing a high-temperature plasma.

The success of the tokamak prompted the construction of larger devices and the operation of which began in the first half of the 1980s, including the Joint European Torus (JET) in Culham, UK, the Tokamak Fusion Test Reactor (TFTR) in Princeton, USA and the Japanese Tokamak (JT-60) in Naka, Japan. Many complementary devices and facilities were also built around the world, to investigate the broad range of science, technology and engineering challenges. An important milestone was achieved in the 1990s when JET and TFTR generated fusion energy using a mixture of tritium and deuterium. On this basis, Europe developed a first coherent, comprehensive goal-driven programme for building a next generation fusion device on a power plant scale, based on the tokamak concept.

However, achieving commercially viable fusion requires a substantial number of coordinated resources deployed at a European level over a long period of time, in order to get a clear and structured guidance for the programme. The European roadmap to fusion energy was released based on the common view of all the fusion stakeholders [3], [6].

This roadmap rests on three main pillars: ITER, DEMO and a fusion material testing facility IFMIF-DONES. A few years after, high performance DT operation of ITER is achieved and the first results from the ITER Test Blanket Modules (TBMs) are available, the engineering design should be ready for construction of a DEMOnstration Fusion Power Plant (DEMO), aiming to have DEMO operational around 20 years after high power burning plasmas are demonstrated in ITER. In parallel, the need to build up fusion relevant neutron source facilities to obtain data of materials under irradiation for design, licensing, construction and safe operation of DEMO is widely recognized. This includes the IFMIF (International Fusion Materials Irradiation Facility) project, also called DONES program. The critical technical milestones for fusion by magnetic confinement are summarized as follows:

1. Technical demonstration of large-scale fusion power. This is the first goal of ITER (500 MW for 400 second);

2. Electricity generated by DEMO and delivered to the grid, yielding hundreds of MW of electricity for several hours and operating with a closed fuel cycle and including other features that could be extrapolated to early commercial fusion power plants;

3. In parallel, a science, technology, innovation and industry basis to allow the transition from DEMO to affordable devices suitable for large-scale commercial deployment (also stellarators might prove particularly attractive);

4. Large scale industrial production of fusion plants.

The roadmap in a nutshell is shown in Figure 1.2. As part of its innovation and backup strategy, the roadmap also proposes a probable long-term alternative to tokamaks: the stellarator, a concept that confines plasma differently with potential advantages, but the design is technically much more challenging. The fusion community regards Wendelstein 7-X as Europe's flagship stellarator device, which is well integrated in the overall research line, and is complementary to ITER and DEMO.

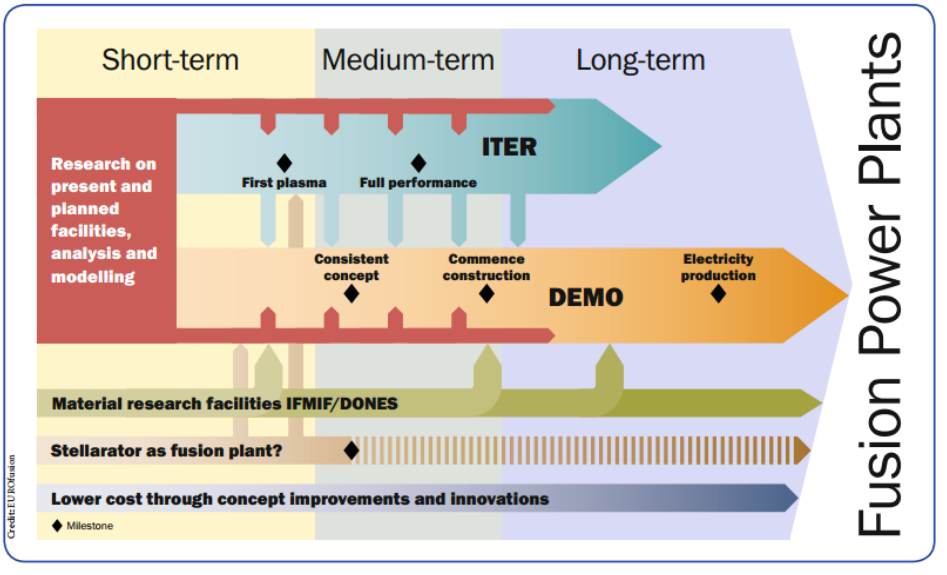


Figure 1.2: European roadmap of nuclear fusion development in a nutshell. The short-term, medium-term, and long-term periods roughly range from the year 2000 to 2030, 2030 to 2040, and 2040 to 2060, respectively [3].

## 1.2 Tokamak magnetic confinement

In magnetic confinement for fusion, a magnetic field configuration is designed specifically so that the charged plasma particles are trapped in traces keeping them away from the wall materials. It requires that the steady magnetic field is strong enough to restrain the motion of the charged particles and let them follow the magnetic field lines under the influence of Lorentz force.

Until now, the most successful device for controlling the plasma particles along the magnetic field lines is the tokamak. In a tokamak, the plasma is formed in the shape of a donut, by arranging a set of D-shaped coils in the form of a torus, the magnetic field lines are then bent and formed into a toroidal magnetic field. However, a purely toroidal field is not sufficient to obtain an equilibrium of the plasma. The magnetic field line curvature results in opposite particle drifts, which leads to a charge separation and a rapid loss of plasma to the walls due to the generated electric field. A poloidal magnetic field is added and the combination of the toroidal and poloidal magnetic fields produces helical magnetic

field lines, which are spiraling around the torus and forming globally closed magnetic flux surfaces. A schematic of a tokamak magnet system is shown in Figure 1.3. The hot plasma is confined by the helical magnetic field created by coils and plasma current, keeping it far away from the vacuum vessel walls in a stable way and for sufficient duration. Inside the nested magnetic flux surfaces, the hot plasma in the core is thermally insulated from the colder plasma near the edge. The charged particles are not able to move freely across the magnetic surfaces only by collisions with other charged particles or through turbulence.

In a tokamak, huge magnetic forces are applied to act against the plasma pressure and confine the plasma. The plasma pressure is proportional to the product of the density and the temperature, and it is always much smaller than the magnetic field pressure. For practical devices, the maximum magnetic forces in such magnetic field configurations are limited by technological constraints, like the maximum magnetic field that can practically be generated in the superconducting coils [7].

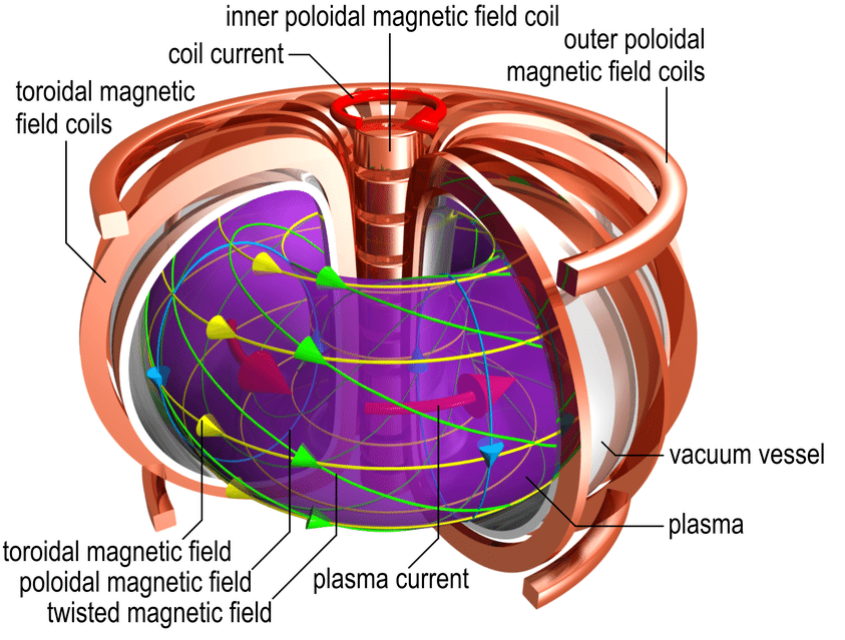


Figure 1.3: Schematic of a tokamak. The plasma is confined by a helical magnetic field created by superconducting magnet coils and the plasma current.

### 1.2.1 ITER magnet system

The tokamak is the most advanced toroidal confinement system and is presently the most promising candidate for the first generation of fusion reactors. This has culminated in the ongoing construction of the ITER device based on the tokamak concept [8]. Thousands of scientists and engineers from the European Union, China, India, Japan, the Republic of Korea, the Russian Federation and the USA, also called Domestic Agencies (DAs),

have come together in an unprecedented international collaboration to build the ITER device at Cadarache, in the south of France. ITER aims to demonstrate the scientific and technical feasibility of fusion reactors and aims to be the first fusion device to produce energy with $Q = 10$, corresponding to an output of 500 MW for 50 MW of input power. Considering the overall energy efficiency (ratio of final electric energy output to the grid, to the fusion energy produced in the devices) of the reactors is about 35%. This implies that a sustainable fusion reactor could be achieved when operating with $Q$ between 20 and 40. It should be noted that ITER is an experimental fusion device not intended to generate electric energy.

For ITER, its magnet system consists of 18 Toroidal Field (TF) coils, a Central Solenoid (CS) with 6 individually powered modules and 6 Poloidal Field (PF) coils providing inner and outer poloidal fields respectively, and 18 Correction Coils (CCs). All coils are wound with superconductors. The structure of the ITER magnet system is shown in Figure 1.4. The TF coils generate the magnetic field to confine the charged particles in the plasma, the CS coils provide the inductive flux to ramp up the plasma current and contribute to the plasma shaping, the PF coils provide the position equilibrium of plasma current and the plasma vertical stability. The CCs provide a correction of error field harmonics coming from position errors, particularly toroidal asymmetry, as well as from busbars and feeders [9].

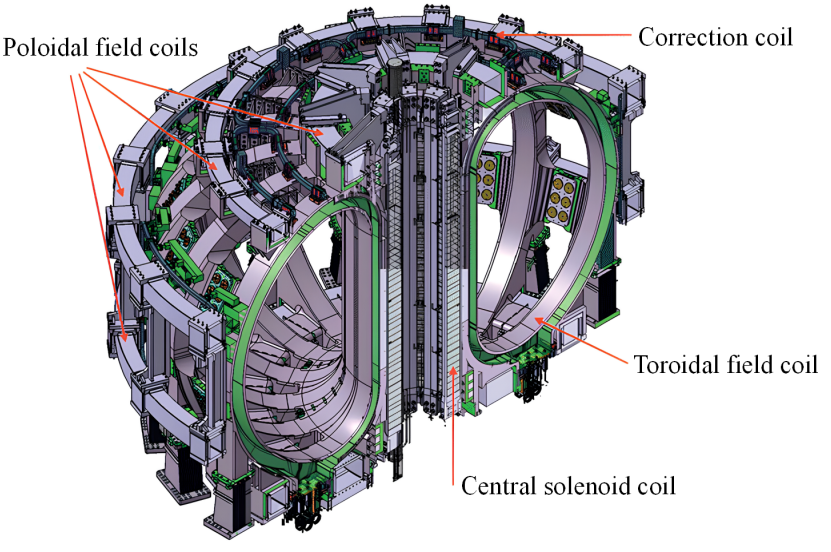


Figure 1.4: Schematic cross section of the ITER magnet system.

- TF Coils

The TF coils are D-shaped with centerline length of 34.1 m, and forming the main structure of the magnet system. The TF coils are designed to carry a 68 kA steady-state current, and generate a constant toroidal field of 5.3 T to confine the plasma during a burn

cycle, however, the maximum field reaches about 12 T at the inner legs of the TF coil. For this reason, large Cable-In-Conduit (CIC) superconductors with high current density $Nb_3Sn$ strands are used for the windings. Furthermore, the TF coils have to withstand huge centripetal and shear loads, so sufficient mechanical support is added to the design of the coils. The conductor is first encased in steel radial plates to form a double pancake (DP), and seven DPs are arranged together to form a winding pack, which is then inserted into a massive austenitic steel case and welded to the coil support structure. The coils are supported fully independently of the vessel and associated components [10]–[12].

- CS Coils

The set of CS coils is the backbone of the ITER magnet system, six independent coil modules, with diameter of 3.6 m and height of 2.1 m, are stacked vertically to satisfy the plasma equilibrium and shaping requirements. The CS coils are hung from the top of the TF coils through their pre-load structure, which consists of a set of tie-plates to provide axial pressure on the stack, located at both inner and outer sides of the coil stack. The currents of the coils are driven up to 40 or 45 kA independently and they are capable in providing a peak magnetic field of 13 T with a magnetic field ramp rate of 1.3 T/s, thus satisfing a range of operating scenarios like the pulsed mode [13], [14].

- PF Coils

The Poloidal Field system consists of six horizontal solenoids placed outside the toroidal magnet structure, with diameters in the range of 8 to 24 m. The six PF coils are attached to the TF coil cases through flexible plates or sliding supports allowing radial displacements. The operating conditions are different for each coil and the dimension specifications as well. Therefore, three different types of PF CICCs (PF 1/6, PF2-4 and PF5) are designed to satisfy the requirements, all made with niobium-titanium (NbTi) superconductors. The conductors are wound into double-pancakes with a two-in-hand winding scheme, and 6 to 9 DPs are stacked vertically to build a single PF coil. The coils are capable in providing a maximum current of 48 to 55 kA, and a peak magnetic field of 6 T [15], [16].

- Correction Coils

As a complementary part of the ITER magnet system, the correction coils are inserted between the Toroidal and Poloidal Field coils and distributed around the tokamak circumference. The CC system consists of three independent sets of CCs with six coils each, located at the top, side and bottom regions respectively, with respect to the equator of ITER. The top and bottom CCs measure approximately 3 meters by 7 meters, while the side CCs measure approximately 7 meters by 8 meters. Within each set, the coil is connected to the opposite coil in anti-series, to produce an asymmetric mode and avoid coupling with axisymmetric magnetic fields. The coils are used to correct error fields from positioning inaccuracies in the TF, CS and PF coils, as well as from the neutral beam systems and feedback control of plasma resistive wall modes. The operating current of the CCs is up to 10 kA with a minimum design temperature margin of 1.5 K under 5 T nominal peak magnetic field [17], [18].

The main parameters of the four types of coils are summarized in Table 1.1 [12].

Table 1.1: Main parameters of the ITER magnet system coils [12], [18], [19].

| Parameters | TF | CS | PF | CC |
|---|---|---|---|---|
| Material | $Nb_3Sn$ | $Nb_3Sn$ | NbTi | NbTi |
| Number of coils | 18 | 6 | 6 | 18 |
| Number of turns per coil or WP | 134 | 549 | 115-459 | 32/20/32 |
| Stored magnetic energy [GJ] | 41 | 7 | 4 | n/a |
| Maximum operating current [kA] | 68 | 45 | 45 | 10 |
| Nominal peak field [T] | 11.8 | 13.0 | 6.0 | 5 |
| Electrical discharge time constant [s] | 15 | 11.5 | 18 | n/a |
| Coil total weight[a)] [t] | 6540 | 954 | 2163 | 85 |
| SC strand total weight [t] | 410 | 104 | 240 | 21 |
| Centring force per coil [MN] | 403 | n/a | n/a | n/a |
| Vertical force per coil, max [MN] | n/a | 327 | 160 | n/a |
| In plane bursting force per half coil [MN] (maximum for CS and for each PF) | 205 | 220 | 43,13,30,19,64,54 | n/a |
| Cross section of coil [$m^2$] | 0.562 | 0.86 | 0.44,0.2,0.32,0.29,0.37,0.82 | 0.02,0.01,0.02 |
| He mass flow rate in conductor [g/s] | 8 | 8 | 8-14 | 1-4 |
| He mass flow rate of structures [kg/s] | 2.5 | 2.0 | 0.3-0.4 | 0.02,0.09,0.02 |

[a)] includes case and supporting structures.

## 1.3 Superconductivity in technical conductors

Superconductivity is a phenomenon of zero electrical resistance and expulsion of magnetic field observed in certain materials, when cooled below a critical temperature. Superconductivity is a quantum mechanical phenomenon and was discovered by the Dutch physicist Heike Kamerlingh Onnes in 1911. Besides the critical temperature $T_c$, which characterizes the material, the transition from normal conducting to superconducting state also depends on an upper critical magnetic field $B_{c2}$ and a critical current density $J_c$. The latter is usually normalized to the wire cross-section, and referred to as engineering current density. The critical values of several most practical superconducting materials are summarized in Table 1.2.

Table 1.2: Critical temperature, upper critical field and engineering critical current density for practical superconductors [20], [21].

| Material | $T_c$ at 0 T [K] | $B_{c2}$ at 0 K [T] | $J_c(B, 4.2\ \mathrm{K})$ [$\mathrm{A/mm^2}$] |
|---|---|---|---|
| NbTi | 9.2 | 14.6 | 1800 (5 T) |
| $Nb_3Sn$ | 18.3 | 24-28 | 1900 (12 T) |
| YBaCuO | 92 | >100 | 400 (20 T) |
| Bi-2212 | 94 | >100 | 600 (20 T) |
| Bi-2223 | 110 | >100 | 600 (20 T) |

The properties of superconducting materials are also sensitive to strain $\epsilon$, although the effect is insignificant for NbTi, while for the crystal-like superconductors, like $Nb_3Sn$, the effect of strain on the critical behavior is substantial. Strain generates shifts in the field-temperature phase boundary and then alters $B_{C2}$ and $T_c$. The changes affect the critical

current density $J_c$ [22].

Considering the multiple constraints, the performance of a superconductor is generally described by means of a critical surface, which is the boundary between superconductivity and normal resistivity in the 3 dimensional $J$-$B$-$T$ space, see Figure 1.5. In order to maintain superconductivity, the applied magnetic field $B$, the temperature $T$ and the current density $J$ of the material must be below the critical surface with some margin, otherwise, a transition to the normal conducting state will occur.

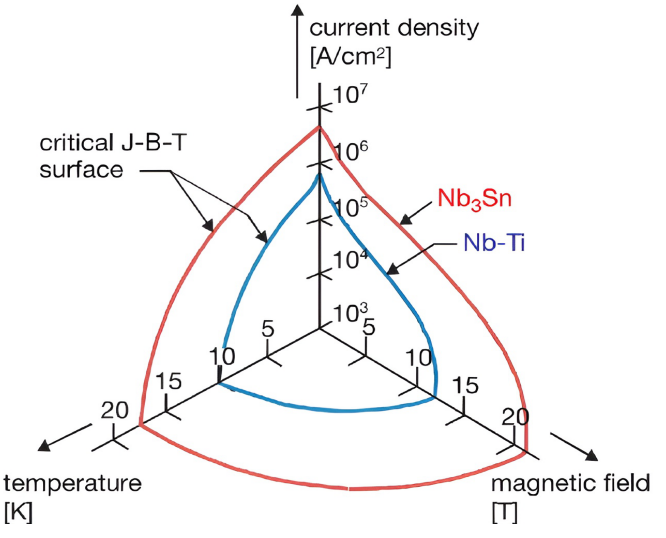


Figure 1.5: Critical surface of niobium-titanium (NbTi) and niobium-tin ($Nb_3Sn$).

In practical applications of superconductivity, the operating temperature is often set around 4.2 K, which is the temperature of liquid helium at one atmosphere. Therefore, a relevant description reserved for different superconducting materials is the critical current density variation with respect to the applied magnetic field. Figure 1.6 illustrates the engineering critical current density dependence on the applied magnetic field at 4.2 K for a number of practical superconductors.

Until now, NbTi and $Nb_3Sn$ are the most used superconducting materials and they are also the superconductors used for the ITER magnets. Equations 1.4 [23], [24] and 1.8 [25], [26] corresponding to both materials respectively, are commonly adopted to describe the $J_c$ changes with temperature and magnetic field and, eventually, strain for $Nb_3Sn$.

$$\textbf{NbTi}: J_c = \frac{C_0}{B}(1-t^{1.7})^{\gamma} b^{\alpha}(1-b)^{\beta}\,[\mathrm{A}\cdot\mathrm{mm}^{-2}], \tag{1.4}$$

with $t$ reduced temperature, $b$ reduced magnetic field and $B$ applied magnetic field. $C_0$, $\gamma$, $\alpha$ and $\beta$ are fitting parameters for the specific wire. The reduced temperature is defined as

$$t = \frac{T}{T_{C0}}, \tag{1.5}$$

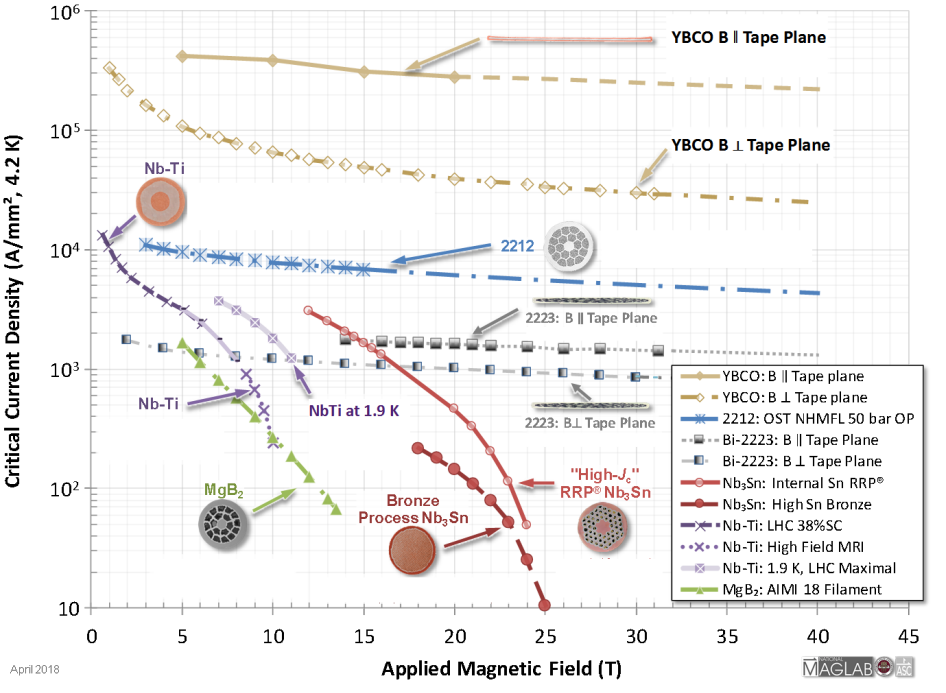


Figure 1.6: Engineering critical current density versus applied magnetic field for practical superconductors available in long lengths, specifications of samples are detailed in [21].

where $T$ is the operating temperature and $T_{C0}$ is the critical temperature at 0 T. The reduced magnetic field is defined as

$$b = \frac{B}{B_{c2}(T)}, \tag{1.6}$$

where $B_{c2}(T)$ is the upper critical magnetic field at the operating temperature $T$, as expressed in Equation 1.7

$$B_{c2}(T) = B_{c20} \cdot (1 - t^{1.7})\ [\mathrm{T}], \tag{1.7}$$

where $B_{c20}$ is the upper critical magnetic field at 0 K.

$$\mathbf{Nb_3Sn}: J_c = \frac{C_1}{B} \cdot S \cdot (1 - t^{1.52})(1 - t^2) b^p (1 - b)^q\ [\mathrm{A \cdot mm^{-2}}], \tag{1.8}$$

with $t$ reduced temperature, $b$ reduced magnetic field, $S$ strain dependent term and $B$ applied magnetic field. $C_1$, $p$ and $q$ are fitting parameters for the specific wire. The reduced temperature is defined as

$$t = \frac{T}{T_c^*(\epsilon)}, \tag{1.9}$$

with

$$T_c^*(\epsilon) = T_{cm}^* \cdot S^{\frac{1}{3}} \text{ [K]}, \tag{1.10}$$

where $T_{cm}^*$ is the inhomogeneity averaged critical temperature. The reduced magnetic field is given by

$$b = \frac{B}{B_{c2}^*(\epsilon, T)}, \tag{1.11}$$

where

$$B_{c2}^*(\epsilon, T) = B_{c2m}^*(0) \cdot S \cdot (1 - t^{1.52}) \text{ [T]}, \tag{1.12}$$

with $B_{c2m}^*(0)$ the inhomogeneity averaged upper critical magnetic field at 0 K. The strain dependent term $S$ is defined as

$$S = \frac{C_{a,1} \cdot [\sqrt{\epsilon_{shift}^2 + \epsilon_{0,a}^2} - \sqrt{(\epsilon_{axial} - \epsilon_{shift})^2 + \epsilon_{0,a}^2}] - C_{a,2} \cdot \epsilon_{axial}}{1 - C_{a,1} \cdot \epsilon_{0,a}} + 1, \tag{1.13}$$

where $C_{a,1}$ and $C_{a,2}$ are the second and third invariant of the axial strain sensitivity, $\epsilon_{axial}$ is the axial strain (sum of applied and pre-compression strains), $\epsilon_{0,a}$ is the remaining strain component when $\epsilon_{axial} = 0$, and $\epsilon_{shift}$ is the measurement related strain given by

$$\epsilon_{shift} = \frac{C_{a,2} \cdot \epsilon_{0,a}}{\sqrt{C_{a,1}^2 - C_{a,2}^2}}. \tag{1.14}$$

NbTi is widely used in practical applications of superconductivity, of which the operating magnetic field is below about 8 T. In the ITER magnet system, NbTi is used in the Poloidal Field coils and Correction Coils. $Nb_3Sn$ compound is able to operate in a higher magnetic field range up to about 16 T. However, $Nb_3Sn$ is very brittle and thus the wires in the CICCs of the superconducting magnets should not be subjected to irreversible strain levels. For $Nb_3Sn$ so far, the ITER Central Solenoid and Toroidal Field coils are the first large-scale applications requesting large commercial wire production.

Both NbTi and $Nb_3Sn$ are low-temperature superconductors that need cooling with liquid helium at about 4.5 K. At such cryogenic temperature, the specific heat of the materials is reduced significantly and is about 2000 times lower than at room temperature. This implies that even a small energy release can produce a temperature rise that can trigger a quench, which is a sudden transition from the superconducting to the normal state [27]. The quench enforces the conversion of the stored energy into mostly heat. Therefore, it is necessary to control the heat in the coils with a quench protection strategy, enabling a safe temperature limit for the conductors.

An appropriate temperature margin $\Delta T$ is considered to ensure a reliable operation during the most critical scenarios like a plasma disruption in the tokamak. The temperature margin $\Delta T$ is defined as [20]

$$\Delta T = T_{cs} - T_{op} = (T_c(B) - T_{op}) \cdot (1 - \frac{I_{op}}{I_c}) \text{ [K]}, \tag{1.15}$$

where $T_{cs}$, $T_{op}$ and $T_c(B)$ are the current sharing temperature, operating temperature and critical temperature at the applied magnetic field $B$ respectively, whereas $I_{op}$ and $I_c$ are the operating and critical currents. Different from the ideal superconductor that exhibits an abrupt transition from superconducting to normal state, in practical superconductors the transition occurs over an extended current or temperature range. Thereby, a certain criterion determining the two-state transition was established. For low temperature superconductors, the current sharing temperature $T_{cs}$ is adopted with a criterion defined as the temperature at which an electric field of $10\ \mu\mathrm{V/m}$ is detected along the sample while slowly ramping the temperature at fixed current. In analogy to the critical temperature $T_c$ of ideal superconductors, the $T_{cs}$ is thus determined by current, magnetic field and strain. The operating temperature $T_{op}$ is the local temperature of the superconductor, which results from the balance between the cooling capacity and the heat generation within the windings.

### 1.3.1 Strands

For practical applications, the low temperature superconductors are shaped into wires, also called strands when part of a cable, with a diameter normally in the range of 0.7 to 1.3 mm. The superconductor in a wire is subdivided into a large number of fine superconducting filaments, with diameters in the range of 1 to 100 µm. The filaments are embedded in a matrix of normal conducting metal, typically copper or aluminium with low-resistivity and twisted to electromagnetically reduce coupling to transverse magnetic field [27].

Flux jumping is the fundamental reason for the subdivision of the superconducting material in strands. The magnetic flux penetrates the superconductor by means of flux lines and each flux line contains a quantum of flux ($2 \cdot 10^{-15}$ Wb) in a core of normal material surrounded by circulating supercurrents. Normally, the flux lines are pinned at certain pinning sites, however, in the case of a thermal perturbation, the resulting temperature rise can decrease the pinning potential and reduce the critical current density eventually resulting in a collective flux line motion or jump [28]. An effective method to minimize the risk on a quench is to decrease the cross section of the superconductor by subdividing it into multi-filaments with smaller diameter. Like wise the diameter of the wire is limited as well forcing to use relatively thin wires of some 0.7 to 1.3 mm.

In steady state, the currents flow in the filaments without resistance, however, when the strand is subjected to a time-varying magnetic field, inter-filament coupling currents are induced transferring through the resistive matrix. The coupling currents can be effectively reduced by twisting the filaments, thus the magnetic flux embraced by the current loops changes sign every half-twist pitch.

Superconductors in the normal state are usually characterized by poor electrical conductivity. In the case of a transition to the normal state, it is necessary to provide a low resistive parallel path for the current and avoid excessive ohmic heating in the superconductors. The twisted filaments are embedded in a low resistive matrix for protection. The typical matrix materials, like Cu for NbTi, CuSn/Cu for $Nb_3Sn$ and Ag for BSCCO-2212 wires, exhibit an electrical resistivity that is several orders of magnitude lower than that of a superconducting filament in the normal state.

The residual resistivity ratio (RRR) is used to reflect the main properties of copper used as matrix material in the strands. It is defined as the ratio of the wire resistance at

293 K to the resistance at a sufficiently low temperature, like liquid helium temperature of 4.2 K, or the practically choices of 10 or 20 K [29], [30]. The RRR of the strands is one of the quality assurance parameters, related to the electrodynamic stability of the coils and for limitation of the hot spot temperature in the case of a quench [29].

For practical superconductors, the voltage drop along the superconducting strands is a non-linear function of the strand current, temperature and magnetic field (and strain in the case of $Nb_3Sn$). The transition to the normal state is normally described by a so-called $E$-$J$ power law

$$E = E_c \cdot (\frac{I}{I_c})^n \ [\mathrm{V/m}], \tag{1.16}$$

where $I$ and $I_c$ are the strand current and critical current respectively. The criterion field $E_c$ is typically set to 10 or 100 $\mu\mathrm{V/m}$ for low- or high-temperature superconductors respectively. The $n$-value is usually considered as a 'quality index' that characterizes the steepness of the $E$-$J$ transition. Similar to the critical current, the $n$-value is strongly dependent on magnetic field, temperature and strain [31], [32].

ITER TF and CS coils are wound with $Nb_3Sn$ strands, which are chromium plated to prevent sintering during heat treatment and limit coupling current loss. There are two typical wire processing methods called "bronze" and "internal-tin" routes, developed to manufacture $Nb_3Sn$ strands [33]. Two types of NbTi strands are used for other coils. Type 1 NbTi strand is used for the top and bottom PF coils (PF 1&6) where the conductor peak magnetic field is higher, while the Type 2 NbTi strand is used for the other PF coils (PF 2-5), all CCs and all feeder conductors. Both NbTi strand types are nickel-plated to control the coupling currents [34]. The main specifications for the ITER NbTi and $Nb_3Sn$ strands are detailed in Table 1.3, while a few characteristic strand cross-sections are shown in Figure 1.7.

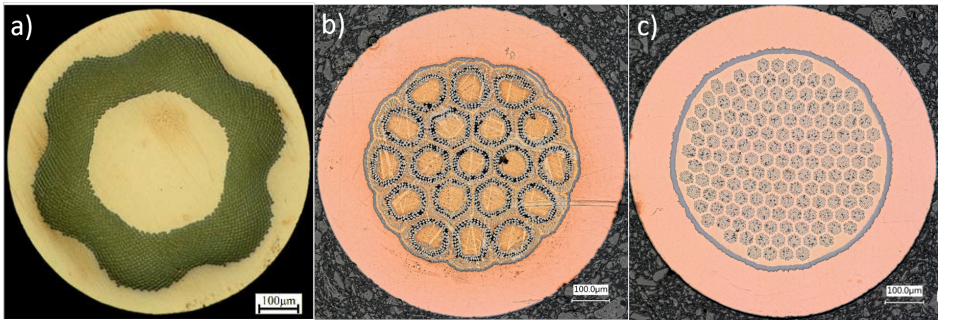


Figure 1.7: Cross-sections of ITER strands, (a) WST NbTi Type 2 strand for Poloidal Field conductors [35], (b) OST internal tin $Nb_3Sn$ strand for Toroidal Field conductors and (c) Furukawa bronze routed $Nb_3Sn$ strand for Central Solenoid conductors.

Table 1.3: Specifications of ITER NbTi and $Nb_3Sn$ strands [34].

| Parameter | **NbTi** | | **$Nb_3Sn$** | |
|---|---|---|---|---|
| | Type 1 | Type 2 | TF | CS |
| Outer diameter [mm] | $0.730 \pm 0.005$ | $0.730 \pm 0.005$ | $0.820 \pm 0.005$ | $0.830 \pm 0.005$ |
| Plating type | Ni | Ni | Cr | Cr |
| Plating thickness [µm] | 2 | 2 | 2 | 2 |
| Twist pitch [mm] | $15 \pm 2$ | $15 \pm 2$ | $15 \pm 2$ | $15 \pm 2$ |
| Twist direction | right hand | right hand | right hand | right hand |
| Cu-to-non-Cu ratio | 1.0 | 1.0 | 1.6 | 2.3 |
| Filament diameter [µm] | $\leq 8$ | $\leq 8$ | $\leq 5$ | $\leq 5$ |
| RRR of plated strand | $\geq 100$ | $\geq 100$ | $\geq 100$ | $\geq 100$ |
| Min. critical current[a)] [A] | 306 (6.4 T) | 339 (5.0 T) | 190 (12.0 T) | 228 (12.0 T) |
| n-value[b)] | $\geq 20$ (6.4 T) | $\geq 20$ (5.0 T) | $\geq 20$ (12.0 T) | $\geq 20$ (12.0 T) |
| Max. hysteresis loss[c)] [mJ/cm$^3$] | 55 ($\pm$1.5 T) | 45 ($\pm$1.5 T) | 500 ($\pm$3.0 T) | 500 ($\pm$3.0 T) |

[a)] on ITER barrel at 4.22 T and field $B_{ref}$.
[b)] in 0.1-1 µV/cm range, on ITER barrel at 4.22 T and magnetic field $B_{ref}$.
[c)] per strand unit volume at 4.22 T and reference magnetic field cycle $B_{ref}$.

### 1.3.2 Cable-In-Conduit Conductors

Considering that the current capacity of one single strand is limited, many strands are cabled to obtain a large current for generating high-magnetic fields. The high current is needed to limit the self-inductance of the coils, in order to control the time needed to extract the current in the case of a quench. The cabling strategy is in analogy to the twisting of multi-filaments in a strand, also for reducing inter-strand coupling loss. In all ITER coils and busbars the design concept of Cable-In-Conduit Conductor (CICC) is used [36], by which hundreds of superconducting and copper strands are twisted in multiple cabling stages following a certain cable pattern. The bundle of strands with a central cooling spiral inside, are inserted into a strong metal jacket called conduit. The helium leak-tight conduit primarily provides mechanical reinforcement by taking up practically all the Lorentz force in the coil windings during operation. An ITER TF CIC conductor disassembled following its five cabling stages is illustrated in Figure 1.8.

The inter-strand contact resistances in CICCs are critical for current sharing among strands and the coupling losses, and thus affect the electro-magnetic and thermal stability. Besides the inherent characteristics like strand resistivity and surface plating, the cabling pattern, twist pitches and void fraction also affect the contact resistances significantly. Copper strands are usually mixed with the superconducting strands in the cable to provide low resistivity current paths in the case of transition from superconducting to normal state, and hence improve the stability. In order to reduce the inter-strand coupling loss in pulsed operation, especially between strands belonging to different sub-cables (petals), stainless steel strips are wrapped around the petals for suppressing large current loops, with an overlap ratio of about 50% in consideration of a good helium cooling simultaneously.

With regard to cooling, supercritical helium flows through the central cooling spiral and the interstices between the strands with a typical void fraction of about 30%. The central channel provides lower hydraulic impedance and pressure relief to the flow of the supercritical helium coolant. In the cable bundle region, a transverse thermal-hydraulic

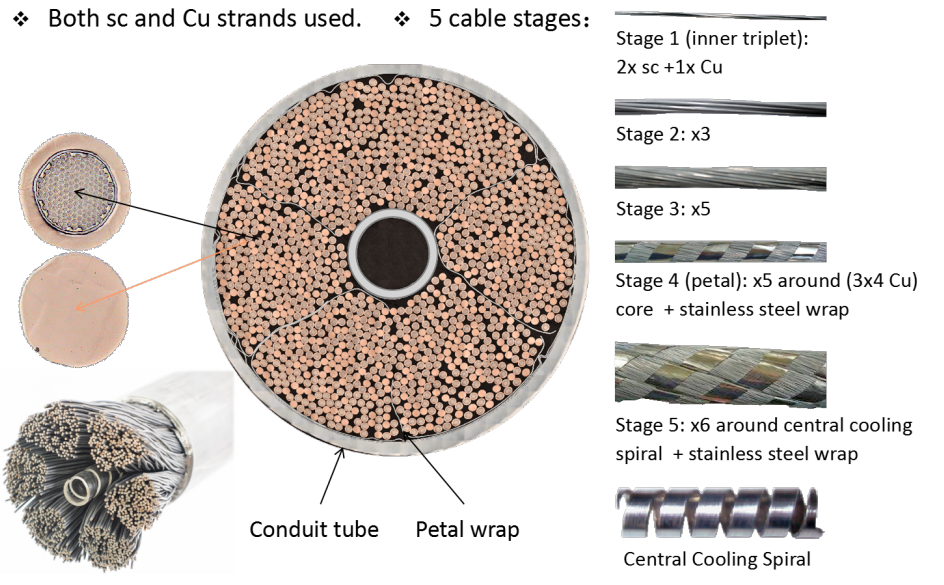


Figure 1.8: View of an ITER Toroidal Field CIC conductor showing the underlying multi-stage structure (picture courtesy of C. Sanabria and P. J. Lee [37]).

inhomogeneity produces transverse transport fluxes, which relates to friction factors and heat transfer coefficients. The structure of the spiral cooling tube allows mass, momentum and energy transfer between cable bundle region and central channel. Mass transfer enables the pressure relief in the case of sudden heating in the strands. Momentum transfer determines the pressure drop along the CICC and the related cost of pumping. While heat transfer significantly affects the most relevant time scales of thermal-hydraulic transients in a CICC, there are different heat transfer channels in an ITER CICC, connecting the helium, strands and jacket [38], [39]. Actually, CICCs with large heat transfer coefficients and large wetted surfaces, together with bath-cooling using supercritical helium, are sufficient to provide a large stability margin for operation.

The main specifications of the ITER CIC conductors are detailed in Tables 1.4 and 1.5.

Table 1.4: Specifications of ITER Toroidal Field, Central Solenoid and Correction Coil conductors [34], [40]–[43].

| Parameter | TF | CS | CC |
|---|---|---|---|
| Cable pattern | ((2SC+1Cu)×3×5×5+C)×6 | (2SC+1Cu)×3×4×4×6 | 3×4×5×5 |
| Core diameter [mm] | 0.82×4 (3Cu) | n/a | n/a |
| Central spiral[a)] [mm] | 10×9.0 | 9×8.85 | n/a |
| Petal wrap[b)] | 0.10 mm × 50% | 0.05 × 70% | n/a |
| Cable Warp[c)] | 0.10 × 40% | 0.08 × 40% | 0.08 × 40% |
| Nr. of SC strands | 900 | 576 | 300 |
| Void fraction | 29.7% | 33.5% | 35.4% |
| Cable size [mm] | Φ39.7 | Φ32.6 | 14.8×14.8 |
| Jacket shape | Circular | Circle in square | Square |
| Jacket size | Φ43.7 | 49×49 | 19.2×19.2 |
| Twist pitches [mm] | | | |
| 1st stage | 80 | 20 | 45 |
| 2nd stage | 140 | 45 | 85 |
| 3rd stage | 190 | 80 | 145 |
| 4th stage | 300 | 150 | n/a |
| Final stage | 420 | 450 | 250 |

[a)] outer diameter [mm] × pitch; the thickness is 1 mm.
[b)] thickness [mm] × coverage area [%].
[c)] thickness [mm] × overlap area [%].

Table 1.5: Specifications of ITER Poloidal Field Coil conductors [34], [40], [43].

| Parameter | PF 1,6 | PF 5 | PF 2,3,4 |
|---|---|---|---|
| Cable pattern | 3SC×4×4×5×6 | (3SC×4×4×4+C)×6 | (((2SC+1Cu)×3×4+C1)×5+C2)×6 |
| Core diameter [mm] | - | 2.85 | 1.20(C1)/2.70(C2) |
| Central spiral[a)] [mm] | 12×8.85 | 12×8.85 | 12×8.85 |
| Petal wrap[b)] | 0.05 × 50% | 0.05 × 50% | 0.05 × 50% |
| Cable Warp[c)] | 0.10 × 40% | 0.10 × 40% | 0.10 × 40% |
| Nr. of SC strands | 1440 | 1152 | 720 |
| Void fraction | 34.3% | 34.1% | 34.2% |
| Cable size [mm] | Φ37.7 | Φ35.3 | Φ35.3 |
| Jacket shape | Circle in square | Circle in square | Circle in square |
| Jacket size | 53.8×53.8 | 51.9×51.9 | 51.9×51.9 |
| Twist pitches [mm] | | | |
| 1st stage | 45 | 45 | 45 |
| 2nd stage | 85 | 85 | 85 |
| 3rd stage | 145 | 145 | 145 |
| 4th stage | 250 | 250 | 250 |
| Final stage | 450 | 450 | 450 |

[a)] outer diameter [mm] × pitch [mm], the thickness is 1 mm.
[b)] thickness [mm] × coverage area [%].
[c)] thickness [mm] × overlap area [%].

### 1.3.3 Electrical joints

Large fusion magnets call for high-current conductors (up to 70 kA in ITER). Considering the large dimensions of the coils and the limited conductor production length, several unit lengths of conductor are joined at their extremities for winding the coils. Besides connecting superconductors, joints are also essential for interfacing the coils with bus bars and feeders connecting to the power supplies. A few key specifications have to be considered in particular for the joint design: a large number of strands (around 1000), a low resistance at high current (1 to 2 nΩ) to limit the cryogenic load, low loss in pulsed magnetic field operation, $Nb_3Sn$ heat treatment, helium tightness control and limited available space.

A conceptual lap joint design was developed by CEA to satisfy these requirements, by clamping two separate twin boxes together to provide a reliable connection [44]. Each twin box (half joint) is a leak-tight bi-metallic box manufactured by explosion bonding of a copper sole and a stainless steel plate. Inside the box, the strands on the cable periphery are freed of Ni/Cr coating by brushing to obtain a bare copper surface, or even plating with silver or tin is applied, to improve the electrical conductivity. Furthermore, the outer parts of the petal wraps are removed at the joint cable section. After the treatment, the strands in contact with the copper sole are either soldered to or pressed onto the sole to get an improved cable-sole interface condition. The cable section is compacted to about 20% void fraction with a box cover to ensure low and stable electrical resistance of the joints. A twin box is then completed when the cover is sealed with welds. Two of such twin boxes are soldered or compressed with indium wires in between to form a joint. Depending on the specific connection or assembly requirements, the twin-box lap-type joint can be assembled in either "shaking hands" or "praying hands" configuration [45].

The lap type joint is used everywhere in the ITER magnet system except in the CS coils. The cross-sections of several ITER CIC joints are shown in Figure 1.9, corresponding to PF and TF full-size joints and two half joint boxes of CC and MB conductors for the Feeders, respectively.

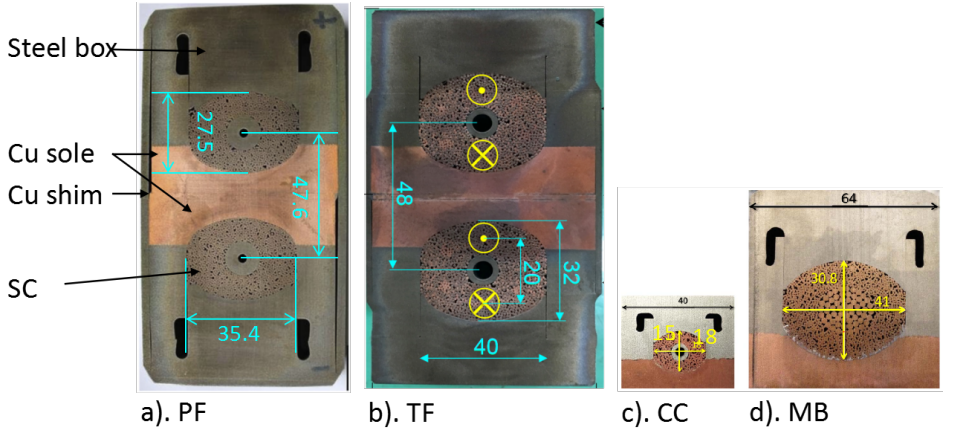


Figure 1.9: Family of twin box joints: a) PF6 joint by ASIPP, b) TF joint by NIFS (similar design with the CS lead joint), half joint box of c) CC and d) MB conductors. The copper shim in between the joint boxes is to mitigate assembly tolerances [46]–[48].

The differences in the joint design among the coils are summarized in Table 1.6, arising from the functional requirements of the joints, manufacturing route for the coils and experience of the manufacturers.

For example, the joints for the TF conductors and CS leads will be heat treated at about 650 ℃ to form $Nb_3Sn$ in the strands. Thus it is not allowed to use solder or strand/copper coating at the interface between the strands and the copper sole. Instead, a diffusion bonding method is adopted to obtain a low-resistive connection. While for the most mechanically loaded PF and feeder joints with NbTi strands, it is appropriate to solder the strands-copper and box-box interfaces together so as to provide additional mechanical strength. Furthermore, for the Feeder joints, an improved way of using indium to bond the interfaces is used for the sake of manufacturing simplicity [46]. However, this is not suitable for the PF coil joints because of the elevated temperatures for the epoxy resin curing [45].

For the CS coils, joints are used for three types of connections: joints connecting hexapancakes within each module, connecting module terminals to busbar extensions and connecting busbar extensions to the feeders. The available space for CS joints is limited, and a soldered lap type joint actually doubles the cooling lines and significantly increases (basically doubling) the joint volume. Thus, except the joints connecting busbar extensions to the feeders, the lap type twin-box joints are not used for the other two kinds of joint connections.

The CS design originally had a butt joint as a baseline compact joint to connect hexapancakes within modules [49], but later on in 2007, a sintered joint (also called splice joint) was introduced, which is a six-finger design with high electrodynamical reliability. In contrast to the butt joint, the sintered joint is less tightly compacted and features helium in the cable space and the central channel all the way through [50]. A coaxial joint was developed for connecting module terminals to busbar extensions [51], [52]. The assembly and cross-section of the three types of CS joints are shown in Figure 1.10.

The joints are so critical for the coils that improvements always kept proceeding. For example, ASIPP Feeder teams designed a sub-cable overlap joint with smaller volume, lower resistance and more uniform tension insulators. In this sub-cable overlap joint, the cable is untwisted at the sub-cable stage, and sub-cables of two cables are connected by indium-coated copper soles [53]. Furthermore, many joint variations are developed for $Re$BCO superconductors due to the particular material characteristics and tape shape, as shown in Figure 1.11.

In general, advancing joint technology aims for two main directions [55]. The first is jointless coils, considering that joints always constitute weak points. As the jacketing by longitudinal welding can be done in unlimited lengths, one can imagine that manufacturing the conductor length for the whole coil can be done in one go. Surely this requires R&D and quality assurance, increases the risk of coil failure, significantly complicates and slows down the coil winding, and calls for cold testing with transport current. The other direction is for the segmented or demountable coils, like the helical coils of the FFHR-d1 device with a total of 3900 joints [56], or the demountable TF coils of the ARC Tokamak [54], [57].

Table 1.6: Design parameters of ITER lap-type joints [45].

| Parameter | PF | Feeder MB/CB | CC | TF | CS |
|---|---|---|---|---|---|
| Void fraction [%] | $19 \pm 1$ | $21 \pm 1$ | $22 \pm 1$ | $21 \pm 1$ | $22 \pm 1$ |
| Ni/Cr removal method | brush/PF6 reverse plating | reverse plating | brush | brush | brush |
| Box annealing prior to use | no | no | no | 4 h at 400 ℃ | no |
| SS wraps btw petals | preserved | n/a | n/a | removed | preserved |
| Outermost strands plating | pure tin | silver | silver | no | no |
| Cu sole inner side plating | pure tin | silver + In tinned | silver | no | no |
| Cable-sole interface | soldered $Sn_{96}Ag_4$ | pressed | pressed | pressed, sintered | pressed, sintered |
| Box-box interface | soldered $Pb_{60}Sn_{40}$ (In wires to feeder) | pressed, In wires | pressed, In wires | soldered $Pb_{60}Sn_{40}$ (In wires to feeder) | pressed, In wires |
| Central pipe [mm] | 3/12 | MB: n/a, CB: 3/6 | n/a | 6/10 | 3.5/9 |
| Sole RRR[a)] | 5÷6 copper C12200 | 70÷100 copper C10200/C12200 | 70÷100 copper C10200 | 450÷500 copper C10100/C10200 | 170÷230 copper C10200 |
| Jacket-box / cover-box welds | FP/FP | MB:FPB, CB:FT/FPB | FPB/PP | FT/PP | FT/PP |
| Joint clamps, connected by | side plates, weld | brackets, weld | brackets, weld | brackets, weld | brackets, weld |

[a)] Tested at 0 T, after bonding and HT (CS/TF).

* The flat side of the copper sole is either electroplated (PF) or hot tinned (TF) with $Pb_{60}Sn_{40}$ prior to soldering.

* All terminal boxes are silver plated on the flat side.

* The feeder boxes for the TF and CS terminals will be with copper C12200. The TF EU coil boxes will be with copper C10200.

* PP - partial penetration weld, FPB - full penetration but weld, FT - fillet weld.

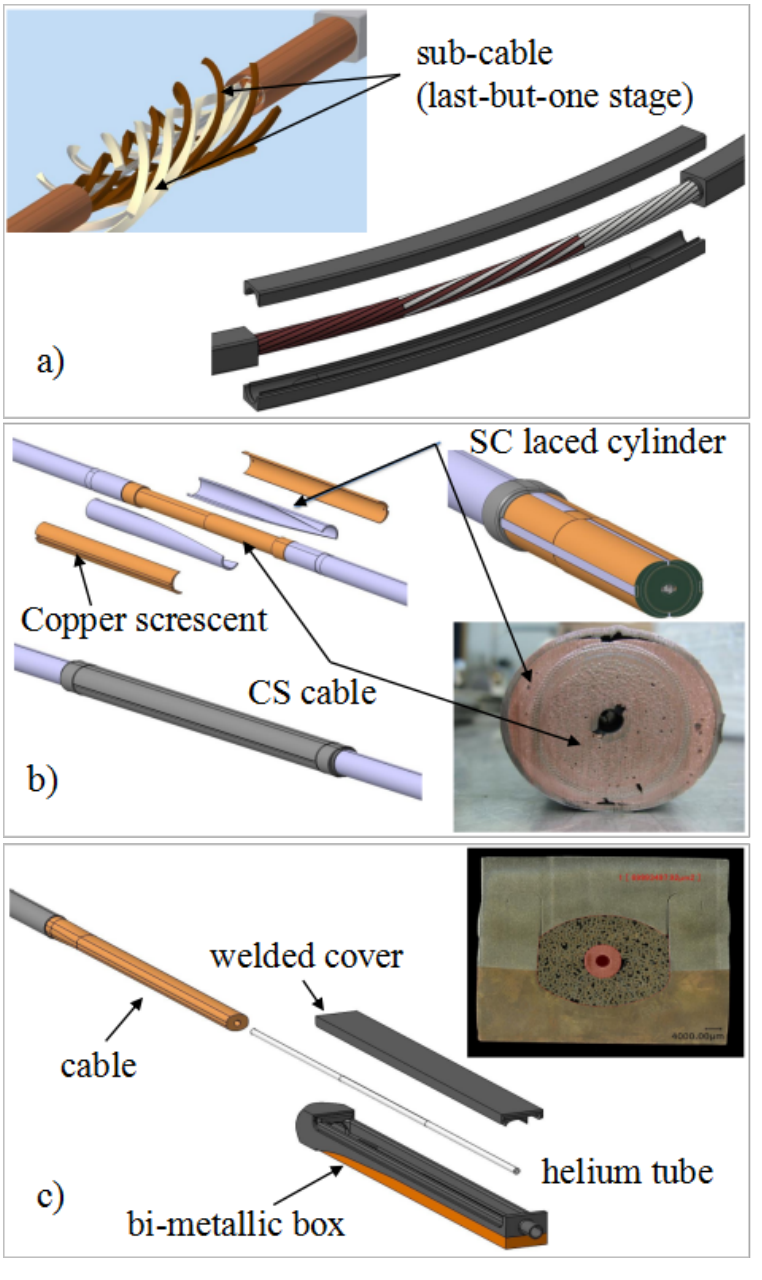


Figure 1.10: Assembly and cross-section of three types of CS joints: a) sintered joint connecting hexapancakes, b) coaxial joint as bus joint and c) twin box joint as termination joint.

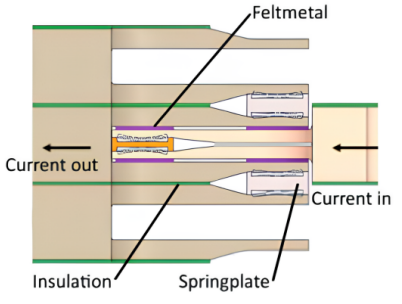


(a) Sliding joint

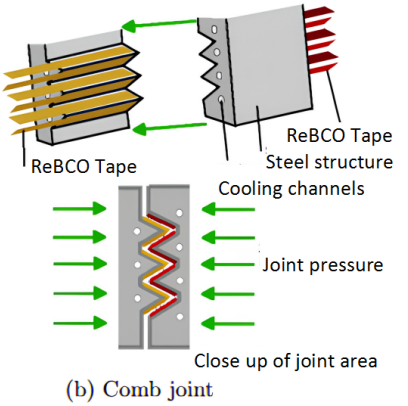


(b) Comb joint

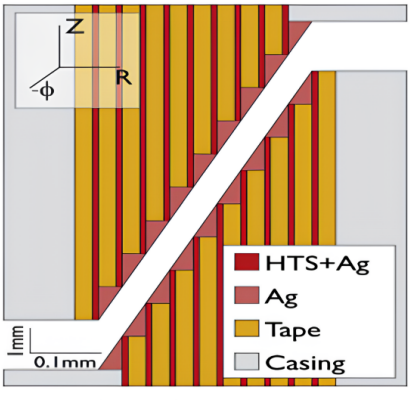


(c) Lap/butt joint

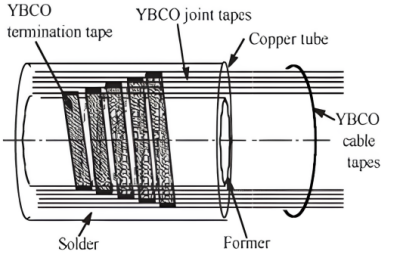


(d) Round joint

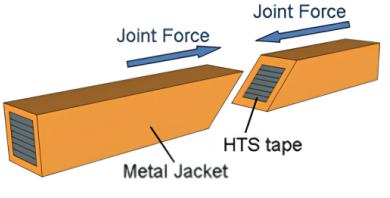


(e) Butt joint

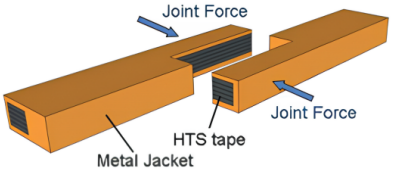


(f) Edge joint

Figure 1.11: Different types of joints for $Re$BCO superconductors [54].

## 1.4 AC loss in the electrical joint

When superconductors are subjected to time varying magnetic fields or transport currents, energy dissipation is generated, referred to as AC loss, which is contributed by three main terms: hysteresis loss in the superconducting filaments, coupling loss in wires and cables and eddy current loss in normal conductive components. The energy loss terms can be understood as originating from the electric field induced in the conductor.

Hysteresis loss is intrinsic to the magnetization of superconducting filaments, which is independent of frequency or ramp rate of the applied magnetic field and is the main dissipation mechanism at low magnetic field sweep rates. It is a type of effective resistive loss produced by the flux line movement within the superconducting material caused by the changes of magnetic field. This energy dissipation depends only on the energy stored in the line tension of the flux lines enclosing normal cores and have a hysteretic characteristic.

As introduced previously, the superconducting filaments are embedded in a low resistive matrix of normal conducting copper. Under time-dependent magnetic field and current conditions, inter-filament currents are induced and travel through the matrix material, generating ohmic heating loss [27].

Inter-strand coupling loss in cables has a similar nature as inter-filament coupling loss in strands. The inter-strand contact conductance allows induced currents to pass across the strand interfaces and generate power dissipation at the contact points. Particularly, in the joints, where the cables are more tightly compacted, the inter-strand contact resistance decreases and then the coupling loss can increase significantly when the joint is subjected to rapid magnetic field sweeps.

Furthermore, depending on the joint assembly orientation with respect to the direction of the changing magnetic field, inter-cable coupling currents may arise when enclosing the two conductors and the copper sole. The inter-cable coupling loss is highly dependent on the resistivity of the copper sole. The eddy current loss can also contribute significantly to the AC loss of the conductor and joint. However, the mechanisms of both are different.

### 1.4.1 Hysteresis loss

As a superconducting filament is exposed to a changing magnetic field, the magnetic field penetrates the superconductor in the form of moving flux lines. Due to the electrical field induced, currents with density $\pm J_c$ are built up in the exterior region of the filament, screening the interior from the changing magnetic field. The two regions are referred to as screening current and current-free regions. Figure 1.12 illustrates the process of a round filament without transport current in a changing transverse magnetic field.

As the magnetic field increases, the induced electrical field drives the screening currents of which the density is limited. The boundary between the two regions is shifted towards the center of the filament. When the screening current fully occupies the filament and reaches the maximum value, the corresponding magnetic field is the so-called full-penetration magnetic field $B_p$, which for cylindrical filaments with transverse magnetic field can be expressed as

$$B_p = \frac{\mu_0 J_c d_f}{\pi} \text{ [T]}, \tag{1.17}$$

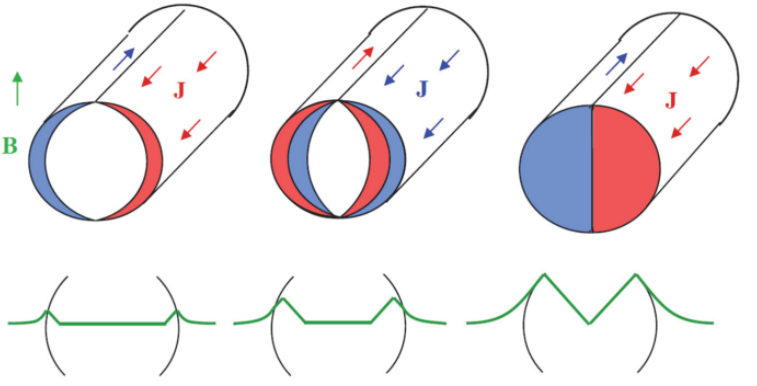


Figure 1.12: Screening current density and magnetic field profiles in a superconducting filament subjected to a transverse time-varying magnetic field $B$ (picture courtesy of M. N. Wilson [27]).

with $J_c$ the critical current density and $d_f$ the filament diameter.

The screening currents produce a magnetization $M$, which is defined as the magnetic moment per unit volume. For a cylindrical filament, the magnetization generated by transverse and parallel magnetic fields is defined by

$$M = \frac{2}{3\pi} J_c d_f \ [\mathrm{A \cdot m^{-3}}], \tag{1.18}$$

$$M = \frac{1}{6} J_c d_f \ [\mathrm{A \cdot m^{-3}}]. \tag{1.19}$$

A typical magnetization loop of a $Nb_3Sn$ wire is shown in Figure 1.13, the shape is time independent and not affected by the frequency. The hysteresis loss per magnetic field cycle in a unit volume is equal to the area enclosed by the magnetization loop, depending only on the magnetic field amplitude and the superconductor properties. The hysteresis loss is calculated by

$$Q_{hys} = \oint M dB \ [\mathrm{J/m^3 \cdot cycle}]. \tag{1.20}$$

It can be expressed in an equivalent way in terms of a power loss per unit volume

$$P_{hys} = M\dot{B} = \frac{2}{3\pi} J_c d_f \left|\frac{dB}{dt}\right| \ [\mathrm{W \cdot m^{-3}}]. \tag{1.21}$$

The magnetization is reduced in the case a transport current $I_t$ is added to the filaments. However, in order to keep $I_t$ constant, an extra work of the power supply is needed to generate the external magnetic field, then the loss is increased by a factor $1 + [I_t/I_c]^2$

$$P_{hys} = \frac{2}{3\pi} J_c d_f \cdot [1 + \frac{{I_t}^2}{{I_c}^2}] \cdot \left|\frac{dB}{dt}\right| \ [\mathrm{W \cdot m^{-3}}]. \tag{1.22}$$

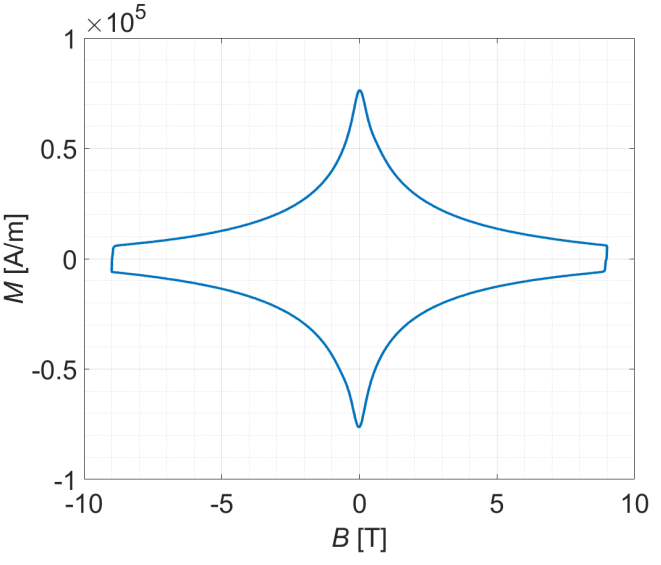


Figure 1.13: Magnetization versus applied magnetic field in a WST $Nb_3Sn$ strand at $T = 4.2$ K, $B_a = 3$ T.

### 1.4.2 Inter-filament coupling loss

When a multi-filamentary wire is subjected to a uniform external magnetic field $B_e$, changing with a rate $\dot{B}_e$, coupling currents flow along the filaments and cross over through the resistive matrix every half twist pitch. The paths of the inter-filament coupling currents are illustrated in Figure 1.14. The crossing currents in the matrix follow paths, which are parallel to the changing magnetic field [58].

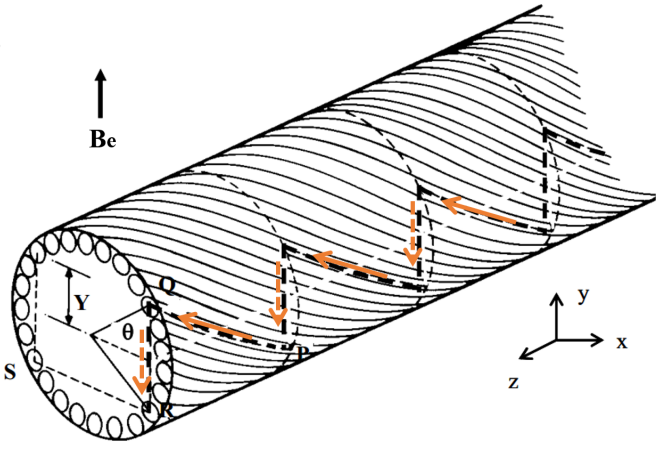


Figure 1.14: Coupling current paths in a twisted multi-filamentary composite wire (picture courtesy of M. N. Wilson [27]).

In the case of a harmonic field variation, the coupling currents produce an axial $\cos\theta$-like current distribution around the wire, which then generates a dipole field in its interior and finally a uniform internal magnetic field $B_i$ is generated

$$B_i = B_e - \dot{B}_i \tau \,[\mathrm{T}], \tag{1.23}$$

in which

$$\tau = \frac{\mu_0}{2\rho_t}\left(\frac{L}{2\pi}\right)^2 \,[\mathrm{s}], \tag{1.24}$$

where $L$ is the twist pitch and $\rho_t$ is the transverse inter-filamentary resistivity.

The parameter $\tau$ is called the time constant of the system. It characterizes the time needed for the coupling currents to decay after the external magnetic field has stopped changing. The power per unit volume dissipated by the induced currents is obtained integrating $J^2\rho$ along the current path, which results in

$$P = \frac{\dot{B}_i^2}{\rho_t}\left(\frac{L}{2\pi}\right)^2 = \frac{2\dot{B}_i^2}{\mu_0}\tau \,[\mathrm{W}\cdot\mathrm{m}^{-3}]. \tag{1.25}$$

If the external magnetic field is given by a sinusoidal magnetic field $B_a \sin\omega t$, the induced coupling loss per cycle is

$$Q = \frac{B_a^2}{\mu_0}\frac{2\pi n_s \omega\tau}{(1+\omega^2\tau^2)} \,[\mathrm{J/m^3}\cdot\mathrm{cycle}], \tag{1.26}$$

where $n_s$ is the shape factor of the filamentary core, $n_s = 2$ for a wire with circular cross section. Detailed treatments of the inter-filament coupling loss for different cross-sectional shapes, types of magnetic field variation and frequencies can be found in [27], [58]–[62].

Besides a shape related factor, the inter-filament coupling loss also relies on the time constant $\tau$, which equals to the period maximizing the coupling loss. The time constant depends on the twist pitch, the filamentary-core dimensions and the effective transverse resistivity, the latter is a function of the filament-to-matrix contact resistance, effective matrix resistivity and cross-sectional layout of the filaments.

The coupling currents occupy a distinct volume at the outer radius of the strands called the 'saturation' region, where the filaments are forced to carry the critical current density. As coupling currents increase, the saturated region shifts towards the center of the wire. From a loss computation point of view, the change of position of the boundary can be generally ignored, but the extra loss due to the penetration of the flux through the saturated region has to be added [63].

### 1.4.3 Inter-strand coupling loss

The way to calculate the inter-strand coupling loss is generally analogous to inter-filament coupling loss. Therefore, the expressions given for the calculation of the inter-filament coupling loss, like Equations 1.25 and 1.26 are also used for a cable, except an appropriate effective time constant $\tau_{eff}$ should be adopted. Theoretically, it offers an effective way to calculate the losses of a cable with any number of cabling stages.

For the multi-stage CIC conductors with a large number of different current loops induced, the effective time constant is defined as a sum of the multiple time constants $\tau_i$ over the $N$ stages composing the cable, as seen in Equation 1.27 [64], by assuming that the coupling currents in a given stage do not interfere with the coupling currents of the other stages, and the losses in each stage can be evaluated independently

$$n\tau_{eff} = \sum_{i=1}^{N} n_i \tau_i \text{ [s]}, \tag{1.27}$$

where each $n_i\tau_i$ accounts for the increase of the loss at each new cabling stage $i$.

However, this expression of inter-strand coupling loss has some limitations since the coupling between the various cabling stages cannot be neglected. In practice, for a magnetic field applied with a sinusoidal profile $B_a(f) = B_a \sin(2\pi ft)$, a more preferable method to obtain the effective time constant is experimentally defined by Equation 1.28 [64], in which the parameter $\alpha$ is the slope of the initial linear section of the AC loss versus frequency curve

$$n\tau_{eff} = \alpha \frac{\mu_0}{2\pi^2 B_a^2} \text{ [s]}. \tag{1.28}$$

It is suitable to estimate the coupling loss at low magnetic field ramp rates with this single time constant, however, for higher frequencies or faster ramp rates, more influence factors need to be considered. Moreover, it is also not easy to deal with a conductor subjected to a magnetic field variation of any orientation (neither purely transverse nor parallel) and shape.

### 1.4.4 Inter-cable coupling loss and eddy current loss

The primary task when designing a joint between superconducting cables is to control the cable-to-cable resistance under certain criteria. However, the situation becomes far more complex if two large size CIC conductors are connected and the variations in local heat dissipation, both resistive loss and AC loss need to be considered. Moreover, also the current non-uniformity driven by resistance and inductance variations in the joint, plays a role in the thermal stability as it drives strands locally to carry currents higher than their critical currents. As a result, part of the strands may be subjected to transition to the normal state and the risk is that the coil can become unstable. Thus, current and power distributions in the joint have to be controlled carefully to warrant sufficient temperature margin in the superconductors and avoid to affect stable operation of a magnet.

With regard to AC loss in the joint, besides the coupling loss in the individual superconductors, and the eddy current loss in the copper sole component, the coupling loss induced by the inter-cable currents especially under radial magnetic field, contributes significantly to the total losses. As introduced in the previous sections, the global coupling loss can be estimated by choosing proper shape factors and current decay time constants.

Furthermore, considering the current transfer in the joint, a Joule heating is then added by $P_{joule} = R \cdot I_{coil}^2$ , with $R$ the joint DC resistance and $I_{coil}$ the coil current. In this case it is simply assumed that the transport current is uniformly distributed among the main subcables. Therefore, it is a relatively rough estimation by using coil current instead of the actual inter-cable current [65].

## 1.5 Stability of superconducting joints

Electro-magnetic and thermal stability as well as quench protection are fundamental aspects of the physics of superconducting cables that have deserved much attention ever since the first practical application of superconductors in magnets [66]. In spite of the substantial progress in understanding and improvement in the manufacturing techniques, stability and protection methods are very critical for high-performance magnets. For ITER that is aiming to achieve some 60,000 plasma cycles, a well proven stability margin of the magnet system is compulsive for reliable operation. Otherwise, it does not just mean significant loss of operating time and high cost for re-cooling of the magnets after interruption, but in the worst situation it could result in an irreversible damage of a magnet.

A superconducting magnet is always subjected to a series of energy inputs of very different nature, time scale and magnitude, the so-called disturbance spectrum. The energy input increases the temperature of the superconducting cable and can be sufficient to exceed the critical surface, where the superconductor becomes resistive and severe ohmic heating is generated. In essence, stability is an issue related to the energy balance of heat production and heat removal. Different phenomena can occur in superconducting cables and joints that limit their performance, some are emphasized in this thesis.

Firstly, the current in a cable is not uniformly distributed among all strands, also caused by differences in contact resistances at the different contact interfaces. The current non-uniformity can be driven by resistive variations in strands and joints, or by inductive coupling variations between strands along the cable. Transition between these two drivers is controlled by the time instant of circulating currents in the cable, which is of the order of 1,000 to 10,000 s. For the ITER coils, the CS and PF coils are expected to have an inductance-dominated current distribution and the TF coils to have a resistance-dominated distribution. Current non-uniformity is not a problem in itself, only if it leads to degradation of the thermal stability level of the cable. As mentioned previously, unbalanced currents in particular strands can result in exceeding their critical condition and lead to a transition from superconducting to normal state. The successive evolution of such an initial normal zone into a quench or into recovery depends on the capability of the saturated strand to expel excess current into the surrounding strands and thereby limit ohmic heating and temperature rise sufficiently. Joint non-uniformity usually causes critical current degradation of the overall cable at the typical joint resistance levels [19].

Secondly, coupling currents are induced both within the individual strands and between strands in multi-strand cables while exposed to a time-varying magnetic field. The flow of coupling currents through the resistive matrix or contact interfaces then produces ohmic heating and a temperature rise, thus coupling loss is a potential source of instability. This issue is even critical for the joints due to the unavoidable resistive connection, the DC and AC performances need to be considered simultaneously. On the one hand, low-resistive joints enable a reduction of the ohmic heating and improve the current uniformity by facilitating current sharing among strands. On the other hand, highly resistive copper sole parts or barriers around strands and petals can be helpful to limit eddy, inter-strand and inter-cable coupling currents in pulsed operation. To be mentioned here, the coupling loss in CICCs has two key features. One is that the coupling loss of the cable depends on the local electromagnetic forces, which press the strands together and reduce the cable transverse resistance during the load cycling history. The other is the dependence of

the effective time constant of the cable on the rate of change of magnetic field, due to screening effects [67].

## 1.6 Scope of the thesis

The objective of this thesis is to enhance the understanding of the performance of full-size ITER lap-type joints with particular attention to the Poloidal Field joints. The joints are tested experimentally and numerically under various working scenarios. The ultimate goal is to control and warrant sufficient stability margin of conductors and joints anywhere in the magnet system and under the most demanding operating conditions.

The joints essentially are transition points between superconducting and normal state materials, thus they can be critical for the safe operation of the ITER magnet. Qualification tests of the full-size joint samples are essential for the ITER magnet R&D program. However, practical test conditions may differ significantly from real operating ones due to the limitations imposed by the test facility. Therefore, in order to assess the relevance of the specific test configuration as well as to systematically study and optimize the samples under real operating conditions, precise numerical simulations are mandatory. The code JackPot AC/DC [68], featuring the description of CIC conductors with strand-level details, is used throughout this work to analyze the performance of cables and joints. A series of tests, including contact resistance and AC loss tests were performed primarily to obtain the key parameters for the JackPot simulations. The JackPot AC/DC numerical code has been extended and simulations were performed and verified with the experimental results carried out in the SULTAN facility [69].

The outline of the thesis is shown in Figure 1.15.

- In chapter 2, an overview is presented of the experimental setups for testing the superconductors and joints. Furthermore, the main features of the JackPot AC/DC model are introduced.
- In chapter 3 the characterization measurements of two types of ITER strands are described and a practical scaling law is derived for the $Nb_3Sn$ strand at low magnetic field. The angular dependence of the hysteresis loss of NbTi strand is determined, providing an accurate way to evaluate the hysteresis loss of a complete joint.
- Chapter 4 introduces the measurements and simulations of the contact resistance and AC loss of an ITER joint with the purpose to obtain the key input parameters for the further modeling analysis.
- In chapter 5, the electro-magnetic and thermal performance of an ITER joint with a specific design improvement, referred to as mask, is analyzed. A general quantitative analysis is obtained of the joint in pulsed mode.
- In chapter 6 the performance of a joint under steady-state conditions is evaluated, including mainly two aspects, one is the non-linear voltage-current characteristics as observed in some qualification tests, the other is the evaluation of the $T_{cs}$ and thermal behavior.
- In chapter 7, the stability of a joint under various operating scenarios is discussed.

- In chapter 8 general conclusions and recommendations are presented concerning the performance and limitations of lap-type joints, as well as the impact on the operational margin of the superconducting magnets in ITER.

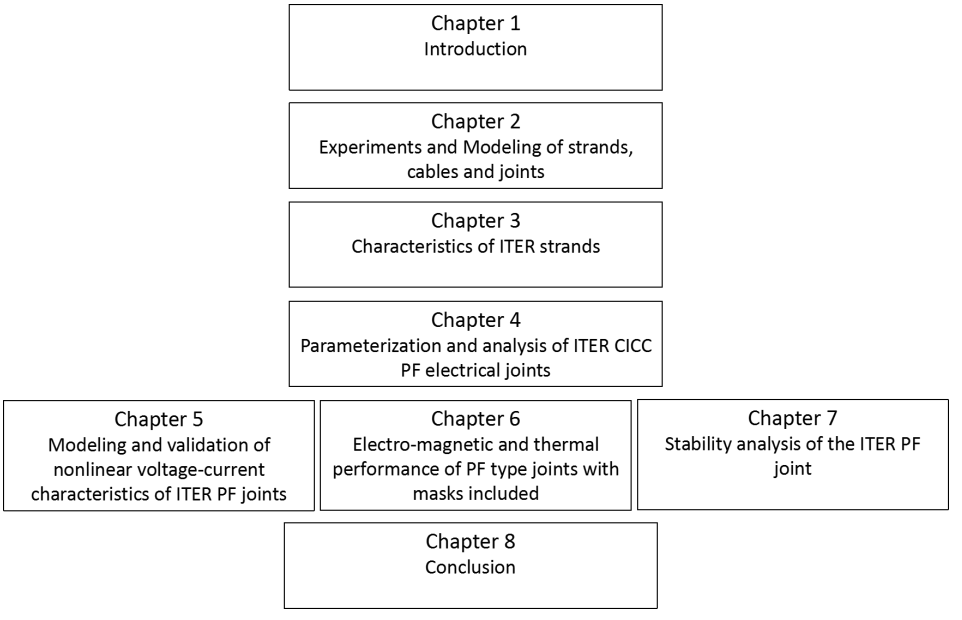


Figure 1.15: Outline of the thesis showing the relation between chapters.

## 1.7 Publications in journals

The content of the thesis chapters is based on the following publications in peer reviewed journals:

Table 1.7: List of publications.

| # | Publication | Thesis chapter |
|---|---|---|
| 1 | J Huang, Y Ilyin, D Bessette, C Zhou, R Lubkemann, C Vermeer, W A J Wessel, A Nijhuis, "Effective low magnetic field $J_c(B)$ scaling of ITER $Nb_3Sn$ strands by magnetization and critical current measurements", *IEEE Trans. Appl. Supercond.* 32 4204110 (2022) (10pp) `https://doi.org/10.1109/TASC.2022.3190921`. | Chapter 3 |
| 2 | J Huang, Y Ilyin, W A J Wessel, R Lubkemann, H J G Krooshoop and A Nijhuis, "Contact resistance, coupling and hysteresis loss measurements of ITER poloidal field joint in parallel applied magnetic field", *Supercond. Sci. Technol.* 35 025016 (2022) (13pp) `https://doi.org/10.1088/1361-6668/ac4201`. | Chapters 3 & 4 |
| 3 | J Huang, Y Ilyin, Y Zhai and A Nijhuis "Quantitative analysis of ITER Poloidal Field joints through rigorous resistivity parameterization" (accepted by *Supercond. Sci. Technol.*). | Chapter 4 |
| 4 | J Huang, T Bagni, Y Ilyin and A Nijhuis, "Modeling and validation of nonlinear voltage-current characteristics of ITER PF joint sample tested in the SULTAN Facility", *Supercond. Sci. Technol.* 35 025014 (2022) (14pp) `https://doi.org/10.1088/1361-6668/ac455c`. | Chapter 5 |
| 5 | J Huang, T Bagni, Y Ilyin, A Nijhuis "Pulsed Field Stability and AC Loss of ITER PF Joints by Detailed Quantitative Modeling", *IEEE Trans. Appl. Supercond.* 33 4201711 (2023) (11pp) `https://doi.org/10.1109/TASC.2023.3299590`. | Chapter 6 |
| 6 | J Huang, Y Ilyin, H H J ten Kate and A Nijhuis, "Electro-thermal performance analysis of ITER PF joints in SULTAN and ITER operating conditions" (submitted to *Supercond. Sci. Technol.*). | Chapter 7 |
| 7 | J Huang, Y Ilyin, H H J ten Kate and A Nijhuis "An effective electro-thermal analysis method for evaluating transient stability of ITER PF joints" (submitted to *Supercond. Sci. Technol.*). | Chapter 7 |

# Chapter 2

# Experiments and Modeling of strands, cables and joints

## 2.1 Introduction

We briefly introduce the experimental techniques as well as the numerical software code used to characterize the essential properties of CICCs and their joints. A description in full details is beyond the scope of this thesis and the reader is referred to the references provided. Here we provide a flavor of the tools used and describe the essence of the software code applied.

The ITER magnet system comprises a large volume of NbTi and $Nb_3Sn$ Cable-In-Conduit Conductors (CICCs), all of them have to satisfy strict qualification tests, from the design verification phase to manufacture.

The qualification tests of the CICCs are mostly performed in the SULTAN (SUpraLeiter TestANlage) test facility of the Swiss Plasma Center (SPC) at EPFL, Switzerland. It was built in 1984, aiming to test high current, forced flow superconductors for fusion magnets. The magnet system of SULTAN comprises a split solenoid with a 100 mm access bore and a superconducting transformer to feed the straight, short length sample with current up to 100 kA, and pulsed magnetic field coils for AC loss and transient stability measurements. Today, SULTAN is the worldwide largest magnet facility to test forced flow, high current superconductors up to 11 T, including DC transport properties like joint resistance, AC loss, transient stability and thermal-hydraulic behaviour [69], [70].

Besides using the large-scale testing facility, ITER also established a few independent reference laboratories to qualify the conductor production. All superconductors have been supplied by ten strand suppliers from six domestic agencies (DAs: China, European Union, Japan, South Korea, Russia, and the United States). The distributed supply network and the requirement for many conductor unit lengths to operate in series, demand uniform production quality assurance at all suppliers and DAs. Each DA has to establish at least one reference laboratory to verify the acceptance tests by independent measurements [30], [71]. The laboratory at the University of Twente (UT) is one of the thirteen ITER reference laboratories, where test methods are developed and used for wire, CICC and joint qualification tests.

The test facilities provide worldwide benchmarking of strands and conductors. Considering the high cost of tests, limited number of samples and, for some conductors, in particular $Nb_3Sn$, presence of magnetic field or magnetic field rates lower than the peak values in ITER, it is very necessary to extend the understanding of CICC behaviour by using dedicated simulations. Various models have been developed to analyze the behaviour of strands and cables. The JackPot-AC/DC numerical model developed at the University of Twente [68], [72], is capable of simulating the electromagnetic and thermal behaviour of CICCs or joints with strand level detail.

The samples presented here were tested in the SULTAN facility or the superconductor test laboratory at University of Twente, while the numerical analyses were mainly performed with the JackPot-AC/DC numerical model. More specific details of the test facilities are introduced below.

## 2.2 Experimental setups

### 2.2.1 CICC sample testing in the SULTAN facility

The SULTAN magnet system comprises three split solenoids and two saddle-shaped coils to provide DC and AC magnetic fields, respectively. The split coil free bore bore for introducing a sample is about 100 mm, and allows a straight short conductor sample to be positioned in the high field zone (HFZ). The schematic of the SULTAN magnet system and the orientations of DC and AC magnetic fields with respect to the sample, is illustrated in Figure 2.1. The solenoidal magnet is able to generate up to 10.89 T over a 1% uniformity length of 450 mm, and the AC coil can generate a varying magnetic field on the sample with fast field transients. It is capable of mimicking to some extend the pulsed operating mode close to ITER like conditions, like present in poloidal field coils, and enables AC loss measurements and stability analysis.

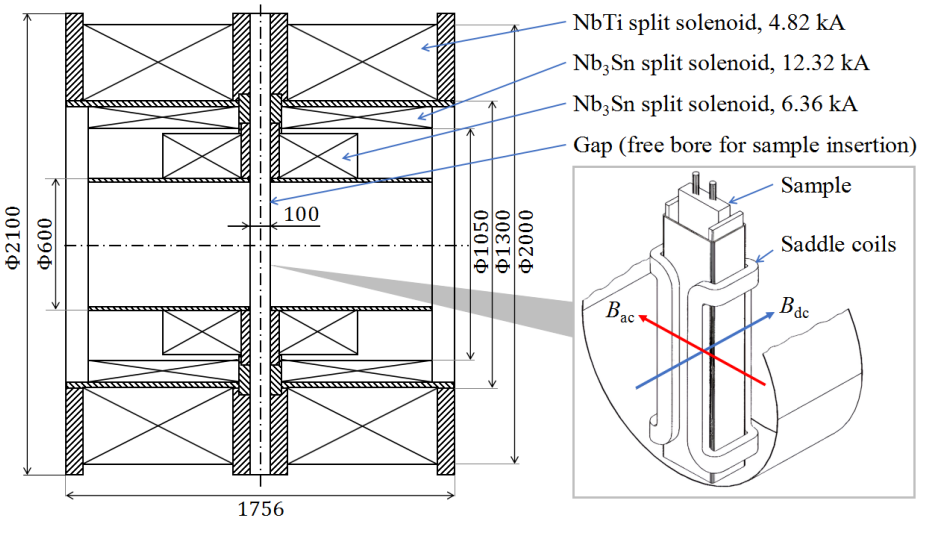


Figure 2.1: Schematic of the SULTAN magnet system and the orientations of magnetic fields with respect to the surface of the sample. The background magnetic field $B_{dc}$ is provided by three split solenoids, and the varying magnetic field $B_{ac}$ is provided by the saddle coils.

Presently, SULTAN is the only facility in the world capable of featuring high-magnetic field, high current and high mass flow rate of supercritical helium for cooling. The 94 mm $\times$ 144 mm testing bed cross section can accommodate most of the large superconductors for present and future fusion devices.

#### Sample preparation and instrumentation

A sample is usually prepared in hairpin shape with two straight conductor legs joined at the bottom and electrically connected at the top to the current leads of the superconducting transformer. This layout allows both legs to be operated by a single power supply and

provides the possibility of testing two conductors simultaneously [73]. It is fabricated using mainly two techniques, the U-shaped hairpin and making a high-quality solder-filled joint [74], [75]. For ductile NbTi conductors, the hairpin method by bending the conductor into a U-shape directly can be used. This method avoids the use of a resistive joint between the two conductors and diminishes the impact of non-uniform current distribution in the sample due to the bottom joint. For $Nb_3Sn$ conductors, the two sample legs are connected by a bottom joint and at the joint region completely filled with solder except for the helium flow paths. The solder serves to immobilize the strands and minimize the inter-strand contact resistance [73], [76]. Both methods work satisfactory, but in some NbTi samples prepared with the hairpin technique, premature quench is observed. Also, due to the different geometry, the self-field generated in the U-shape box is larger than in the solder-filled joint [75].

The two conductor legs in a SULTAN sample are equipped with voltage, temperature, mass flow rate and pressure sensors, in some cases also strain gauges and coils for $T_c$ measurements are present [77]. The samples are cooled through a forced flow of supercritical helium from the bottom connection to the upper terminations. The central channels of the conductors are usually blocked to only allow helium flowing in the voids between strands with a mass flow rate of 1 to 10 g/s. Electrical heaters are mounted on the helium inlet to adjust the helium temperature when performing measurement of the current sharing temperature $T_{cs}$. The temperature sensors and voltage taps are installed on the conductor jacket, each set with 4 or 6 sensors distributed symmetrically around the legs. Sets of sensors are located upstream and downstream of the high field zone along the conductor axis. The longitudinal distance is usually 450 mm between the voltage taps and 800 mm between the temperature sensors [70], [73], [78], [79].

The SULTAN facility also allows to test the ITER full-size joints in praying hands configuration [45], by shortening the conductor length in order to position the joint in the high field zone. The layout of conductor and joint samples with respect to the SULTAN testing area is shown in Figure 2.2.

After the instrumentation in place and assembly of the clamping system that ensures the sample to withstand the electromagnetic force, the sample is vertically inserted in the aperture and the upper terminations are electrically connected to the current leads of the superconducting transformer.

The SULTAN samples are tested under operating conditions that replicate the features of ITER scenarios in terms of magnetic field, transport current, temperature and mass flow rate of liquid helium.

**DC test**

A complete series of measurements normally comprises the so-called DC and AC tests [80]. The DC test includes the measurement of the critical current $I_c$ and current sharing temperature $T_{cs}$ of the conductor sample [78]. For the joint sample, usually the joint resistance $R$ and quench temperature $T_q$ are tested. The measurements are performed by adjusting the operating current, the mass flow or inlet temperature of the helium. The current sharing- or quench temperature at nominal operating current and magnetic field is the vital test for qualification and acceptance of the ITER conductors. The $T_{cs}$ is defined as the conductor temperature at which an average, longitudinal electric field of $E_c = 10\ \mu\mathrm{V/m}$

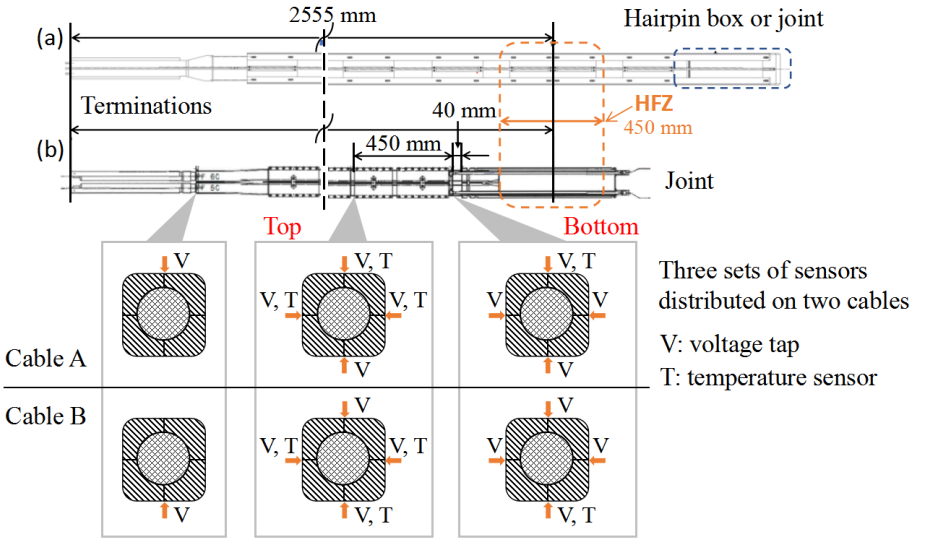


Figure 2.2: Schematic of SULTAN sample instrumentation: (a) conductor sample and (b) joint sample assembly in the SULTAN magnet with respect to the high field zone (HFZ). Three sets of sensors (V: voltage taps and T: temperature sensors) are distributed on two cables, of which two sets of sensors are positioned at distances of 490 mm and 40 mm with respect to the joint copper sole's end, denoted as the top and bottom sensors, respectively.

is observed at specific transport current $I$ and static background magnetic field $B$. The critical current and so-called $n$ value representative for the transition steepness in the $VI$ curve of the conductors, are measured in a separate test by holding the conductor temperature at the previously measured $T_{cs}$ and increasing the input current until a transition from superconducting to normal state occurs.

For the joint resistance, the voltage differences $V$ between two sets of voltage taps at the two joint legs are measured, with respect to the specific transport current $I$ and background magnetic field $B$. Then the joint resistance is determined by $R = V/I$. For example, the test conditions of the so-called PFJEU6 joint sample discussed later in this thesis, are as follows. The quench temperature $T_q$ is measured at a background magnetic field of 3 T, transport current of 55 kA and helium mass flow rates of 3 and 10 g/s, by which the coolant inlet temperature is increased in both legs in steps of 0.2 or 0.5 K.

### AC test

The AC test consists of AC loss and stability measurements. The AC coil generates a trapezoidal magnetic field or continuous sinusoidal field in the frequency range of 0.1 to 5 Hz, and the amplitude is generally fixed at 0.1 or 0.2 T. The total loss is measured with a gas flow based calorimetric method [78]. The error declared by SULTAN in AC loss measurements is $\pm 5\%$ for a frequency below 5 Hz.

**Stability test**

Stability tests are performed to define the Minimum Quench Energy (MQE) of the conductor. Generally, it is possible to deposit a certain amount of energy in a conductor without causing a quench and conductors can recover to the initial stable superconducting condition. A quench occurs if the conductor is no longer able to recover the superconducting state. The minimum energy just enough to initiate a quench is called MQE [81]. Different from continuous sinusoidal excitation in AC loss measurements, the deposited energy in the stability test is produced by a single sinusoidal magnetic field wave. For the case of a joint sample, a trapezoidal pulse with different ramp up/down rates is applied to simulate the operating scenarios and evaluate the stability.

**Cycling load test**

Beside the DC test and AC loss test, which aim to verify the basic acceptance criteria, the electromagnetic cyclic loading test intends to mimic the ITER lifetime. For example, up to 10,000 electromagnetic load cycles applied to the ITER Central Solenoid conductors, may show performance degradation [70], [82], [83]. Furthermore, thermal cycles can cause a change in the $T_{cs}$ of $Nb_3Sn$ conductors. For this reason the qualification program includes thermal cycles of warming-up and cooling-down (WUCD) applied after the electromagnetic cyclic loading to check for thermal cycle degradation [84].

It is important to note that the testing condition refers to the peak magnetic field locally in the conductor, while the SULTAN test program refers to the background magnetic field applied to the samples. The peak magnetic field applied to the sample can be approximated as the background magnetic field plus the self-field generated by the test current in the two conductor legs using

$$B_{peak} = B_{dc} + \frac{\mu_0 I_{op}}{2\pi} \cdot (\frac{1}{r} + \frac{1}{a-r}), \tag{2.1}$$

where $B_{dc}$ is the background magnetic field, $I_{op}$ is the operation current, $\mu_0$ is the magnetic permeability in vacuum, $r$ is the conductor bundle radius and $a$ is the distance between the centers of both legs. For example, the PF5 conductor tested with $45$ kA transport current, $a$ and $r$ is $60$ mm and $17.65$ mm respectively, the induced self-field is about $0.7$ T [85].

## 2.2.2 High current superconductivity lab at the UT

As a main ITER reference laboratory [30], the characterization and testing of technical superconductors is performed in the high current superconductivity lab at the University of Twente. Facilities for cryogenic testing of AC loss, stability and critical current of strand and conductor as well as joints are available. Tailored, in house designed and manufactured test rigs as well as auxiliary equipment as superconducting coils, transformers and dedicated instrumentation have been developed and tested in this lab.

**Inter-strand contact resistance measurement**

In CICC conductors, the current distribution among strands is seldom uniform, due to the non-homogeneity of the contact resistance distribution between strands and their connections to the copper sole in the joints. In the case of large current unbalance, the overloaded strands start to reach the critical current, producing a current sharing voltage, which then drives the current redistribution and dominates the distribution driven by strand to joint contact resistances. In the joint, at which the inter-strand resistance is much lower than in the regular conductor regions, a relatively low electric field is sufficient to drive an effective redistribution of the current to the less loaded strands [86], [87]. Especially for large NbTi CICCs, which operate at high-current density, a so-called sudden take-off easily occurs due to the large self-field gradients, and triggers a quench before any inter-strand current redistribution occurs [88]. In such cases, an even resistance distribution in the joints aids to prevent a dramatic performance degradation. Furthermore, the average electric field in conductors increases up to few $\mu V/m$ before the take-off that produces an inter-strand current redistribution and levels the initial current unbalance to some extent. This effect makes the non-homogeneous resistance distribution at the joint become more tolerable [89].

The contact resistance distribution is so critical for the stability of NbTi joints or even coils, that a comprehensive measurement is necessary for the performance evaluation. It is usually measured by selecting a pair of superconducting strands in a conductor sample and performing a four-point measurement with an externally applied current. Normally a DC background magnetic field $B_{dc}$ is applied to exclude the possible influence of a weakly superconducting barrier inside the conductor [87], [90], [91]. Sometimes, the contact resistance measurement is also performed by shunting the strands of the conductor into parallel channels first and then measuring the contact resistance between two channels [89].

In terms of measurement between single strands, the strands are chosen following a way that they are from different cabling stages and as comprehensive and representative as possible. The intra- or inter-petal contact resistance in a specific CICC, is defined as

$$R_c = \frac{V}{I} \cdot l \ [\Omega\text{m}], \tag{2.2}$$

where $V$ is the measured voltage, $I$ is the applied current through the selected strands and $l$ is the length of the relevant conductor section.

In the case of a joint with copper sole present in between the two cables, an overall measured value with unit of $\Omega$ is adopted to express the cable to cable, or cable to copper sole resistances, instead of the normalized resistance with unit of $\Omega$m.

In the UT laboratory, the full-size ITER joint sample is placed inside a superconducting solenoidal magnet providing a DC background field. The current leads and voltage taps are connected through a switchboard outside the cryostat. The detailed assembly of the testing setup and the joint sample preparation in the case of ITER PF conductor are described in chapter 4.

**AC loss measurement**

Several conventional methods are in use to measure the AC loss in superconductors, including electric, magnetic and calorimetric methods [92], [93]. The electric method is realized by detecting the induced voltage along the conductor with AC transport current over a range of frequencies and amplitudes. Normally pick-up coil and lock-in-amplifier techniques are used to distinguish the loss voltage components. The compensation coils are connected in anti-series with the pick-up coil or voltage taps on the sample before connecting to the input of the lock-in-amplifier, respectively. Generally, the samples carrying AC current are exposed to AC magnetic field simultaneously, which is essential for the pick-up coil technique. The total AC loss is measured by combination of both techniques [92].

The magnetic method is performed by measuring the changes of magnetic moment of the superconducting sample. The so-called magnetization loss can be measured by using pick-up coils, Hall probes, SQUIDs or vibrating sample magnetometers (VSMs), mainly depending on the sample volume [93].

SQUID and VSM techniques are commonly used for short strand or tape samples, and are not sufficiently responsive for measurements at power frequencies. Here the hysteresis loss of ITER superconducting strands is measured with VSM. Two anti-series connected detection coils are placed in a uniform magnetic field and the measured sample is vibrating vertically in one. The anti-series connection enables to eliminate the effect of the background magnetic field. The magnetization of the sample is derived by detecting the induced voltage of the two coils [94], [95].

The pick-up coil method is suitable for measuring the average loss of large samples like the ITER conductors and joints presented in this thesis. After detecting the voltage of the pick-up coil positioned on the surface of the sample, and the voltage of the compensation coil induced by the pure applied field, the magnetization loss is calculated using the voltage difference of both coils. A calibration is made regarding the demagnetization effect.

All types of AC losses result in heat dissipation in the superconductor and thus can be measured with a calorimetric method as well, either through the amount of evaporated helium or the increased temperature measured with a thermometer. However, this boil-off method is not able to detect whether the heat originates from magnetization or from transport current loss, the latter component needs to be eliminated by a calibration [92].

For the ITER joint sample measured in the UT lab, the AC loss measurement is carried out with the boil-off based calorimetric method as well as magnetic method using pick-up coils simultaneously. Due to its large size, the joint sample is placed inside a calorimeter chamber filled with 4.2 K liquid helium, which is used for measuring the evaporated helium during the power dissipation in the joint. The whole object is inserted in a solenoid providing the external magnetic field. The magnet provides a sinusoidal modulated magnetic field with amplitudes of $B_{ac} = 0.2$ or $0.4$ T and an offset magnetic field of $B_{dc} = 0$ or 1 T, in a direction parallel to the joint axis. The magnetic field frequency ranges are 1 to 160 mHz and 1 to 85 mHz for the 0.2 T and 0.4 T magnetic field amplitudes, respectively. The calorimetric method is applied at high loss for calibration purpose while the more sensitive magnetization method is used to extend the measurement to the low-loss range. The schematic of the AC loss measurement setup is shown in Figure 2.3.

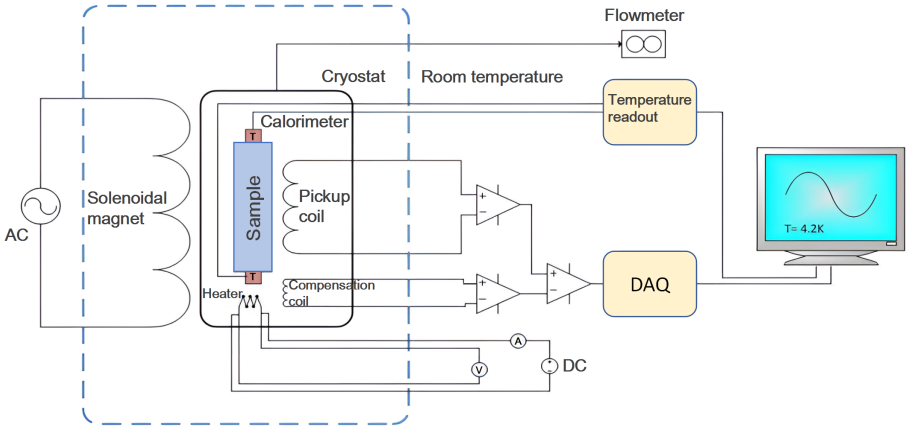


Figure 2.3: Schematic representation of the instrumentation of the AC loss test setup.

## 2.3 Electro-magnetic and thermal model JackPot-AC/DC

JackPot-AC/DC is a numerical network model developed at the University of Twente, aiming at the analysis and optimization of CIC conductors and their joints. The code was initiated to solve the JACKet POTential distribution (hence the name JackPot) of the ITER full-size CIC conductors tested at steady-state in the SULTAN facility [68]. After consistent upgrades, especially in consideration of the effect of self- and mutual inductances, as well as coupling with a changing background magnetic field, the code is capable to simulate the pulsed operating mode and the plasma scenarios. In addition, the model of a lap-type joint that consists of two CIC conductors and a non-superconducting copper sole in between has been developed further [72], [96]–[98].

Now the JackPot-AC/DC code combines both the electro-magnetic and thermal modules and enables to simulate AC and DC performances of CIC conductors and their lap-type joints under relevant operating conditions [99]–[101]. The JackPot-AC/DC code features quantitative analysis of CICCs with strand level precision. Except heat transfer coefficients, there are nearly no other free parameters in the model so the electro-magnetic and thermal behaviour are mainly depending on the sample configuration and the input contact resistances, in the form of inter-strand, inter-petal and strand to copper sole resistance, which are normally derived from dedicated measurements.

The key advantage of JackPot-AC/DC over other models [102] is that it can handle considerably large objects thanks to the application of the Matlab programming environment, in combination with advanced computing techniques. The MultiLevel Fast Multiple Method (MLFMM) and Graphics Processing Units (GPUs) technology make it possible to perform large-scale parallel calculation with relatively high computation speed [96], [103], [104]. At present, JackPot-AC/DC is to our knowledge the only available code that is capable of enabling steady-state and pulsed analysis of ITER-like CIC conductors and full-size lap-type joints with length up to tens of meters but keeping strand-level details.

### 2.3.1 Cable model

The fundamental process in the simulation model is to reproduce the complicated trajectories of strands since the layout of strands determines the electro-magnetic characteristics, like in particular the resulting contact resistances [105], [106]. For an ITER TF conductor, the cabling process represented in the model is illustrated in Figure 2.4, according the cable pattern and twist pitches of cabling stages, as specified in Table 1.4. Three strands from the first cabling stage are twisted into a bundle first, then three such bundles are twisted into a new sub-cable. The procedure is repeated for each stage, until the final cable layout is reached [68]. Furthermore, a reshaping function is necessary to rearrange sub-cables and compact them into the next cabling stage.

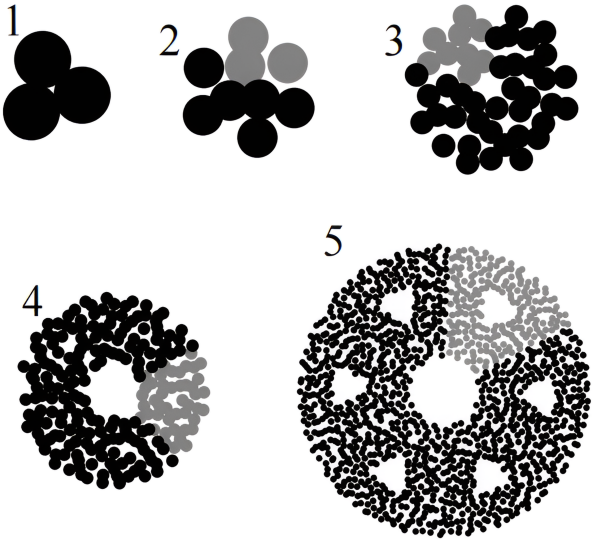


Figure 2.4: Cross-sectional view of the successive cabling stages for an ITER Toroidal Field conductor in the JackPot model. In each stage, the grey strands represent a sub-cable shaped and defined in the previous step [68].

### 2.3.2 Joint model

The joint consists of superconducting and non-superconducting components. The mutual inductances between strands and copper sole elements are taken into account. Different from the discretization procedure of strands that follows the trajectories and then confirms the coordinates at each cross-section, the discretization of the copper sole is achieved with the so-called PEEC technique, by treating the object as a 3-dimensional electrical grid [107].

This technique is effective for rectilinear objects and is easy to implement and it is straightforward to expand to a 3D model. Figure 2.5. a) shows a 2D object modelled with the PEEC technique. An orthogonal grid of voltage nodes is created across the object

connected through resistive paths. Mutual inductive couplings can be evaluated analytically by only considering the parallel current paths, which saves a considerable amount of computation time and memory but without losing significant precision [97]. In the spatial discretization of a copper sole of lap-type joint, the nodes located in the two cable areas as well as the current paths connecting to such nodes are removed from the model, as shown in Figure 2.5. b).

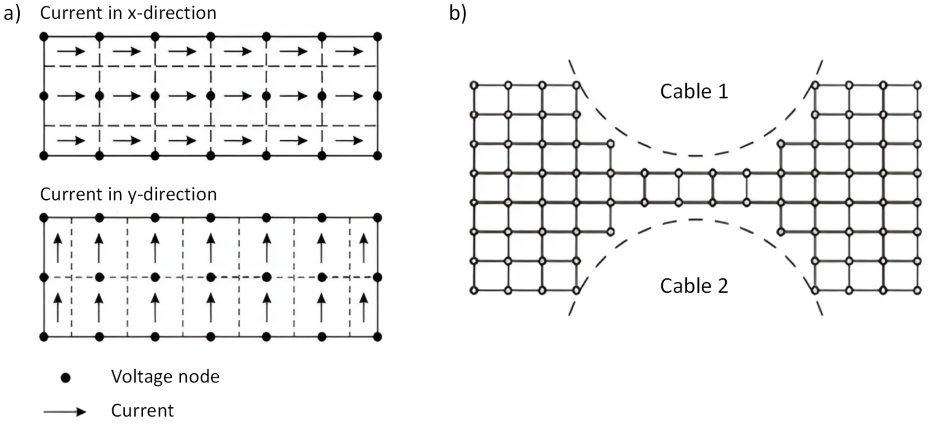


Figure 2.5: a) 2D rectangular object modelled with the PEEC technique. b) Voltage nodes (circles) and current paths (straight lines) in the cross-section of the copper sole as simulated with the PEEC method [97].

### 2.3.3 Resistances

JackPot-AC/DC assigns discrete contact resistances between strands or strands and joint members, based on the geometry of the physical contact areas [68]. In general, the contact resistance is reversely related to the area $A$ [m$^2$] and proportional to the contact resistivity $\rho'$ expressed in [$\mu\Omega \cdot$ m$^2$], as given by

$$R = \frac{\rho'}{A} \ [\mu\Omega]. \tag{2.3}$$

The spatial contact areas are determined after the reshaping of the cable and joint geometry model, while the contact resistivities $\rho'$ with respect to the individual inter-strand, inter-petal and strand to copper sole situations, are unknown but required as input parameters for the JackPot-AC/DC simulations. They are normally obtained from dedicated contact resistance measurements, e.g. as performed in the UT laboratory, or indirectly obtained by fitting the results of AC loss measurements and simulations.

#### Inter-strand resistances

During the discretization process, the cable is divided into a number of sections along its axis. The length of the section $dz$ is normally chosen to be 5 to 10 times smaller than the

shortest twist pitch, so as to minimize the probability of missing inter-strand contacts but without increasing too much the computation.

The inter-strand contact area $A$ is defined as the overlap area between strands. A schematic view of the contact areas is illustrated in Figure 2.6 for three strands. The distance between strands $d_{ss}$ is counted from the strand centers. Considering the probability that strands are disconnected when their distance is larger than their diameter, or the unlikely event that two strands intersect completely, the probable contact width $w_{ss}$ is defined as

$$w_{ss} = d \cdot \sqrt{1 - min[1, (\frac{d_{ss}}{d})^2]}, \tag{2.4}$$

where $d$ is the strand diameter [68].

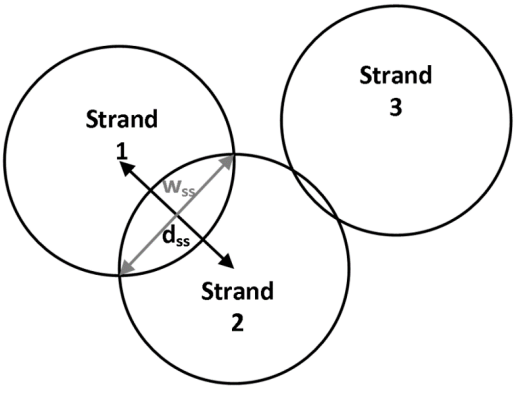


Figure 2.6: Schematic view of contacts between 3 strands, the inter-strand distance and width between strands for the evaluation of the contact area [68].

If the petal wraps of the conductor are present, the inter-petal resistivity is usually assumed to be several times larger than the inter-strand resistivity, or derived from the fitting method.

**Strand to sole resistances**

The contact resistance between strands and the copper sole in the joint is calculated in a similar way as the inter-strand contact resistance. The inter-strand distance is replaced by the distance between the strand center and the inner edge of the cable, as illustrated in the left plot of Figure 2.7. When considering the compaction of the cable in the joint-box, the radius of the curvature of the cable circumference is still much larger than the strand radius, and it is allowed to approximate the curved cable edges as flat surfaces.

The simplified schematic view with respect to the strand to sole distance $x_{sj}$ and the contact width $d_{sj}$ is shown in the right plot of Figure 2.7. $x_{sj}$ is the distance between the center of the strand and the inner edge of the cable, and $x_{sj} = r_{out} - d_{rc} - r$, with $r_{out}$ the outer radius of the cable and $r$ the radial position of the strand within the cable. The parameter $d_{rc}$ is used to vary the inner radius of the cable and then adjust the number of

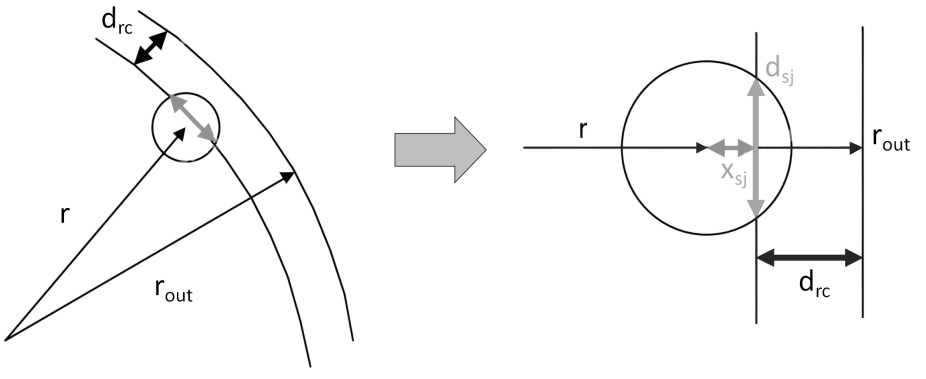


Figure 2.7: Schematic view of the strand-to-sole distance $x_{sj}$ and the contact width $d_{sj}$ used to determine the effective contact area in the model.

strands in the ring that are in direct contact with the sole, the value is normally determined by counting and matching the number of contacts observed in a photograph of the joint cross-section.

Considering the probable situations that there are no contacts ($r - d_{rc} < r_{out}$) or strands exceeding the limitation of the outer cable radius ($r > r_{out} - d_{rc}$), the expression of $x_{sj}$ is corrected to

$$x_{sj} = min(\frac{d}{2}, max(0, r_{out} - d_{rc} - r)). \tag{2.5}$$

The contact width $d_{sj}$ is obtained correspondingly, $d_{sj} = 2 \cdot \sqrt{(d/2)^2 - x_{sj}^2}$, with $d$ the strand diameter. The contact area is calculated by multiplying the contact width $d_{sj}$ with the longitudinal distance between two successive intersections $dz$.

To improve the electrical and thermal contacts between cable and sole as well as the current uniformity [75], [76], solder filling is used in the joint by either applying at the cable perimeter or the voids between strands completely. However, due to the difference in the soldering techniques, it is difficult to estimate the thickness of the solder that varies within a certain range. In the JackPot-AC/DC model, the thickness of solder $d_{sol}$ is expressed with a multiplying factor $k$ with respect to the diameter of the strands $d$, $d_{sol} = k \cdot d$. An empirical value of $k = 1.5$ [68] is normally adopted. By choosing a proper strand to sole resistivity, in combination with the solder penetration depth and width given, the distribution of the strands, the physical properties of the joint become realistic at the strand-sole contacting layer.

**Copper sole resistance**

The copper sole resistance is calculated with the PEEC technique as well, as illustrated in Figure 2.5, the three dimensional network of the current paths which connecting the voltage nodes is confirmed, the resistance is then given by $R = \rho \cdot l/A$, where $l$ and $A$ is the length and cross-section of the current path between two voltage nodes.

### 2.3.4 Self- and mutual inductances

In the JackPot-AC/DC model, in order to calculate the coupling loss of a CICC or a joint generated by a time-varying external field and a self-field, the mutual inductances between all strand segments and copper sole elements have to be known and are calculated in advance [96]. Similar to contact resistances, the calculation of mutual inductances is also based on the trajectories of all strands in the cable and discretization of copper sole elements.

#### Inductances in CICCs

Due to the inter-strand resistivity, the current density crossing strands is much lower than in the individual strands. Thus for simplicity, the inter-strand current can be neglected in the coupling loss calculation in JackPot-AC/DC. The inductance is calculated in the strand segments instead of the complete current circuits. In the CICCs, the calculation of mutual inductances between two current carrying elements $\overrightarrow{L_i}$ and $\overrightarrow{L_j}$ is illustrated in Figure 2.8.

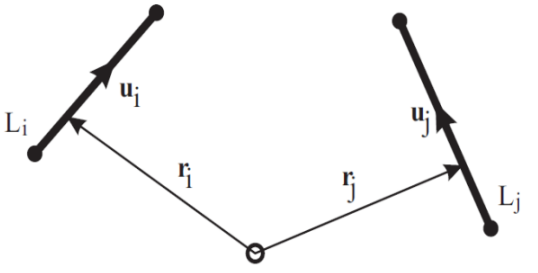


Figure 2.8: Configuration for the calculation of the mutual inductances between current carrying elements $\overrightarrow{L_i}$ and $\overrightarrow{L_j}$ [96].

The mutual inductance is defined by

$$M_{ij} = \frac{\mu_0}{4\pi} \int_{L_i} \int_{L_j} \frac{d\overrightarrow{L_i} \cdot d\overrightarrow{L_j}}{|\overrightarrow{r_{i,j}}|} \text{ [H]}. \tag{2.6}$$

In JackPot-AC/DC, the so-called MLFMM method [103] is implemented to reduce the computation load but with little accuracy lost. The method distinguishes mutual interactions of line elements that are close to each other (near-field interactions) and elements that are further away (far-field interactions) [96]. The mutual inductances of the near-field interactions are evaluated directly, while for the far-field interactions with relatively large quantities, the mutual inductances are calculated with an approximation for simplicity [96].

The self-inductances of the strand segments are calculated following [108]

$$L = 0.002 \cdot l \cdot [ln(\frac{l}{GMD} + \sqrt{1 + \frac{l^2}{GMD^2}}) - \sqrt{1 + \frac{GMD^2}{l^2}} + \frac{GMD}{l}] \text{ [μH]}, \tag{2.7}$$

where $l$ is the length of the strand segment and $GMD$ is the Geometric Mean Distance of the filaments, corresponding to the radius of the filament bundle, both expressed in centimeters.

**Inductances of the jointbox**

For the jointbox parts like the copper sole elements, the self- and mutual inductances are derived following a similar procedure as for the strands, except the line integration is substituted by the integration over the volume of the elements as given by, the grid established using the PEEC method [97]. As illustrated in Figure 2.9, two rectilinear blocks $i$ and $j$ carrying parallel currents and their mutual inductance is calculated as

$$M_{ij} = \frac{\mu_0 \overrightarrow{u_i} \cdot \overrightarrow{u_j}}{4\pi S_i S_j} \int_{V_i} \int_{V_j} \frac{1}{|\overrightarrow{r_i} - \overrightarrow{r_j}|} dV_i dV_j \text{ [H]}, \tag{2.8}$$

where $V_i$ and $V_j$ are the volumes of blocks, $\overrightarrow{r_i}$ and $\overrightarrow{r_j}$ are the vectors pointing to locations inside the blocks, $\overrightarrow{u_i}$ and $\overrightarrow{u_j}$ are unit vectors pointing in the direction of the current flow, and $S_i$ and $S_j$ are the areas perpendicular to this current flow.

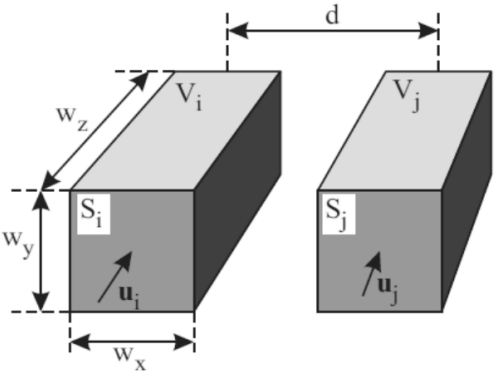


Figure 2.9: Configuration for the calculation of the mutual inductances between joint box elements [97].

Following the volume discretization by the PEEC method, the calculation of mutual inductance can be reduced to one volume integral. However, the computational load is still considerable due to far-field interactions between volume elements. The MLFMM method also used to simplify the calculation of mutual inductance between blocks, which distances are large enough, like further than one box with respect to the spatial grid.

### 2.3.5 Self magnetic field and coupling to external magnetic field

JackPot-AC/DC includes the effect of coupling with a transient or harmonic external magnetic field. The internal magnetic field locally in the conductor is the sum of the external field and the self-field induced in the conductor.

### Self-magnetic field

The Biot-Savart law is used for the magnetic self-field calculation

$$\overrightarrow{B} = \frac{\mu_0}{4\pi} \int I \frac{d\vec{I} \times \vec{r}}{|\vec{r}|^3} \text{ [T]}, \tag{2.9}$$

with $I$ the element current, $\vec{r}$ the distance between the current element and the point where the magnetic field is calculated and $d\vec{I}$ the current direction vector.

For steady-state analysis of a conductor with transport current, the magnetic field is calculated by a simple approach. First, eight points located symmetrically around the conductor's perimeter are selected. Then their magnetic field is calculated correspondingly with the Bio-Savart law following Equation 2.9, where the current is assumed to flow in a straight line along the conductor axis. For other points inside the cable, the magnetic field is obtained by interpolating the magnitude and angle of the magnetic field in the eight selected points on the surface, instead of applying the Biot-Savart law along the trajectory of each strand. In this way a considerable computation time is saved. The self-field profile is illustrated in Figure 2.10 [68].

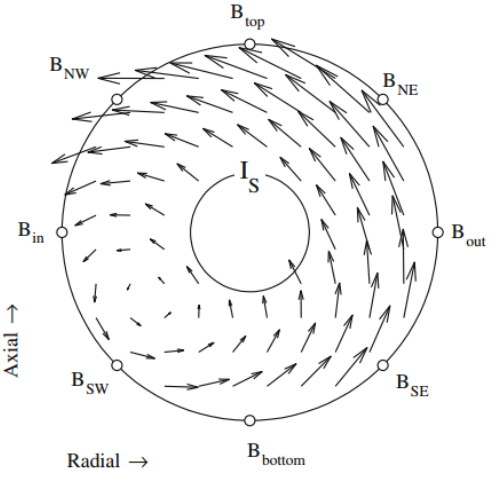


Figure 2.10: Illustration of the self-field distribution in direction and strength (arrows) in the cable's cross-section.

For the complicated situation of the conductor working in pulsed mode, the coupling currents can be potentially large, as well as the high-magnetic field generated correspondingly and a more refined approach based on the MLFMM method is adopted [109].

### Coupling with external magnetic field

The external magnetic field is expressed in terms of magnetic vector potential $\overrightarrow{B} = \nabla \times \overrightarrow{A}$. The vector potential is not unique, thus the expression can be adjusted according to the types of magnetic field [97]. Then exists

$$\overrightarrow{A} = |B|\overrightarrow{A'} \text{ [V} \cdot \text{s/m]}, \tag{2.10}$$

where $\overrightarrow{A'}$ is the vector potential normalized to the magnetic field magnitude.

The voltage induced by the changing external magnetic field is given by Faraday's law

$$V = -\frac{\partial \Phi}{\partial t} \text{ [T]}. \tag{2.11}$$

The magnetic flux can be formulated in terms of the magnetic vector potential

$$\Phi = \oint_{L_j} \overrightarrow{A} \cdot \overrightarrow{L_j} \text{ [T]}. \tag{2.12}$$

Considering that $f(B)$ does not depend on the position and $f(\vec{r})$ does not vary with time, the induced voltage is

$$V = -\frac{\partial \oint_{L_j} \overrightarrow{A} \cdot \overrightarrow{L_j}}{\partial t} = -(\oint_{L_j} \overrightarrow{A'} \cdot \overrightarrow{L_j}) \frac{d|B|}{dt} \text{ [V]}. \tag{2.13}$$

The term between brackets is the coupling coefficient with the time-varying external magnetic field and depends on the vector potential, normalised to the magnetic field magnitude.

### 2.3.6 System of equations

The JackPot AC/DC equation system is based on Kirchhoff's first and second Laws and is applied to the voltage and current nodes defined by the geometry.

The system of equations can be summarized as

$$\begin{aligned} G \cdot V + G \cdot C^T \cdot \dot{B}_e + D_i \cdot I &= 0 \\ D_v \cdot V + C^L \cdot \dot{B}_e + \Delta V &= M \frac{\partial I}{\partial t}. \end{aligned} \tag{2.14}$$

The first equation describes the current balance at each voltage node, with

- $G \cdot V$ inter-strand currents through the transverse conductance matrix $G$;
- $G \cdot C^T \cdot \dot{B}_e$ induced transverse currents due to the coupling $C^T$ with the time-varying magnetic field $B_e$;
- $D_i \cdot I$ current balance along the axial direction.

The second equation describes the voltages across the current elements, with

- $D_v \cdot V$ voltage difference between the nodes delimiting the current element;
- $C^L \cdot \dot{B}_e$ induced voltage due to the coupling $C^L$ with the time-varying magnetic field $B_e$;
- $\Delta V$ voltage drop across the strand or joint box resistance.
- $M\frac{\partial I}{\partial t}$ self- and mutual voltages induced;

### 2.3.7 Thermal model

Thermal models of the CIC conductor and joint have been included in JackPot-AC/DC, providing the capability to calculate the temperature evolution and current margin resulting from pulsed current and magnetic field operation [110]. Utilizing the computed heat generation and its distribution, along with the thermal parameters encompassing heat conductivity and transfer coefficients of the NbTi strand, copper sole, and liquid helium, the heat transfer dynamics between these main components and the ensuing heat propagation are determined. Due to the relatively gradual change in thermal performance compared to electrical parameters, average temperatures of the strand bundle and helium flow in each petal (sub-cable) are chosen to represent thermal behaviors. The model accounts for 13 elements corresponding to 6 petals and 1 central channel in each half joint.

It is worth noting that for the ITER joint sample tested in the SULTAN facility, the two central channels in the joint box section are deliberately blocked with rods to ensure adequate heat exchange between strands. In this case the temperature in the central helium channel is not considered. For other cases like the feeder of TF coils, the central channel is substituted by a copper rope, which results in an additional temperature distribution that can not be neglected [111]. Depending on the unique joint configuration, a comprehensive selection of 14 temperature variables is deemed essential for thermal analyses. This ensemble encompasses six strand bundles, six helium bundle channels, one central channel, and one sole half, each contributing distinct thermal characteristics [99], [100]. A schematic view of the thermal model in a cross-section of a conductor is shown in Figure 2.11.

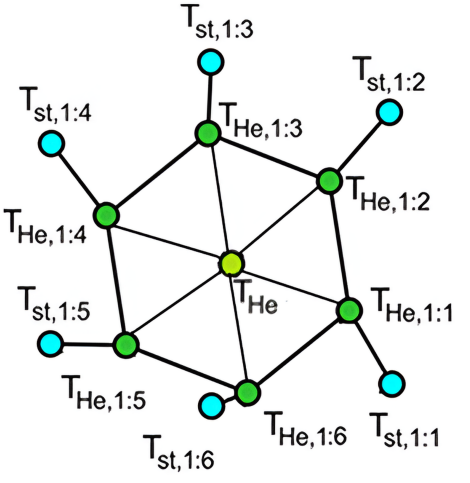


Figure 2.11: Schematic view of the thermal model of a conductor. $T_{st,1:i}$ represents the temperature of the six strand bundles (petals). $T_{He,1:i}$ and $T_{He}$ represent the helium temperature in the petals and in the central channel, respectively [111].

The heat exchange between each strand bundle and the sole half parts is proportional to the helium contact area, which is affected by the cabling pattern. The corresponding heat transfer coefficients are derived from dedicated experiments on transverse heat trans-

fer in CIC conductors accounting for both heat conduction and convection [112], [113]. Particularly, the helium mass flow in the bundle region of the conductor is assumed as $1/3$ of the total mass flow [100], [113].

### 2.3.8 Post processing of 3D visualization and animation

After solving the system equations, a vector containing the values of $V$ and $I$ is obtained, which is arranged in a form following the spatial and time discretization. Post processing is then needed to analyze phenomena like current distribution, power dissipation and temperature evolution. It is not intuitive to deal with such an enormous dataset for which a post-processer called ParaView is introduced to realize the 3-dimensional visualization and animation of the physical properties [114]. ParaView is an open-source, multi-platform data analysis and visualization application, and is capable to comply with the JackPot code output developed in the Matlab programming environment.

## 2.4 Conclusion

A comprehensive analysis of the superconducting cable behavior and connecting joints is the basic prerequisite for a safe and reliable operation of the ITER magnet system. In this chapter the relevant measurements performed on strands, cables and joints, as well as the test devices and facilities were introduced.

The SULTAN facility provides a series of qualification tests, including the DC, AC and stability measurements of full-size conductors and joints. As a reference laboratory, the high current superconductivity lab at the University of Twente also undertakes key investigations addressing strand and CICC characteristics, interstrand contact resistance and AC losses in joints of which some are reported in this thesis. The results are not only crucial for understanding magnet characteristics and performances, but also form unique input parameters for performance simulation through numerical analysis.

As regards the numerical modeling, a strand level detail code named JackPot-AC/DC was developed at the University of Twente. JackPot-AC/DC first reproduces the trajectories of all strands following the cabling pattern of a real conductor. Then the inter-strand and strand-to-sole contacts, self- and mutual inductances as well as the coupling with time-varying magnetic fields are computed correspondingly. Except the input of axial strain characteristics of $Nb_3Sn$ strands and heat transfer coefficients, the only required parameters are the inter-strand, inter-petal and strand-to-copper sole resistivities, that are usually obtained from dedicated $R_c$ measurements or measured AC loss data, like performed in the SULTAN facility or at the UT laboratory. The code combines electro-magnetic and thermal modules and enables to simulate AC and DC performances of CIC Conductors and lap-type joints under relevant operating conditions. Some details of the code structure and operational principles were briefly introduced in this chapter.

# Chapter 3

# Characteristics of ITER strands

The content of this chapter is mainly based on the following publications:

- J Huang, Y Ilyin, D Bessette, C Zhou, R Lubkemann, C Vermeer, W A J Wessel, A Nijhuis, "Effective low magnetic field $J_c(B)$ scaling of ITER $Nb_3Sn$ strands by magnetization and critical current measurements", *IEEE Trans. Appl. Supercond.* 32 4204110 (2022) (10pp) `https://doi.org/10.1109/TASC.2022.3190921`;
- J Huang, Y Ilyin, W A J Wessel, R Lubkemann, H J G Krooshoop and A Nijhuis, "Contact resistance, coupling and hysteresis loss measurements of ITER poloidal field joint in parallel applied magnetic field", *Supercond. Sci. Technol.* 35 025016 (2022) (13pp) `https://doi.org/10.1088/1361-6668/ac4201`.

## 3.1 Introduction

The ITER magnet system requires approximately 650 tons of $Nb_3Sn$ strands for TF and CS conductors and some 250 tons of NbTi strands [115], [116]. A significant scale-up of the worldwide production was therefore needed. Since a relatively large number of strand suppliers around the world were involved in the mass production, it was critical to ensure standardization and uniformity of the strand and cable production, including the characterization of the strands in terms of critical current $I_c$, $n$-value, copper stabilizer resistivity and AC loss. Such qualification and certification measurements provide a solid basis to analyze and predict the operational limits of the manufactured CIC conductors [117].

The performance of the conductors relies on a thorough knowledge of the superconducting strand's properties. In the procurement arrangements of ITER, measurements on strands at 4.2 K rather than higher temperatures is considered practical for the mass production, however, the characterization at temperatures higher than 4.2 K is obviously required as well. Furthermore, the full-size conductor comprises hundreds of strands, which need to be highly uniform in both microstructure and physical properties, like pinning mechanism, $B_{c20}$ and $T_{c0}$. Therefore, an appropriate way to describe and estimate the collective behavior is required [118]. For this engineering purpose, parameterization for the dependence of the critical current $I_c$ or critical current density $J_c$ on magnetic field $B$, temperature $T$ and mechanical strain $\varepsilon$ for $Nb_3Sn$, have been developed, with just a limited number of measurements. The scaling parameterization not only allows to characterize the strand performance in a reliable way, but also helps with the interpretation of the mechanisms determining this performance [24].

Several attempts to find a generic scaling of the critical surface yielded a number of, apparently, different parameterizations [119]. The apparent dissimilarities can be reduced by adopting the idea of a separable parameterization of the Unified Scaling Law [120]–[122], which is a relation that can quickly and accurately provide extrapolation of limited datasets to obtain full three-dimensional $I_c$ dependences, although the scaling parameters are conductor specific and need to be fitted individually.

To ensure consistency of strand measurements and of the corresponding acceptance criteria, several rounds of benchmarking $Nb_3Sn$ and NbTi strand measurements were performed [116], and the practical parameterizations suitable to characterize the ITER production were selected [119]. The single pinning mechanism parametrizations were based on criteria of simplicity and stability [23], [26], [119] and Equations 1.4 and 1.8 were selected as ITER reference scaling laws for NbTi and $Nb_3Sn$ multifilamentary wires, respectively.

For the ITER NbTi strands throughout mass production, the optimized single scaling parameterization is obtained through measurement results of $I_c$ and $n$ in a wide range of applied magnetic field (1.5 to 11 T) and temperature (3.5 to 7.0 K). It shows that the deviations between measured and predicted $I_c(B,T)$ are mainly below $15\%$, and even less than $5\%$ in the ITER operational window. Although sometimes deviation for $n(I_c)$ is larger than that for $I_c(B,T)$, it is considered acceptable since the error in measurement for the $n$ value is normally higher [117]. Another phenomenon observed in the single scaling parameterization of NbTi is that the reduced pinning force curve does not scale well with temperature [24], and the scaling is normally not very precise in the low magnetic field

domain typically below 3 T [123]. For these reasons, a two-pinning components model is proposed, which can accurately describe data in the relevant ranges of magnetic field and temperature. Furthermore, the range is wider than for the conventional single-component models [24]. The pinning force equation adopted is

$$\begin{aligned} F_p &= F_p^1 + F_p^2 \\ &= C_1 \cdot (1-t^n)^{\gamma 1} \cdot b^{\alpha 1} \cdot (1-b)^{\beta 1} + C_2 \cdot (1-t^n)^{\gamma 2} \cdot b^{\alpha 2} \cdot (1-b)^{\beta 2}, \end{aligned} \tag{3.1}$$

where

$$b = \frac{B}{B_{irr}(T)} = \frac{B}{B_{irr\_0}(1-t^n)}, \tag{3.2}$$

$$t = \frac{T}{T_{c0}}, \tag{3.3}$$

with $B_{irr\_0}$ the upper critical field at zero temperature and $T_{c0}$ the critical temperature at zero magnetic field.

A summary of the practical parameterizations derived from large ITER datasets is shown in reference [123]. In the JackPot-AC/DC code, the single-component model for $Nb_3Sn$ and two-pinning components model for NbTi are used. Since the scaling parameters are highly dependent on the specific strand type, two sets of representative parameters from [123] for PF and CS strands are listed in Table 3.1.

Table 3.1: Scaling law parameters of NbTi and $Nb_3Sn$ strands used in the JackPot-AC/DC model for PF and CS conductors [24].

| NbTi in PF conductor | | $Nb_3Sn$ in CS conductor | |
|---|---|---|---|
| $C_1$ | 396 | $C_{a,1}$ | 45.33 |
| $C_2$ | 60 | $C_{a,2}$ | 0.0 |
| $T_{C0}$ | 8.908 | $\epsilon_{0,a}$ | 0.325% |
| $B_{irr\_0}$ | 14.156 | $\epsilon_m$ | -0.164% |
| $\alpha_1$ | 2.714 | $B_{c2m(0)}$ | 29.26 |
| $\beta_1$ | 1.951 | $T_{cm}$ | 16.17 |
| $\gamma_1$ | 2.564 | $C$ | 12499 |
| $\alpha_2$ | 0.542 | $p$ | 0.419 |
| $\beta_2$ | 1.584 | $q$ | 1.431 |
| $\gamma_2$ | 1.646 | | |

During the operation of the ITER machine, a significant fraction of the $Nb_3Sn$ conductors will be operating at a low magnetic field ($B < 4$ T), like the outer turns of the CS modules and TF winding packs, while so far the $I_c(B,T,\varepsilon)$ parameterization has been derived from measurements carried out at a higher magnetic field ($B \geq 7$ T) [119]. For analysis purposes, it may be not accurate enough to use the existing $I_c(B,T,\varepsilon)$ parameterization for extrapolation to the lower magnetic field region. In particular, for a proper evaluation of the critical current $I_c$, current sharing temperature $T_{cs}$ and hysteresis loss in the $Nb_3Sn$ coils during the plasma operating scenario.

Motivated by the demand of a more detailed insight into strand heat generation at low-magnetic field, a characterization work concerning five $Nb_3Sn$ strands has been carried out by CERN [124], also being one of the reference laboratories for ITER strand benchmarking [116]. A comparable approach was followed to characterize a batch of ITER reference $Nb_3Sn$ strands in a new testing campaign at Twente, to obtain the effective low magnetic field $J_c(B)$ scaling of ITER $Nb_3Sn$ strands by magnetization and critical current measurements, as described in section 3.2.

The scaling law provides a generic way to characterize the strand with respect to temperature, strain and magnetic field applied in a certain direction. Due to the twisting pattern of the subsequent cabling stages in CICCs, the angle between strands and applied magnetic field direction is varying periodically. This affects not only the sensitivity of the parameterization with respect to the varying field angle, but also the accurate estimation of the hysteresis loss. The effect is illustrated in section 3.4, by testing the hysteresis loss density of a NbTi strand for different angles with the applied magnetic field. Since a PF joint consists of some two thousand NbTi strands, its hysteresis loss can be estimated by multiplying the total volume of strands to the angular dependent hysteresis loss density. Furthermore, the hysteresis loss of a joint can also be derived from an AC loss measurement, as described in chapter 4. By comparing the hysteresis loss obtained by both methods, an effective angle for the twisted strands in the CICCs is derived and used for further analysis.

## 3.2 Effective low-magnetic field scaling of ITER $Nb_3Sn$ strands through magnetization and critical current measurements

For ITER $Nb_3Sn$ strands, six Domestic Agencies are in charge of the procurement, and eleven companies carry out the specific manufacturing tasks under the supervision of the ITER Organization (IO), eight for the TF coils and three for the CS coils. Furthermore, two types of production processes are accepted for the ITER $Nb_3Sn$ strands, the bronze route (BR) and internal-tin (IT) route. Four TF and two CS strand types were made by the BR process, and the rest made by the IT process [116].

In total six TF and one CS type of ITER $Nb_3Sn$ strands were tested at the University of Twente, of which three are BR and four are IT processed. The strands were manufactured at seven companies, and named TFBR01, TFBR02, TFIT01, TFIT02, TFIT03, TFIT04 and CSBR01, respectively. The specifications of the TF and CS $Nb_3Sn$ strands are shown in Table 3.2. For each stand, two measurements are performed: transport critical current measurement at magnetic field of $7 \leq B \leq 12$ T and magnetization measurement performed with a Vibrating Sample Magnetometer (VSM), at the magnetic field region of $0 < B \leq 9$ T. There is an overlapping magnetic field range from 7 to 9 T. There is a relation between the magnetization and critical current density and the idea of the scaling method is to connect the two sets of measurement at the overlapping magnetic field range of $7 \leq B \leq 9$ T, then extend the critical current characteristic to the low-field region via the measured magnetization data. Finally, an effective scaling law $J_c(B)$ for the entire magnetic field region, from zero to 12 T is then obtained.

Table 3.2: TF and CS $Nb_3Sn$ strand specifications and achieved values [34], [115], [125].

| | TF | | CS |
|---|---|---|---|
| | Bronze route | Internal tin | Bronze route |
| Outer diameter | $0.820\,\text{mm} \pm 5\,\mu\text{m}$ | $0.820\,\text{mm} \pm 5\,\mu\text{m}$ | $0.830\,\text{mm} \pm 5\,\mu\text{m}$ |
| Strand twist pitch | $15 \pm 2\,\text{mm}$ | $15 \pm 2\,\text{mm}$ | $15 \pm 2\,\text{mm}$ |
| Cr-coating thickness | $2 + / - 1\,\mu\text{m}$ | $2 + / - 1\,\mu\text{m}$ | $2 + / - 1\,\mu\text{m}$ |
| $I_c$ at 12 T, 4.2 K | 190-255 A | 240-315 A | > 260 A |
| Hysteresis loss over $\pm$ 3 T field cycle, 4.2 K | $40 - 500\,\text{kJ/m}^3$ | $180 - 600\,\text{kJ/m}^3$ | $\leq 500\,\text{kJ/m}^3$ |
| $n$-value at 12 T, 4.2 K | > 20 | > 20 | > 20 |
| Residual-Resistance Ratio (RRR) | > 100 | > 100 | > 100 |
| Cu:nonCu ratio | $1.0 \pm 0.1$ | $1.0 \pm 0.1$ | $1.0 \pm 0.1$ |

### 3.2.1 Experimental setup and sample preparation

$Nb_3Sn$ is a brittle A15 material formed during a diffusion heat treatment, thus the winding of the strands is performed prior to the Nb-Sn reaction. For the bronze route strands, the $Nb_3Sn$ layers are typically formed around each original Nb filament embedded in the bronze matrix. The internal-tin processed strands consist of three main constituents, Cu, Sn and Nb. During the heat treatment, the Cu and Sn elements are first converted into high-Sn bronze phases at temperatures up to about 500 °C, and then react with the Nb filaments after the temperature is increased up to 600 to 700 °C [126]. The specific heat treatment schedules for the seven samples are shown in Table 3.3.

Table 3.3: Heat treatment schedule of the various strand samples and resulting RRR ratios.

| Sample | Heat treatment cycle | RRR |
|---|---|---|
| TFBR01 | 595 °C (160 h) – 620 °C (320 h) | 117 |
| TFBR02 | 570 °C (250 h) – 650 °C (100 h) | 150-170 |
| CSBR01 | | 146 |
| TFIT01 | 210 °C (50 h) – 340 °C (25 h) - 450 °C (25 h) - 575 °C (100 h) - 650 °C (100 h) | 158 |
| TFIT02 | | 170 |
| TFIT03 | 210 °C (50 h) – 340 °C (25 h) - 450 °C (25 h) - 575 °C (100 h) - 650 °C (120 h) | 138 |
| TFIT03 | 210 °C (50 h) – 340 °C (25 h) - 450 °C (25 h) - 575 °C (100 h) - 650 °C (200 h) | >150 |

For the transport critical current measurement, the strand is wound on a standard ITER-type VAMAS barrel [127], which is a molybdenum sulfide coated and preoxidized Ti6Al4V cylinder with a spiral groove and two copper end caps. The coefficient of thermal expansion of Ti6Al4V matches closely that of $Nb_3Sn$. The outer cylinder diameter is 32 mm and the height is 28.6 mm [128], as shown in Figure 3.1 a. After heat treatment, the transport critical current measurement of the barrel samples is carried out in a solenoidal magnet with applied magnetic fields of 7, 8, 9, 10, 11 and 12 T, which is oriented parallel to the axis of the VAMAS barrel. The direction of the applied magnetic field with respect to the transport current is shown in Figure 3.1 a, and the operating temperature is 4.2 K.

For the magnetization measurement a VSM is used [95]. After heat treatment, the mini-coil sample with a length of about 8 mm, is mounted on the end of a rod made from PEEK material and covered with a Teflon tape for fixation, as shown in Figure 3.1 b. The

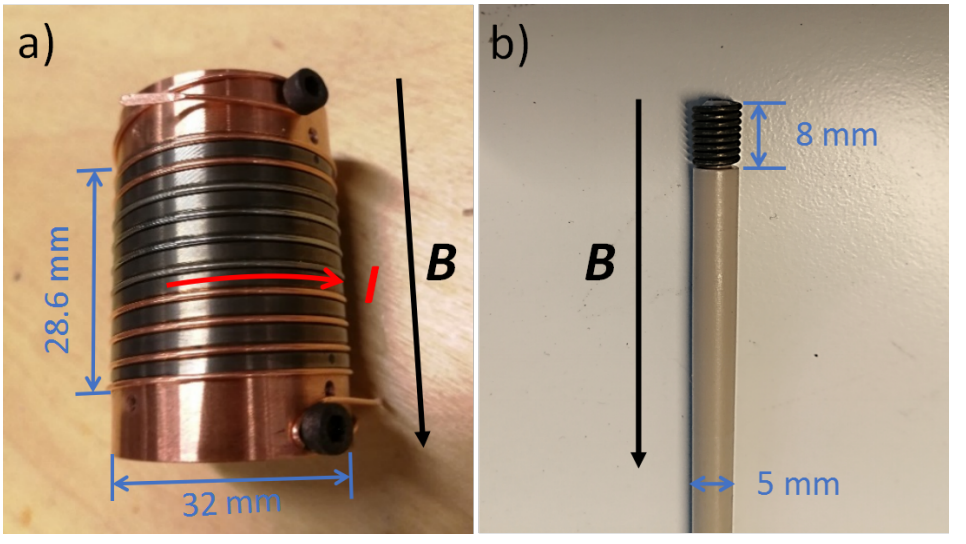


Figure 3.1: Photographs of a) an ITER type VAMAS sample for heat treatment and critical current measurement, b) mini-coil sample assembled on the probe for the VSM measurement after heat treatment.

magnetic moment of the sample is measured in the VSM, by detecting the induced voltage of the two anti-series connected detection coils [94]. The uniform magnetic field applied is parallel to the axis of the mini-coil, as seen in Figure 3.1 b, and continuously swept between a minimum and maximum magnitude $-B_m$ and $+B_m$, and with a constant ramp rate $r$. The employed sequence of the maximum fields $B_m$ is: 0.2, 0.3, 0.4, 0.5, 0.7, 1.0, 2.0, 3.0, 5.0, 7.0, 8.0 and 9.0 T. The ramp rate is $r = 0.07$ T/min for the sweeping magnetic field with a maximum magnitude less than or equal to 2.0 T, and $r = 0.5$ T/min for the higher magnetic field magnitudes. The testing temperature is 4.2 K [128]. The magnetization of the strand is derived from the magnetic moment measured and the volume of the sample. The volume $V$ of the mini-coils is derived indirectly using $V = m/\sigma$, where $m$ is the mass of the mini-coil and $\sigma$ is the density of the strand, which is derived from measuring a relevant straight wire sample. The specifications of the seven mini-coils for the VSM measurements are listed in Table 3.4.

Table 3.4: Specification of the $Nb_3Sn$ strands and the mini-coil type samples for the VSM measurements.

| | $d$ [mm] | $m$ [mg] | $\sigma$ [mg/mm] | $V$ [$mm^3$] | $D_{coil}$ -outer [mm] | $D_{coil}$ -inner [mm] | Nr. of turns [−] |
|---|---|---|---|---|---|---|---|
| TFBR01 | $0.818 \pm 0.001$ | $4.72 \pm 0.01$ | $108.6 \pm 0.2$ | $57.1 \pm 0.2$ | $5.02 \pm 0.01$ | $3.40 \pm 0.01$ | 7.9 |
| TFBR02 | $0.820 \pm 0.001$ | $4.54 \pm 0.01$ | $114.8 \pm 0.3$ | $60.6 \pm 0.2$ | $5.27 \pm 0.01$ | $3.60 \pm 0.01$ | 8.1 |
| TFIT01 | $0.823 \pm 0.001$ | $4.46 \pm 0.01$ | $109.6 \pm 0.2$ | $58.3 \pm 0.2$ | $4.97 \pm 0.01$ | $3.30 \pm 0.01$ | 8.0 |
| TFIT02 | $0.826 \pm 0.001$ | $4.61 \pm 0.01$ | $107.1 \pm 0.2$ | $57.4 \pm 0.2$ | $4.97 \pm 0.01$ | $3.28 \pm 0.01$ | 7.9 |
| TFIT03 | $0.826 \pm 0.001$ | $4.48 \pm 0.01$ | $110.9 \pm 0.2$ | $59.4 \pm 0.2$ | $5.00 \pm 0.01$ | $3.32 \pm 0.01$ | 8.1 |
| TFIT04 | $0.827 \pm 0.001$ | $4.64 \pm 0.01$ | $129.0 \pm 0.3$ | $69.3 \pm 0.2$ | $5.22 \pm 0.01$ | $3.58 \pm 0.01$ | 9.0 |
| CSBR01 | $0.828 \pm 0.001$ | $4.66 \pm 0.01$ | $109.6 \pm 0.2$ | $59.0 \pm 0.2$ | $5.02 \pm 0.01$ | $3.34 \pm 0.01$ | 8.0 |

Besides magnetic field and temperature, the critical current density of the $Nb_3Sn$ superconductor is strongly dependent on the strain applied [129], [130]. The $Nb_3Sn$ composite wire will contract under axial strain after cooling down to 4.2 K, and typically contracts more in comparison to a Ti6Al4V ITER barrel. It means the wire will be slightly stretched during cool down on an ITER barrel [22], [131]. Furthermore, the intrinsic strain stays within a narrow window, the average values for BR and IT strands on the barrel are $-0.19$ and $-0.13\%$, respectively [83]. However, in order to scale the eventual fit parameters to more realistic values, a generic compressive strain state $-0.15\%$ is assumed for all wires in the critical current measurements throughout the analysis.

For the mini-coils in the magnetization measurements, the thermal expansion coefficient of the PEEK material is higher than that of $Nb_3Sn$ [132], [133]. The assembly of the mini-coils is slightly loose after cool down and needs to be fixed with Teflon tape. Thus, the strain in the mini-coils is attributed to the precompression exerted by the bronze matrix on the $Nb_3Sn$ filaments and an intrinsic strain value of $-0.20\%$ is assumed. Both critical current and magnetization measurements are then adjusted for the correct strain.

Considering the demagnetization effect in the VSM, a calibration is performed by using a standard reference sample for comparison [95]. A mini-coil is prepared from nickel wire, having a high and well-known saturation moment of 641 mT at 4.2 K [134], [135].

## 3.3 Measurement results

### 3.3.1 Hysteresis loss

The magnetic moments of the mini-coil $Nb_3Sn$ strand samples, as well the nickel mini-coil for calibration, were measured for sweeping magnetic field cycles up to 9.0 T. The magnetization, which is defined as the magnetic moment per unit volume, is derived by dividing the calibrated magnetic moment by the sample volume, as listed in Table 3.4. The magnetization of the seven strand samples versus applied magnetic field $B$ with different magnetic field amplitudes is shown in Figure 3.2.

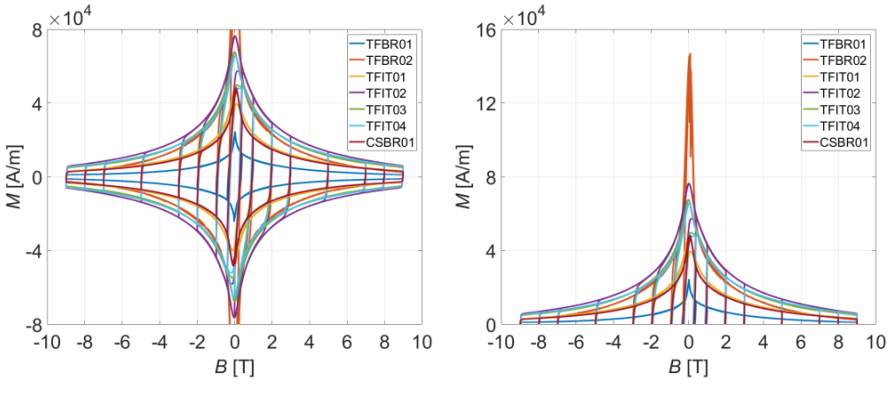


Figure 3.2: Magnetization curves of the seven mini-coil type samples for different magnetic field amplitudes (left) and an emphasis on the upper branches of the loops (right).

The results show that the two TF bronze route strands exhibit a quite distinctive behavior, especially the TFBR02 strand reveals a very high magnetization at low magnetic field. For the four internal tin processed TF strands, the magnetization behavior is quite similar.

The area enclosed by the magnetization loop represents the hysteresis loss following

$$Q_{hys} = \oint M \, \mathrm{d}B \; [\mathrm{J/M^3 \cdot cycle}]. \tag{3.4}$$

If the width between the upper and lower branches of the magnetization loop is denoted as $\Delta M(B) = M^{+}(\mathrm{B}) - \mathrm{M}^{-}(\mathrm{B})$, the $\Delta M(B)$ dependence on the magnetic field can be derived from the magnetization loops. The $\Delta M(B)$ plots for two typical strands, TFBR02 and TFIT01, are shown in Figure 3.3. The sharp peak of TFBR02 indicates that a very high magnetization is induced in the low magnetic field range. Besides, flux jumps occur at the peak, as seen in the inserted zoom in the left plot of Figure 3.3. The TFIT01 sample is typical for the other samples, a smoother change of the magnetization is observed passing zero magnetic field.

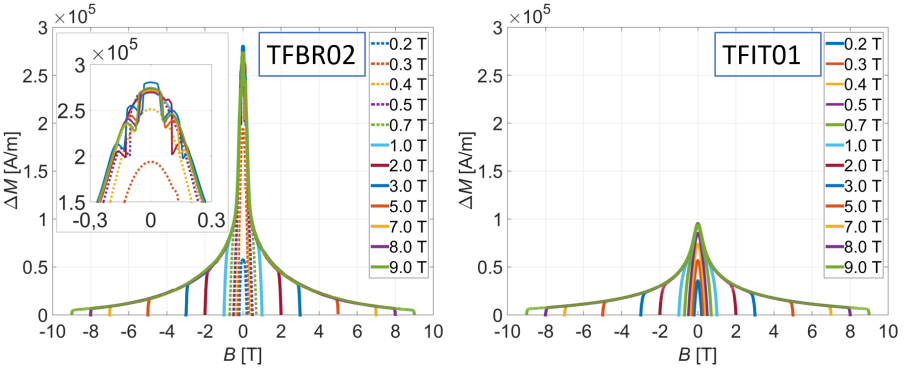


Figure 3.3: Magnetization $\Delta M$ of two typical strand samples, TFBR02 and TFIT01, versus the sweeping magnetic field amplitude. Flux jumps are observed in sample TFBR02, as shown in the inserted zoom of the left plot.

Following the calculation of $\Delta M$, the hysteresis loss of the strand with respect to the magnetic field maximum amplitude $B_m$, is calculated using

$$Q_{hys}(B_m) = 2 \int_0^{B_m} \Delta M(B) \, \mathrm{d}B \; [\mathrm{J/M^3 \cdot cycle}]. \tag{3.5}$$

The hysteresis loss of all seven samples are summarized in Figure 3.4, showing that the data of all strands satisfy the ITER $Nb_3Sn$ maximum criterion for hysteresis loss at $B_m$ of $\pm 3$ T magnetic field cycle [34], [115], [125], as listed in Table 3.2.

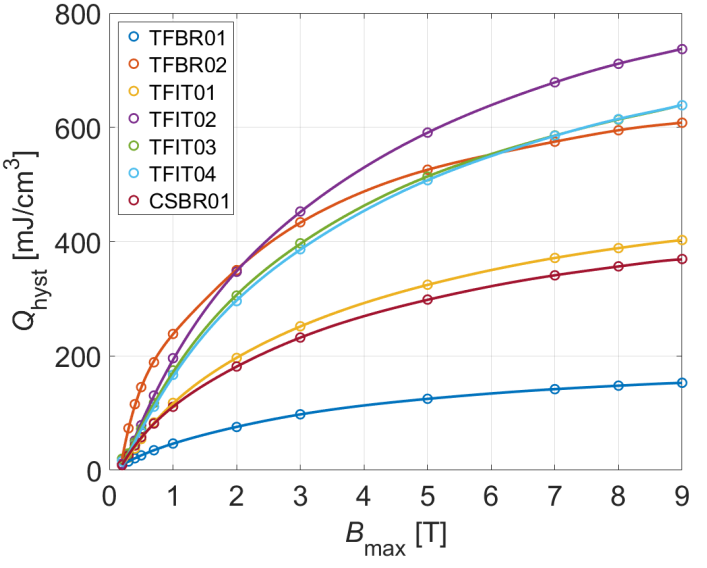


Figure 3.4: Hysteresis loss of the seven strand samples versus the applied magnetic field magnitude.

### 3.3.2 Transport current and parameterization

In addition to the magnetization measurements, that show the strand behaviour for $B \leq 9$ T, transport current measurements are performed in the magnetic field range of $7 \leq B \leq 12$ T. The critical current of the seven ITER samples are measured at 4.2 K, with an electrical field criterion of 10 µV/m in the magnetic field range of 7 to 12 T with steps of 1 T. For the ITER barrel sample, the self-field generated by the wire cannot be ignored [136] and Equation 3.6 is introduced to calculate the magnetic field after self-field correction [137]

$$B_{corr} = B_e + (2/R - 0.90)I_c \times 10^{-4}, \tag{3.6}$$

where $R$ (in mm) is the radius of the $Nb_3Sn$ filamentary area in the strand cross section and $I_c$ in A.

The corrected magnetic field dependence of the critical current of the seven samples, in comparison with original measured data is shown in Figure 3.5.

Since the magnetization values reflect the total sample volume, likewise, an engineering critical current density is adopted in consideration of the total cross section of the strand, $J_{ce} = I_c/S_{total}$, where $S_{total}$ is the area of the strand cross section taking into account the non-copper material. For a cylindrical superconducting strand fully penetrated in a perpendicular magnetic field, like the measured ITER multi-filamentary superconducting wires, the relation between magnetization and critical current density can be described by Equation 3.7 [124], [138]

$$J_{ce} = \frac{3\pi}{4d_{eff}}\Delta M, \tag{3.7}$$

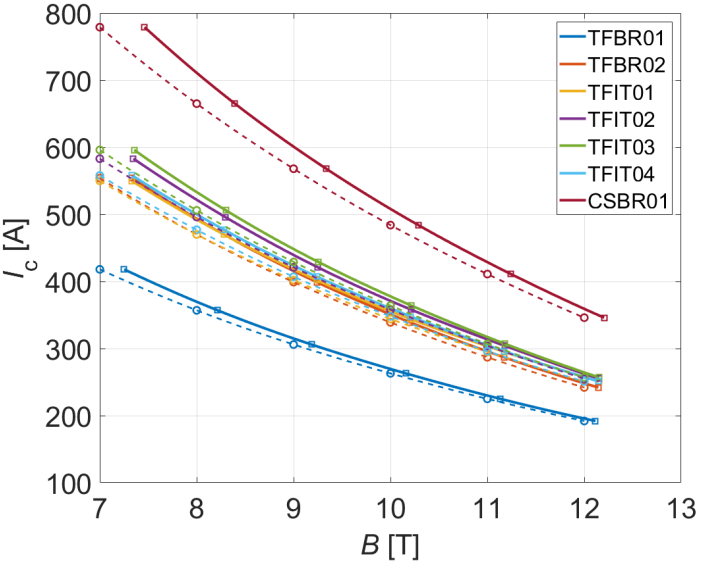


Figure 3.5: Self-field corrected (solid lines) of the critical current versus magnetic field of seven $Nb_3Sn$ strands measured on standard ITER barrels, in comparison with the data without correction (dashed lines).

where $d_{eff}$ is the effective filament diameter of the strand, regarded as a geometrical proportionality constant between $\Delta M$ and $J_c$.

Since both magnetization and critical current measurements are performed at common magnetic fields of 7, 8 and 9 T, the $d_{eff}$ for the three magnetic fields, as well as the average magnetic field, are calculated and shown in Table 3.5.

Table 3.5: Effective filament diameter of the seven samples, derived from the magnetization and critical current measurements at the overlapping magnetic field range.

| | $d_{eff}$ [µm] | | | |
|---|---|---|---|---|
| | $B = 7$ T | $B = 8$ T | $B = 9$ T | Average |
| TFBR01 | 9.4 | 9.1 | 8.6 | $9.0 \pm 0.4$ |
| TFBR02 | 19.5 | 16.8 | 14.8 | $17 \pm 2$ |
| TFIT01 | 20.1 | 19.3 | 18.3 | $19 \pm 1$ |
| TFIT02 | 36.1 | 34.9 | 32.3 | $34 \pm 2$ |
| TFIT03 | 29.7 | 28.6 | 26.7 | $28 \pm 2$ |
| TFIT04 | 34.1 | 33.1 | 30.4 | $33 \pm 2$ |
| CSBR01 | 13.0 | 12.6 | 12.2 | $12.6 \pm 0.4$ |

The results show that the impact of the magnetic field and current density on the effective filament diameter is not significant. The average filament diameter is taken as

a constant strand characteristic and used for the extension of $J_c(B)$ at the full magnetic field range. For the magnetization $\Delta M$ measured at the magnetic field range from 0.2 to 9 T, the corresponding engineering critical current density is derived by means of Equation 3.7. Together with the values directly derived from the critical current measurements performed at the magnetic field range from 7 to 12 T, a normalized $J_{ce}$ relation at the full magnetic field range from 0.2 to 12 T is obtained and shown in Figure 3.6.

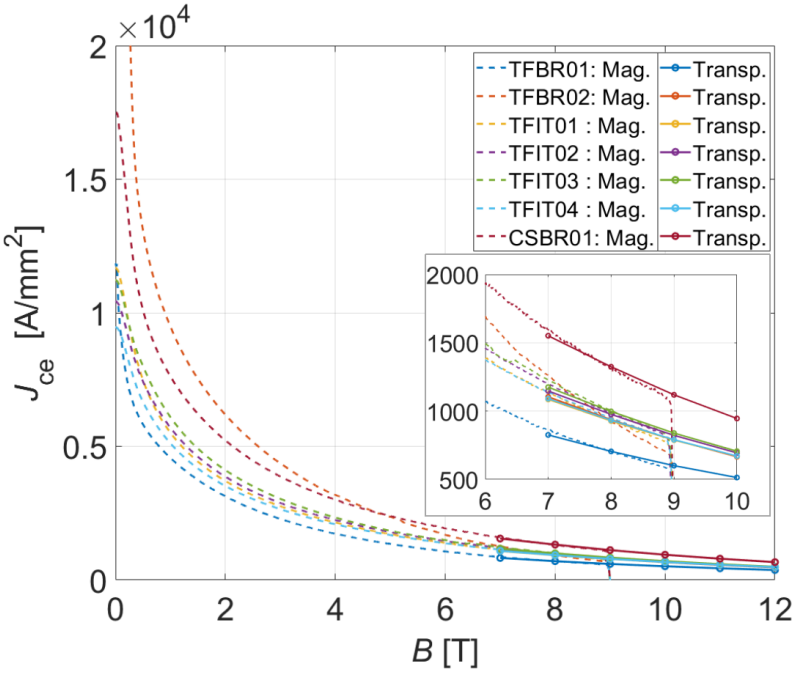


Figure 3.6: Extended $J_{ce}$ curves for the full field range for the seven samples, derived from both the magnetization and transport critical current measurements. The insert delineates the coherence of $J_{ce}$ determined by the two types of data sources at the overlapped magnetic field region.

The $J_{ce}$ of the TFBR02 sample is increasing further and approaching nearly $4 \times 10^4$ A/mm$^2$ at the lowest magnetic field. The insert emphasizes the coherence of the two types of data sources at the overlapping magnetic field. In general, a fair correlation of the $J_{ce}$ derived from the different sources is observed, which indicates a satisfying extension of the $J_c(B)$ across the full magnetic field range. Some deviation observed at the overlapping region is mainly caused by the applied $d_{eff}$, which is an average value and closer to the value calculated at 8 T, and usually slightly lower than the value at 7 T. However, a relatively poor correlation is observed for the TFBR02 strand.

### 3.3.3 Scaling law parameterization

Empirical relations between the critical current, magnetic field, temperature and strain of the $Nb_3Sn$ wires can be derived based on microscopic mechanisms, however, some are

relatively complex and use a significant number of parameters to describe the conductors involved [26], [139]. The magnetic field dependence of the critical current density in $Nb_3Sn$ wires is determined by the de-pinning of the flux-line lattice and thus by the magnetic field dependence of the bulk pinning force $F_p = J_c \times B$. The critical current density scaling law is normally obtained by interpolating and extrapolating the measured critical current data. A general description for $F_p(B)$ is like

$$F_p \propto \frac{B_{c2}^{\nu}}{\kappa_1^{\gamma}} f(b), \tag{3.8}$$

in which $b$ is the reduced magnetic field $B/B_{c2}$, $\kappa_1$ is related to the thermodynamic critical field, both powers $\nu$ and $\gamma$ are regarded as free parameters to allow for errors in the temperature dependences, usually $\nu \approx 2$ and $\gamma \approx 1$ [26], [140].

Based on the magnetization measurements with the VSM and that $\Delta M$ is proportional to the critical current density $J_c$, as in Equation 3.7, with $F_p = J_c \times B \propto \Delta M \times B$, a fitting function is introduced to analytically describe the $\Delta M(B)$ dependence [124]

$$\Delta M(B) \times B = C(\frac{B}{B_{c2}})^p(1 - \frac{B}{B_{c2}})^q, \tag{3.9}$$

in which $p$ and $q$ are $f(b)$ related parameters. However, it is divergent at $B = 0$, and thus conflicts with the calculation of hysteresis loss as shown in Equation 3.4. This problem is solved by introducing a magnetic field component $B_i$, which is related to the superconducting current circulating inside the sample, and regarded as a smooth and exponentially decaying function of $B$

$$B_{int} = 0.5B_{p0} \exp(-\frac{B}{aB_{p0}}). \tag{3.10}$$

An effective magnetic field $B_{eff} = B + B_{int}$ is adopted to describe the general scaling relation

$$\Delta M(B) = \frac{C}{B + B_{int}}(\frac{B + B_{int}}{B_{c2}})^p(1 - \frac{B + B_{int}}{B_{c2}})^q. \tag{3.11}$$

Considering the potential effect of the "internal magnetic field" $B_i$, the fitting procedure is first applied at relatively high magnetic field to determine the parameters $p$, $q$ and $B_{c2}$, and then determine the internal magnetic field relevant parameters $a$ and $B_{p0}$ by applying magnetic field covering $B_i$. Specifically, three main steps are involved to derive the fitting parameters.

In the first step, as the applied magnetic field is sufficiently higher than the field corresponding to the position of the pinning force maximum [139], like $B > 6$ T, the pinning force $F_p$ is equivalent to the product $\Delta M \times B$, by which the effect of $B_i$ is ignored, $B_i = 0$ T. In this region, the shearing of the flux-line lattice is the primary de-pinning mechanism, and the parameters $p = 0.5$, $q = 2$ are chosen because of their normally good magnetic field dependence across the entire relevant temperature and strain ranges [26], [141]. Only the parameters $C$ and $B_{c2}$ are left free. In the second step, the $\Delta M \times B$ data at applied magnetic fields higher than 1.5 T were considered and fitted.

The parameter $B_{c2}$ ought to be fixed to the value determined in the first step, however, considering the effect of strain and temperature, the $B_{c2}$ is corrected at zero strain and

temperature [130], [142], [143], by using the model, $B_{c2}(\epsilon) = B_{c2}(0,0) \cdot S(\epsilon) \cdot (1 - t^{1.52})$, in which $S(\epsilon)$ includes the strain dependence [26], [119], $t = T/T_c(\epsilon)$, $T_c(0,0) = 16.7$ K [136].

The remaining parameters $C$, $p$ and $q$ are left free. While in the third step, the magnetization data $\Delta M$ in the full range of the applied magnetic field is considered after taking into account the effect of $B_i$. In the fitting procedure using Equation 3.11, the parameter $B_{c2}$ is still fixed to the corrected value determined previously. The parameter $p$ mainly defines the shape of the pinning force in the low magnetic field region [130] and $q$ affects the maximum pinning force and its position [26]. They are set to the values determined in the second step, thus only $C$, $B_{p0}$ and $a$ are free parameters. In doing so, all six fitting parameters are obtained.

Except for the TFBR02 strand sample, the other six samples are subjected to the three-steps fitting procedure as described above. For the TFBR02 strand, a distinct high magnetization in the low magnetic field range is observed, as shown in Figure 3.2 and Figure 3.3. The large difference is related to the diffusion barrier material, niobium for the TFBR02 strand and tantalum for the other six strands. The diffusion barrier is used to isolate the Cu stabilizer from regions in the conductor where Sn diffuses to Nb during the reaction heat treatment [144].

Wires with a niobium diffusion barrier usually have a higher hysteresis loss than the ones with a tantalum barrier [145]. Since the $B_{c2}$ of pure niobium at 4.2 K is about 0.3 to $0.4$ T [146], superconductivity in the niobium diffusion barrier affects the magnetization behaviour below $B_{c2}$. For comparison, the effect of a tantalum barrier works only below 0.1 T [147]. Thus the influence of the superconducting niobium barrier has to be considered during the scaling law fitting of the TFBR02 strand. A threshold value $B_{th}$, close to $B_{c2}$, is set to determine the effective contribution of the superconducting niobium barrier. The contribution is considered to be negligible if the magnetic field exceeds $B_{th}$, otherwise, the total magnetization is determined by the $Nb_3Sn$ and Nb components simultaneously. The contribution of $Nb_3Sn$ at the low magnetic field range $B_{min} < B < B_{th}$ is derived by an extrapolation of the $\Delta M(B)$ curve from the magnetic field range $B_{th} < B < B_{max}$. Then the corresponding contribution of the Nb is defined as $\Delta M_{\mathrm{Nb}}(B) = \Delta M_{\mathrm{total}}(B) - \Delta M_{\mathrm{Nb_3Sn}}(B)$. In practice, the extrapolation line is tangential to the $\Delta M$ curve at the magnetic field $B_{th}$, thus it is sensitive to the curvature and evolution of the curve. An engineering $B_{th}$ value of 0.55 T, which is slightly higher than the $B_{c2}$ of niobium, was determined from a smooth and optimal extrapolation. The contribution of the $Nb_3Sn$ and Nb components to the magnetization $\Delta M$ is shown in Figure 3.7, in which the green point corresponds to the threshold field $B_{th}$.

For the TFBR02 strand, the $\Delta M$ fitting of the $Nb_3Sn$ and Nb components are executed in the magnetic field ranges of $0.55 \leq B < 9$ T and $0 \leq B < 0.55$ T, respectively. The fitting process of the $Nb_3Sn$ contribution follows the three-steps method as described above, while the fitting of the Nb contribution considers only the last step, except the parameter $q$, which is fixed to 2, while all the other parameters are left free.

With the VSM magnetization measurement, a set of $\Delta M$ data was derived directly with magnetic fields up to 9 T. Furthermore, according to Equation 3.7, the $J_{ce}(B)$ relation is extended at the full magnetic field range from 0 to 12 T and a set of extended $\Delta M(B)$ data can be obtained correspondingly. However, the transport current measurements are only performed at six magnetic fields, far less than the thousands of sampled data derived from

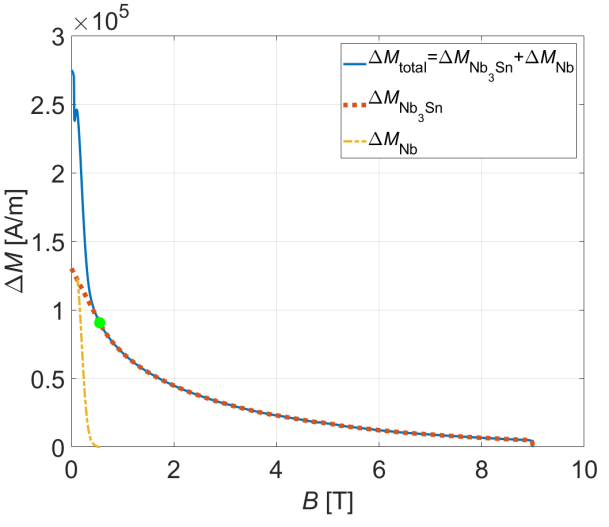


Figure 3.7: Contributions of $Nb_3Sn$ and Nb to the magnetization of the TFBR02 strand with Nb diffusion barrier. The green point represents $B_{th}$, which indicates the start of the extrapolation line.

the magnetization measurements. Therefore, an interpolation is applied for the six $\Delta M$ data curves from the transport current measurements, to obtain a similar data density as for the VSM magnetization measurement. This way an appropriate dependency is achieved by the weight of sampling points for the fitting routine. The deviation between the two datasets at the overlapped magnetic field region, as observed in the right plot of Figure 3.6, is treated with a smoothing and sparse processing method.

After the necessary data pre-processing, the two $\Delta M$ datasets were optimized, with maximum magnetic field up to 9 and 12 T. The three-steps fitting process is performed on the $\Delta M$ datasets individually to obtain the scaling parameters. The zero-temperature upper critical fields $B_{c2}$, derived from the first fitting step are summarized in Table 3.6.

Table 3.6: Zero-temperature upper critical field $B_{c2}$ [T] derived from the first fitting step with different experimental data sources. The estimated error in the $B_{c2}$ data is $\pm 0.4$ [T].

| | TFBR01 | TFBR02 | TFIT01 | TFIT02 | TFIT03 | TFIT04 | CSBR01 |
|---|---|---|---|---|---|---|---|
| $\Delta M$ data fit | 24.8 | 18.3 | 25.8 | 26.2 | 25.6 | 28.2 | 26.6 |
| $\Delta M + I_c$ data fit | 30.3 | 25.1 | 29.7 | 28.6 | 28.9 | 29.7 | 29.8 |
| $I_c$ data fit | 32.5 | 30.3 | 32.0 | 30.4 | 29.9 | 31.4 | 30.7 |

In contrast to the relatively large difference in critical current density, the upper critical field $B_{c2}$ of the ternary $Nb_3Sn$ strands are strikingly similar, reaching 30 T or slightly higher [142], [148], [149]. However, as seen in Table 3.6, for all samples, the $B_{c2}$ derived from fitting the VSM experimental data are lower than the empirical values, while the ones derived from fitting the combined VSM and $I_c$ experiments are considered reasonable. Except for the TFBR02 sample, of which the $B_{c2}$ is 18.3 and 25.1 T respectively, both are

lower than the empirical values and not comparable to the other samples. The first step fitting curves with respect to different experimental $\Delta M$ data sources are shown in Figure 3.8 for TFBR01 and TFBR02 strand samples, respectively. In addition, the fitting curve of the $\Delta M$ data derived from $I_c$ measurement alone is included.

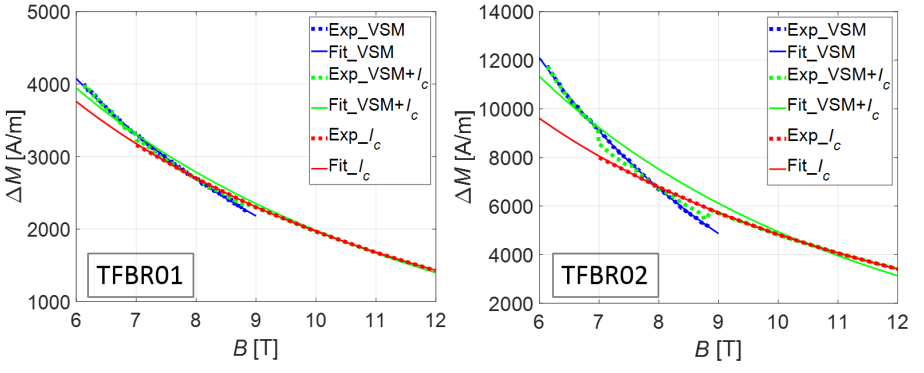


Figure 3.8: Fitting the experimental $\Delta M$ data versus magnetic field $B$ from different measurements to obtain the $B_{c2}$ parameter, for TFBR01 and TFBR02 strand samples, respectively.

Similar to the lacking consistency within the overlapping range between VSM and $I_c$ data sets, as shown in Figure 3.6, a significant deviation between the three fitting curves is also observed, especially for the TFBR02 strand sample. The fitting curve behaviors of the other six strands are quite similar and the TFBR01 sample was selected as being representative. The $B_{c2}$ values derived from two fitting curves, which correspond to the combined data of VSM and $I_c$ measurements or the $I_c$ data alone, respectively, are in the expected range based on empirical values [142], [150], while for the TFBR02, only the value derived from the $I_c$ measurement is reasonable. The evaluation of the $B_{c2}$ also implies that the deviation between the VSM and $I_c$ data is most probably attributed to the limited accuracy of the VSM data and the impact of the niobium diffusion barrier for the TFBR02 sample. When considering the underestimation of the $B_{c2}$, it is not suitable to use measured VSM data alone for the parameterization. Considering the empirical $B_{c2}$ values and the experimental data coherence, the $\Delta M$ data derived from the $I_c$ measurement for TFBR02, and the data derived from both the VSM and $I_c$ measurements for the other six samples, were specially selected to obtain $B_{c2}$.

Regarding the TFBR02 sample with the niobium diffusion barrier, the fitting was processed separately for very low magnetic field. For the $Nb_3Sn$ component of the TFBR02 strand, as well as for the other six strands, the final fitting curves are shown in Figure 3.9, with satisfactorily good fits for all samples. The parameters were derived through minimization of the overall error in the least squares fit, with an error less than 0.3%. The fitting result for the niobium diffusion barrier strand TFBR02 is shown in Figure 3.10. The scaling law fit parameters of both $Nb_3Sn$ and Nb contributions are summarized in Table 3.7. The parameter $p$ mainly defines the shape of the pinning force in the low magnetic field region and $q$ is the higher magnetic field parameter and affects the maximum pinning force and its position.

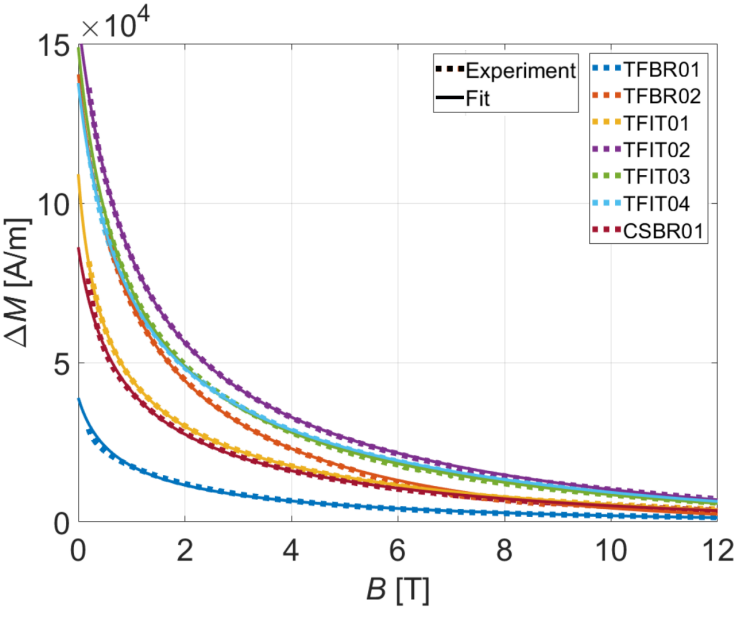


Figure 3.9: Scaling law function fit to the extended measured magnetization $\Delta M$ in the magnetic field range from 0 to 12 T.

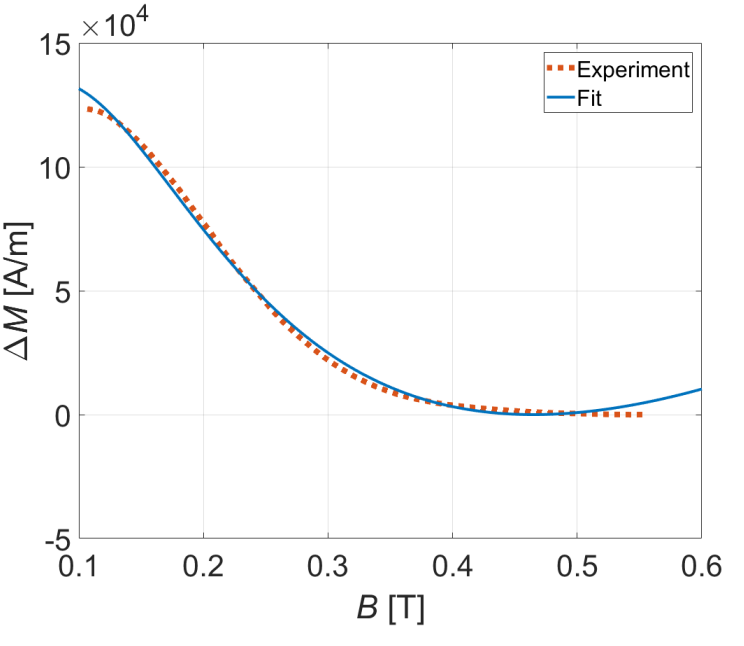


Figure 3.10: Scaling law fit of the magnetization component $\Delta M$ versus magnetic field for the strand TFBR02 with niobium diffusion barrier.

Table 3.7: $\Delta M$ fit parameters (not rounded) for magnetization data in the magnetic field range from 0 to 12 T.

| Sample | material | $C/10^5$ [T · A/m] | $B_{c2}$ [T] | $p$ | $q$ | $B_{p0}$ [T] | $a$ |
|---|---|---|---|---|---|---|---|
| TFBR01 | $Nb_3Sn$ | 0.880 | 30.27 | 0.409 | 2.628 | 0.701 | 2.7471 |
| TFBR02 | $Nb_3Sn$ | 5.591 | 30.32 | 0.551 | 4.867 | 0.597 | 1.473 |
| | Nb | 0.740 | 0.467 | 0.100 | 2.000 | 0.451 | 0.230 |
| TFIT01 | $Nb_3Sn$ | 2.815 | 29.74 | 0.498 | 2.682 | 0.444 | 2.701 |
| TFIT02 | $Nb_3Sn$ | 5.179 | 28.63 | 0.500 | 2.569 | 0.701 | 1.251 |
| TFIT03 | $Nb_3Sn$ | 4.056 | 28.87 | 0.457 | 2.529 | 0.701 | 1.711 |
| TFIT04 | $Nb_3Sn$ | 4.850 | 29.68 | 0.526 | 2.636 | 0.624 | 1.429 |
| CSBR01 | $Nb_3Sn$ | 2.319 | 29.75 | 0.460 | 2.481 | 0.663 | 1.921 |

### 3.3.4 Discussion

As observed in Table 3.7, with exception of the TFBR02 sample, the values of $p \approx 0.5$ and $q \approx 2.5$ are consistent for all other samples, which are close to the empirically set values of 0.5 and 2.0, respectively. The $\pm 25\%$ variation of $q$ mainly changes the maximum pinning force and its position. A larger $q$ implies a reduced maximum pinning force with a shift of its position towards lower magnetic field [26]. Since the different values of $p$ and $q$ implicate a slightly different pinning behaviour, and most probably originate from inhomogeneity averaging [26], [151], the particularly high value of $q \approx 4.9$ of the TFBR02 sample seems to imply a severe inhomogeneity due to the large differences of Sn content and gradient [152]. Although for bronze route strands the inhomogeneities are usually mitigated [151], different Sn gradients are observed for filaments that are located at different positions with respect to the strand center [153].

For each strand, a straight sample was prepared as well, and all samples were heat treated at the same time. The magnetization measurements have been performed on both, the mini-coil and short-straight shaped samples for mutual validation. A good coherence is observed between the measured magnetization results, including the TFBR02 strand.

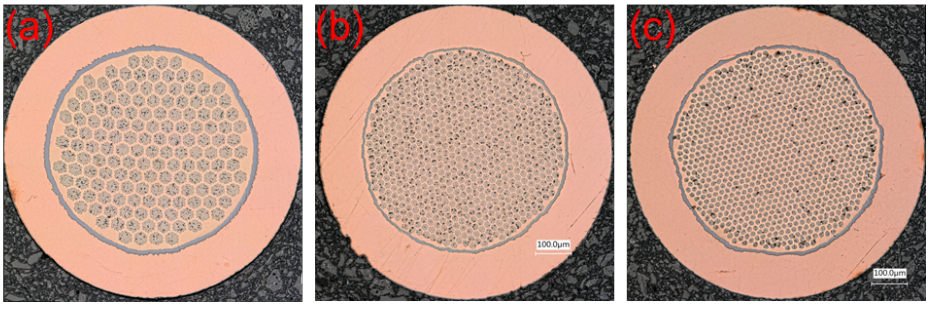


Figure 3.11: Microscope images of the cross sections of three Bronze route $Nb_3Sn$ strands: (a) TFBR01, (b) TFBR02 and (c) CSBR01.

Microscopic cross sections of the three bronze route strands (TFBR01, TFBR02 and CSBR01) are shown in Figure 3.11.

Due to the limitation of the microscopic resolution, the grain morphology of the $Nb_3Sn$ strands after heat treatment cannot be distinguished. However, when checking the filament level images, there are no abnormal phenomena are observed, as shown in Figure 3.12.

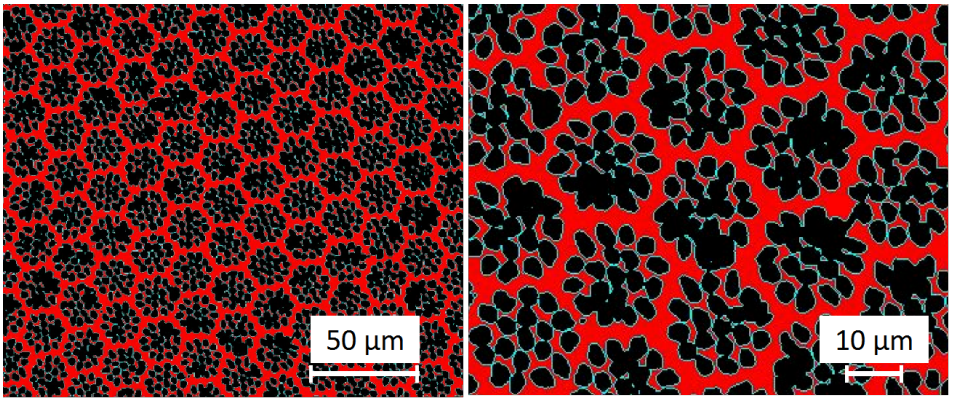


Figure 3.12: Microscopic images of the filaments of TFBR02 sample in different scales.

Many factors affect the strand behavior, such as the content and spatial diffusion gradient of Nb and Sn [151], [153], heat treatment [154], filament diameter, filament spacing and diffusion barrier material. The specifications of the three BR strands are listed in Table 3.8.

Table 3.8: Characteristics of three bronze route processed $Nb_3Sn$ strands.

| Sample wire | $N_f$ | $d_f$ [µm] | Barrier material | Barrier thickness [µm] | |
|---|---|---|---|---|---|
| | | | | UT $*$ | ITER $**$ |
| TFBR01 | 8305 | 4.7 $*$ | Ta | $\sim 14*$ | $\sim$ |
| TFBR02 | 1277 | 2.8 $**$ | Nb | $\sim 10*$ | 7.0 $**$ |
| CSBR01 | 17347 | 3.0 $*$ | Ta | $\sim 10*$ | $\sim$ |

$*$ — data derived from microscopic images at University of Twente (UT).
$**$ — data provided by ITER International Organization.

The TFBR02 and CSBR01 strands have a similar filament diameter $d_f$ and diffusion barrier thickness, and both were subjected to the same heat treatment. The larger number of filaments $N_f$ of the CSBR01 strand implies a smaller filament spacing and it could thus be more susceptible to a proximity effect, which occurs in the case that the $Nb_3Sn$ and normal copper are thin enough and in good contact and superconductivity is able to extend across the normal copper layer [155]. CSBR01 still shows a "better" scaling law fitting. A plausible explanation for this particular characteristic of the TFBR02 strand is the presence of the niobium diffusion barrier as mentioned before. It is possible that a $Nb_3Sn$ layer is formed on the internal surface of the barrier. This way the barrier itself

becomes an active path for the screening currents and leads to an increase of the loss significantly, even in the case when the applied magnetic field exceeds the penetration field [156], [157]. In this case, the hysteresis loss is anywhere dependent on the thickness of the Nb component layers [155].

## 3.4 Angular magnetic field dependence in ITER NbTi strand behavior

The angles between the axis of strands in CICCs and the magnetic field are varying periodically with the twisting pattern of the subsequent cabling stages. The critical current depends on the direction of the applied magnetic field [158], [159], while the hysteresis loss is positively correlated to the critical current density, as illustrated in section 1.4.1.

A PF joint (PFJEU6) was measured in the SULTAN facility first and then at the University of Twente, subjected to transverse and parallel applied AC magnetic fields, respectively, details are described in chapter 4. The angular dependence of the hysteresis loss in the NbTi strands then becomes a key issue for an accurate assessment of the joint's AC loss.

A series of measurements on the angular dependent hysteresis loss were performed at the University of Twente using the VSM method as introduced in section 3.2. The tested PF NbTi strand is of Type 2 and the properties are shown in Table 1.3 [160]. The magnetization $M$ is defined as the moment of a unit volume, $M = m/V$, where $V$ is the volume of the strand sample, of which the measured diameter $d = 0.725 \pm 0.005$ mm and length $L = 5.0 \pm 0.2$ mm. The short strand sample is mounted on a PEEK sample holder and covered with Teflon tape for fixation during the VSM measurement. The schematic of the sample holder is shown in Figure 3.13. Seven slots with different angles to the background magnetic field are engraved in the platform of the sample holder to hold the wire in position. The specific angles are $\theta$ = 0, 15, 36, 45, 54, 75 and 90° with respect to the magnetic field $B$ of the VSM magnet.

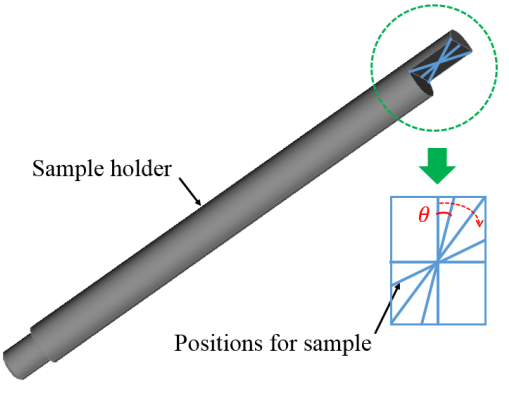


Figure 3.13: Sample holder for the VSM hysteresis loss measurement. The straight NbTi strand sample is mounted on the platform with different angles $\theta$ with respect to the background magnetic field $B$.

The magnetic field of the VSM magnetization measurement is set as same as the AC loss measurement of the joint sample at the University of Twente, with parallel magnetic field conditions $B_{dc} = 0$ and 1 T and $B_{ac} = 0.2$ and 0.4 T. The applied magnetic field on the strand sample is continuously swept between minimum and maximum magnitudes with a constant rate of magnetic field change, while the operating temperature is 4.2 K.

In order to take into account the demagnetization effect, a calibration with a pure nickel strand is performed prior to the NbTi sample measurements, of which the dimension and shape is similar to the NbTi sample. The measured saturation magnetization $\mu_0 M$ of the nickel sample is shown in Figure 3.14 and Table 3.9, with respect to the adjustable angle $\theta$.

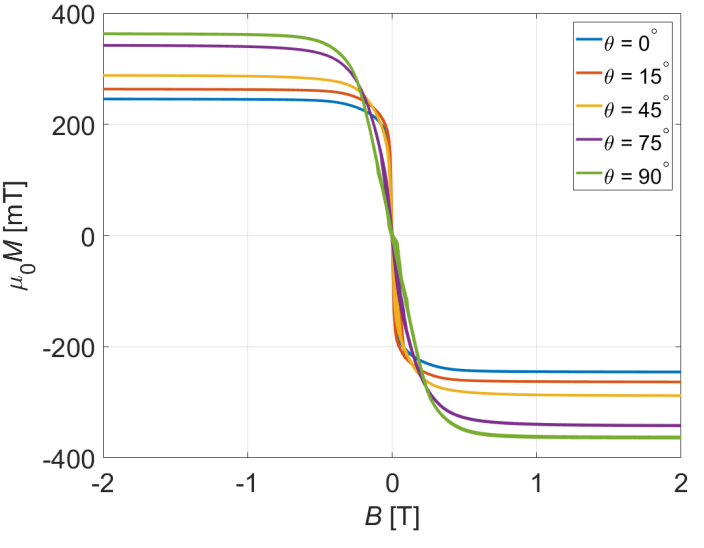


Figure 3.14: Saturation magnetization $\mu_0 M$ of the nickel sample versus magnetic field in different directions.

The saturation magnetization of the nickel wires is dependent on the orientation of the applied magnetic field [161], [162]. The reference saturation magnetizations of nickel at 4.2 K are derived from previous measurements performed at the University of Twente [163], $\mu_0 M_{ref} = 565$ and 646 mT for the magnetic field parallel and perpendicular, respectively. The difference between the measured $\mu_0 M$ and reference $\mu_0 M_{ref}$ values, is mainly caused by the demagnetization effect, which is related to the sample's shape and dimension. A correction factor is introduced to account for this influence. The correction factor is defined as $k = \mu_0 M_{ref}/\mu_0 M$, the values correspond to the parallel magnetic field $0^\circ$ and transverse magnetic field $90^\circ$ are 2.30 and 1.78, respectively, while the values at the other three angles are derived by an interpolation and fitting method, as well as the reference saturation magnetization. The saturation magnetizations and correction factors at five angles are listed in Table 3.9. Since the theoretical saturation magnetization of nickel with perpendicular magnetic field is 641 mT [134], and taking into account the errors in sample volume and sample holder position, an overall error of $\pm 3\%$ was adopted for both magnetic field orientations [163].

Table 3.9: Saturation magnetization of the nickel sample measured with VSM, with applied magnetic field orientation in five directions, with an estimated error of $\pm 3\%$ [163].

| $\theta$ | $0^\circ$ | $15^\circ$ | $45^\circ$ | $75^\circ$ | $90^\circ$ |
|---|---|---|---|---|---|
| $\mu_0 M$ [mT] | 246 | 264 | 289 | 343 | 363 |
| $\mu_0 M_{ref}$ [mT] | 565 | 577 | 595 | 632 | 646 |
| Correction factor $k$ | 2.30 | 2.19 | 2.06 | 1.84 | 1.78 |

The magnetization of the NbTi strand sample for the relevant applied magnetic field conditions and different angles is measured and the results are shown in Figure 3.15 and Figure 3.16, corresponding to magnetic field amplitudes of $B_{ac} = 0.4$ and $0.2$ T respectively.

In general, the magnetization is positively correlated to the magnetic field angle, except a slight discrepancy observed for the magnetization loops with magnetic field angle of $36^\circ$ and $45^\circ$, $75^\circ$ and $90^\circ$, measured at a background magnetic field of $1$ T. It is suggested that this can be caused by the imperfect fixation of the strand sample in the VSM.

The hysteresis loss per unit volume of the NbTi sample measured at different magnetic field conditions is derived by calculating the area enclosed by the magnetization loop according to Equation 3.5 [124]. The angular dependence of the calculated hysteresis loss densities is summarized in Table 3.10.

Table 3.10: Hysteresis loss density of the NbTi sample for different magnetic field amplitudes and directions.

| $B_{dc}$ | $B_{ac}$ | $q_{hys}$ [mJ/cm$^3$/cycle] | | | | | | |
|---|---|---|---|---|---|---|---|---|
| [T] | [T] | $0^\circ$ | $15^\circ$ | $36^\circ$ | $45^\circ$ | $54^\circ$ | $75^\circ$ | $90^\circ$ |
| 0 | 0.2 | $1.9 \pm 0.1$ | $2.2 \pm 0.4$ | $5.5 \pm 0.3$ | $6.4 \pm 0.4$ | $8.3 \pm 0.5$ | $12.5 \pm 0.7$ | $13.0 \pm 0.7$ |
| | 0.4 | $4.0 \pm 0.2$ | $5.5 \pm 1.0$ | $11.6 \pm 0.7$ | $12.8 \pm 0.7$ | $15.9 \pm 0.9$ | $21.2 \pm 1.2$ | $23.0 \pm 1.3$ |
| 1 | 0.2 | $0.5 \pm 0.1$ | $1.2 \pm 0.2$ | $2.8 \pm 0.2$ | $2.8 \pm 0.2$ | $3.3 \pm 0.2$ | $4.1 \pm 0.2$ | $3.7 \pm 0.2$ |
| | 0.4 | $1.2 \pm 0.1$ | $4.1 \pm 0.8$ | $6.5 \pm 0.4$ | $6.2 \pm 0.4$ | $7.1 \pm 0.4$ | $8.7 \pm 0.5$ | $8.2 \pm 0.5$ |

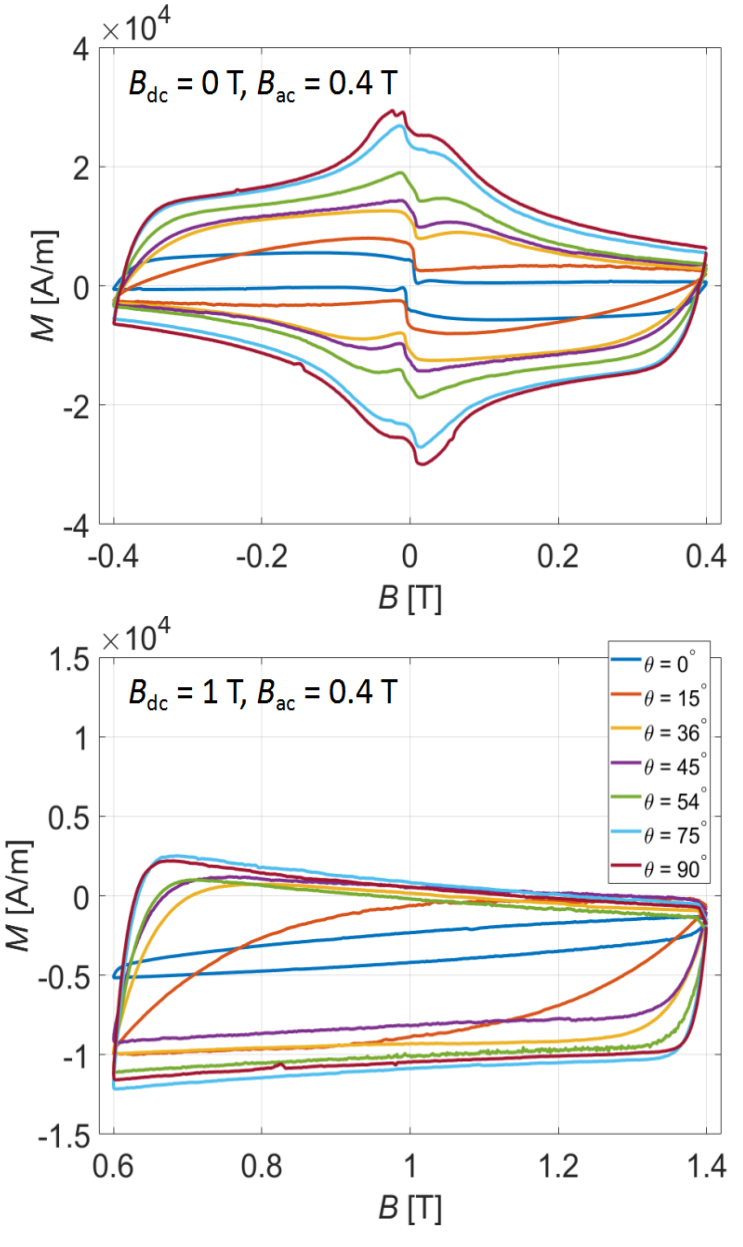


Figure 3.15: Measured magnetization $M$ versus magnetic field of the ITER NbTi strand, with magnetic field amplitude $B_{ac} = 0.4$ T, and background magnetic field $B_{dc} = 0$ and $1$ T, for seven angles.

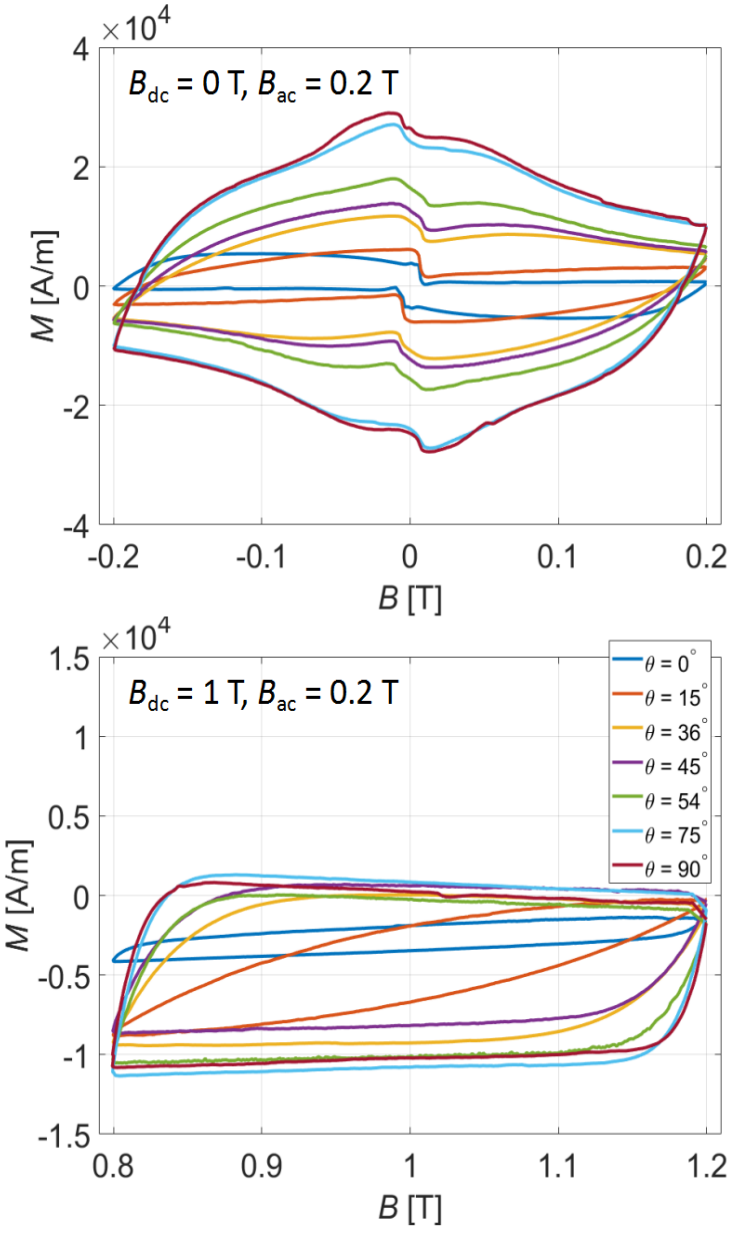


Figure 3.16: Measured magnetization $M$ versus magnetic field of the ITER NbTi strand, with magnetic field amplitude $B_{ac} = 0.2$ T, and background magnetic field $B_{dc} = 0$ and $1$ T, in seven directions corresponding with seven angles.

## 3.5 Conclusion

In order to obtain a practical scaling law for the ITER $Nb_3Sn$ strands in the operating magnetic field region below 4 T, a series of magnetization and transport current measurements of seven ITER $Nb_3Sn$ strands were performed. The magnetization was measured in magnetic field up to 9 T while the critical current of the samples was measured at magnetic field from 7 to 12 T. Since the transport current density is proportional to the magnetization, it is possible to combine the two series across the common magnetic field range of 7 to 9 T. The scaling law is derived by fitting the $\Delta M(B)$ in the full magnetic field range up to 12 T. Four internal-tin route samples and two bronze route samples with tantalum diffusion barriers exhibit a good fitting behavior. The bronze route sample with niobium diffusion barrier shows an extremely high $\Delta M$ at low magnetic field, leading to a large deviation in the fitting curve. The fit has been improved by separating the Nb and $Nb_3Sn$ components in the low magnetic field range.

The angular dependence of the hysteresis loss on the applied magnetic field in the CICCs is estimated in order to improve the accuracy assessment of the hysteresis and coupling losses at very low frequencies of the applied magnetic field.

# Chapter 4

# Parameterization and analysis of ITER CICC PF electrical joints

The content of this chapter is mainly based on the following publications:

- J Huang, Y Ilyin, W A J Wessel, R Lubkemann, H J G Krooshoop and A Nijhuis, "Contact resistance, coupling and hysteresis loss measurements of ITER poloidal field joint in parallel applied magnetic field", *Supercond. Sci. Technol.* 35 025016 (2022) (13pp) `https://doi.org/10.1088/1361-6668/ac4201`;
- J Huang, Y Ilyin, Y Zhai and A Nijhuis, "Quantitative analysis of ITER Poloidal Field joints through rigorous resistivity parameterization" (accepted by *Supercond. Sci. Technol.*).

## 4.1 Introduction

The four main types of ITER coils are designed for different operating conditions but working together to fulfil the fusion confinement conditions [9]. For the coils that are operating in mostly stationary mode, the series resistance of the current carrying strands at the electrical termination (joint) determines the current distribution among the strands [89]. While for the coils operating in alternating or pulsed current mode, both AC and resistive losses are produced by the induced and transport currents. The impact of joints on the current distribution is critical due to the presence of superconducting to non-superconducting material transitions present due to the strand's copper matrix and the copper sole in between the two cables forming a joint.

The current sharing between strands with joints involved, usually leads to current non-uniformity, which is driven by the spread in the resistances and inductive coupling of strand-to-strand and strand-to-copper sole contacts. If the strands in the cable are electrically insulated, then the current unbalance due to an uneven resistance or inductance distribution at the joint may cause critical performance limits. In PF coils for example, the current distribution in the conductors and joints is mostly inductance-dominated due to the pulsed operating mode [19]. For the large NbTi CICCs operating at high current, the quench take-off voltage is very low due to the large self-field gradient in the cable cross section and local quenches appear easily before any significant inter-strand current redistribution occurs [88]. Therefore, an even contact resistance distribution at the joints helps to avoid a dramatic performance limitation. On the one hand, if the average axial electric field in the conductors increases up to few $\mu V/m$, the inter-strand current redistribution is able to level the current unbalance, thus making the non-uniform resistance distribution at the joint tolerable [89]. On the other hand, if the current unbalance is large enough, the current in the overloaded strands may exceed the critical current and generate a relatively high-current sharing voltage causing a current limiting effect. Thus, the distributions of the contact resistances between strands and strand to copper sole determine the current redistribution and drives the current from the uppermost to less loaded strands [87].

Normally, an experimental assessment of the contact resistance distribution at a joint enables to estimate the level of current unbalance in the conductor and then to qualify the joint property. Aiming to understand and quantify the phenomena related to the overloaded strands, AC loss and stability in a transient magnetic field [72], an ITER PF Coil joint sample (named PFJEU6) was manufactured with PF5 type conductor [34] at CNIM (France). The joint was first tested in the SULTAN facility (Switzerland) to evaluate the stationary transport current properties and AC loss when a transverse magnetic field is applied [164]. After that it was shipped to CEA Cadarache (France) for pressure drop measurements. Then it was delivered to the University of Twente (The Netherlands), to measure the inter-strand, inter-petal and strand-to-copper sole contact resistances $R_c$ and AC loss in parallel alternating magnetic field. The hysteresis loss of the joint was further detailed by means of measuring the magnetization loops of the NbTi strand with a Vibrating Sample Magnetometer (VSM), as described in section 3.4.

Besides measurements, the electromagnetic and thermal properties of the CICCs and joints were numerically assessed using the JackPot-AC/DC code. Since the most important input parameters for the JackPot-AC/DC simulations are the contact resistivities. Therefore, a primary task is to obtain the resistivity parameter $\rho$ from the measured re-

sistance $R_c$. For the CICCs, it is normally achieved by adjusting the resistivity until the simulations match the measured resistance data, but for the joint, the presence of a copper sole allows additional current transfer requiring extra confinement like fitting with AC loss results as well.

Many factors can affect the parameterization and a sensitivity analysis of the individual resistivity or solder related parameters was performed by evaluating the effect on the overall contact resistance distribution and AC loss.

Due to the rather large size of the joint sample, the available test facilities are limited. Dipole and solenoidal magnets were used in the SULTAN facility and University of Twente respectively, and the AC magnetic field is applied in the transverse and parallel directions accordingly. The resistivity parameters obtained from the measurements performed in the solenoidal magnet, were used in the numerical analysis of the SULTAN tested sample.

## 4.2 Analysis of the PF joint in parallel magnetic field

### 4.2.1 Contact resistance and AC loss measurements

The section of the SULTAN PFJEU6 joint sample as delivered to the University of Twente and its dimensions are shown in Figure 4.1. The total length is about 1700 mm, the lengths of the joint-box region with stainless steel and the regular conductor sections are 580 mm and 1120 mm, respectively.

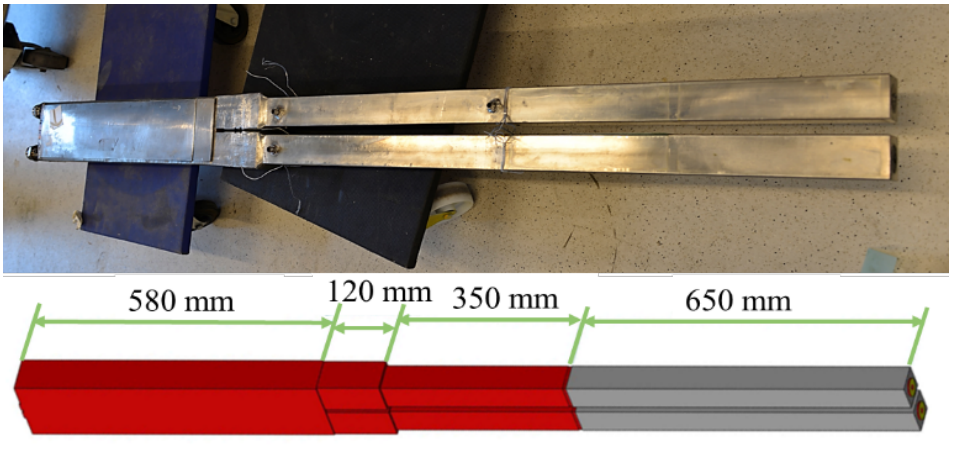


Figure 4.1: ITER PF5 joint sample (PFJEU6) before measurements (top) and the dimensions (bottom).

The PF5 CICC has a circle-in-square shape with outer stainless steel jacket dimension of 52 mm $\times$ 52 mm. The outer- and inner diameter of the superconducting cable are 35.3 mm and 10.0 mm, respectively, as shown in Table 1.5. The fabrication procedure and main properties of the twin box lap-type joint are described in section 1.3.3 [16]. The minimum thickness of the copper parts between the two cables is 20.1 mm, including a

shim layer with a thickness of 7.1 mm. The resistivities of the copper sole and shim are the same, $\rho = 3.34$ nΩm at $T = 4.5$ K. The axial- and transverse cross-sections of one termination are shown in Figure 4.2, including a cross-sectional view of the regular PF5 conductor. The shaded area represents the strands. The different areas along the length show the compacted conductor in the bimetallic box with a void fraction of 19% at left and towards the right, a gradual increase to the nominal CICC void fraction of 34%. The effective length of the compacted cable section is around 500 mm, which is similar to the length of the contact with the copper sole.

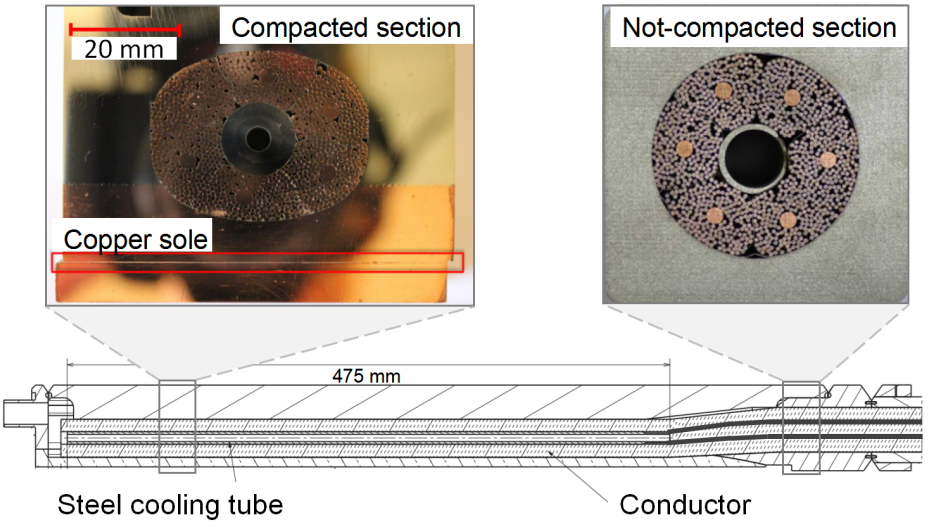


Figure 4.2: Transverse- and axial cross-sections of one PF termination (half joint). The conductor is compacted in the bimetallic box and evolves to the nominal configuration outside the box region.

## • Contact resistance measurement

The contact resistances measurement is performed before the AC loss measurement. The CICC sections with a length of 650 mm, shown in grey color in Figure 4.1, are cut first. Then the jackets of the remaining 350 mm long CICC cable sections are removed by a milling machine. The PF5 conductor consists of 1152 NbTi strands evenly distributed in 6 petals P1 to P6. The scheme of the strand selection in one cable cross section is shown in Figure 4.3, with 33 strands selected from each cable, and marked as AR1-33 and BR1-33 for cables A and B, respectively. All other superconducting and copper strands of both cable sections outside the joint section are cut shorter, and their cable and sub-cable wraps are removed. Not only the combinations of strands within the cables, like the inter-strand resistance from the first to fourth cabling stages and the inter-petal resistance from the fifth stage, were measured, but also cable-to-cable and strand-to-copper sole resistances were measured. The latter is done by means of selecting a superconducting strand and one of the current leads attached to the copper sole. The scheme of the current leads and voltage taps on the copper sole/shim is shown in Figure 4.4. Three current lead and voltage tap

groups are evenly distributed along the joint axis and in the middle of the joint, where the stainless-steel jacket is removed by milling. Small but deep holes are drilled on the exposed copper sole/shim, where the current lead and voltage tap are separately inserted into the holes and pressed tightly to obtain a direct copper to copper electrical contact without using solder. The assembly is displayed in Figure 4.10. Finally, the combination of all the three types of contact resistance measurements is summarized in Table 4.1.

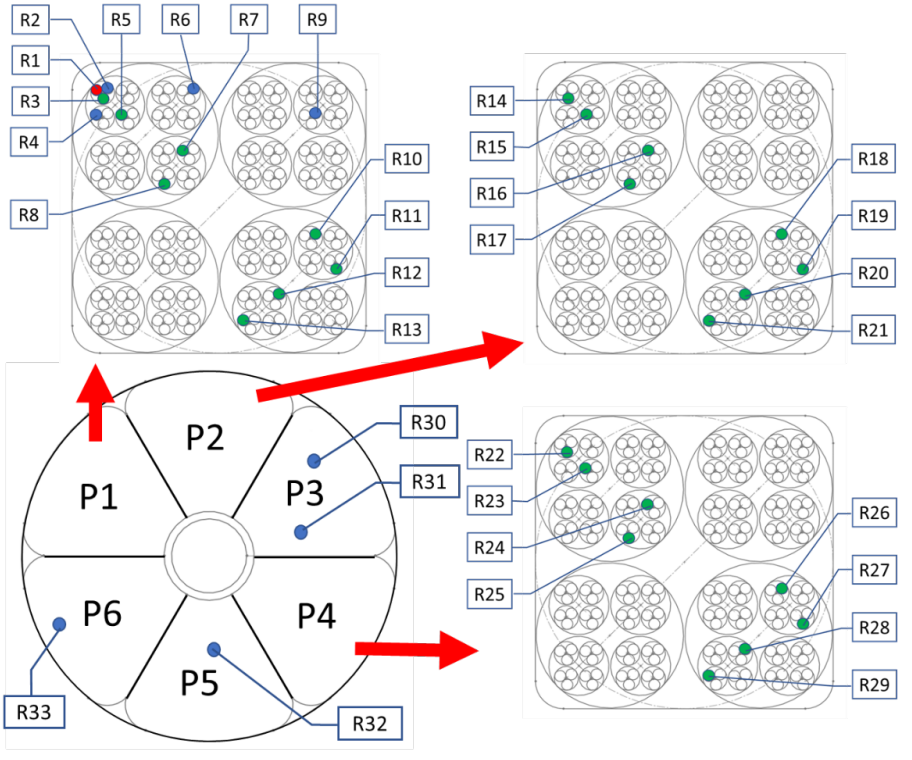


Figure 4.3: Scheme of strand selection in one cable cross-section for contact resistance measurement. The two cables are following the same scheme.

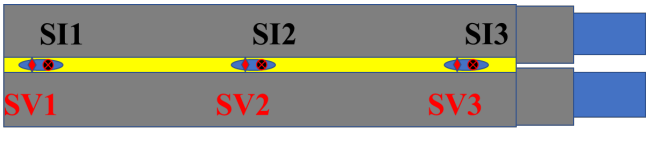


Figure 4.4: Scheme of current leads (SI1-3) and voltage taps (SV1-3) selection on the copper shim of the joint (side view of the face of joint).

The joint sample is placed inside a superconducting solenoid providing a stationary background magnetic field, to make sure that the solder used is in the normal state and not partly superconducting. The contact resistance is measured by selecting a pair of strands

Table 4.1: Combinations of superconducting strands or current leads on the copper sole of the PF-JEU6 joint, for different types of contact resistance measurements.

| | |
|---|---|
| Inter-strand resistance (strands from cable A or cable B) | |
| Stage 1 | R1–R2, R1–R3, R2–R3. |
| Stage 2 | R1–R4, R1–R5, R7–R8, R10–R11, R12–R13, R14–R15, R16–R17, R18–R19, R20–R21, R22–R23, R24–R25, R26–R27, R28–R29. |
| Stage 3 | R1–R6, R1–R7, R1–R8, R5–R6, R5–R7, R14–R16, R18–R21, R22–R24, R26–R28. |
| Stage 4 | R1–R9, R1–R11, R5–R10, R14–R18, R22–R26. |
| Stage 5 | R3–R14, R3–R16, R3–R18, R3–R21, R3–R22, R3–R24, R3–R26, R3–R28, R3–R31, R3–R32, R10–R14, R10–R16, R10–R18, R10–R21, R10–R22, R10–R24, R10–R26, R10–R28, R14–R24, R14–R26, R14–R28. |
| Strand-to-copper sole resistance | |
| | R1–SI1, R1–SI2, R1–SI3,<br>R16–SI1, R16–SI2, R16–SI3,<br>R26–SI1, R26–SI2, R26–SI3. |
| Cable-to-cable resistance (strands from two cables) | |
| | AR1–BR1, AR1–BR5, AR1–BR22, AR1–BR26, AR3–BR7, AR3–BR9, AR3–BR11, AR3–BR30, AR16–BR16, AR16–BR20. |

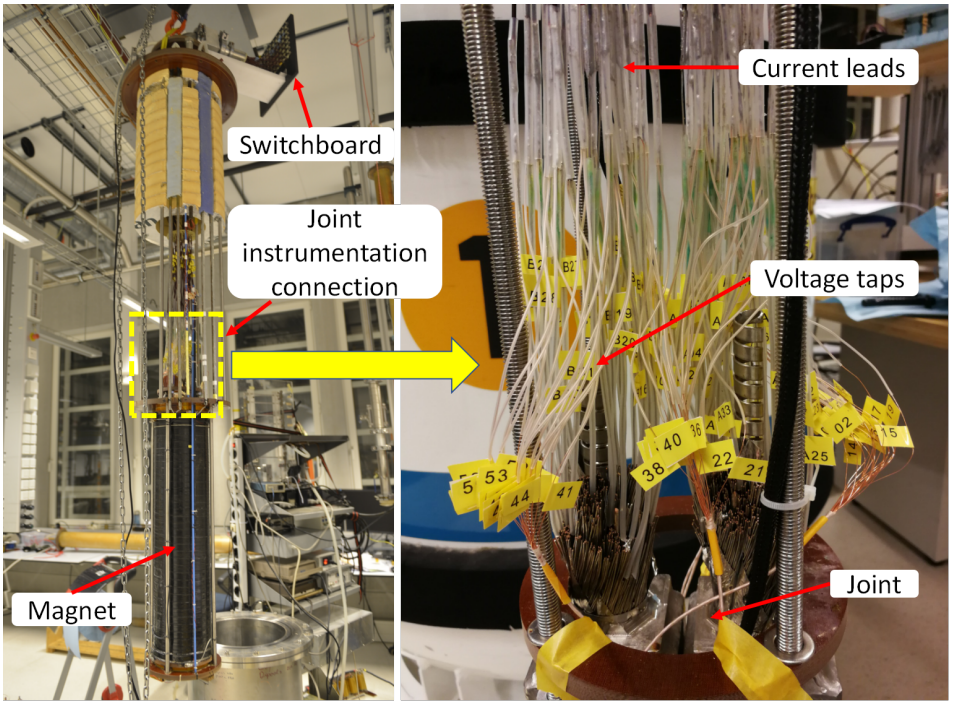


Figure 4.5: Test setup for the contact resistance measurement of the ITER PFJEU6 joint sample with the electrical connections of current leads and voltage taps. Left: cryostat insert with joint positioned in the magnet. Right: detail of the joint instrumentation.

and performing a four-point measurement [90], [91], as described in section 2.2.2. The final assembly of the setup and sample is shown in Figure 4.5, including the specific electrical connections of the current leads and voltage taps, which are connected through a switchboard outside the cryostat.

For the inter-strand or inter-petal resistance measurements in a specific CICC, the normalized contact resistance is defined as $R_c = \frac{V}{I} \cdot l$ [Ωm], in this case with a conductor length $l$ of $0.50$ m. A series of contact resistance measurements between strands in a triplet was performed in advance, as a function of the input current $I$ up to 50 A. The applied magnetic field slightly increases the average inter-strand resistance due to the magnetoresistance effect of the copper matrix [165] with a background magnetic field of 0.35 T applied.

Following the testing scheme in Table 4.1, the inter-strand and inter-petal resistances of strand combinations from the individual cables were measured and the results are shown in Figure 4.6.

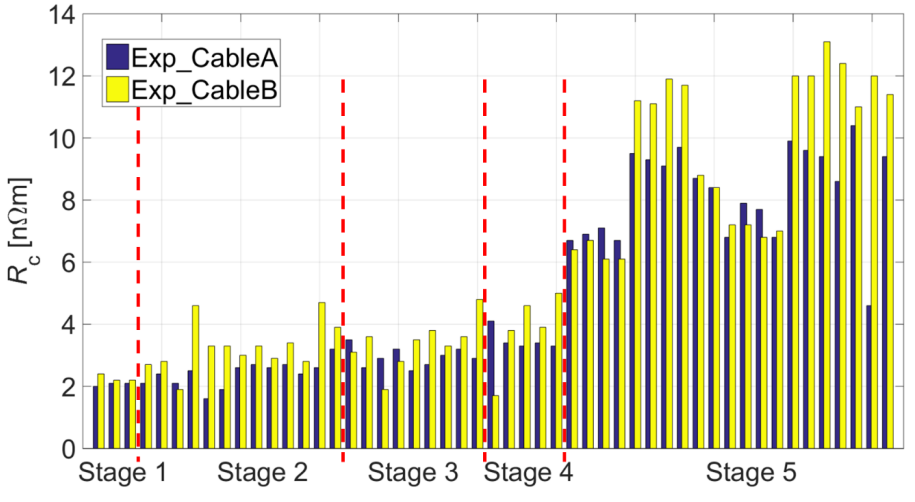


Figure 4.6: Collection of inter-strand and inter-petal contact resistances measured between strands from different stages, for two cables of the PFJEU6 joint.

The average resistances from the five individual stages are shown in Figure 4.7. The results show that the inter-strand resistance of cable A is slightly lower than of cable B. The inter-strand resistances from the first to the fourth stage exhibit only a slight increase of $1.5$ nΩm. The inter-petal (Stage 5) resistance is about 2.5 to 4.5 times larger caused by the stainless-steel foil in between the neighbouring petals [166]. The relatively high and low data correspond to the opposite and neighbouring petal combinations, respectively.

Besides the inter-strand resistance, the current distribution also depends on the strand-to-copper sole resistivity. The strand-to-copper sole resistivity is assessed by measuring the resistance between a selected strand and a current lead attached to the copper shim layer, as shown in Figure 4.4 and Table 4.1. The resistance between strands from three petals (R1, R16 and R26) and the current leads on the copper sole (SI1, SI2 and SI3) were

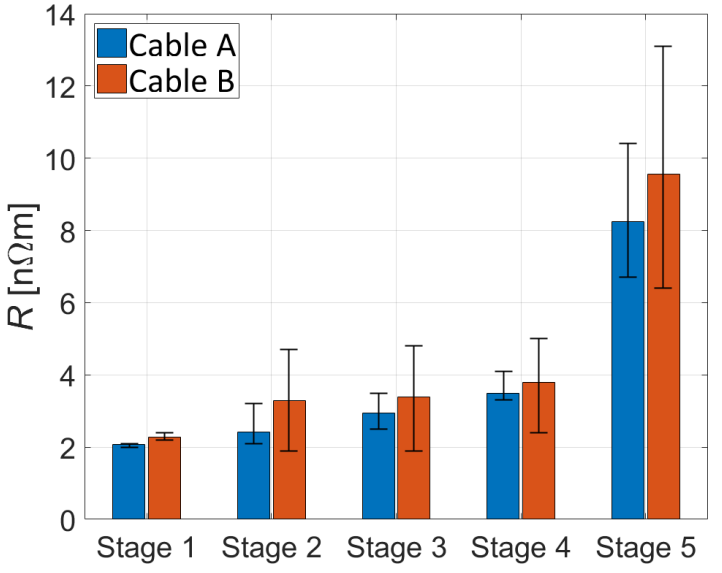


Figure 4.7: Average inter-strand contact resistance measured between strands from different stages for the two cables of the PFJEU6 joint.

measured, respectively, and the results are shown in Figure 4.8 with resistance unit of nΩ instead of the normalized resistance of nΩm, since the length is not defined in this case.

A significant spread in resistance is observed, not only for strands within the same cable, but also between the two cables. Depending on the strand path in the cabling pattern and the location of the attached current leads, as shown in Figure 4.4 and Figure 4.10, the distances between the strand-sole contact point and the respective current lead in the current loops can be quite different, this way contributing to the spread in resistances.

Another way to assess the strand to copper sole resistance is by measuring two strands each from different cables. The strand selection is shown in Table 4.1 and the measured resistances are shown in Figure 4.9.

The average strand to strand resistance is about $16 \pm 4$ nΩ. The lowest value of $7 \pm 1$ nΩ was measured on the AR1-BR26 strand pair. It is approaching the overall joint resistance of $4.8 \pm 0.2$ nΩ as measured in the SULTAN facility [164].

The inter-strand contact resistance is linked to the void fraction of the conductor, the contact resistance decreases as the void fraction decreases [167]. In the PFJEU6 joint, the cables are compacted from a void fraction of 34% to 19%. The contact resistance derived from the measurements after 1,000 load cycles in SULTAN, as shown in Figure 4.6 and Figure 4.7, amounts to 2 to 5 nΩm for the inter-strand resistance and 6 to 13 nΩm for the inter-petal resistance. The average resistance of the first and last stage is about 2 and 9 nΩm, respectively.

In order to investigate the influence of the void fraction on the contact resistances, two prototype full-size ITER Poloidal Field NbTi conductors (EM1 and EM2) [90], a full-size

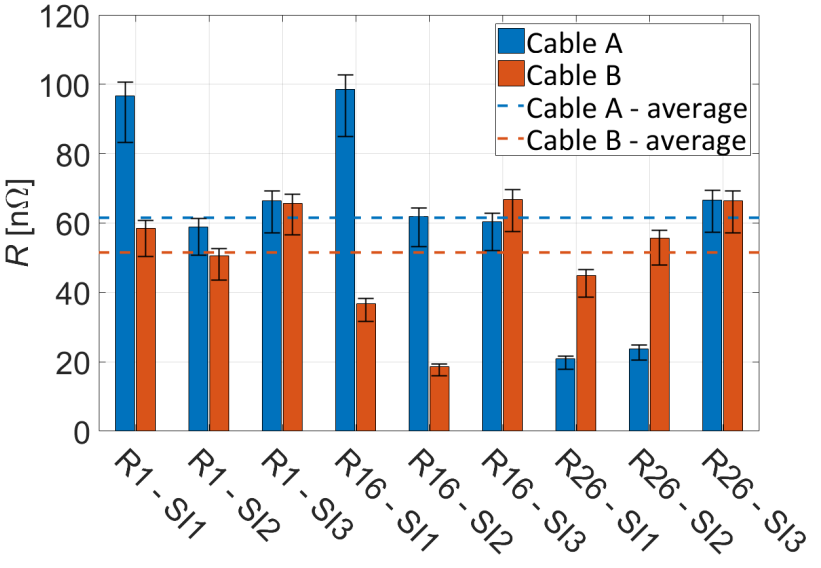


Figure 4.8: Contact resistance measured between strands in cables and current leads attached to the copper sole.

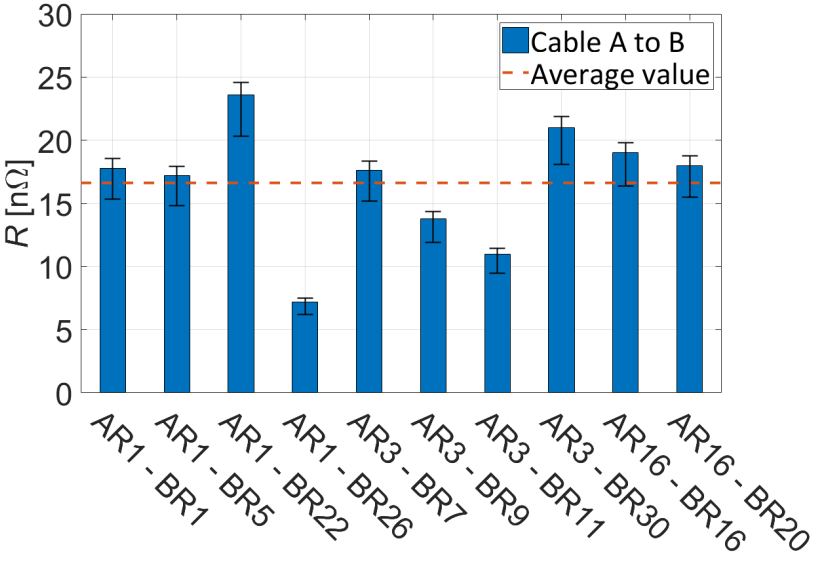


Figure 4.9: Contact resistance measured between strands between the two different cables.

Poloidal Field Conductor Insert sample (PFISw) [78], [168] and a sub-size NbTi conductor (sub-size CICC #4) [169] were selected to compare with the PFJEU6 joint conductor. The specifications of the four types of conductors and the contact resistances measured with different load conditions are summarized in Table 4.2.

Table 4.2: Specification of the NbTi conductors and comparison of the measured inter-strand contact resistance for various void fractions, and different load conditions.

| Sample | PFJEU6 | EM1 | | EM2 | | PFISw | | Sub-size CICC #4 | |
|---|---|---|---|---|---|---|---|---|---|
| Strand coating | Ni | Ni | | Ni | | Ni | | Ni | |
| Diameter of strand [mm] | 0.73 | 0.81 | | 0.81 | | 0.73 | | 0.70 | |
| Cu:nonCu | 2.3 | 1.9 | | 1.9 | | 1.41 | | 1.05 | |
| Void fraction [%] | 19 | 36 | | 36 | | 35.5 | | 35 | |
| Cable pattern | 3/4/4/4/6 | 3/4/4/4/6 | | 3/4/4/4/6 | | 3/4/4/5/6 | | (6+1)/3/4/4 | |
| Nr. of SC strands | 1152 | 1152 | | 1152 | | 1440 | | 288 | |
| Sub-cable wrap | Yes | Yes | | Yes | | Yes | | Yes | |
| Load [kN/m] | 165 | 220 | | 220 | | 315 | | 200 | |
| Load cycles | 1,000 | 1,000 | 40,000 | 1,000 | 40,000 | 1,000 | 40,000 | 1,000 | 40,000 |
| Rc(first stage) [nΩm] | 2 | 680 | 72 | 600 | 58 | 1,200 | 45 | 280 | 23 |
| Rc(last stage) [nΩm] | 9 | 10,000 | 2,960 | 8,500 | 2,160 | 2,000 | 552 | 1,240 | 280 |

The joint sample PFJEU6 has experienced 1,000 load cycles of 165 kN/m when tested in the SULTAN facility. The effect of cyclic loading at 165 kN/m and 220 kN/m on the resistance is expected almost the same, especially after a large number of cycles [90]. A comparison is made with the resistance in the regular conductors after 1,000 cycling loads of 220 kN/m. The inter-strand (first stage) resistance is 680 nΩm and 600 nΩm, while the inter-petal (last stage) resistance is much larger and at the level of 10 μΩm and 8.5 μΩm for EM1 and EM2, respectively. When comparing the resistance behaviour of the joint conductor to the normal conductors EM1 and EM2 after 40,000 cycles, the average inter-strand and inter-petal resistance are 65 nΩm and 2,560 nΩm, respectively, being some 33 and 284 times larger than in the compressed PFJEU6 conductor. The ratios of inter-petal to inter-strand resistance are 40 and 4.5 for the regular and compressed conductors, respectively.

For the PFISw conductor with more strands and a higher experienced load of 315 kN/m, the inter-strand and inter-petal resistances after 1,000 cycles are 1200 nΩm and 2000 nΩm, respectively. After 40,000 cycles, the inter-strand resistance drops faster than the inter-petal resistance and becomes 45 nΩm and 552 nΩm, respectively. The latter is smaller than found for EM1 and EM2, probably due to the tighter strand configuration. A comparison with the sub-size conductor #4 was made as well. The magnitude of the first stage resistance is in accordance with the EM1 and EM2 conductors. The last stage resistance is smaller because it has only four stages, however, the inter-petal to inter-strand ratio has still a relatively high value of 12, like for the PFISw conductor.

## • AC loss measurement

The AC loss measurement is performed after the contact resistance measurement. The conductor sections outside the joint-box region, as shown in Figure 4.1, are removed by spark erosion and the nominal length of 580 mm remains.

As introduced in section 2.2.2, the AC loss measurement is carried out with the magnetic method using pick-up coils and the boil-off based calorimetric method simultaneously.

For the magnetization method, a pick-up coil is wound around the joint sample and aligned to the middle plane of the compressed joint-box section. Three compensation coils are located at the top, middle and bottom of the sample, respectively. Three different locations of the compensation coils are chosen in order to investigate the influence of the position on the compensation. The relative locations of the four coils with respect to the joint is shown in Figure 4.10. After subtracting the signal of the compensation coil from the pick-up coil the magnetization induced in the sample is calibrated against the calorimetric data. For the calorimetric method, the evaporated helium gas flow is measured with a mass flowmeter by which the mass flow at room temperature was calibrated with a known heater power in the calorimeter at 4.2 K.

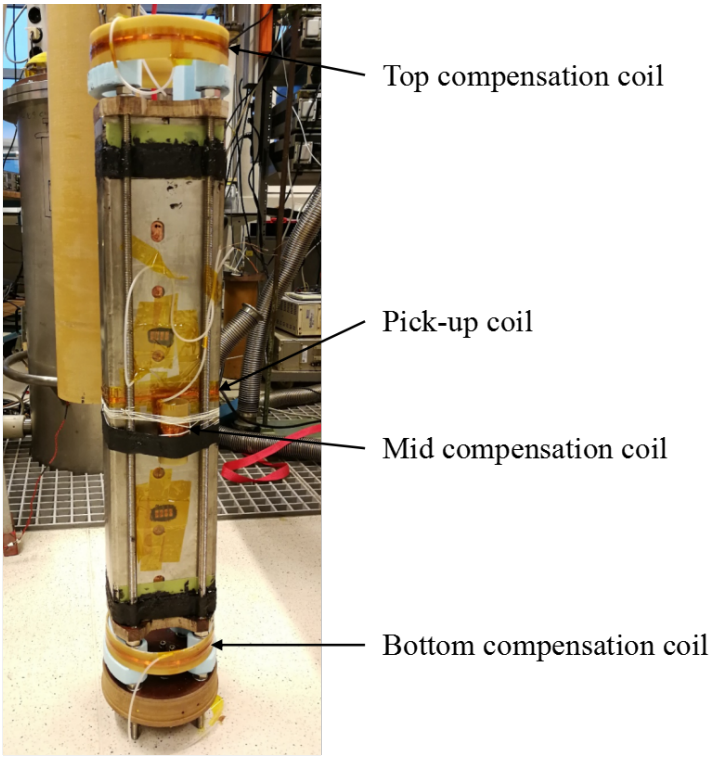


Figure 4.10: ITER PFJEU6 joint sample for AC loss measurement. One pick-up coil and three compensation coils are present to measure the magnetization of the joint.

The prepared joint sample is first placed inside the calorimeter chamber and then the calorimeter is inserted into the solenoid providing the external magnetic field with amplitudes $B_{ac}$ of 0.2 T and 0.4 T and an offset field $B_{dc}$ of 0 T or 1 T, in a direction parallel to the joint axis. The magnetic field frequency ranges are 1 to 160 and 1 to 85 mHz for the 0.2 T and 0.4 T magnetic field amplitudes, respectively. Although the overall length of

the sample is 580 mm, the effective contact length of the compressed cable with the copper sole is only 500 mm. The uniformity of the magnetic field is 2% across 480 mm. The position of the joint in the magnetic field profile of the AC magnet is shown in Figure 4.11.

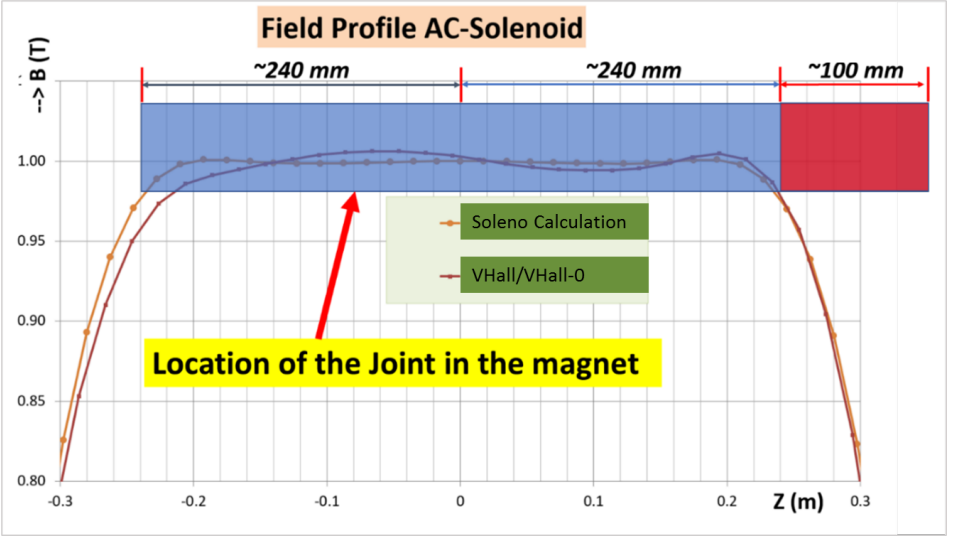


Figure 4.11: Profile of the magnetic field of the solenoid and the position of the PFJEU6 joint during the measurement.

A series of tests were carried out first to evaluate the effect of the location of the individual compensation coil on the resulting magnetization signal and to select the compensation coil yielding most accurate results. The bottom compensation coil is quite close to the joint and some magnetic flux induced in the joint is being picked up by this coil. It was decided to not use the bottom coil. The AC loss per cycle measured by the magnetization method using the middle and top compensation coils and the results obtained from the calorimetric method are shown in Figure 4.12.

Across the entire frequency range, good agreement is observed between the data measured by the calorimetric and magnetization methods using the signal from the middle compensation coil. Therefore, the middle compensation coil is chosen for processing the AC loss measurements with the magnetization method.

The AC loss per cycle of the joint exposed to the four applied magnetic fields, $B_{dc} = 0$, 1 T, $B_{ac} = 0.2$, 0.4 T, are measured by the calorimetric and magnetization method simultaneously and the results are shown in Figure 4.13 with the curves representing the fits of the magnetization data. The comparison shows a very good agreement between magnetization and calorimetric data. For the calorimetric data measured at $B_{apl} = \pm 0.2$ T, a slight discrepancy is observed, most likely caused by fluctuations in the helium pressure during the measurement.

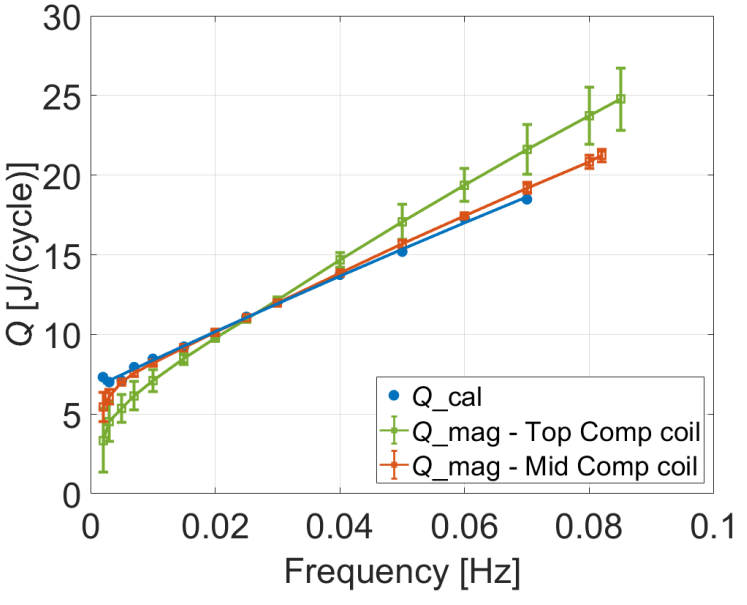


Figure 4.12: AC loss per cycle of the joint measured by the calorimetric method and the magnetization method. The magnetization data are processed with the signals from the Top and Middle compensation coils, respectively. The alternating applied magnetic field $B_{dc}$ = 0 T, $B_{ac}$ = 0.4 T.

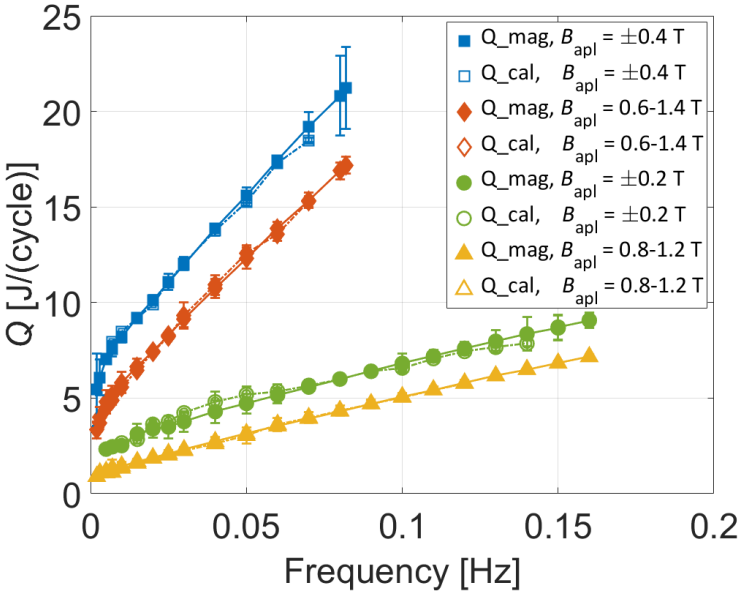


Figure 4.13: Comparison of the AC loss per cycle of the PFJEU6 joint measured by the magnetization and calorimetric methods, using different applied magnetic field conditions.

## • Hysteresis loss determination

The hysteresis loss density of the ITER NbTi strand is derived as shown in Table 3.10. For the PF5 NbTi conductor, depending on the cabling pattern, the local angle between the strand axis and the applied magnetic field is changing periodically with the twist pitches of the different cable stages. The method of local angle calculation is demonstrated by an intersection of one single strand, as seen in Figure 4.14.

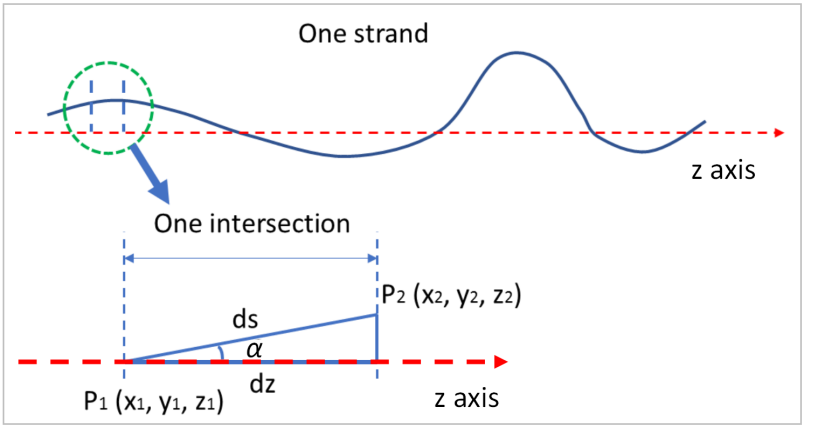


Figure 4.14: Schematic representation of the angle variation between one strand and the z-axis parallel to the length direction of the cable.

The corresponding angle distribution (absolute values) along a strand length is calculated with the JackPot-AC/DC code and is shown in Figure 4.15 [68], [72], [105].

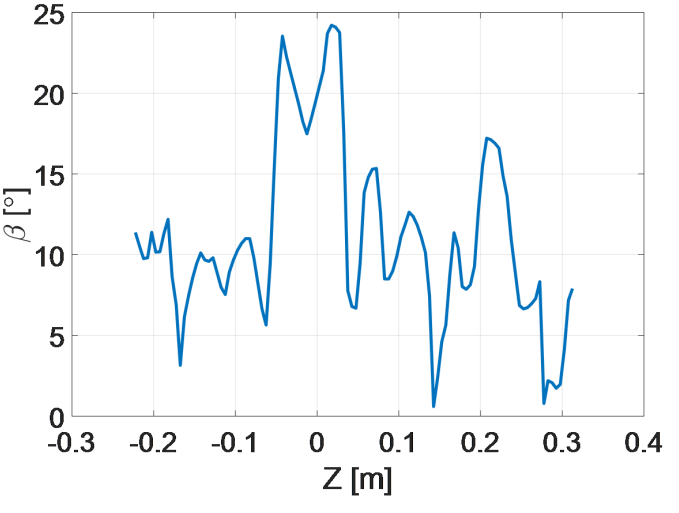


Figure 4.15: Absolute angle variation between a single strand and the z-axis of cable A in the PF5 joint.

The calculated physical average angle of the compacted joint section is $\alpha = 11.4°$ [158], [159]. However, considering the weighted effect of the angle on the hysteresis loss, as illustrated in Table 3.9, an effective average angle $\beta = 15.5°$ is obtained and applied to calculate the hysteresis loss.

The hysteresis loss of the PFJEU6 joint is calculated as

$$Q_{hys} = \sum_{i=1}^{N} q_{hys}(i) \cdot V_{NbTi}\,[\mathrm{J/cycle}], \tag{4.1}$$

with $V_{NbTi}$ the volume of the NbTi strand intersections, $N$ the number of all strand intersections in the joint.

For the magnetic field angle of $15.5°$, the calculated hysteresis losses $Q_{\mathrm{vsm}}$ of the joint sample subjected to different magnetic field conditions are calculated and shown in Figure 4.16 and Table 4.3.

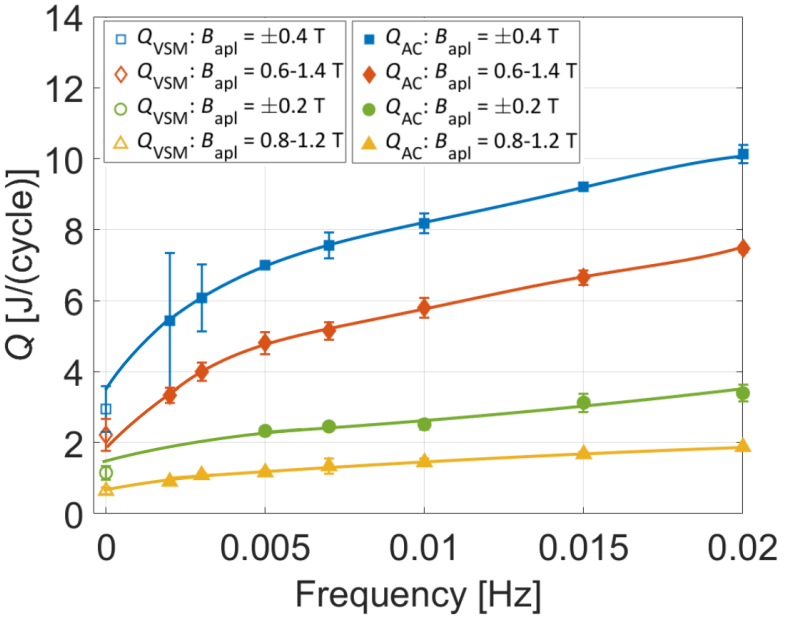


Figure 4.16: Hysteresis loss per cycle estimated from the intercepts at 0 Hz of measured AC losses in the low frequency range of Figure 4.13, in comparison with the calculated hysteresis loss based on VSM measurements on strands, for different field conditions.

The hysteresis loss of the full joint can also be obtained from the extrapolation of the curves fit to the measured AC loss data at low frequency, in Figure 4.13. For the applied AC magnetic fields, the polynomial fits are derived and shown in Figure 4.16, the corresponding intercepts and fitting orders are listed in Table 4.3. The deviation of the values at low magnetic fields is affected by the choice of fitting function, the orders of the polynomial fitting curves vary from 2 to 5.

Table 4.3: Hysteresis loss per cycle of the joint determined by the intercepts at 0 Hz in AC loss measurements compared to calculated hysteresis loss based on VSM measurements on strands, for different magnetic field conditions.

| $B_{dc}$ [T] | $B_{ac}$ [T] | $Q_{\text{VSM}}$ [J/cycle] | $Q_{\text{AC}}$ [J/cycle] | Polynomial fit order |
|---|---|---|---|---|
| 0 | 0.2 | $1.2 \pm 0.2$ | $1.8 \pm 0.4$ | 2 |
| 0 | 0.4 | $3.2 \pm 0.7$ | $3.6 \pm 0.8$ | 4 |
| 1 | 0.2 | $0.7 \pm 0.1$ | $0.8 \pm 0.3$ | 2 |
| 1 | 0.4 | $2.4 \pm 0.5$ | $2.2 \pm 0.6$ | 5 |

The hysteresis losses obtained through the two methods exhibit a relatively favourable agreement under applied field conditions with $B_{dc} = 1$ T. However, when comparing the results derived from AC loss measurements without a DC background, they appear to be somewhat higher than those obtained from the VSM measurements, though the values are still within their error margin. It is noteworthy that VSM results may be influenced by factors such as the precision of angle positioning on the VSM sample holder [170] and the dissimilarity in demagnetization between a single-strand sample in the VSM and densely packed strands in the joint sample.

### 4.2.2 Simulation of the joint in parallel magnetic field

A numerical analysis of the contact resistance and AC loss experimental data is performed by using the JackPot-AC/DC code [72]. The twin-box lap-type joint is treated in the code as three electrically coupled components. The two cables are implemented following the trajectories of all the strands, and the copper sole in between is implemented as a 3-dimensional electrical grid following the PEEC technique as described in section 2.3.

The configuration in the model of the tested PFJEU6 joint is shown in Figure 4.17 and the specifications are summarized in Table 4.4. The magnetic field configurations for both simulations are set alike the corresponding measurements and the solenoidal field is applied in z-direction.

In order to improve the electrical conductivity between the strands and the copper sole, a foil of eutectic AgSn solder is put in between [16]. During the next melting process, the solder penetrates into the peripheral strands and fills up the voids along the copper sole arc region [171]. Therefore, the solder affects not only the contact interface between cable and copper sole, but also the contact resistances between strands that are soldered. It was already found that the response of the contact resistivities under electromagnetic load is highly dependent on the presence of solder [91], [167]. In order to simplify the model, the oval shaped conductor in the joint-box, as shown in Figure 4.2, is treated as a circular shaped conductor with diameter $\Phi$. The schematic of the termination and the dimensional parameters related to the solder layer in between cable and copper sole is shown in Figure 4.18.

The solder is treated as a uniformly distributed layer, ignoring the accumulating effect under gravity [171]. The thickness $\Delta r_s$ is defined indirectly with respect to the diameter of the strand $d$, $\Delta r_s = k \cdot d$, where $k$ is a multiplying factor [171]. Similarly, the width of

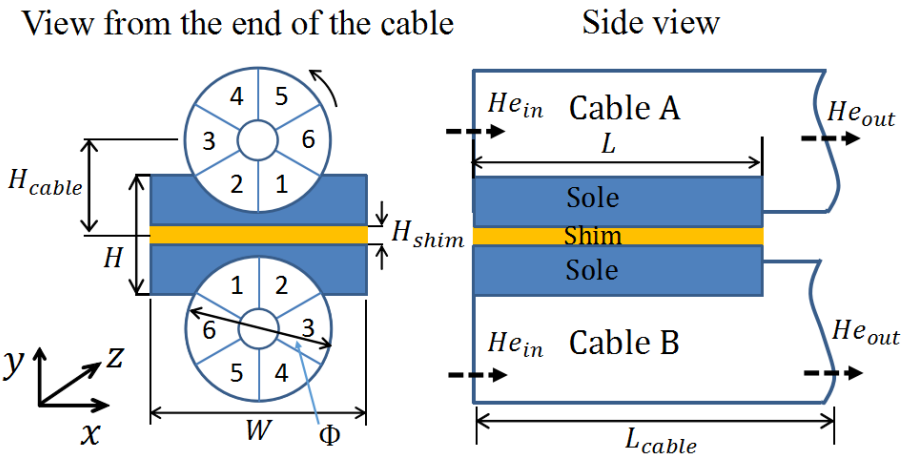


Figure 4.17: Schematic of ITER Poloidal Field joint PFJEU6 in the JackPot-AC/DC model.

Table 4.4: Geometric and electrical parameters of the ITER Poloidal Field joint (PFJEU6) in the simulation model.

| Parameter | Value |
|---|---|
| Sole length $L$ [mm] | 500 |
| Sole width $W$ [mm] | 64 |
| Sole height $H$ [mm] | 35 |
| Shim thickness $H_{shim}$ [mm] | 7 |
| Cable length $L_{cable}$ [mm] | 520 |
| Cable offset to midplane $H_{cable}$ [mm] | 27.9 |
| Cable diameter Φ [mm] | 35.3 (v.f. 34%) or 31.6 (v.f. 19%) |
| Sole resistivity $\rho_{sole}$ @4.5 K [nΩm] | 3.34 |
| Shim resistivity $\rho_{shim}$ @4.5 K [nΩm] | 3.34 |
| Mask resistivity $\rho_{mask}$ @4.5 K [μΩm$^2$] | 50 |

the solder layer $W$ is defined with respect to the cable diameter Φ.

For the simulation of regular conductors, the two main free parameters are the interstrand $\rho_{ss}$ resistivity and the interpetal $\rho_{ip}$ resistivity. They are normally derived by fitting the measured AC losses [72], [101]. For lap-type joints, the presence of the copper sole and solder introduces a few extra parameters that affect the joint performance, like the strand-to-copper sole resistivity $\rho_{sj}$, the thickness $\Delta r_s$ and width $W$ of the solder layer [68], and makes the fitting procedure more complicated [104].

As regards the full-size PF joint (PFJEU6), simulations of the interstrand and interpetal contact resistances are performed by selecting pairs of strands from the 1152 superconductor strands, somewhat analogous to the specific scheme of strand selections used in the measurements, as seen in Table 4.1 [172]. A current of 50 A is supplied to the selected pair of strands at each round of simulation, in the meantime the other strands disconnected. The resistance is derived by dividing the calculated voltage between the selected pair of

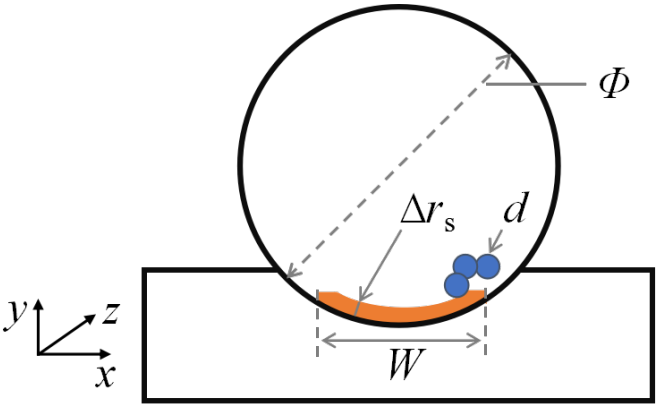


Figure 4.18: Schematic illustration of a termination highlighting key dimensional parameters associated with the solder layer positioned between the strand and conductor, wherein $d$ represents the diameter of the strand and $\Phi$ denotes the diameter of the conductor.

strands by the given current.

Three sets of resistivity parameters as listed in Table 4.5, are used to evaluate the transition from contact resistance to relevant resistivity, and the results are shown in Figure 4.19.

Table 4.5: Experimental parameters detailing three combinations of resistivity and solder properties employed in the parameterization methods.

| Simulation set | $\rho_{ss}$ [$10^{-12}$ Ωm$^2$] | $\rho_{ip}$ [$10^{-12}$ Ωm$^2$] | $\rho_{sj}$ [$10^{-12}$ Ωm$^2$] | $\Delta r_s$ [mm] | $W$ [mm] |
|---|---|---|---|---|---|
| #1 | 0.5 | 400 | 2.4 | $1.5\,d$ | $0.8\,\Phi$ |
| #2 | 0.5 | 5 | 2.4 | $1.5\,d$ | $0.8\,\Phi$ |
| #3 | 0.5 | 5 | 40 | $1.5\,d$ | $0.8\,\Phi$ |

The yellow bars are simulated data with the different resistivity parameters, and the blue bars are the average measured data of the contact resistances of two conductors. It shows that the interstrand resistance, corresponding to stages 1 to 4, is mainly affected by the parameter $\rho_{ss}$, and similar behaviors are observed for three fits. However, for simulations #1 and #3 with quite different resistivity parameters, the comparable distributions of overall contact resistances implies that either the $\rho_{ip}$ or $\rho_{sj}$ can significantly affect the interpetal resistance as indicated in stage 5. The comparison also reveals the uncertainty in the resistivity parameterization based on the method of just fitting the contact resistances.

The uncertainty in the various parameters and in particular the impact of the strand-to-copper sole resistivity implies that, besides the contact resistances inside the cables, the influence of the copper sole has to be taken into account in the resistivity parameterization of the joint. Another method is to consider the resistances between strands that belong to different cables. The so-called cable-to-cable resistances simulated with the three sets of parameters in Table 4.5, and the measured data for comparison, are shown in Figure 4.20.

It shows that the cable-to-cable resistances increase with either $\rho_{ip}$ or $\rho_{sj}$, as illus-

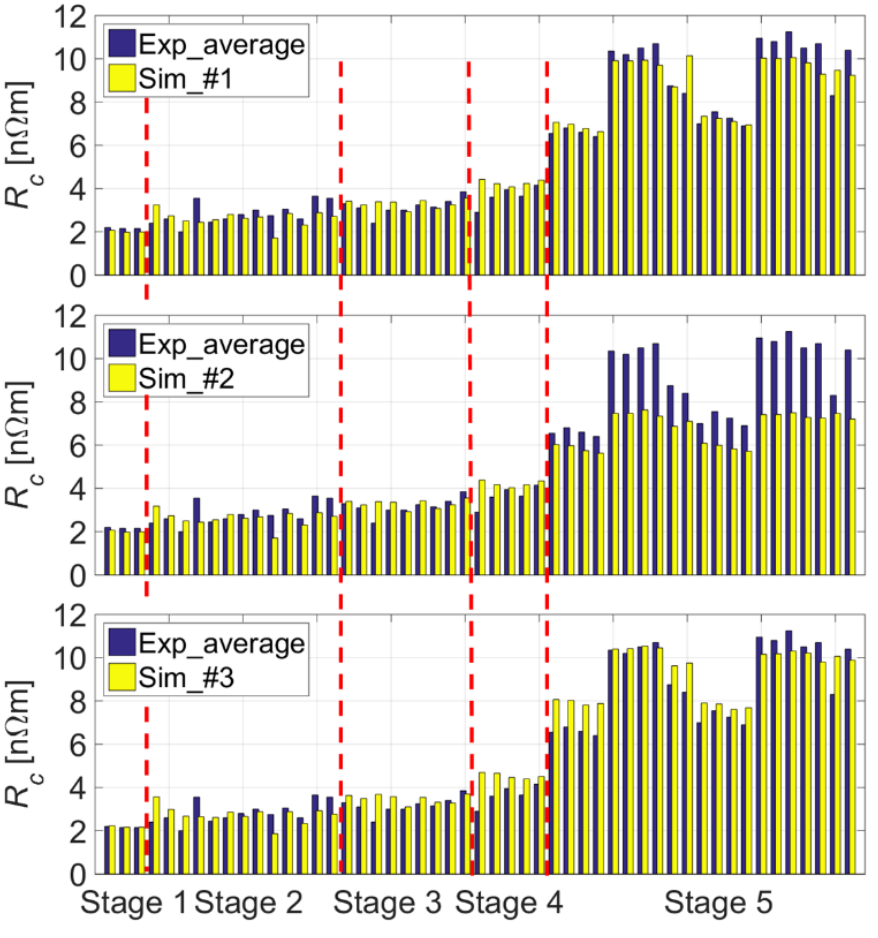


Figure 4.19: Comparative analysis depicting the variations in interstrand and interpetal contact resistances of the PF joint, simulated under diverse resistivity parameter sets, as given in Table 4.5.

trated in simulation sets #1 and #3, respectively. The spread in resistances between different strand combinations can be related to the cabling pattern and the specific contact points between cable and sole. Yet another method for the parameterization is to use the calculated AC losses of joint. A comparison of the AC losses of the joint for the three sets of parameters is shown in Figure 4.21. It shows that the AC loss decreases as either $\rho_{ip}$ or $\rho_{sj}$ increases, especially for higher frequencies.

Since the spread in cable-to-cable resistances can be significantly affected by specific contact points, the error in the derived parameters is usually larger than in the data derived from AC loss simulations. To achieve a more accurate result, an improved method for resistivity parameterization is proposed by combining the confinements of the interstrand contact resistance and AC losses, while the confinement from the cable-to-cable resistance is only used as reference.

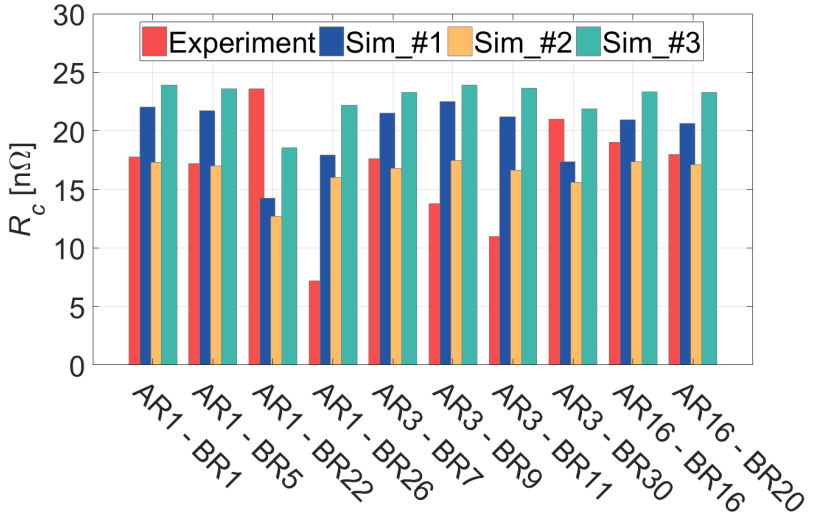


Figure 4.20: Comparative analysis illustrating variations in cable-to-cable resistances among selected strands, simulated for three distinct resistivity and solder parameter sets.

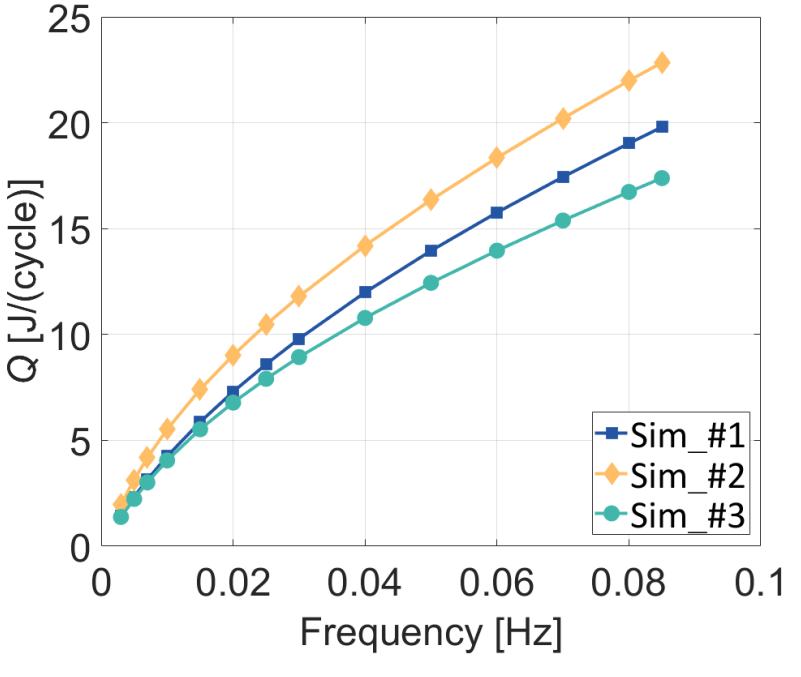


Figure 4.21: Comparative evaluation of calculated AC losses of the PF joint, simulated with the three sets of resistivity and solder parameters.

## • Sensitivity analysis of parameters

The confinements in terms of interstrand contact resistances and AC losses mainly reflect the overall behavior of the joint as affected by the five parameters together, instead of the impact of the individual parameters. In order to improve the parameterization itself and the simulation of the joint behavior, a series of sensitivity analyses was performed by adjusting one parameter each time, as summarized in Table 4.6.

Table 4.6: Summary of parameters employed in the sensitivity analysis, with each case featuring a singular adjustment of a specific parameter, elucidating the nuanced effects on the contact resistance and AC loss.

| Set | $\rho_{ss}$ [$10^{-12}$ Ωm$^2$] | $\rho_{ip}$ [$10^{-12}$ Ωm$^2$] | $\rho_{sj}$ [$10^{-12}$ Ωm$^2$] | $\Delta r_s$ [mm] | $W$ [mm] |
|---|---|---|---|---|---|
| A | 0.2, 0.4, 0.6, 1.2 | 4.4 | 40 | $1.5\,d$ | $0.8\,\Phi$ |
| B | 0.4 | 0.4, 1.6, 4.4, 6.4 | 40 | $1.5\,d$ | $0.8\,\Phi$ |
| C | 0.4 | 4.4 | 20, 40, 80, 160 | $1.5\,d$ | $0.8\,\Phi$ |
| D | 0.4 | 4.4 | 40 | $0\,d$, $0.2\,d$, $0.7\,d$, $1.5\,d$ | $0.8\,\Phi$ |
| E | 0.4 | 4.4 | 40 | $1.5\,d$ | $0.2\,\Phi$, $0.5\,\Phi$, $0.8\,\Phi$, $1.0\,\Phi$ |

The corresponding evolutions of the contact resistances (A.1 to E.1) and AC losses (A.2 to E.2) are evaluated and shown in Figure 4.22 and 4.23. To emphasize the overarching evolutionary trend and mitigate the impact of dispersion, the contact resistances are presented in the form of a cumulative frequency distribution, facilitating a focused analysis on the overall evolution. The AC losses only comprises coupling and eddy current losses, without hysteresis loss [172].

The simulations show that, in general, a larger $\rho_{ss}$ let increase both the interstrand resistance and interpetal resistance, but cause a decrease of the AC loss. The $\rho_{ip}$ mainly impacts on the interpetal current and when it increases, the AC losses decrease evenly in the full range of frequency. The impact of the $\rho_{sj}$ on the contact resistance is relatively small, and mainly affects the interpetal instead of the interstrand resistance, However, significant influence on the AC loss is observed. When the $\rho_{sj}$ increases, the AC loss drops fast with increasing frequency. As regards the solder related parameters, when the thickness of solder $\Delta r_s$ increases from zero to 1.5 times the strand diameter, the interpetal resistance decreases slightly, while the AC loss increases, especially for the high frequency. The effect of the width of the solder $W$ is similar to that of its thickness; a wider solder layer decreases the interpetal resistance and let the AC loss increase.

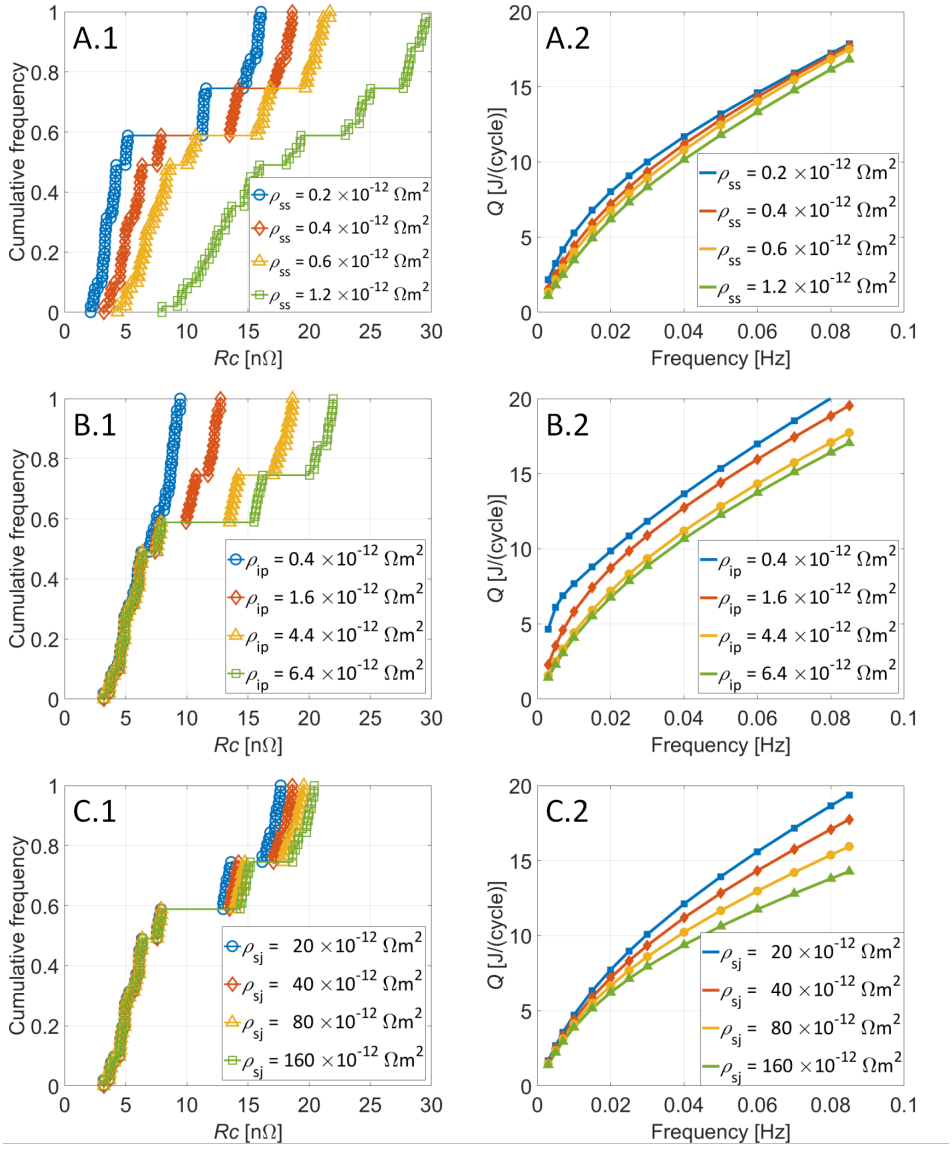


Figure 4.22: Effect of systematic variation of resistivity parameters, in terms of the contact resistance (A.1 to C.1) and coupling and eddy current losses (A.2 to C.2), respectively, in accordance with Table 4.6.

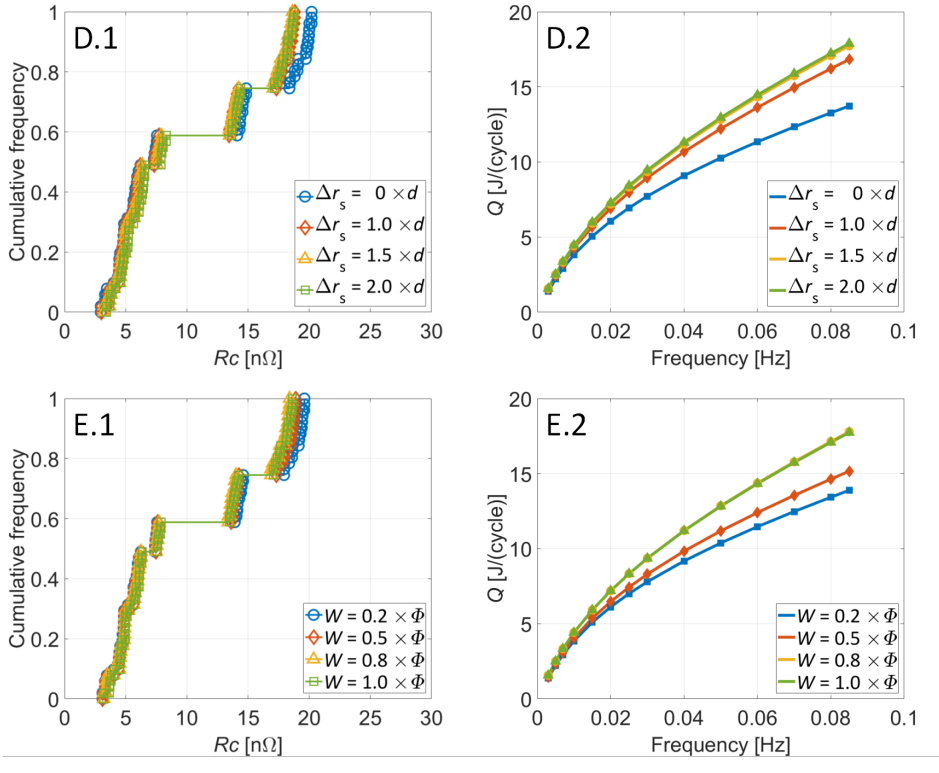


Figure 4.23: Effect of systematic variation of solder parameters, in terms of the contact resistance (D.1 to E.1) and coupling and eddy current losses (D.2 to E.2), respectively, in accordance with Table 4.6.

## • Parameterization in parallel magnetic field

Building upon insights garnered from the sensitivity analysis, a comprehensive set of resistivity and solder-related parameters, denoted as set 1, has been meticulously derived and detailed in Table 4.7. The ensuing fitting procedure involves a rigorous comparison of interstrand and interpetal contact resistance distributions derived from both simulated and measured datasets. The results of this analysis presented in Figure 4.24, reveals a notably commendable fitting behavior, attesting to the robust alignment between simulated and experimental data.

Table 4.7: Summary of three sets of contact resistivities and solder parameters used for the simulations with two cable compaction configurations, 34% and 19% void fraction in the PFJEU6 joint. $d$ and $\Phi$ are the diameter of the strand and the cable, respectively.

| # | void fraction [%] | | $\rho_{ss}$ [$10^{-12}$ Ωm$^2$] | $\rho_{ip}$ [$10^{-12}$ Ωm$^2$] | $\rho_{sj}$ [$10^{-12}$ Ωm$^2$] | $\Delta r_s$ [mm] | $W$ [mm] |
|---|---|---|---|---|---|---|---|
| set 1 | 19 | cable A | 0.70 | $16 \times 0.70$ | 12 | $1.5 \times d$ | $0.8 \times$ |
| | | cable B | 0.80 | $16 \times 0.80$ | 10 | $1.5 \times d$ | $0.5 \times$ |
| set 2 | 34 | cable A | 0.40 | $16 \times 0.40$ | 12 | $1.5 \times d$ | $0.8 \times$ |
| | | cable B | 0.55 | $16 \times 0.55$ | 12 | $1.5 \times d$ | $0.5 \times$ |
| set 3 | 19 | cable A | 0.40 | $16 \times 0.40$ | 12 | $1.5 \times d$ | $0.8 \times$ |
| | | cable B | 0.55 | $16 \times 0.55$ | 12 | $1.5 \times d$ | $0.5 \times$ |

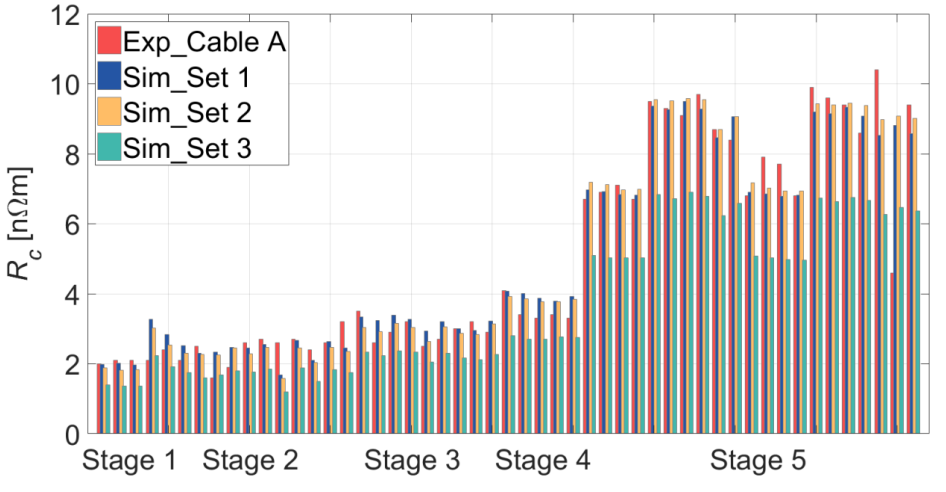


Figure 4.24: Influence of cable compaction on the interstrand and interpetal contact resistances of the PF joint. Comparison of experimental data and simulations with three sets of different resistivity parameters and void fractions.

The AC loss measurements of the PFJEU6 joint were conducted at the University of Twente, wherein four distinct magnetic field levels were applied in parallel orientation relative to the joint axis. The results are shown in Figure 4.13. Following the deduction of corresponding hysteresis losses, the resultant losses are quantified and denoted as $Q_{exp}$. Utilizing the set 1 resistivity parameters, the coupling and eddy current losses of the joint $Q_{sim}$ are calculated, which are subsequently juxtaposed against the measured data $Q_{exp}$. The outcomes of this comparative analysis are succinctly presented in Figure 4.25, demonstrating a general and commendable agreement.

In the ultimate stage of our investigation, subsequent to the meticulous satisfaction of constraints pertaining to contact resistances and AC losses, the parameters encapsulated in set 1 are judiciously deemed optimal values for the PFJEU6 joint. These selected parameters are subsequently employed for further numerical analyses, thus affirming their

efficacy in encapsulating and characterizing the nuanced behavior of the joint under varied operational conditions.

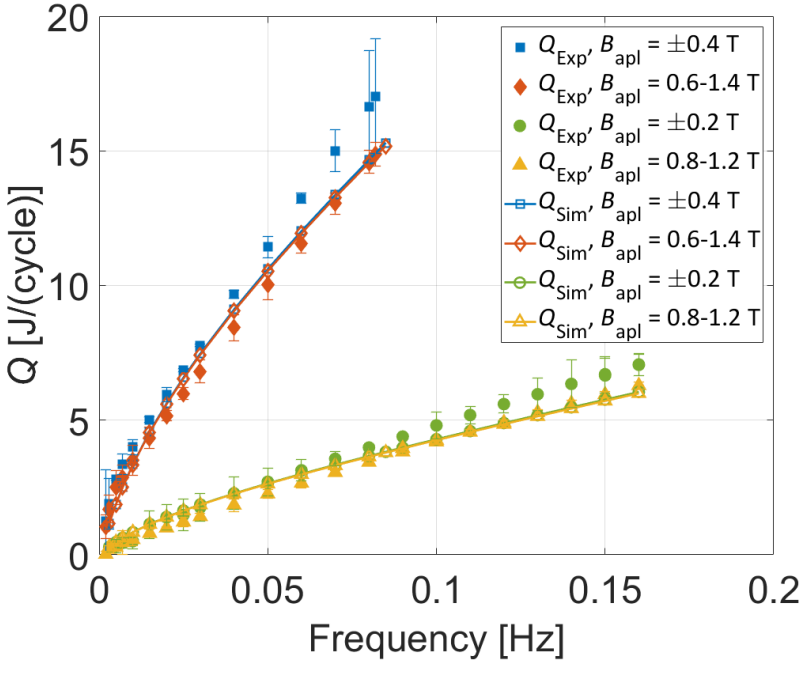


Figure 4.25: Comparative analysis of the sum of coupling and eddy current losses per cycle in PF joint PFJEU6 exposed to a parallel applied AC magnetic field, contrasting experimental data with simulations employing parameter set 1, and accounting for variations in magnetic field conditions.

### • Effect of cable compaction (void fraction)

For the lap-type twin-box joint, in order to improve the electrical conductivity, the conductor in the joint box section is compacted tightly. The conductor diameter is decreased from 35.3 mm to 31.6 mm, and the void fraction is decreased from 34% to 19% correspondingly. The cross-sectional view of the conductors at different positions is shown in Figure 4.1. Since the conversion of the measured contact resistances to the resistivities is dependent on the contact areas between strands, the compaction of the cable can affect the resistivity parameterization significantly, especially for CICCs with complicated twisting pattern.

This effect on the contact resistance evolutions are illustrated in Figure 4.24, using the set 2 and 3 parameters with the same resistivity and solder related values but different void fractions, as shown in Table 4.7. The results reveal that, a higher void fraction leads to smaller contact areas between strands leading to underestimated resistivities. The interstrand and interpetal resistivities are decreased by about 60%.

The set 1 parameters in Table 4.7 were derived under the assumption that the conductor is inside the joint box section, where they are actually affected by the copper sole. As regards the regular conductor outside the joint box section, the PF5 conductor sample PFEU3 was measured at the SULTAN facility for its AC loss [101], [173]. Without the influence of the copper sole, the two main resistivity parameters $\rho_{ss}$ and $\rho_{ip}$ are derived by fitting the measured data to the results of the simulation model, as shown in Figure 4.26.

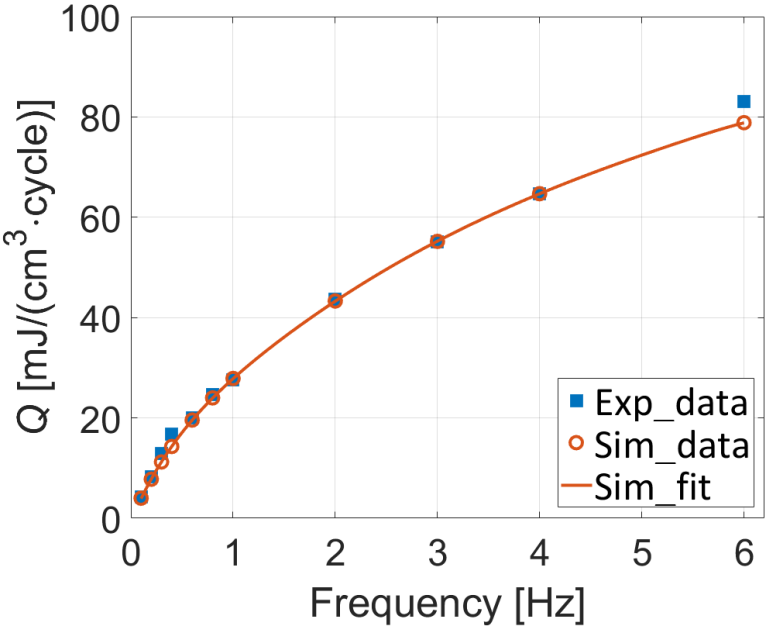


Figure 4.26: Coupling loss density per cycle versus frequency for a PF5 conductor outside the joint box. Data measured in the SULTAN facility in comparison with a polynomial fitting curve through the simulated data points.

The extracted resistivity parameters are shown in Table 4.8. The average values of the two compressed conductors inside the joint box are included for comparison. It shows that, for the regular conductor without the transfer effect of the copper sole, the interstrand resistivity is $27 \pm 3$ times larger, increases from $(0.75 \pm 0.05) \times 10^{-12}$ $\Omega$m$^2$ to $(20 \pm 1) \times 10^{-12}$ $\Omega$m$^2$. The interpetal resistivity is increased correspondingly, but the relevant ratio between interpetal and interstrand is actually decreased from 16 to 4.

Table 4.8: Contact resistivities of the not-compacted and compacted conductor sections of a PF5 joint.

| Conductor | $\rho_{ss}$ [$10^{-12}$ $\Omega$m$^2$] | $\rho_{ip}$ [$10^{-12}$ $\Omega$m$^2$] |
|---|---|---|
| Not-compacted conductor (outside jointbox) | $20 \pm 1$ | $4 \times 20 \pm 10$ |
| Compacted conductor (inside jointbox) | $0.75 \pm 0.05$ | $16 \times 0.75 \pm 1$ |

The effect of the compaction, in terms of AC loss, is assessed by considering two types of conductors with the same length of 0.50 m. The conductor samples are exposed to a transverse harmonic magnetic field with an amplitude $B_{ac} = 0.4$ T and in zero background magnetic field. The coupling loss density per cycle versus frequency is shown in Figure 4.27.

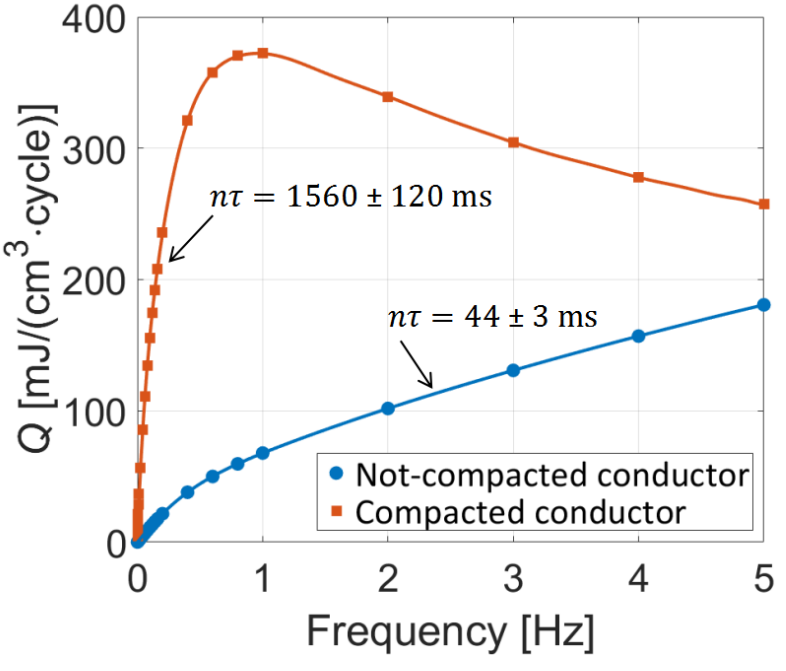


Figure 4.27: Calculated coupling loss density per cycle versus frequency for both not-compacted and compacted PF5 conductors under the influence of a transverse applied AC magnetic field. The coupling loss time constant $n\tau$ is derived from the initial slope at low frequency, offering insight in the dynamic response of the conductors to varying harmonic magnetic field conditions.

High coupling losses are generated in the compacted conductor with much lower contact resistivities, and early saturation is observed at a frequency around 1 Hz. The coupling loss can be characterized by a time constant $n\tau$, defined as [105], [174]:

$$n\tau = \alpha \frac{\mu_0}{2\pi^2 B_{ac}^2}, \tag{4.2}$$

where $\alpha$ is the initial slope at low frequency of the fitting curve [174].

The $n\tau$ is $44 \pm 3$ ms and $1560 \pm 120$ ms for the not-compacted and compacted conductors, respectively. The corresponding ratio is $35 \pm 5$. When comparing this to the ratio of $27 \pm 3$ for the $\rho_{ss}$, the similarity implies a strong correlation between the interstrand contact resistance and coupling loss.

## 4.3 Analysis of the PF joint in transverse magnetic field

### 4.3.1 Measurement in the SULTAN facility

In order to qualify and optimize the joint design and manufacture, a campaign of PF joint qualification measurements was carried out in the SULTAN facility, including DC, AC and stability performance determination. The magnet system in the SULTAN facility consists of a DC and an AC coil. The DC magnetic field $B_{dc}$ is in the x-direction, and the AC magnetic field $B_{ac}$ is in the y-direction, details are seen in Figure 2.1. The positions of the voltage taps and temperature sensors for the SULTAN AC loss measurement are shown in Figure 2.2.

The AC loss tests of the joints are performed with zero or 3 T background DC magnetic field, and a sinusoidal magnetic field pulse with amplitudes of $\pm 0.1$ T or $\pm 0.2$ T in the frequency range of 0.02 Hz to 5 Hz, while the transport current is either zero or 55 kA. The AC loss is measured using the calorimetric method by determining the helium enthalpy variation from upstream to downstream of the joint.

The dimensions and parameters of the tested joints are illustrated in Figure 4.28, also showing the cable compaction causing a deviation from the ideal configuration in Figure 4.17. A few representative PF joint samples were selected and the corresponding parameters are shown in Table 4.9.

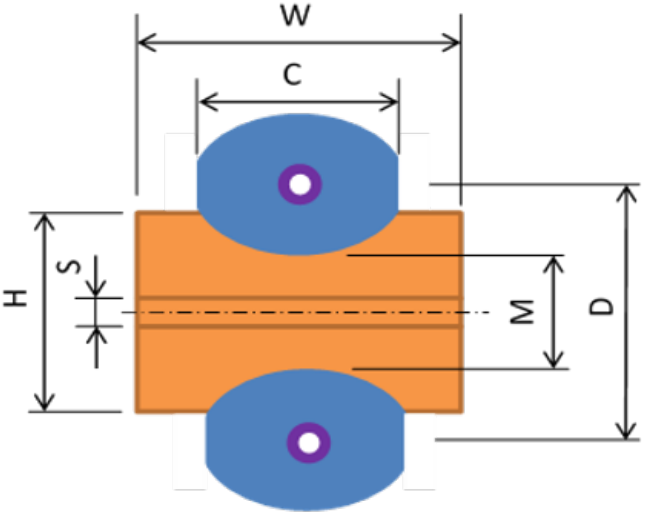


Figure 4.28: Dimensions and parameters of joint samples tested in the SULTAN facility.

The AC loss test results of these full-size ITER PF joints measured with $B_{dc} = 3$ T, $B_{ac} = 0.2$ T and $I =$ zero, are shown in Figure 4.29. The typical measurement error in this figure is estimated at $10\,\%$ in the loss per cycle.

Table 4.9: Dimensional parameters of a few representative PF type of joint samples measured in the SULTAN facility.

| Joint | Conductor | H [mm] | S [mm] | M [mm] | D [mm] | C [mm] | W [mm] | $\rho_{sole}$ [a)] $[10^{-12}\,\Omega m^2]$ | $\rho_{shim}$ [a)] $[10^{-12}\,\Omega m^2]$ |
|---|---|---|---|---|---|---|---|---|---|
| PFJEU3 | PF5 | 32.2 | 7.0 | 19.6 | 47.1 | 35.4 | 64 | 4.55 | 0.43 |
| PFJEU6 | PF5 | 33.1 | 7.1 | 20.1 | 47.6 | 35.4 | 64 | 3.34 | 3.34 |
| PFJEU9 | PF5 | 31.7 | 7.0 | 18.5 | 48.4 | 35.4 | 64 | 3.34 | [b)] |
| PFJEU11 | PF5 | 30.8 | 7.0 | 17.8 | 47.6 | 35.4 | 64 | 3.34 | 3.34 |
| PFJEU12 | PF5 | 30.0 | 7.0 | 17.0 | 46.8 | 35.4 | 64 | 3.34 | 3.34 |
| PFJEU1 | PF6 | 32.0 | 1.8 | 14.8 | 42.2 | 37.8 | 64 | 2.75 | 0.15 |
| PFJEU5 | PF6 | 35.1 | 3.9 | 16.6 | 44.4 | 37.8 | 64 | 2.75 | 2.75 |
| PFJEU8 | PF6 | 33.4 | 3.0 | 16.4 | 42.4 | 37.8 | 64 | 3.14 | 3.14 |
| PFJEU7 | PF2 | 28.9 | 7.0 | 15.9 | 45.7 | 35.4 | 64 | 3.34 | 3.34 |

[a)] Copper resistivity measured at 4.5 K temperature and zero background magnetic field.
[b)] The shim was accidently made of OFE copper instead of DHP copper. The resistivity is unknown.

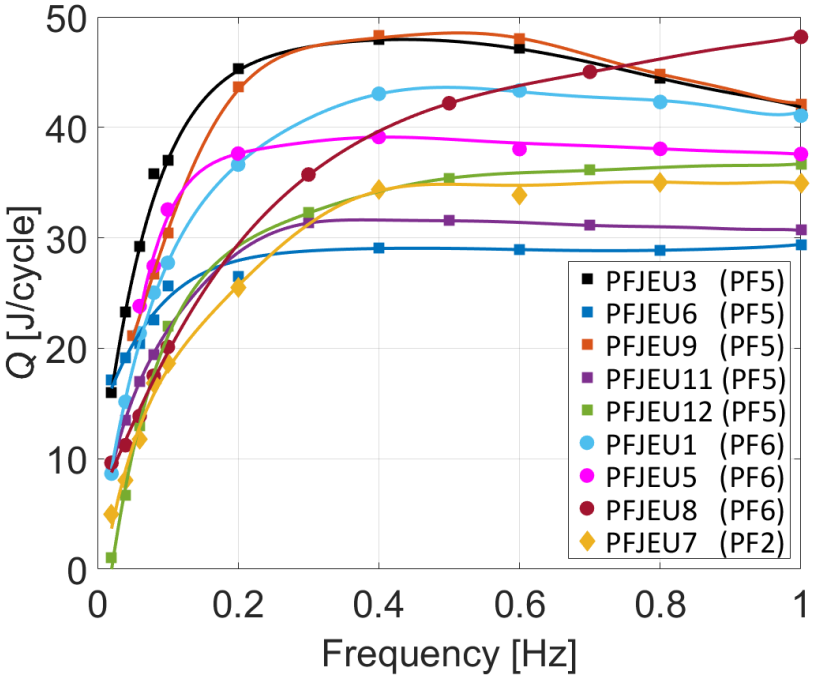


Figure 4.29: AC loss per cycle versus frequency of ITER PF joint samples measured in the SULTAN facility with $B_{dc}$ = 3 T, $B_{ac}$ = 0.2 T, $I$ = zero.

It is observed that the behavior of the PFJEU3 and PFJEU9 samples is quite different from the other three PF5 joints. The difference is mainly caused by the quite different resistivity properties of the copper sole and shim. The relatively high copper shim resistivity of the PFJEU6, 11, 12 joint samples leads to a lower AC loss. The resistivities of

the Deoxidized High Phosphorus (DHP) copper sole and shim are the same for these three samples. In order to make a proper analysis of the PF5 joint, these three joints and the average values are taken as references for the JackPot-AC/DC simulations.

### 4.3.2 Simulation of the joint test in SULTAN

In the SULTAN AC loss and stability measurements, the AC magnetic field is present in a certain region and referred to as the high field zone HFZ, as illustrated in Figure 2.2. In the simulations, the AC magnetic field is composed of its components in three directions (x,y,z) [175], in which the critical component along the joint axis (z direction) is shown in Figure 4.30, referred to as the SULTAN-profile. In order to evaluate the impact of the AC magnetic field on the AC loss of a joint, two other profiles named UT-profiles 1 and 2 are tested as well. Furthermore, the width of the profiles can be scaled by multiplying with a factor $f_w$, with respect to the original width with $f_w = 1.0$. The comparison of the profile variants is shown in Figure 4.30.

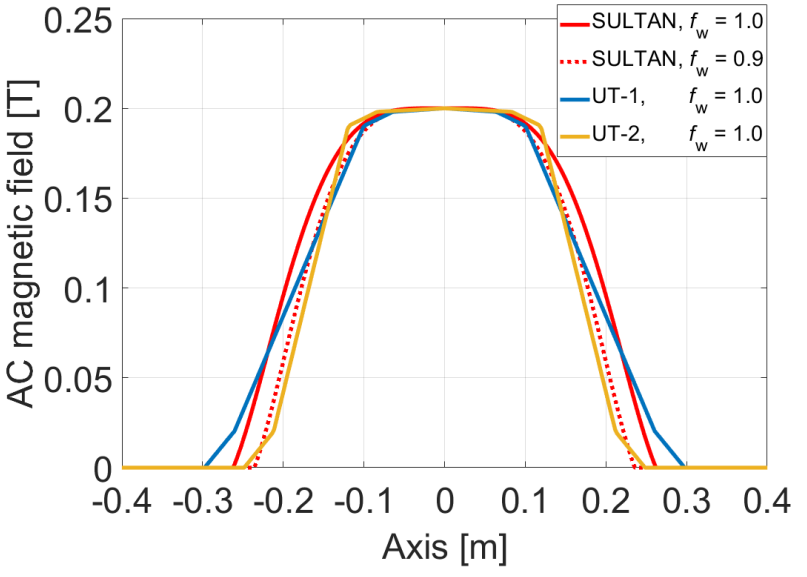


Figure 4.30: Profiles of the SULTAN and UT profiles of the AC magnetic field component along the z-axis applied in the simulations.

For the PF5 joint with 19% void fraction, see Table 4.4, and resistivity parameter set 2, see Table 4.7, the AC losses for the various magnetic field profiles are simulated. The results in comparison to the measured data of three PF5 joints and their average value are shown in Figure 4.31. Considering the influence of the effective angle between strands and magnetic field, as explained in section 3.4, the hysteresis loss in transverse magnetic field $Q_{\text{hys}}$ of 5.0 J/cycle is subtracted from the measured data [111].

The comparison reveals the influence of the four AC magnetic field profiles on the AC losses. Although the amplitudes and widths of the four profiles are similar, quite different

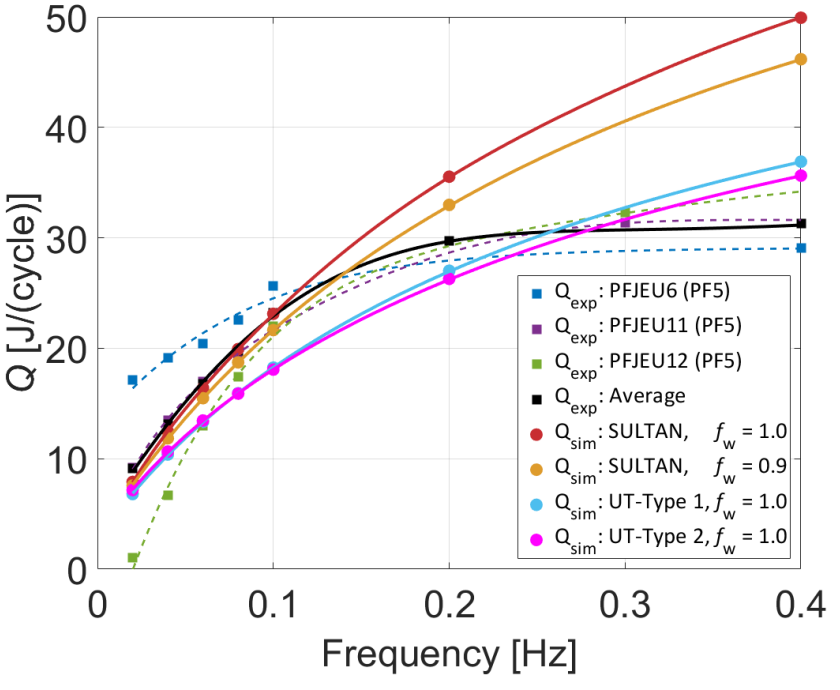


Figure 4.31: Comparison of calculated and measured AC losses of the PF5 joint with four different AC field profiles. Also the curve representing the mean values of three PF5 joints is shown.

AC loss behaviours are observed. For the SULTAN-profile and its variation with $f_w = 0.9$, a relatively good agreement with the measured data is observed in the low frequency range, but significant discrepancy occurs as the frequency increases. For joints tested with the UT-profiles 1 and 2, lower losses are produced. The sensitive dependence of the AC loss on the magnetic field uniformity also indicates the importance of constructing the SULTAN magnetic field profiles accurately.

In the SULTAN measurements, it is found that the maximum AC loss of the reference joints occurs at about 0.4 Hz with a certain magnetic field sweep amplitude [164]. When approaching this frequency, the coupling currents reach the maximum current capability first in the outer strands of the CICC, and the saturated region usually follows a cosine distribution. This is referred to as saturation regime and leaving the other region in the non-saturation state [176]. In JackPot-AC/DC, the saturation is implicitly implemented. This means reaching the superconducting to normal transition for part of the strands, will limit the strand currents and enforces a current redistribution to other strands that have not reached saturation yet. The observation shows that the saturation transition in simulations is not as sharp as in the measurements, as seen in the Figure 4.31. This may be related to details in the distribution of contact resistances, which is not further investigated within this work.

### 4.3.3 Coupling loss in transverse magnetic fields

For the measurements of contact resistances and AC losses performed at the University of Twente, the DC and AC magnetic fields are provided by a solenoid and they are applied along the joint axis and thus referred to as parallel magnetic field. The target of the measurements and simulations in parallel magnetic field is to obtain the relevant resistivity and solder related parameters and then to study by simulation the joint performance as measured in other facilities like SULTAN or under operating condition in ITER, where the magnetic fields are normally applied perpendicularly with respect to the joint axis, referred to as transverse magnetic field.

As described in section 2.2.1, in the SULTAN facility, the effective magnetic field length is about 39 cm and 45 cm for the DC and AC magnetic field cases, respectively. The coupling and eddy current losses of the PFJEU6 joint is simulated for the SULTAN magnetic field conditions, with a background magnetic field $B_{dc}$ of 3 T applied in the x-direction as illustrated in Figure 4.17, and AC magnetic field modulated with an amplitude $B_{ac}$ of 0.2 T, applied in the x and y directions, respectively. Considering the influence of the limited effective lengths, the coupling and eddy current losses of the joint are normalized to a volume of 1088 $cm^3$, which is the sum of copper sole and strand volumes across a 39 cm length.

The calculated coupling loss density per cycle versus frequency is shown in Figure 4.32.

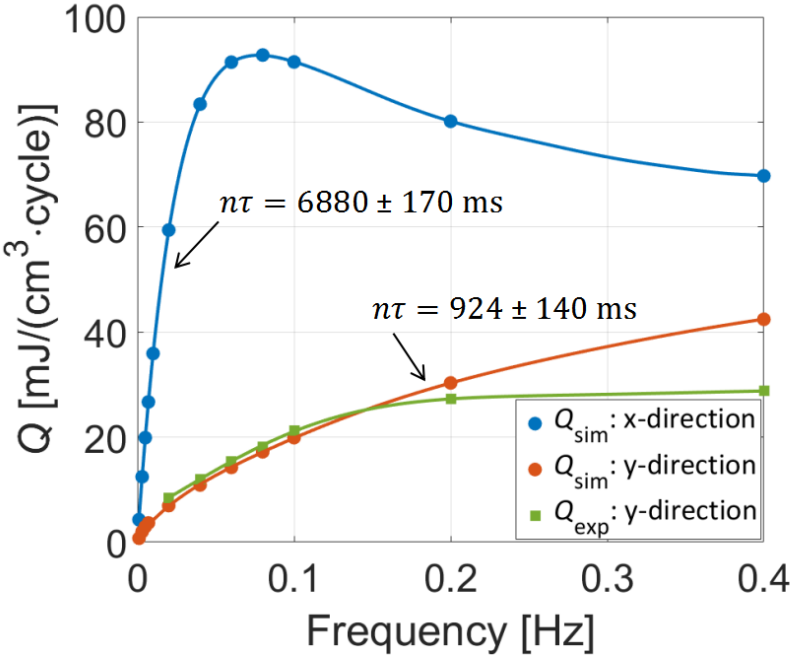


Figure 4.32: Calculated coupling loss density per cycle versus frequency of the PF5 joint sample, with AC magnetic field applied in the x and y directions, with amplitude $B_{ac} = 0.2$ T, at zero external magnetic field.

The coupling loss time constant is derived by fitting the loss density at low frequency up to 20 mHz, yielding $n\tau$ is $6880 \pm 170$ ms and $924 \pm 140$ ms for the AC field in x and y directions, respectively. In the case of x direction, large coupling currents are induced across the two conductors and copper sole, and contribute the largest part to the total losses. In the case of y direction, the coupling currents are rather limited in the individual conductors due to small current loops. Then the dominant contribution is the eddy current loss in the copper sole, thus relatively low losses are observed. This case is analogous to the case of SULTAN measurements. The results of a measured ITER PF joint [164] is also shown and compared in Figure 4.32. Good agreement is observed between the experiments and simulations, especially in the low frequency range, which also validates the accuracy of the resistivity parameterization. The discrepancy at the high frequency range is probably related to the saturation effect in simulations. When the losses are gently increasing, sometimes a delayed saturation is observed.

## 4.4 Conclusion

Qualification tests of full-size joint samples are essential for the ITER magnet R&D program, since badly operating joints can significantly affect the entire magnet performance and potentially leading to a machine failure. A campaign of PF joints qualification measurements was carried out in the SULTAN facility with DC, AC and stability measurements providing global properties. With the aid of the numerical code JackPot-AC/DC, the joint performance can be analyzed in more details, however, reliable input parameters are required. For the JackPot-AC/DC model, besides heat transfer coefficients and geometries, the contact resistivities are the main and crucial input parameters.

After the qualification tests in the SULTAN facility, an ITER PF5 joint sample PFJEU6 was extensively tested at the University of Twente regarding contact resistances and AC losses.

The inter-strand, inter-petal and strand-to-copper sole contact resistivities of the two cables A and B of the joint were measured; the resistance spread in cable B is slightly higher than in cable A. The inter-strand resistances (first to fourth stage) are in the range of $2 \pm 1$ nΩm to $4 \pm 1$ nΩm and increase slightly with subsequent cabling stages. The inter-petal resistance (fifth stage) was found to be in the range of $6 \pm 1$ nΩm to $12 \pm 1$ nΩm, which is about 3 to 5 times higher than the inter-strand resistances. The inter-strand and inter-petal contact resistances of the joint are, respectively, 30 and 300 times smaller than for regular, not-compressed ITER PF conductors. Furthermore, the inter-petal to inter-strand ratio has decreased from 40 to 4.5 as the conductor in the joint is compressed to a void fraction of 19%. The strand-to-copper sole resistivity was determined by measuring the resistance between single strand pairs, each selected from both different cables. The results show an average resistance of $16 \pm 4$ nΩ and a minimal resistance of $7 \pm 1$ nΩ, while the overall joint resistance was measured as $4.8 \pm 0.2$ nΩ.

The AC loss measurement is performed by magnetization and calorimetric methods with fairly good agreement. The strand hysteresis loss and its angular dependence were measured with a Vibrating Sample Magnetometer (VSM).

Lap-type twin-box joints represent critical components where conventional qualification tests typically emphasize global properties. However, a robust research and de-

velopment framework necessitates a comprehensive analysis at the strand level to gain a quantitative understanding of the diverse electrical properties inherent in these joints. In a pioneering effort, the interstrand and interpetal contact resistances of a full-size ITER PF joint were meticulously measured, marking a significant stride towards acquiring essential resistivity parameters for subsequent quantitative numerical analyses using the JackPot-AC/DC model. Through an exhaustive evaluation of their impact on resistance distribution and AC losses, an enhanced parameterization process is undertaken, yielding precise resistivity and solder-related parameters. A sensitivity analysis was conducted to discern the influence of individual parameters, culminating in the derivation of a set of optimal parameters tailored for the PFJEU6 joint. This optimized parameter set serves as the cornerstone for subsequent quantitative numerical analyses.

The varying void fractions of cables within and outside the joint box section introduce notable effects on the contact areas between strands, consequently influencing the resistivity parameterization. An in-depth assessment of the joint's performance was conducted, encompassing the intricate dynamics of cable compaction and the consequential current transfer effect to the copper sole.

Utilizing the optimized resistivity parameters corresponding to different cable sections, the joint's performance was systematically evaluated under parallel and transverse applied magnetic field conditions. Simulation results derived from conditions mimicking SULTAN testing, guided by the input parameter analysis, exhibit commendable agreement with measured data. This systematic investigation establishes a foundational framework for an extensive analysis of lap-type twin-box joints, encompassing DC, AC, and stability properties. The findings contribute to a deeper understanding of the joint's behavior under diverse operational scenarios, paving the way for further advancements in the field.

# Chapter 5

# Modeling and validation of the nonlinear voltage-current characteristics of ITER PF joints

The content of this chapter is mainly based on the following publication:

- J Huang, T Bagni, Y Ilyin and A Nijhuis, "Modeling and validation of nonlinear voltage-current characteristics of ITER PF joint sample tested in the SULTAN Facility", *Supercond. Sci. Technol.* 35 025014 (2022) (14pp) `https://doi.org/10.1088/1361-6668/ac455c`.

## 5.1 Introduction

During the PF joints qualification measurements in the SULTAN facility, a nonlinear voltage-current (*V-I*) characteristic was observed during the joint resistance measurements of PFJEU2, PFJEU3 and PFJEU6 samples. Especially for the sample PFJEU2, a resistance deviation up to 3.5 nΩ was observed for two different electromagnetic load conditions [177]. The PFJEU2 was the first trial sample built by an industrial supplier, well before the manufacturing procedure was stabilized. Similar behavior was observed in the measurement results of some Toroidal Field (TF) conductor joints. A poor current redistribution in the joint with high strand-bundle to copper sole resistance was adopted as the probable reason [178], [179].

Besides the SULTAN measurements, a JackPot-AC/DC model comprising non-homogeneous contact resistances between different components of the joint, like strand-bundle, copper sole and shim, has been built to study possible nonlinear *V-I* characteristics. It was found that a widely spread defective connection between copper sole and shim resembles the observed nonlinear behaviour. The electromagnetic force causes a separation effect on the mechanically and electrically weakly connected parts, resulting in a strongly varying resistance depending on transport current and background magnetic field. The hypothesis stated and model constructed were validated by an experiment on a similar joint sample PFJEU3 and a post-mortem examination of the PFJEU2 joint sample.

## 5.2 Joint resistance test and simulation

During the manufacturing of the PF joints, the outer surface parts of the steel wraps wound around the petals, are removed to get a better electrical contact between the cable and copper sole. In addition, AgSn solder is added at the contact interface to further improve the electrical, mechanical and thermal stabilization [180]. The prepared cable end is pressed into a bimetallic box machined from an explosive bonded stainless steel/copper plate to form a termination. A copper shim is inserted between two of these terminations to compensate for manufacturing and positioning misalignments. PbSn solder is applied at the interfaces between the copper soles and shim, and then the pieces are held together by two side plates welded to the joint boxes. A cross-section of a PF joint including the solder applied between cable, sole and shim, is shown in Figure 5.1 [181].

As described in section 2.2.1, in the SULTAN facility, besides a maximum sample current of 100 kA, magnetic fields are available from both DC and AC coils, orthogonally oriented to each other, as illustrated in Figure 5.1. The samples are vertically inserted into the magnet bore and the terminals are connected to the current leads of a superconducting transformer [69]. Note that the qualification joint samples are praying hands type instead of the shaking hand type (as in the real PF coils) to fit the magnet configuration. The configuration of a PF joint sample is shown in Figure 5.2.

The resistance of the joint is measured at sample currents of 10, 20, 30, 40 and 55 kA in background DC magnetic fields of 0 T, 3 T and 5 T. Two sets of voltage taps named “Bottom” and “Top” taps, are attached to the conductors at 40 mm and 490 mm distance from the end of the joint box. The average smoothed voltage signal $V$ between the two positions are obtained and the joint resistance derived as $R = V/I$. For the PFJEU2

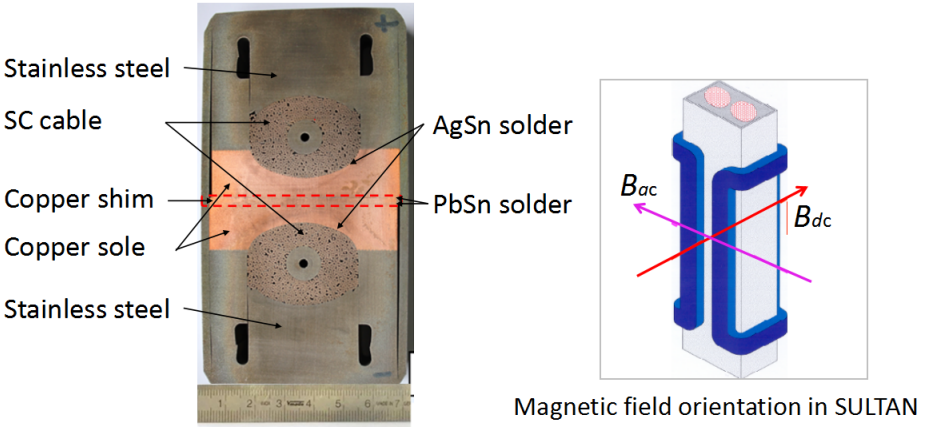


Figure 5.1: Cross section of a Poloidal Field joint, including the solder applied between cable, sole and shim, and a schematic of the SULTAN magnetic fields applied to the joint.

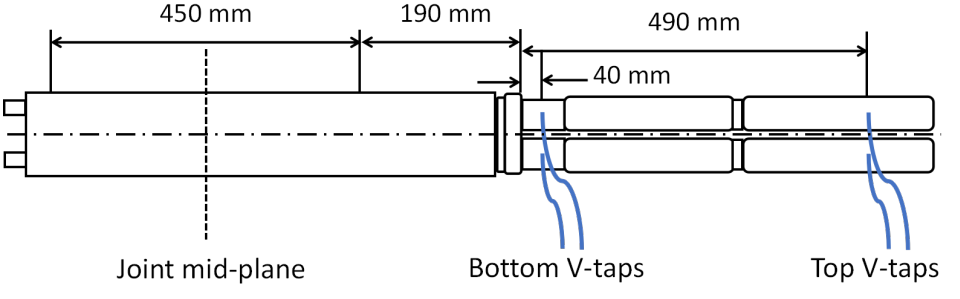


Figure 5.2: Configuration of the PF joint sample as tested in the SULTAN facility. The ”Bottom” and ”Top” voltage taps are attached to the conductors at 40 mm and 490 mm distance from the right end of the joint box, respectively.

sample, after 1000 bipolar load cycles at 6 T / $\pm$ 27.5 kA, the resistances measured at the “Bottom” position, versus current and background magnetic field are shown in Figure 5.3. The joint exhibits a strong nonlinear *V-I* characteristic. The resistance increases by 3.5 n$\Omega$ as the $B \times I$ product increases from 10 kA and zero T, to 55 kA and 5 T. Not only this resistance is too high compared to the design requirement of the PF joint resistance of $\leq$ 5 n$\Omega$ [177], but the variation is also not anticipated.

The tests performed in the SULTAN facility, have been simulated and analyzed with the JackPot-AC/DC model. The schematic of the praying-hands lap type PF joint is shown in Figure 4.17, by which two cables are circular when compared to the more realistic oval shape as shown in Figure 5.1. The copper sole and shim with different resistivities are represented with different colors, but the effect of the solder between them is neglected in the simulation. The geometry and resistivity parameters of the modeled PF joint are summarized in Table 5.1, the mask [182] and patch resistivities are defined and explained in sections 6.1 and 5.3.2, respectively.

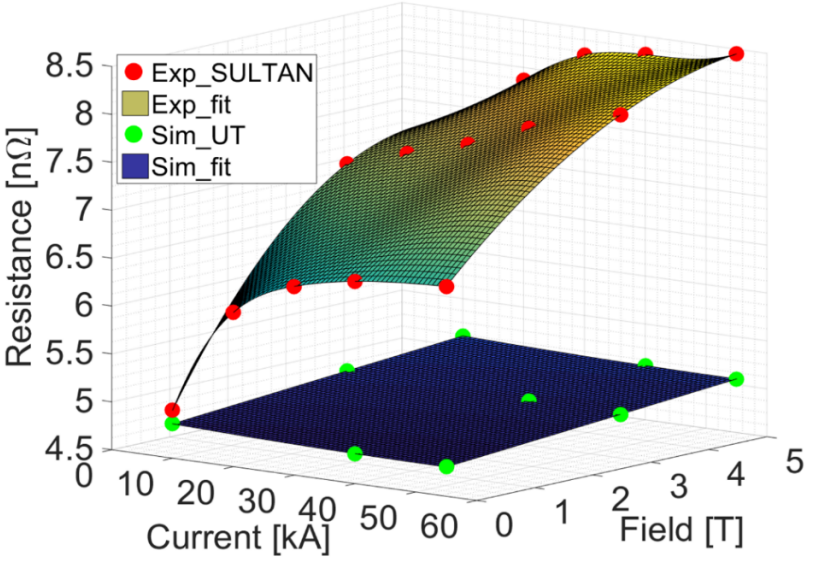


Figure 5.3: Dependency of the measured joint resistance of the PF joint sample PFJEU2 versus the sample current and background magnetic field, in comparison to the simulated results using the JackPot-AC/DC model.

Table 5.1: Geometrical and electrical parameters of the ITER Poloidal Field joint PFJEU2 as simulated using the JackPot-AC/DC model.

| Parameter | Value |
|---|---|
| Sole length $L$ [mm] | 450 |
| Sole width $W$ [mm] | 64 |
| Sole height $H$ [mm] | 35 |
| Shim thickness $H_{shim}$ [mm] | 7 |
| Cable length $L_{cable}$ [mm] | 700 |
| Cable offset to midplane $H_{cable}$ [mm] | 26.2 |
| Cable diameter $\Phi$ [mm] | 35.3 |
| Sole resistivity $\rho_{sole}$@4.5 K [nΩm] | 4.55 |
| Shim resistivity $\rho_{sole}$@4.5 K [nΩm] | 0.43 |
| Equivalent resistivity of joint $\rho_{equ}$@4.5 K [nΩm] | 4.00 |
| Inter-strand resistivity $R_{ss}$ [μΩm$^2$] | $1.25 \times 10^{-5}$ |
| Inter-petal resistivity $R_{ip}$ [μΩm$^2$] | $5.00 \times 10^{-5}$ |
| Strand to sole resistivity $R_{sj}$ [μΩm$^2$] | $3.00 \times 10^{-5}$ |
| Mask resistivity $R_{mask}$ [μΩm$^2$] | 50 |
| Patch resistivity $R_{patch}$ [μΩm$^2$] | 50 |

The transport current flows from the terminals of cable A to cable B, ramping up at $t = 2$ s, with a rate of 2 kA/s to a maximum value of 10 kA. Then the constant current lasts until $t = 30$ s, as seen in Figure 5.4 (a). The background magnetic field is oriented in the x direction. The power dissipations in the whole joint, as well as in the three main components, are calculated assuming a constant transport current. For example, the power dissipation in joints with different strand-to-sole resistivities of $\rho_{sj} = 3 \times 10^{-6}$ μΩm$^2$ and $3 \times 10^{-5}$ μΩm$^2$ have been derived and are shown in Figure 5.4 left and right, respectively.

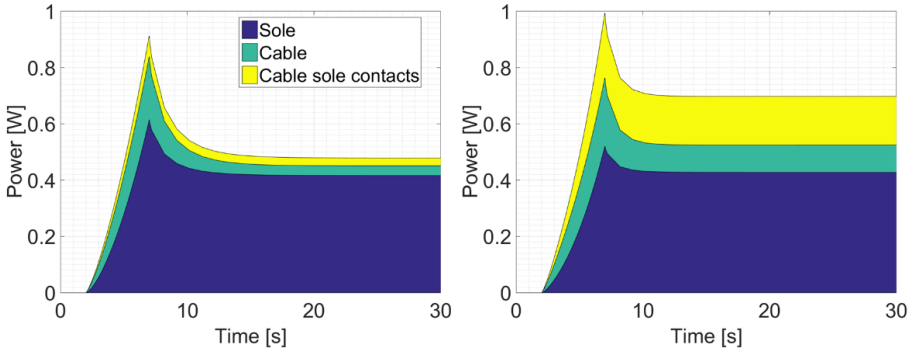


Figure 5.4: Power dissipation versus time in the PF joint sample generated during a current ramp to 10 kA constant value. The power distribution is given for the three components, (left) joint with strand-to-sole resistivity of $3 \times 10^{-6}$ μΩm$^2$, (right) joint with strand-to-sole resistivity of $3 \times 10^{-5}$ μΩm$^2$.

The joint resistance is obtained by dividing the produced power dissipation $P$ in the joint by the squared plateau current following $R = P/I^2$. The joint resistances obtained from the simulations for all current-magnetic field combinations and the SULTAN measurements are compared in Figure 5.3. It shows that the variation of transport current and magnetic field has relatively little influence on the joint resistance according to the model results. Even with the incorporated effect of the magneto-resistance of the copper sole and strands, the computed joint resistance variation is still by far smaller than the maximum difference of 3.5 nΩ observed in the measurements.

In accordance to the power distribution as shown in Figure 5.4, the joint resistance derived from the model is dominated by the component of power dissipated in the sole and shim, implying the importance of their resistivity. For the PFJEU2 sample with a shim layer thickness of 7 mm and a low resistivity of 0.43 nΩm, the total resistance is reduced by 13%. Another important factor affecting the power dissipation is the resistivity of the interface between the strands and the copper sole as demonstrated in Figure 5.4 for joints with strand-to-sole resistivities $\rho_{sj}$ of $3 \times 10^{-6}$ μΩm$^2$ and $3 \times 10^{-5}$ μΩm$^2$ respectively. A regular conductor section comprises relatively large voids between strands for helium flow and heat removal. The conductors in the joint section, however, are further compacted from a void fraction of 34.1 to 24.5%. In addition to the voids occupied by the solder, the remaining void fraction is about $20.0 \pm 0.4$ % [183]. It is expected that the strands in the cable are tightly compacted, which leads to a relatively stable strand to strand resistivity and dissipation in DC condition. This indicates that the observed nonlinear *V-I*

characteristic is most likely related to the contact resistances between copper sole and shim, or between copper sole and cable surface, instead of the inter-strand resistances within both cables.

## 5.3 Non-homogeneous contact resistance model

Two non-homogeneous models were developed to demonstrate the mechanisms behind the potential causes for the nonlinear *V-I* characteristic. One is the non-homogeneous contact resistance distribution between sole and shim, focused on two different configurations with integral and discrete shim layers. The corresponding schematics are shown in Figures 5.5 (a) and (b), respectively. The other is the non-homogeneous contact resistance distribution between the cable and sole interface, of which the schematic is shown in Figure 5.5 (c). In the schematics, the non-homogeneous resistance distribution is represented by the discrete sections with different resistivities. The blue color represents the sections with higher resistivity while the white sections are the regions with low resistivity. The non-homogeneity in resistance distribution can be altered by the dimensions and quantities of the discrete sections.

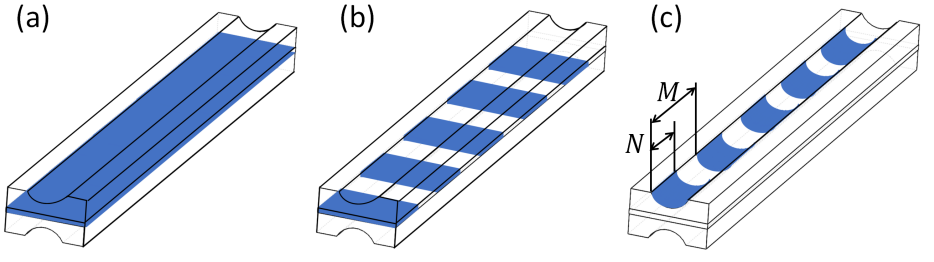


Figure 5.5: Schematics of the joint models for simulating the non-homogeneous contact resistivities between copper sole and shim, or between strands and copper sole. The blue color represents the highly resistive region, (a) integral shim model, (b) discrete shim model, (c) discrete contact resistance between strands and sole.

### 5.3.1 Non-homogeneous contact resistance between copper sole and shim

The model is based on the assumption that the electrical connection between copper sole and shim is changing under the influence of the electromagnetic force. For the conductors in the praying-hands type of joint, the transport currents are reversed while the background magnetic field direction is the same for both. Thus the electromagnetic forces applied on them are in opposite direction, leading to a compressing or separating force. In such a case, the resistivity of the discontinuous interface instead of the sole and shim dominate the resistance deviation. In the model, a conservative simplification is made first by treating the separated copper sole and shim as a whole object with an equivalent copper resistivity $\rho_{equ}$ of 4.0 nΩm. This resistivity is derived from assuming the same power dissipation as generated in sole and shim, both having different resistivities.

Based on this joint sole and shim with equivalent resistivities, the non-homogene-ous contact resistance model is implemented by adjusting the resistivity and size of the sections with high resistivity, conform the blue regions represented in Figure 5.5. The middle layer with equivalent or high resistivity is still referred to as shim for easy description. Two joint configurations with integral or discretized middle shim layer are considered here, corresponding to Figure 5.5 (a) and (b), respectively.

For the shim layer in between both sole parts, the discretization is formed by 11 meshed layers in height (y) direction, the thickness of one layer is 3.2 mm. For the integral shim model as shown in Figure 5.5 (a), the whole shim layer has a high homogeneous resistivity. For the discrete shim model two discrete configurations, one with seven and one with eleven high-resistivity sections are considered: the corresponding widths are $450/(7+6) \approx 35$ mm and $450/(11+10) \approx 21$ mm, respectively. Three joint configurations are simulated to evaluate the effect of the non-homogeneous sole to shim resistance on the current and power distribution: integral shim, discrete shim with seven and one with eleven high resistivity sections.

Unlike the most probable situation in reality that the contact resistivity and areas of the discontinuous connections change gradually, in the model the resistivity of the individual shim sections is fixed. A factor $k_\rho$ is introduced to scale the resistivity of the shim sections with respect to the normal regions with equivalent resistivity, $\rho_{shim} = k_\rho \cdot \rho_{equ}$. For the two cases with integral shim and seven high resistivity shim sections, simulations are performed with 3 T background magnetic field and different transport currents, or for 40 kA transport current but different background magnetic fields. The results are shown in Figure 5.6 and Figure 5.7 , showing that a nice fit can be derived for measured and simulated resistance data by adjusting the shim resistivity by means of the factor $k_\rho$.

In order to catch the increasing resistance tendency observed in the SULTAN measured data, an increasing $k_\rho$ is required for both shim models. As the current increases from 10 to 55 kA at 3 T background magnetic field, the $k_\rho$ needs to be increased from 25 to 85 for the model with seven discrete shim sections. For the integral shim model the change from 5.4 to 7.0 is relatively small. When the areas of the discrete shim sections are increased, the resistivity is decreasing and approaching the shim resistivity of the integral model. A similar tendency is observed when the background magnetic field increases from 0 to 5 T. Keeping the 40 kA transport current constant, the $k_\rho$ changes from 17 to 85 for the model with seven discrete shim sections, and 4.6 to 7.3 for the integral shim model.

The joint resistance is directly derived from the power dissipation and thus largely depending on the contribution of the copper sole. For the three defined shim configurations: the integral shim, the discrete shim with seven and eleven high-resistivity sections, the power distribution along the copper sole length is shown in Figure 5.8 for 40 kA transport current and 3 T background magnetic field.

A pronounced non-homogeneous distribution is observed for both discrete shim cases and the power is generated mostly in a few regions along the joint axis. The number of high-power regions seems positively correlated but not equal to the quantity of the high-resistivity shim sections. There are three and five high power regions in the joint with respect to seven and eleven high-resistivity shim sections.

Considering that the power dissipation is directly related to the current distribution, the current distribution in the sole of the three joint configurations in DC condition, together with the AC condition for comparison, are shown in Figure 5.9.

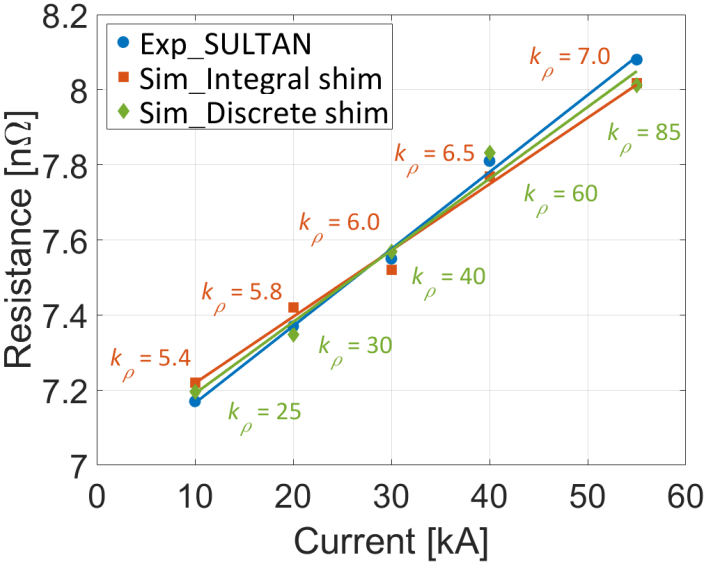


Figure 5.6: Joint resistance versus current calculated with different shim resistivities in the two non-homogeneous sole to shim resistance models, in comparison with the data measured in SULTAN. The background magnetic field is 3 T.

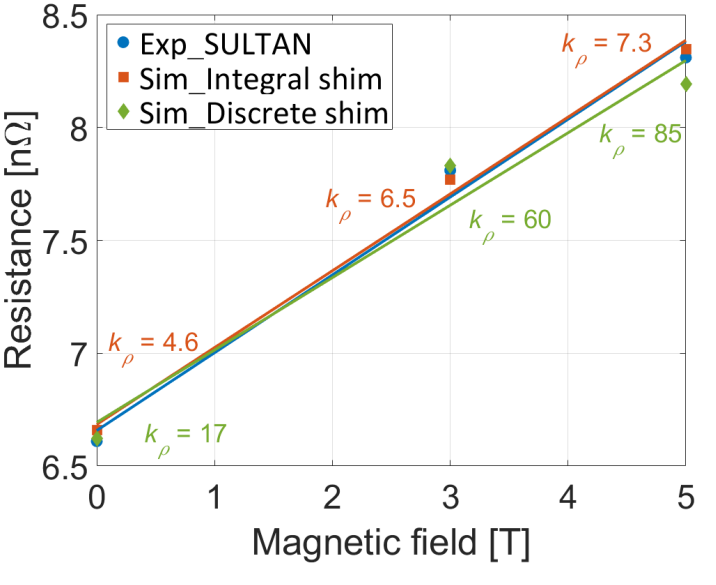


Figure 5.7: Joint resistance versus magnetic field calculated with different shim resistivities in the two non-homogeneous sole to shim resistance models, in comparison with the data measured in SULTAN. The transport current is 40 kA.

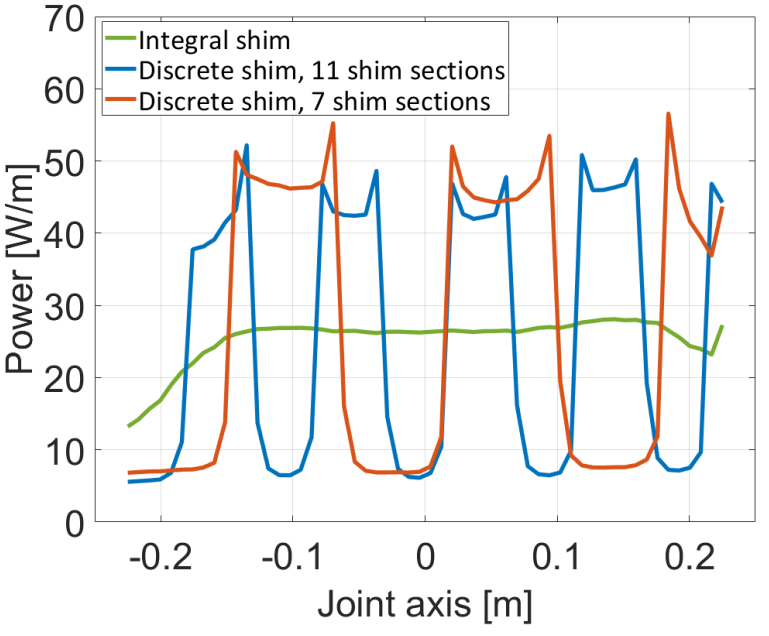


Figure 5.8: Local power dissipation in the copper sole versus position in the joint with different shim configurations, in which the resistance of the joint with integral shim and seven high resistivity discrete shim sections are the same.

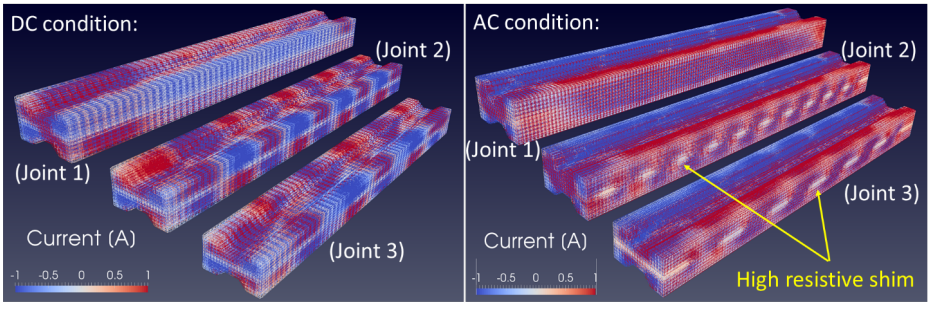


Figure 5.9: Current distribution in the joint for three shim configurations with (left) 40 kA DC transport current and 3 T background magnetic field applied in the x direction, in comparison to the AC condition (right) with ramped field applied in the y direction.

For AC applied magnetic field, the joints are subjected to a magnetic field in the y direction with a ramp rate of 1 T/s for 0.5 s. The present current range is set to $\pm 1$ A to emphasize the distribution itself and ignore the relatively small difference between the magnitudes. The blue color represents the negative current flowing from the far to the near end (figure perspective); the red color represents the opposite current. For DC condition, the current distribution in the joint is partly affected by the non-homogeneous shim

configuration. For AC condition, the power distribution in the sole is determined by the resistivity and quantity of the shim sections.

Besides the current distribution, the current density distributions in the copper sole for the three shim configurations are shown in Figure 5.10, when viewed from the position of cable B. The arrows point in current flowing direction and the color shade represents the density. For joint 1 with integral shim, the copper resistance and the current are almost uniformly distributed along the joint axis. However, still some local current loops induced at both ends of the sole are observed, due to the masks blocking the electrical connections between the sole and one end of the petals having double contacts with the sole [182], [184]. For joints 2 and 3, the highest current density is in a few specific regions indicated by the dark green color. The current is not evenly passing all low-resistivity shim sections, meaning that the current distribution is not just dominated by the resistivity distribution in the sole.

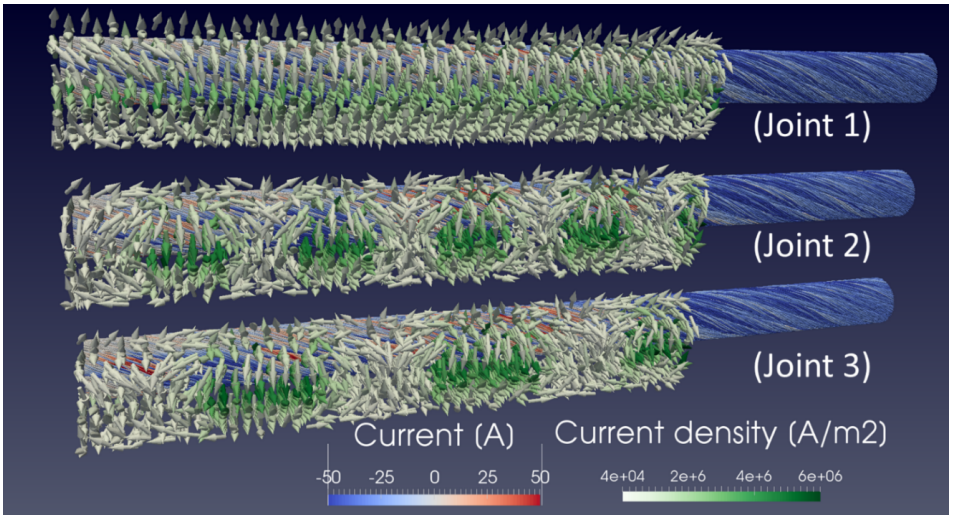


Figure 5.10: Current density in the copper sole and strand currents in cable A for joints with three types of shim configurations.

This can be explained by the current distribution in the cables. For joint 3, with seven high-resistivity shim sections for example, the current density in the sole with respect to the petal current distribution in cable A, is illustrated in Figure 5.11. In order to emphasize the petal current distribution, two plots viewed from the same angle are compared. The upper plot shows the physical arrangement of the six petals of cable A, which are labelled from 1 to 6; the lower plot shows the corresponding current distribution. For both plots, the current distributions in the copper sole are identical and the high-current regions are named as a, b, c. The magnitude of the strand currents is below 20 A in the joint box region. For negative transport current from the cable right end, there are positive currents (red color) produced in some strand sections, which are in direct contact with the copper sole, especially in the regions with low-power dissipation. On first sight it seems there is no resemblance between the shim configuration and the current distribution. The corresponding shim configuration is shown at the bottom of Figure 5.11, using the blue and

white colors to represent the high- and low-resistivity shim sections, respectively. Looking at regions a and b for instance, the distributions of the shim sections are actually opposite, while the current densities appear alike.

According to the observation in Figure 5.10, the current transfer mainly occurs in the center of the sole. As a result, the current is mainly carried by one petal, depending on the specific cable rotation with respect to the cable-sole interface. For joint 3, the currents in petal 1 and 6, petal 2 and 3, and petal 4 and 5 contribute most in regions a, b and c, respectively.

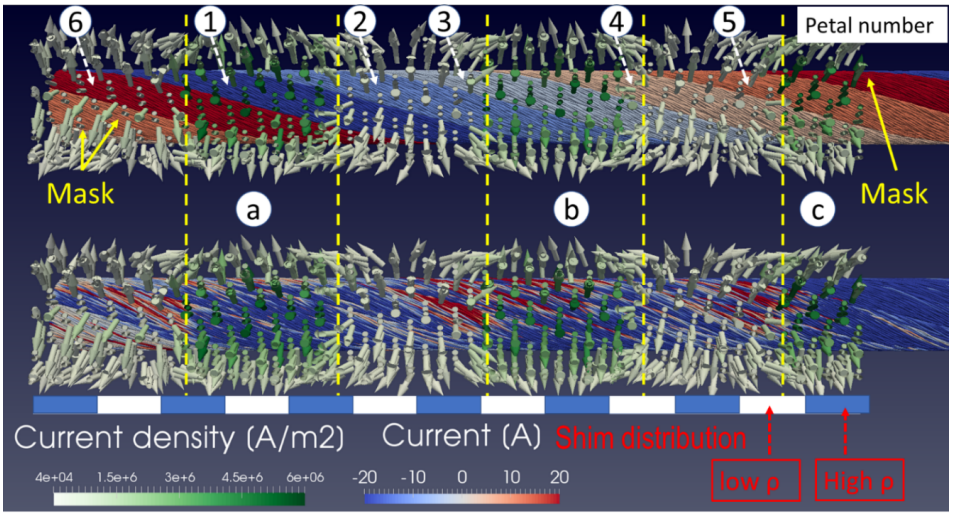


Figure 5.11: Cross-sectional view from the sole to cable A of joint 3, showing the current density in the copper sole with respect to the rotation of six petals in cable A (top) and the strand current distribution in cable A (below). The schematic of the discrete shim configuration is shown at the bottom in blue and white.

### 5.3.2 Non-homogeneous contact resistance between strand and copper sole

A second plausible reason for the nonlinear *V-I* characteristic is a varying contact resistance distribution between strands and copper sole, which is simulated with a non-homogeneous contact resistance model. Two levels of contact resistivities and associated locations, as shown in Figure 5.5 (c), are defined as regions (blue color) with higher resistivity, referred to as "patches". The size of the patches and the corresponding spatial distribution are determined by two factors $M$ and $N$, the overall patch ratio is $P_{ratio} = N/M$. Similar to the non-homogeneous sole-to-shim contact resistance model, only two resistivity levels are considered, the patch resistivity $\rho_{patch}$, which is taken the same as the mask resistivity $\rho_{mask}$ [182], [184], and the resistivity of the remaining regions maintaining the strand-to-sole resistivity $\rho_{sj}$. A summary of the resistivity parameters is listed in Table 5.1.

For the case of 3 T background magnetic field and transport current increasing from 10 kA to 55 kA, a comparison between the SULTAN measured joint resistance and the simulated resistance of joints with different patch ratios is shown in Figure 5.12.

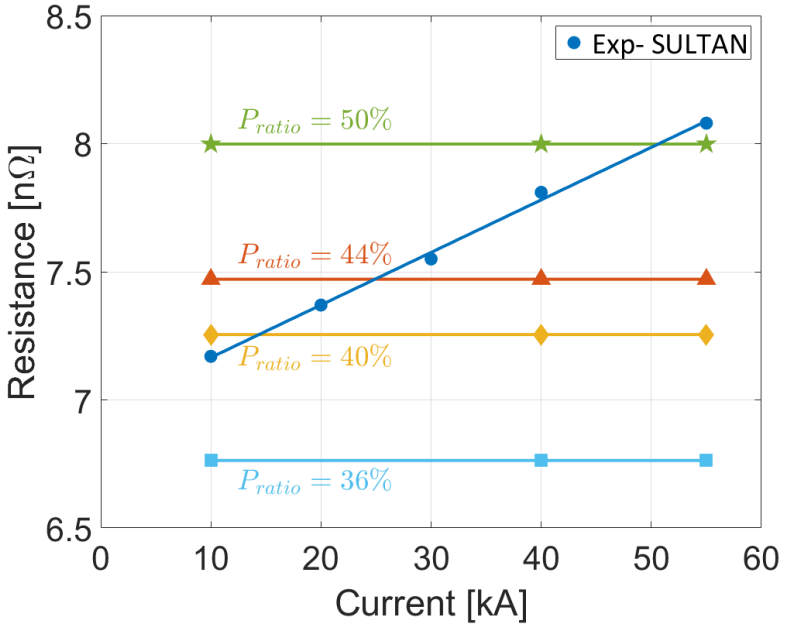


Figure 5.12: Joint resistance versus current calculated with different patch ratios in the non-homogeneous strand-sole resistance model, in comparison to the data measured in SULTAN. The background magnetic field is 3 T.

The patch ratios of 36%, 40%, 44% and 50% are obtained by setting $N = 4$, $M = 11$, 10, 9 and 8, respectively. The comparison shows that in order to match the tendency of increasing measured joint resistances, the patch ratio is required to increase from 40% to 50%. This means that almost half of the interface between cable and copper sole is in low-conductive contact.

Since the calculation of the joint resistance directly depends on the power dissipation, the impact of the patch configuration on the power dissipation is evaluated. Two joints, with and without patches are compared; the patch ratio $P_{ratio} = 0.5$ ($M = 8$, $N = 4$). The distribution of the power in the five components, two cables, two cable-sole interfaces and copper sole, is shown in Figure 5.13.

Although the non-homogeneous connection is at the interfaces between cables and sole, the largest effect is still in the copper sole with a non-homogeneous power distribution along the joint axis. The effect is analogous to the periodic distribution of the joint with non-homogeneous sole-to-shim resistance, as shown in Figure 5.8. In the latter case, the number of power peaks is determined by the combination of shim configuration and cable rotation. While in the case of the non-homogeneous strand-to-sole resistance model, it is solely determined by the patch configuration, with seven power peaks corresponding to the

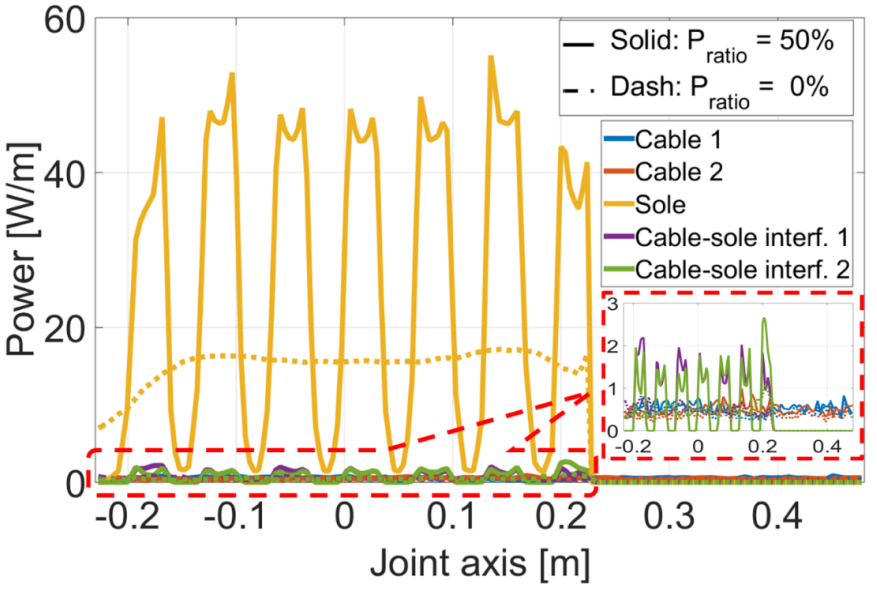


Figure 5.13: Local power dissipation versus position along the joint axis in the five components of joints with patch ratio of zero and 0.5 (50%). The solid lines represent the joint with 50% patch ratio and the dashed lines represent the joint without patch. At right an enlarged view of the cables and cable-sole interfaces power dissipation.

seven patch sections. The power dissipation in the cable-to-sole interface also interlaces with that in the patch distribution, which is illustrated in the enlarged view in Figure 5.13.

The petal current distribution in cable A of the two joint cases are compared in Figure 5.14. For the joint without patches, the petal current transfer into the copper sole is smoothly and in a sequence following the petal rotation pattern. While the implementation of the patches prevents such a continuous current distribution, the current plateaus indicate the barrier effect resulting from the patches. However, even though with a patch ratio of 0.5, there is still an effective current redistribution in the cable.

A 3D view of the current density distribution in the joint with patches is shown in Figure 5.15, where the cable and the copper sole are shown separately to obtain an inside view of the cable-to-sole interface.

The strands in red and blue colors represent the currents flowing in opposite directions indicating that many current loops are induced nearby the patch locations. This is also partly the reason for the periodic current distribution pattern of the cable-to-sole interfaces observed in Figure 5.13. For the current distribution in the copper sole, the arrows represent the current direction and the shade of color indicates the density. The majority of transport current is passing through only a few regions, which are directly determined by the patch configurations. Besides, current is distributed laterally between the main stream passages, illustrating the phenomenon observed in Figure 5.9 that the positive and negative currents occur alternately.

Since a quench is not directly seen by the JackPot-AC/DC model, the impact of the

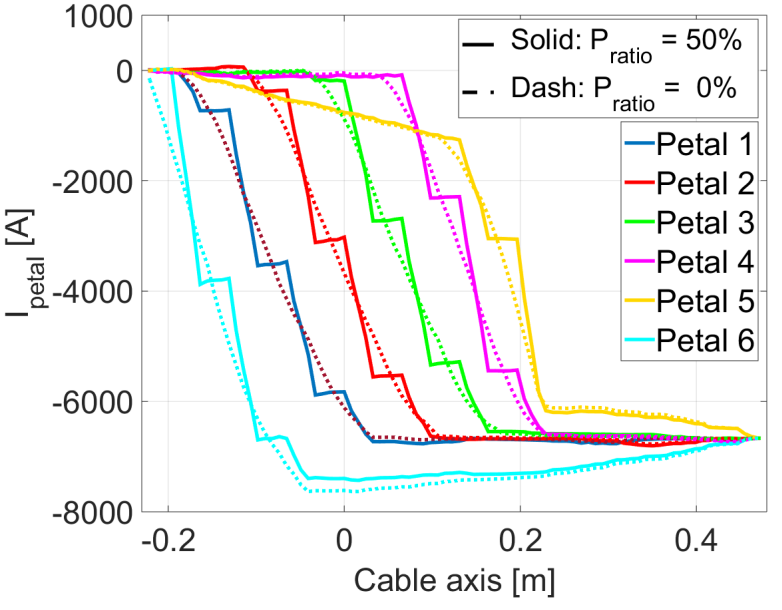


Figure 5.14: Distribution of the petal currents along the cable axis of the joints with 0.5 (50%) and zero patch ratios.

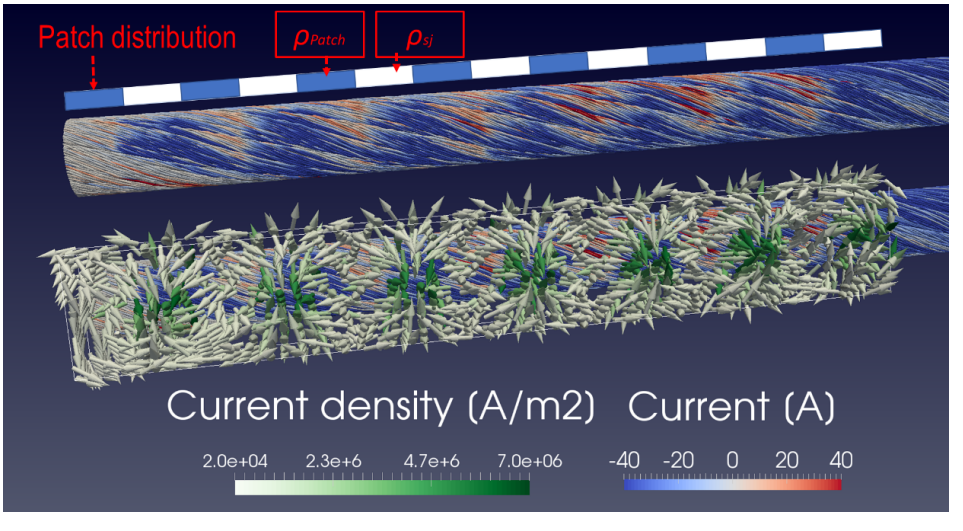


Figure 5.15: Current density in the copper sole and strand currents in cable A along the cable axis of the joint with the non-homogeneous strand to sole resistance, the patch ratio is 0.5 (50%) and the patch configuration is shown at the top.

patches on the current redistribution and stability is evaluated by means of examining the current margin of the strands. The current margin is defined as $I_{margin} = \text{Min}(I_c - |I_s|)$ [100]. A negative current margin means the strand current exceeds the critical current. In addition, the number of strands with negative current margin is also distinguished.

In the case of a maximum operating current of 55 kA and 5 T background magnetic field, the evolution of the joint resistance and the current redistribution was calculated by gradually increasing the patch ratio. The patch factor $M$ was set to 15 and as a result there are only three main outlets for the transport current in the cable. The factor $N = 10$, 11, 12, 13 and 14 are corresponding to ratios of 67, 73, 80, 87 and 93%, respectively. For the joints with these five patch ratios, the evolution of the current margin with time is shown in Figure 5.16.

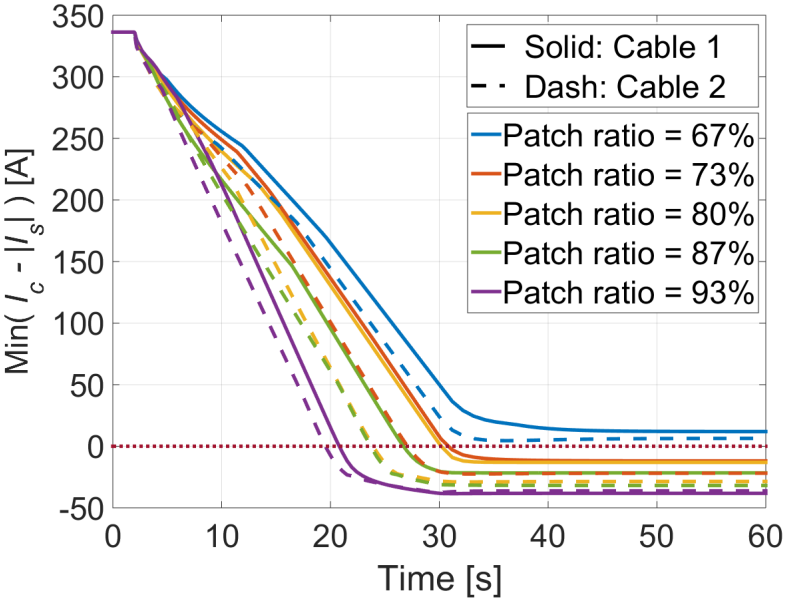


Figure 5.16: Evolution of the minimum current margin versus time of both cables of the joint for different patch ratios.

The time scale here corresponds to the transport current, which after a period of 2 s increases from zero to 55 kA with a ramp rate of 2 kA/s where after it remains constant for 30 s. As the patch ratio increases, an earlier current saturation of the strands is observed. For the case of a patch ratio of 0.93 (93%) , the current saturation occurs at the time instant of about 20 s corresponding to a transport current of 35 kA. Current saturation is observed for all patch ratios except for the smallest patch ratio of 0.67 (67%). A further examination shows that the number of strands that get saturated, is 0, 3, 2, 8, and 17 in cable A and 0, 2, 4, 14 and 19 in cable B, respectively, for increasing patch ratios. Increasing patch ratios degrade the stability of the joint, a conservative estimation is that a patch ratio up to about 0.7 (70%) can be tolerated.

## 5.4 Analysis and validation

A non-homogeneous contact resistance between either copper sole and shim, or strands and sole, both affect significantly the current distribution and power dissipation. However, for any specific configuration, the joint resistance seems independent of the varying input current or background magnetic field, if neglecting the effect of magneto-resistance on the copper sole. However, the magneto-resistance contribution is much smaller than the resistance variation observed in SULTAN measurements.

Thus, to explain the nonlinear *V*-*I* characteristics with the proposed models, one has to assume that the non-homogeneous contact resistance is a function of the current as can be seen in Figure 5.6, Figure 5.7 and Figure 5.12. The most likely explanation is that the electromagnetic force acting on the conductor in the joint boxes is the cause of the changing contact status. Indeed, the transport current $I$ and background magnetic field $B$ as demonstrated in Figure 5.17, result in the electromagnetic force $F = B \times I$ acting on the two cables in opposite direction. The produced separation effect with respect to the joint boxes interface, correlates positively with the applied magnetic field and current, and agrees with the presumed conductive contact mechanism between the cable, sole or shim parts.

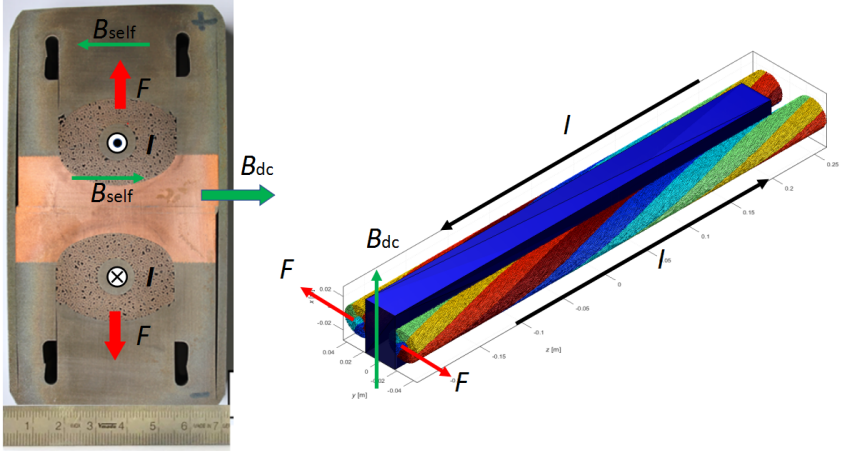


Figure 5.17: Schematic of electromagnetic force $F$ exerted on the SULTAN joint sample, with transport current $I$ and background magnetic field $B_{dc}$.

This hypothesis is confirmed by observing the effect of load cycles on the joint's resistance. It can be seen in Figure 5.18 that after the 1000 bipolar cycles at 6 T/$\pm$27.5 kA, the joint resistance measured at 40 kA has irreversibly increased by some 15% to 18% at 0 and 5 T, and by 35% at 3 T.

During the measurements of the pre-qualification PFJEU3 joint sample [175] built by another supplier, a similar nonlinear *V*-*I* characteristic was observed. Although the resistance variation was smaller compared to the PFJEU2 sample and the maximum joint resistance remained within the accepted value of 5 n$\Omega$ after load cycles. Considering the direction of the electromagnetic force would be changed if changing one direction of

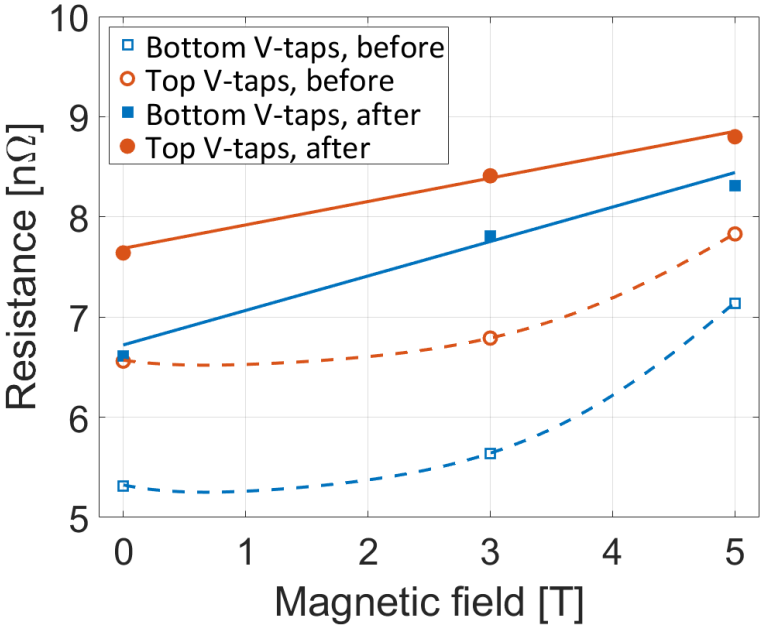


Figure 5.18: Joint resistance versus background magnetic field at 40 kA transport current, before and after load cycling, for the Top and Bottom voltage taps.

the transport current or magnetic field, $-F = -B \times I$, then the joint resistances were measured with opposite transport currents so as to obtain opposite electromagnetic force. The results with different transport current and magnetic field combinations are shown in Figure 5.19.

An opposite resistance evolution is observed, which corresponds to the release and increase of compression respectively, and validates the effect of the electromagnetic force on the nonlinear *V-I* characteristic.

As seen in Figure 5.1, the AgSn solder and PbSn solder are used in the cable-sole and sole-shim interfaces, respectively. A post-mortem examination of sample PFJEU2 was performed at CERN in order to check the soldering conditions [171], [181], [185]. The thickness of the AgSn layer is approximately between 200 and 450 µm. This is obtained from microscope (SEM) images with 60 times original magnification and shows that the solder layer is in good connecting conditions. While for the PbSn solder layer, a defective soldering condition is observed with 100 times magnification. A further energy-dispersive X-ray spectroscopy (EDX) analysis has been performed on the SEM images to detect the probable discontinuity along the interface. A clear gap is observed between the copper shim and PbSn solder, as shown in Figure 5.20.

The separation at this unfavourable solder connection under changing electromagnetic force is the most probable reason for the nonlinear *V-I* characteristic. This observation is in line with the JackPot-AC/DC prediction obtained from the non-homogeneous contact resistance models, a widely spread defective connection between the sole and shim.

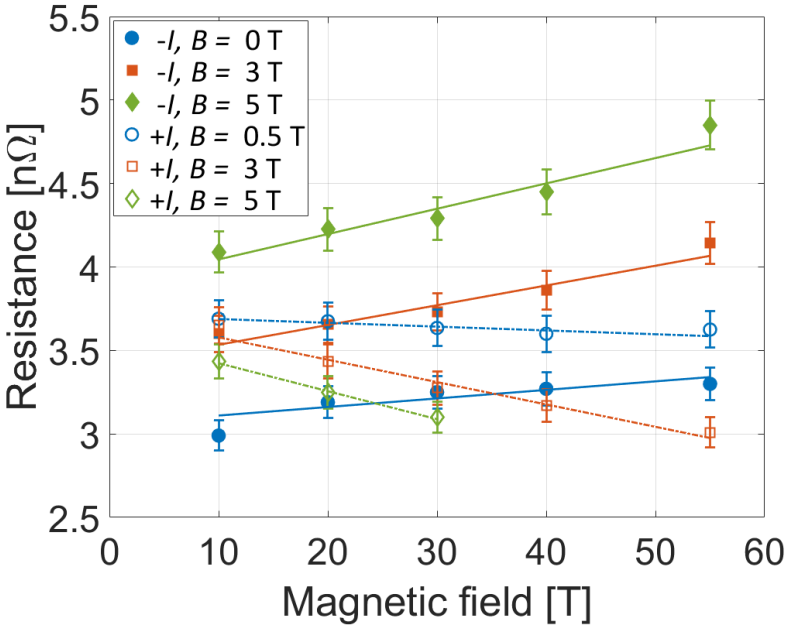


Figure 5.19: Joint resistance of PF5 joint sample PFJEU3 measured in SULTAN, for different background magnetic fields and positive ($+I$) and negative ($-I$) transport current, with the Bottom voltage taps before loading cycles.

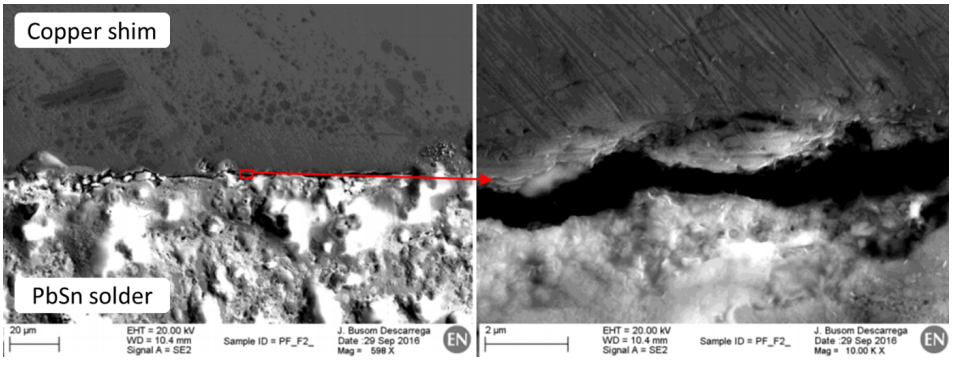


Figure 5.20: Energy-dispersive X-ray spectroscopy (EDX) analysis performed on the SEM images of the PFJEU2 joint, (left) gap observed at the interface between copper sole and shim, (right) zoom of one specific area.

The post-mortem examination performed on the PFJEU3 sample did not reveal any significantly defects at the soldered interface between the boxes and shim, and the cable void fraction in the middle part of the joint was as low as in the PFJEU2 sample. However, the void fraction appeared to be larger in the conductors towards the box ends due to a larger twist pitch, which can be responsible for the sensitivity of the joint resistance to the electro-magnetic load. It should be noted however, that after the trials with the PFJEU2 and PFJEU3 samples and consequent improvement of the technological process, the next qualification and production samples did not reveal any sensitivity to the electro-magnetic load [45].

## 5.5 Conclusion

The joint resistance measurements of the ITER pre-qualification PF joint samples (PFJEU2 and PFJEU3) were performed in the SULTAN facility and unexpected nonlinear voltage-current characteristics were observed during the DC tests. The resistance variation reaches $3.5$ n$\Omega$ as the transport current and background magnetic field increase.

The simulations based on the JackPot-AC/DC model show that the joint resistance is expected to be nearly independent from transport current and background magnetic field. Only a small effect from the magneto-resistance of the copper sole and shim is anticipated. The model was updated to emphasize the possible electrical features related to the interfaces between the components of cable, sole and shim.

The simulations reveal that the strong nonlinear voltage-current characteristic is most likely caused by a defective connection between copper sole and shim, affected by the electromagnetic force. The weakly connected parts generate a separating or compressing force under a varying electromagnetic force from transport current or background magnetic field, causing a varying resistance correspondingly.

Further on a detailed analysis of the local power dissipation and current distribution in the joint and its strands is presented, allowing a quantitative assessment of the joint stability in AC operating conditions.

The model outcome has been validated by an experiment on a similar sample PFJEU3 and a post-mortem examination of the PFJEU2 sample.

# Chapter 6

# Electro-magnetic and thermal performance of PF type joints with masks included

The content of this chapter is mainly based on the following publication:

- J Huang, T Bagni, Y Ilyin, A Nijhuis, ”Pulsed Field Stability and AC Loss of ITER PF Joints by Detailed Quantitative Modeling”, *IEEE Trans. Appl. Supercond.* 33 4201711 (2023) (11pp) https://doi.org/10.1109/TASC.2023.3299590.

## 6.1 Introduction

The advantage of the tokamak among other machine types is highly dependent on the strong magnetic confinement of the burning plasma. For ITER and other tokamaks, all coil systems except TF coils, are operating in pulsed mode. Particularly, the plasma burning scenarios are substantially defined in terms of nominal currents in the PF coils [186].

For PF coils in pulsed mode, the currents vary rapidly thereby introducing relatively high AC loss in the PF joints including coupling-, eddy current- and hysteresis losses, by which the coupling current contributes the most [187]. The distribution of the coupling and transport currents in the conductors can be highly non-uniform [68], [188]. It is driven by the resistance variations in the strand contacts at the joints and the inductive coupling variations between strands along the cable [19].

The current non-uniformity is not a problem in itself, but in certain fast pulsed coils, it can cause critical current degradation at typical ITER joint resistance levels [172], [189]. Furthermore, the ITER PF conductors comprise NbTi strands, which are characterized by a relatively low-temperature margin and high $'n'$ value [19], [32]. For the large NbTi CICCs operating at high current, the take-off voltage is relatively low due to the large magnetic field gradient caused by the self-field contribution. Therefore, in more critical operating regions, local quenches can easily occur before sufficient inter-strand current redistribution can occur and without a measurable resistive development [88].

Consequently, the pulsed magnetic field stability of the PF joint is affected by a combined effect of AC loss, current non-uniformity and properties of the NbTi material.

A method to reduce the current non-uniformity was studied by applying high resistive polyimide layers referred to as masks [166], [184], meant to block the petal current paths in which high coupling losses are introduced. The geometrical configuration of petal twist pitch (last cabling stage of CICCs) and copper sole contacts leads to specific high-current coupling loops that, however, can be influenced by locally blocking the current [34]. The details are explained further on. The effect of masks on the current distribution, power dissipation and thermal behavior is evaluated quantitatively with the JackPot-AC/DC code.

## 6.2 Model description and boundary conditions

A schematic view of a shaking-hands type of lap joint of a PF2 type conductor [34] as implemented in the JackPot model is shown in Figure 6.1, in cross sectional and side views. The geometric specifications as well as the resistivity parameters in unit of $\mu\Omega m^2$ [68], are summarized in Table 6.1 [98], [184], and the properties of the PF2 cable are listed in Table 1.5.

According to the dimensional configurations of cable and copper sole, the maximum angle between two cable-sole contacting edges, referred to as cable-sole-edge angle $\theta$ and indicated in Figure 6.1, is $119.5^\circ$. This is practically equal to the angle of a sector comprising two of the total six petals: $(2/6) \times 360^\circ = 120^\circ$. Considering the random rotating layout of the conductors in the actual joint assembly, the relation between the two angles implies that two or three petals are in direct contact with the sole at both ends, through which large current loops can exist across two cables and copper sole. The ovality of the actual conductor cross-section, as seen in the left plot of Figure 6.1, mainly concerns

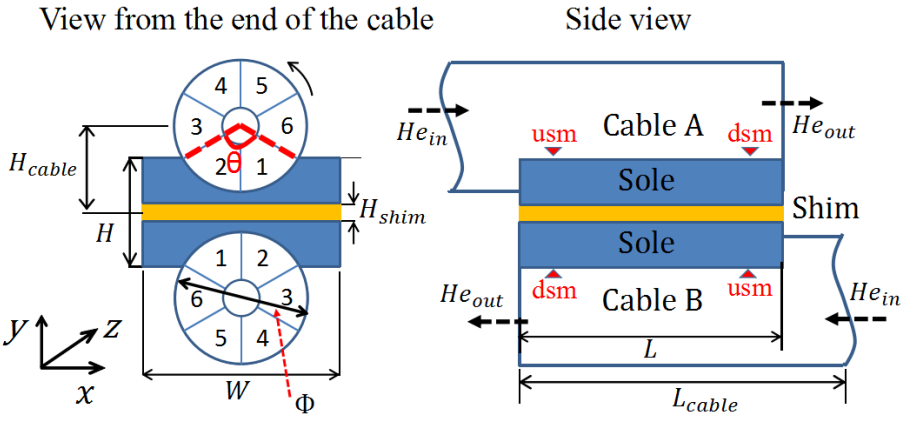


Figure 6.1: Schematic of the joint represented in the JackPot-AC/DC model. The positions of the masks, upstream mask (usm) and downstream (dsm), are indicated in the side view.

Table 6.1: Geometrical and electrical parameters of ITER PF2 coil joint.

| Parameter | Value |
|---|---|
| Cable diameter Φ [mm] | 35.3 |
| Cable length $L_{cable}$ [mm] | 750 |
| Sole length $L$ [mm] | 450 |
| Sole width $W$ [mm] | 64 |
| Sole height $H$ [mm] | 35 |
| Cable offset to midplane $H_{cable}$ [mm] | 26.4 |
| Cable-sole edge angle $\theta$ [°] | 119.5 |
| Shim thickness $H_{shim}$ [mm] | 0 |
| Sole resistivity with RRR = 100, at 4.5 K, $\rho_{sole}$ [nΩm] | 0.18 |
| Shim resistivity with RRR = 100, at 4.5 K, $\rho_{sole}$ [nΩm] | 0.18 |
| Inter-strand resistivity $\rho_{ss}$ [μΩm$^2$] | $1.05 \times 10^{-5}$ |
| Inter-petal resistivity $\rho_{ip}$ [μΩm$^2$] | $4.20 \times 10^{-5}$ |
| Strand to sole resistivity $\rho_{sj}$ [μΩm$^2$] | $5.00 \times 10^{-5}$ |
| Mask resistivity $\rho_{mask}$ [μΩm$^2$] | $4.20 \times 10^{-3}$ |

deformation in vertical direction. As such is the displacement between cable and copper sole contacting edge not significant, and is it allowed to simply use the ideal circular conductor to demonstrate the functionality of masks.

A multi-stage twisted PF2 cable sample and the probable contact configurations are shown in Figure 6.2, where the stripes represent the footprints of the petals on the copper sole.

Due to the same lengths of the cables' last stage (petal) twist pitch and the copper sole length L, the total contact areas between each petal and copper sole are about the same. In order to reduce the induced coupling current and improve the stability of the joint, high

resistive masks (black layers in Figure 6.2) are wrapped around one end of the double contacting petals, thereby heavily insulating them electrically from the copper sole. The blue areas in Figure 6.2 indicate where the petal masks are applied.

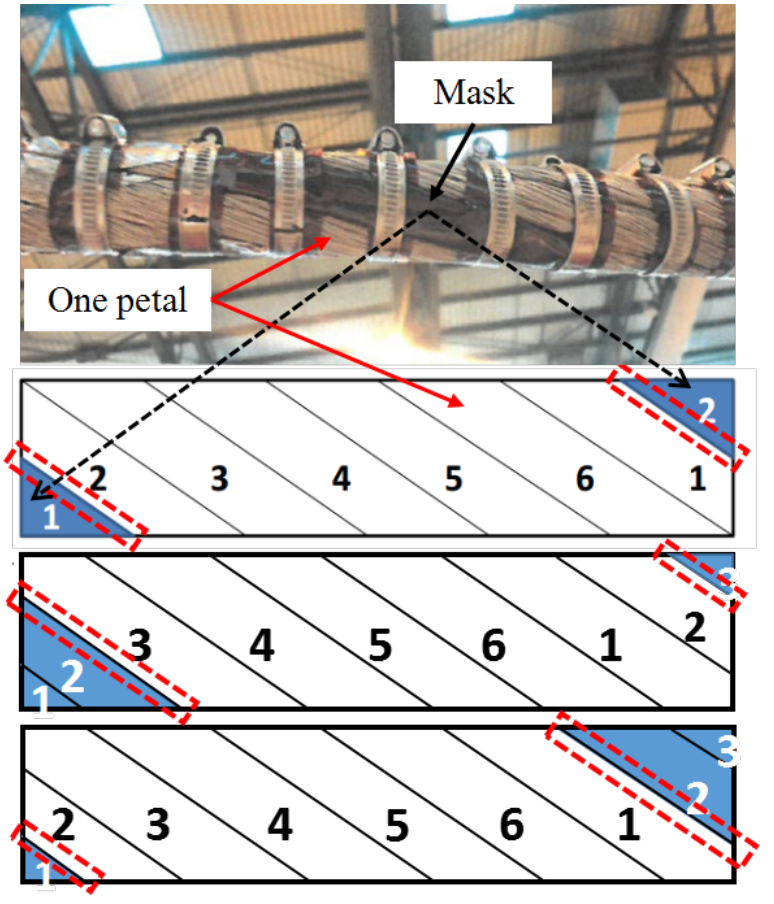


Figure 6.2: Top: conductor of PF joint with a mask (black polyimide layer) wrapped around a petal. Bottom: footprints of the petals on the copper sole of joints with different contact configurations. Two or three petals wrapped with masks, where the dark areas show where the petal masks are applied. The red rectangles specify the inter-petal interfaces where the high coupling current losses are induced.

In order to evaluate the effect of masks on the joint performance, joints with same layout configurations but different mask arrangements, with or without masks, were simulated using the JackPot-AC/DC code. In the study, five joint configurations, corresponding from joint I to V, were simulated and compared, see Table 6.2. For the joint layout with three double contacting petals, there are two optional mask configurations, like blocking petal 1 at one end, and petal 2 and 3 at the other end; or the opposite arrangement as illustrated in the lower plots of Figure 6.2.

Table 6.2: Rotating layouts and mask configurations of seven joints.

| joint type | Cable type | Rotating layout | Mask configuration | |
|---|---|---|---|---|
| | | Double contacting petals | usm | dsm |
| Joint I | Cable A | 2 petals ($\#1, 2$) | none | none |
| | Cable B | 2 petals ($\#5, 6$) | none | none |
| Joint II | Cable A | 2 petals ($\#1, 2$) | $\#1$ | $\#2$ |
| | Cable B | 2 petals ($\#5, 6$) | $\#5$ | $\#6$ |
| Joint III | Cable A | 2 petals ($\#1, 2, 3$) | none | none |
| | Cable B | 2 petals ($\#4, 5, 6$) | none | none |
| Joint IV | Cable A | 2 petals ($\#1, 2, 3$) | $\#1, 2$ | $\#3$ |
| | Cable B | 2 petals ($\#4, 5, 6$) | $\#4, 5$ | $\#6$ |
| Joint V | Cable A | 2 petals ($\#1, 2, 3$) | $\#1$ | $\#2, 3$ |
| | Cable B | 2 petals ($\#4, 5, 6$) | $\#4$ | $\#5, 6$ |
| Joint VI | Cable A | 2 petals ($\#1, 2$) | $\#1$ | none |
| | Cable B | 2 petals ($\#5, 6$) | none | $\#6$ |
| Joint VII | Cable A | 2 petals ($\#1, 2$) | none | $\#2$ |
| | Cable B | 2 petals ($\#5, 6$) | $\#5$ | none |

The cable rotating layouts and mask configurations are specified in Table 6.2. The rotating layout is characterized by the amount (2 or 3 petals) and the serial number (#1 to 6) of the specific petals that have double contacts with the copper sole. The mask configurations are characterized according to their positions with respect to the helium flow direction, named as "downstream mask (dsm)" and "upstream mask (usm)", respectively as indicated in Figure 6.1. For the actual masked joints, all petals with double contacts must be blocked. However, for analysis consistency purpose, two additional joints with only one petal mask in each cable were tested as well, indicated as joints VI and VII in Table 6.2.

In the pulsed operating mode, the PF joint is exposed to a radial magnetic field component in the x direction and an axial magnetic field component in the y direction as indicated in Figure 6.1. The maximum magnetic field ramp rate $\mathrm{d}B/\mathrm{d}t$ is $+0.50$ and $-0.78$ $\mathrm{T/s}$, respectively [190]. The largest current loops are normally induced between both conductors when the magnetic field orients in x direction while the peak value in y direction lasts only for a fraction of a second. Thus, the x-field component is considered more critical for the joint stability and is simulated in the model, as illustrated in Figure 6.3. The transport current in the simulations is zero.

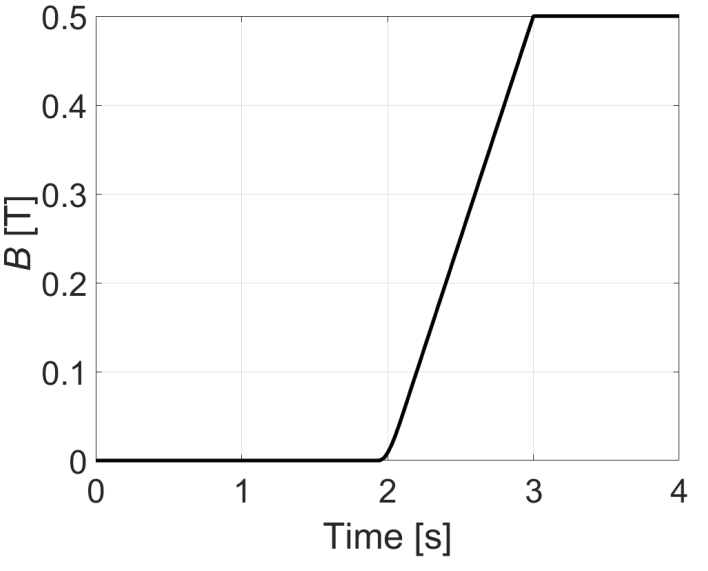


Figure 6.3: Magnetic field versus time applied in the Poloidal Field coil joint performance assessment.

## 6.3 Simulation result

### 6.3.1 Current redistribution

In response to the magnetic field ramp at the time instant $t = 3.0$ s, which corresponds to the maximum magnetic field, the evolution of the strand currents is obtained. Furthermore, the petal currents as sums of all the individual strand currents in a petal, are calculated to show the current distribution. For the five joints (joints I to V) as specified in Table 6.2, the current distribution of six petals of cable A are shown in Figure 6.4.

It is found that for joints without masks, higher currents are induced in the petals with contact to the copper sole at both ends, like petals 1 and 2 of joint I, and petal 1, 2 and 3 of joint III, while for the other joints with masks applied, the high currents induced in these particular petals are decreased gradually. The current induced in the most loaded petals is about 30 kA in joint I without masks, it decreases to 17 kA in joint II with masks. The value is even bigger in joint III and up to 37 kA but decreased to 20 kA in joints IV and V. Since the joint stability is highly dependent on the energy stored in the induced current loops, an approximate current reducing factor of 2 means a factor 4 of the stored energy. The stored energy in the joints with masks satisfies the criteria given by the enthalpy of helium available in the joint volume and the adopted 2 K temperature margin [184].

However, it is also observed that, in the vicinity of the upstream mask in cable A (around $-0.22$ m), a high current peak is produced in some particular petals, like petal 2 of joint II, petal 3 of joint IV and petal 2 of joint V. For joints I and II, a more detailed analysis of the impact of masks on the current redistribution was performed at strand level

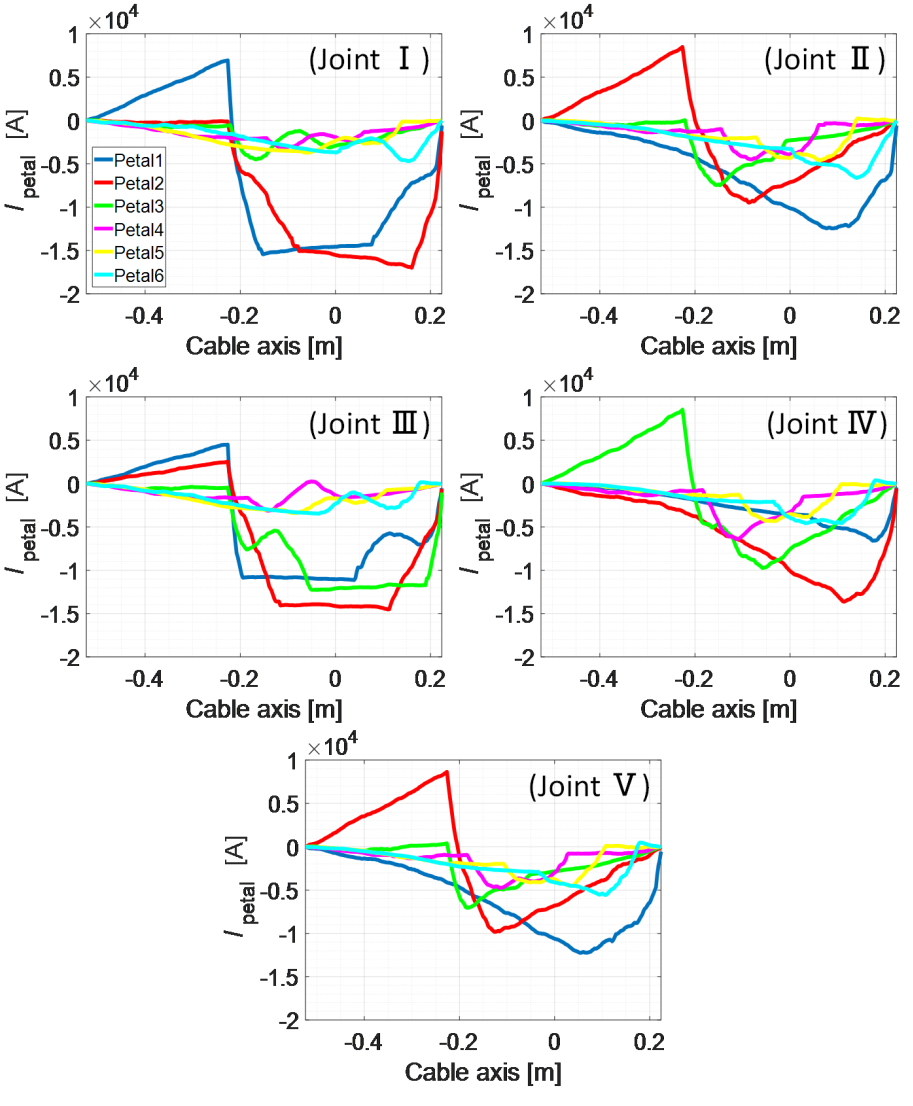


Figure 6.4: Petal currents versus position along cable axis, showing the distribution of currents in five joints with different rotating layouts and mask configurations, joints I and III are without masks.

and shown in Figure 6.5. Here specific petals #1, 2 and neighboring petal 6 are shown, while the other three petals are neglected due to their relatively low currents. Large current loops are induced in petals 1 and 2 of joint I without masks. Two strands in petal 1 even carry currents up to 1200 A, which is way higher than the nominal critical current of 339 A [34]. For joint II with masks, the positions of the upstream mask on petal 1 and the downstream mask on petal 2 are marked by orange boxes. The arrows on the right side indicate the current flow between the petals. A significant current redistribution is

represented by currents that are forced into neighboring petals since they are hindered by the downstream masks.

The current distribution reveals that the current non-uniformity caused by the large current loops is relieved, suggesting thereby a benefit for joint stability. However, some high over-currents are still observed in two strands in the vicinity of the downstream mask. This might be related to current bypasses between petals, also indicating the importance of careful elaborating the positions of the masks.

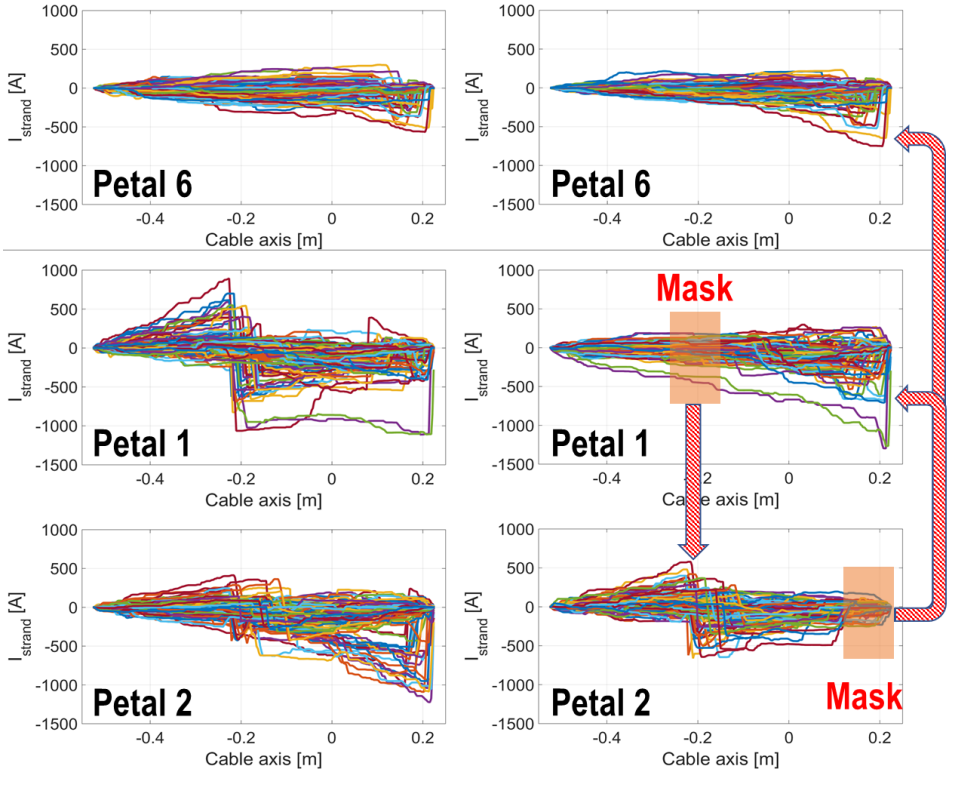


Figure 6.5: Strand currents versus position in the cables, showing the current distribution of strands belonging to three neighboring petals (6, 1 and 2), of joint I without mask (left) and joint II with masks (right). The position where masks are applied are marked by the orange rectangular regions and the arrows represent the current redistribution to the neighboring petals.

The effect of the mask on the petal current redistribution is also demonstrated with a 3D visualization, as shown in Figure 6.6. It shows the spatial location of the individual petals in cable A and the current distribution in joints I and II, respectively. The three plots are viewed from the same angle and emphasize the cable end where the downstream mask is located. The outline of the copper sole is shown as a reference in order to visualize the interfacing cable-sole perimeter directly. Although some strands are carrying currents that reach nearly 1200 A as shown in Figure 6.5, here the display limit of the strand current is set to 600 A to better distinguish the majority of strand currents. The negative currents (blue

wires) in the middle and right plots represent currents that are flowing backwards with respect to the z-direction, while the positive current (red wires) symbolize the opposite direction. When the mask is implemented in the triangular yellow region, the relatively high currents in petal 2 are significantly reduced.

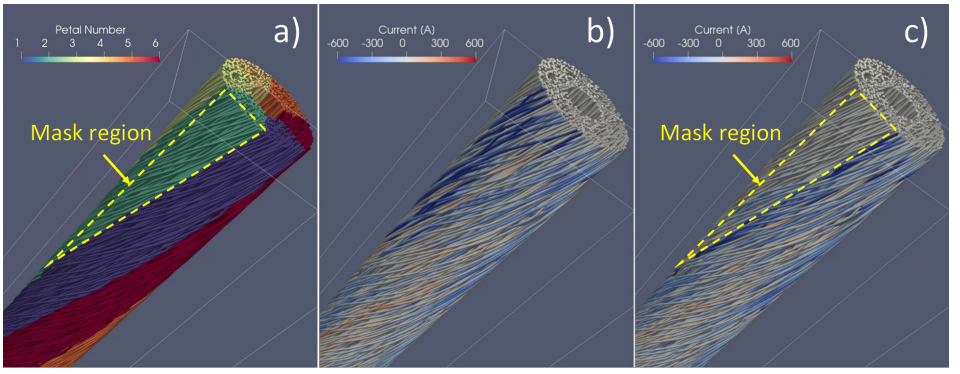


Figure 6.6: 3D visualization of the effect of the mask on the current distribution. Left shows a schematic of the strands in the six petals of cable A in joints I or II. The yellow triangle represents the area of the mask on petal 2. The plot in the middle shows the current distribution in cable A of joint I without mask and at right the current distribution in cable A of joint II with a mask applied.

Besides the strand's currents, the current redistribution in the copper sole is also investigated and a cross-sectional view is shown in Figure 6.7.

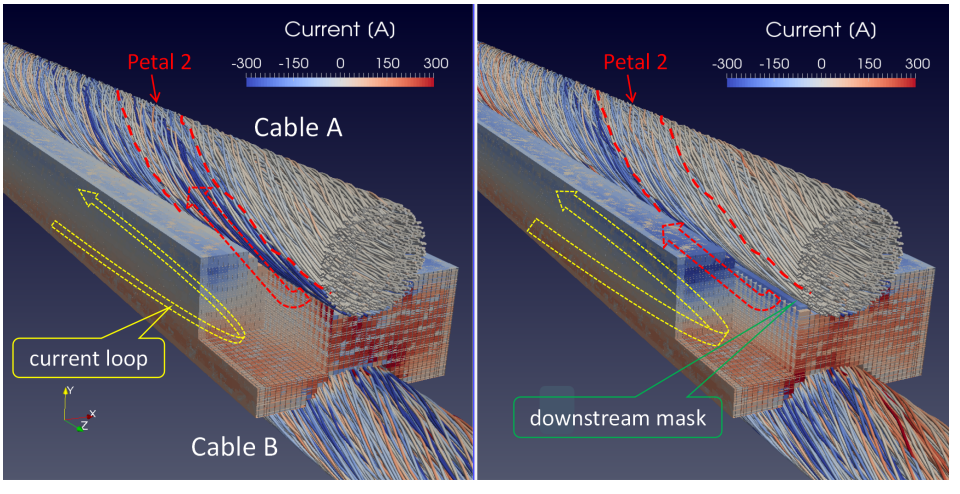


Figure 6.7: 3D visualization of the effect of a mask on the current distribution. Left shows the strands in the six petals of cable A in joints I or II, the yellow triangle represents the area of the mask on petal 2. The plot in the middle shows the current distribution in cable A of joint I without mask and at right the current distribution in cable A of joint II with a mask applied.

The left plot represents joint I without masks, while the right plot shows joint II with

masks. The downstream mask is applied on petal 2 of cable A at the front view end. The different colors (blue and red) in the upper and lower side of the copper sole represent opposite flows of the induced current loops, as indicated by the turning arrows. It is observed that the high-resistivity mask blocks the high currents induced in petal 2 effectively. However, the copper sole provides a parallel bypassing current path for the blocked currents, especially nearby the implemented mask (the petal current is indicated by red arrows in both plots). Except for the part of the blocked currents re-entering into the adjacent petals, the others remain in the copper sole and are superimposed on the circulating current along the sides, as illustrated by the shades of color and the yellow arrows.

### 6.3.2 Current margin

Due to the severe current non-uniformity, strands carrying high current may exceed the critical value in the strands, first triggering more redistribution but then increasing instable behavior manifested further as local strand and sub-bundle quenches. The effect is quantitatively evaluated by means of current margin, which is defined as the local critical current of a strand $I_c$ minus the transport current in the strand $I_s$. The minimum current margin of a conductor is the minimum value among all the strands, $I_{margin} = \mathrm{Min}(I_c - |I_s|)$ [24]. For joints I to V, the minimum current margin of both cables is shown in Figure 6.8, corresponding to the inlet helium temperature of 5.0 K, which normally corresponds to the accumulated value after several consequent plasma pulses.

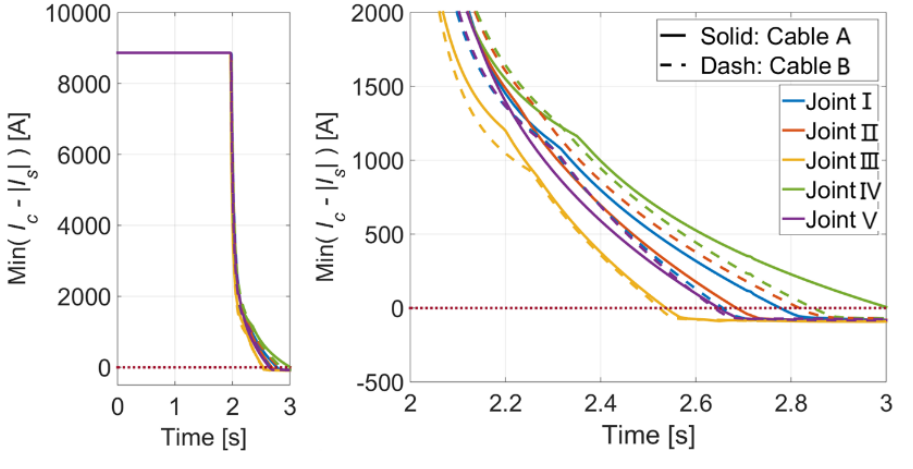


Figure 6.8: Minimum current margin of both cables versus time for the five joints specified in Table 6.2 with different configurations.

The negative value indicates that at least one strand with current exceeds the critical value. Joint III without masks exhibits the smallest current margin. Its current exceeds the critical current at a time instant just around 2.5 s, which corresponds to a relatively small external magnetic field, as known in Figure 6.3. After the implementation of masks, significant improvements in current margin are observed in joints IV and V, especially for cable A of joint IV, of which the maximum current is always below the critical value.

However, in joints I and II having two double contacting petals, the influence on the current margin is quite small.

The minimum current margin determines the first time when the critical current is exceeded. In the meantime, the number of such overloaded strands is calculated and shown in Figure 6.9, with respect to different time intervals.

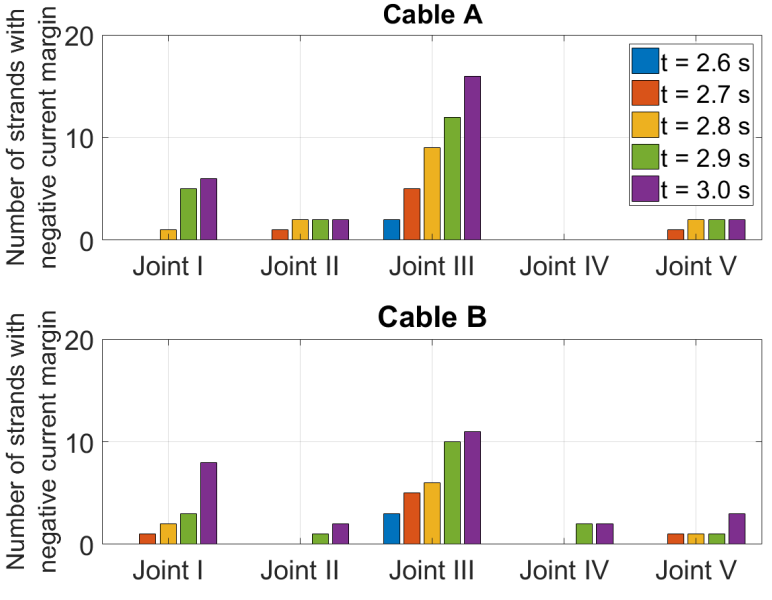


Figure 6.9: Number of strands with negative current margin in the five joints, at different time instants.

The comparison shows that for the two joints without masks, a larger number of strands exceed their critical current and occurring at an earlier instant of time (lower external magnetic field). Like for joint III at the time instant $t = 3.0\,\mathrm{s}$, there are 16 and 11 strands carrying overload currents in cable A and cable B, respectively. Clearly the implementation of masks decreases the number of overloaded strands and reduces the risk of developing an avalanche effect leading to a quench due to current re-distribution from the saturated strands. The best performance is observed in joint IV, in which only 2 strands exceed their critical current.

### 6.3.3 Power distribution

After having studied the influence of current redistribution on coupling and eddy current losses, the power dissipation of joints with different configurations is also evaluated, and the results are shown in Figure 6.10.

Besides the five joints I to V, the two joints VI and VII, which have the same rotating layout as joints I and II, but only one mask, are simulated as well. Further observation

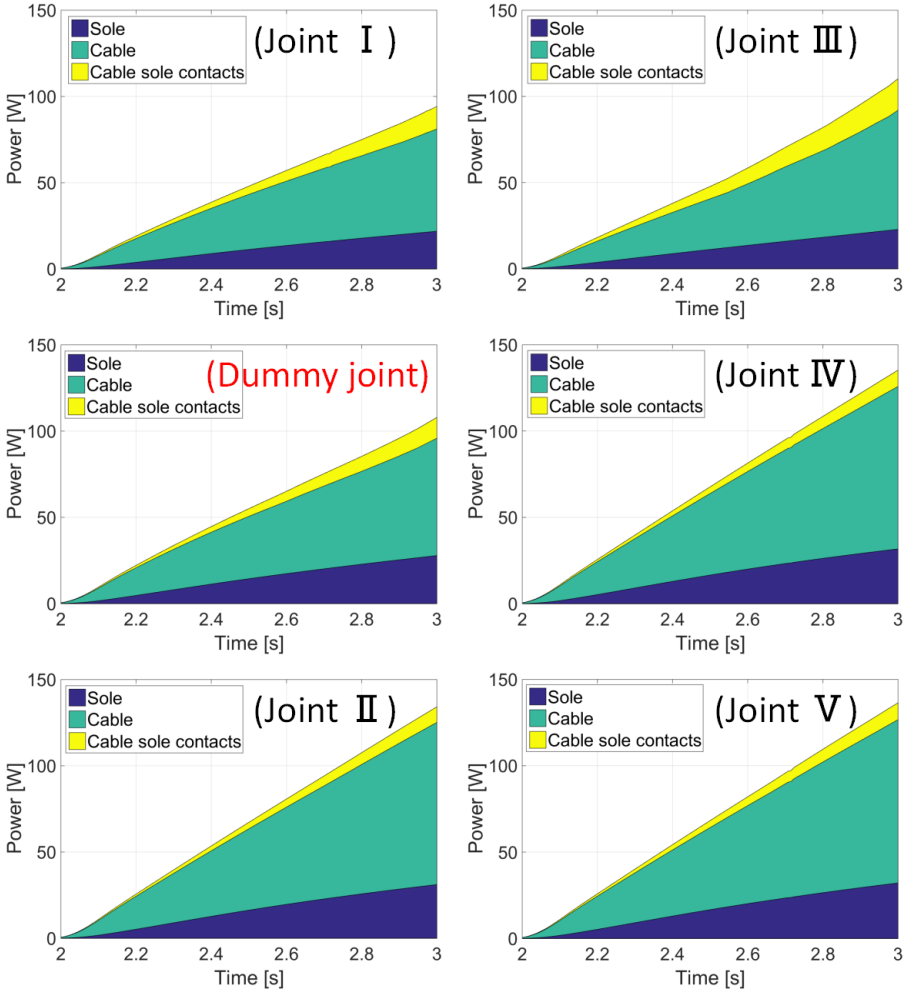


Figure 6.10: Power dissipation versus time in the sole, cables and cable-sole contacts of six joints with different rotating layouts and mask configurations, as specified in Table 6.2.

shows that the power generation of the two additional joints is the same, thus only joint VI is selected and compared here. In the model, the power dissipation of the joint can be divided into different components related to the two cables, copper sole and two cable-sole contact interfaces, of which the coupling current loss in the cables is dominant. It is observed that, no matter what type of rotating layout, the use of masks causes an increase of the total power dissipation, particularly, it seems proportional to the number of masks for the same conductor layout. However, it is also found that for joint II with 2 masks and joints IV and V with 3 masks, the power generations are almost the same.

Besides some increase of power dissipation in the copper sole, which is most likely attributed to the bypassing currents and mainly in the form of eddy current loss, the largest

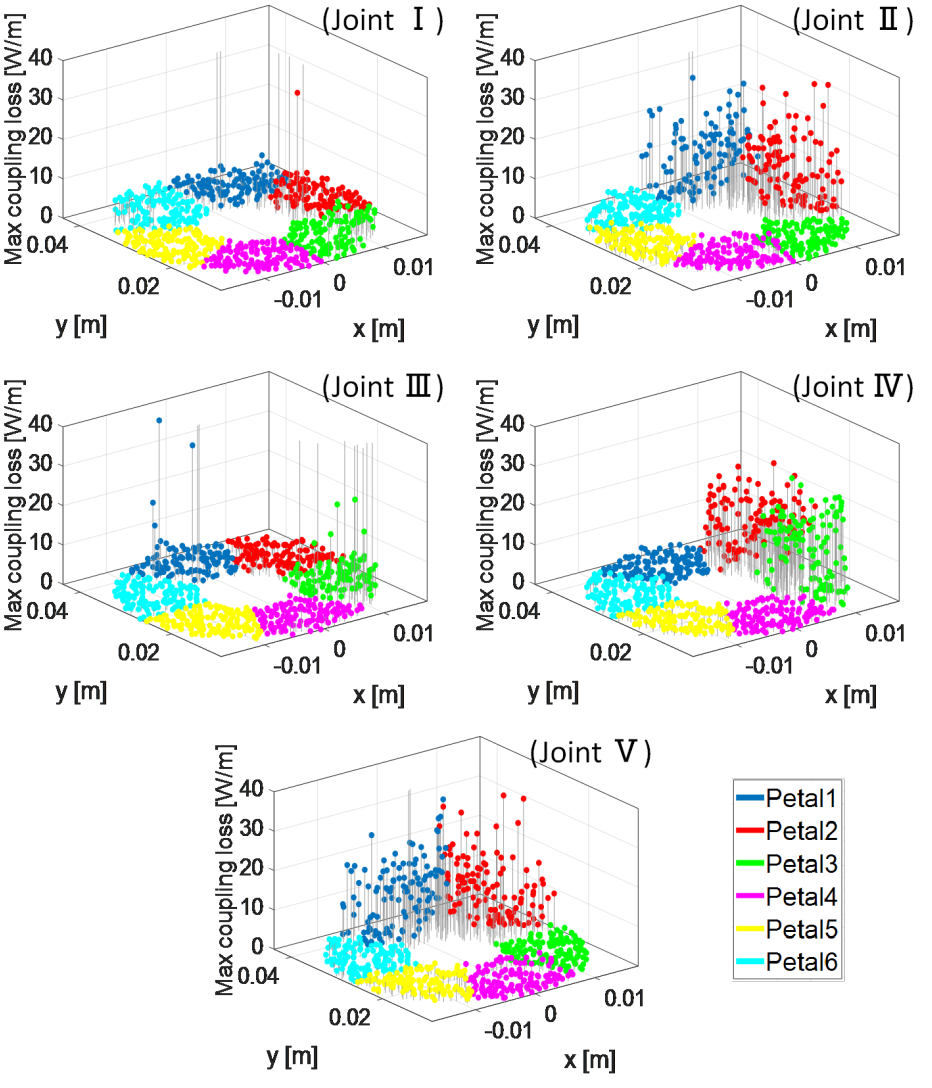


Figure 6.11: Maximum coupling loss in W/m in strands in the cable cross-section (x-y plane) belonging to different petals of the five joints with different configurations, as specified in Table 6.2.

effect of using masks is on the coupling loss induced in the cables. The distribution of the coupling current loss is evaluated by means of computing the maximum power dissipation in each strand. For joints I to V at the time instant of $t = 3.0$ s, the results are shown in Figure 6.11. The height of the stalks represents the strand peak coupling loss. The corresponding petals are indicated with different colors and numbered labels. In order to better distinguish the strand's low magnitude, the coupling loss limit is clipped off at $40$ W$/$m and thus some strands with higher values are not shown completely.

The comparison shows that in joints I and III without masks, the vast majority of strands have relatively low loss. While for the other joints with masks, much more strands exhibit high coupling loss. Furthermore, according to the mask configurations as indicated in Table 6.2, it is found that these high coupling loss strands belong to the two petals with masks applied, which is seen even in joints IV and V where three petals have been implemented with masks.

After confirming the specific petals where the strands with high coupling loss are located, the spatial distribution of the strand maximum coupling loss along the cable axis were determined and shown in Figure 6.12. Due to the performance similarity of joints I and III, the latter is not shown here. The plots exhibit the strands with the coupling loss clipped at 30 W/m.

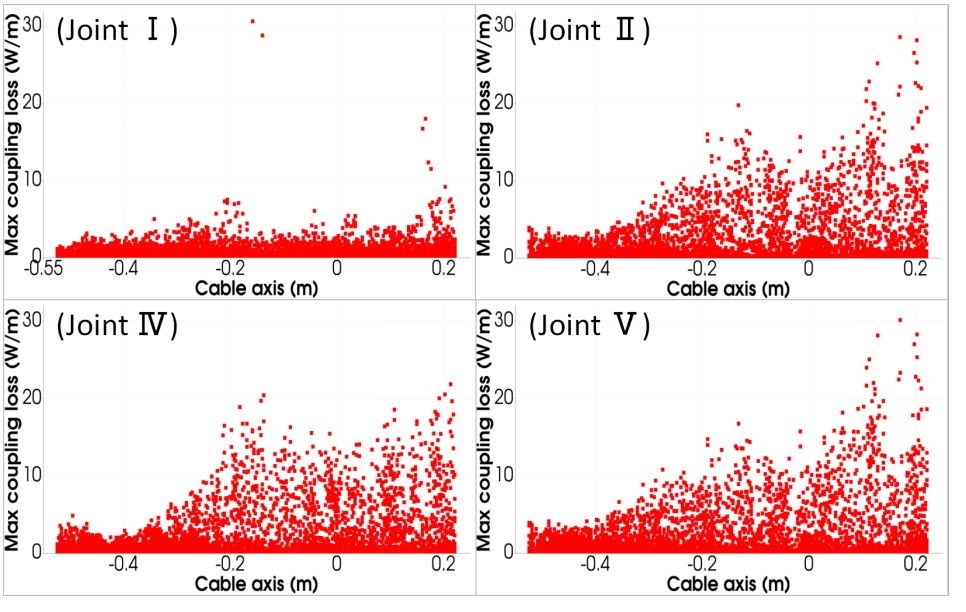


Figure 6.12: Scatter diagram of the coupling loss in W/m in elements of strands in the cable cross-section along the cable axis.

For joint I without masks, only a few strands with high coupling loss are found, located nearby the two ends of the copper sole around -0.225 and 0.225 m, respectively. While for the joints with masks, the highest coupling losses are distributed more uniformly along the whole cable section and not just restricted to the two ends.

A further 3D visualization reveals that the highest coupling loss is generated at the interface between two petals within the joint box region. For joints with different mask configurations, the specific petal-to-petal interfaces are always between the outermost two petals and indicated in Figure 6.2 with red dashed boxes. Note that the lengths of the interfaces of joints I, IV and V are almost the same. This explains the phenomenon observed in Figure 6.11 that joins with different number of masks can have the same power dissipation. Thus, the total loss is not really proportional to the number of masks, but to the length of the petal-to-petal contacting interface.

### 6.3.4 Evolution of temperature

Besides the electromagnetic characteristics like the current distribution and power dissipation, the use of masks also affects the thermal behavior of the joint. In the thermal model, the average temperature of the strand bundles and helium flows in the six petals, as well as the helium flow in the central channel, in total 13 elements, are calculated for of each conductor. The heat exchange between the adjacent petals and the central channel is through the helium, assuming that the helium mass flow in the bundle region of the conductor is $1/3$ of the total mass flow [111], [113]. The main parameters of the thermal model of the PF2 joint are shown in Table 6.3 [110], [112], [191].

Table 6.3: Main parameters in the thermal model of the PF2 joint.

| Parameter | Value |
|---|---|
| Total He mass flow [g/s] | 9.7 |
| He inlet temperature [K] | 5 |
| Heat conductivity of copper @RRR100 [$\mathrm{W/m \cdot K}$] | 800 |
| Heat conductivity of NbTi [$\mathrm{W/m \cdot K}$] | 0.135 |
| Heat conductivity of helium [$\mathrm{W/m \cdot K}$] | 0.02 |
| Petal-He in petal heat transfer coefficient [$\mathrm{W/m^2 \cdot K}$] | 500 |
| Sole-He in petal heat transfer coefficient [$\mathrm{W/m^2 \cdot K}$] | 642 |
| Sole-petal strands in petal heat transfer coefficient [$\mathrm{W/m^2 \cdot K}$] | 10 |
| Petal-petal heat transfer coefficient [$\mathrm{W/m^2 \cdot K}$] | 125 |
| Sole-sole halves heat transfer coefficient [$\mathrm{W/m^2 \cdot K}$] | 46,000 |

For joints I to V at the time instant $t = 3.0$ s, the temperature evolution of the strand bundle and helium in the six petals of cable A are calculated and shown in Figure 6.13, by which the helium flow direction is specified in Figure 6.1. Furthermore, for comparison, the cases with opposite helium flow directions are also evaluated and the results are shown in Figure 6.14.

It is observed that, for all five joints, the heat is mainly accumulated in two petals and enhances the corresponding temperatures, by which the strand bundle temperature is usually higher than the helium temperature in the same petal. The difference indicates the ability of recovery in the case of overheating. For instance, for the two helium flow directions, a relatively high temperature difference of about 1 K is found in petal 3 of joint III.

The two specific petals are the ones with high coupling losses as seen in Figure 6.11. Particularly, for joint III with three petals having double contact, higher heat is accumulated in petal 1 and 3 compared to petal 2. The reason might be related to the layout symmetry as illustrated in Figure 6.2, where the two contact areas of petal 2 are almost the same and behave symmetrically when compared to petal 1 and 3. Therefore, the current and heat exchange in petal 2 are relatively uniform and mild.

Furthermore, it is concluded that the application of masks causes a reduction in temperature peaks despite the heat generation is higher in two petals as explained in section 6.3.3. For joint III without masks, two temperature peaks are found at the copper sole ends and the highest temperature reaches nearly 7.2 K. After application of the masks, the peak

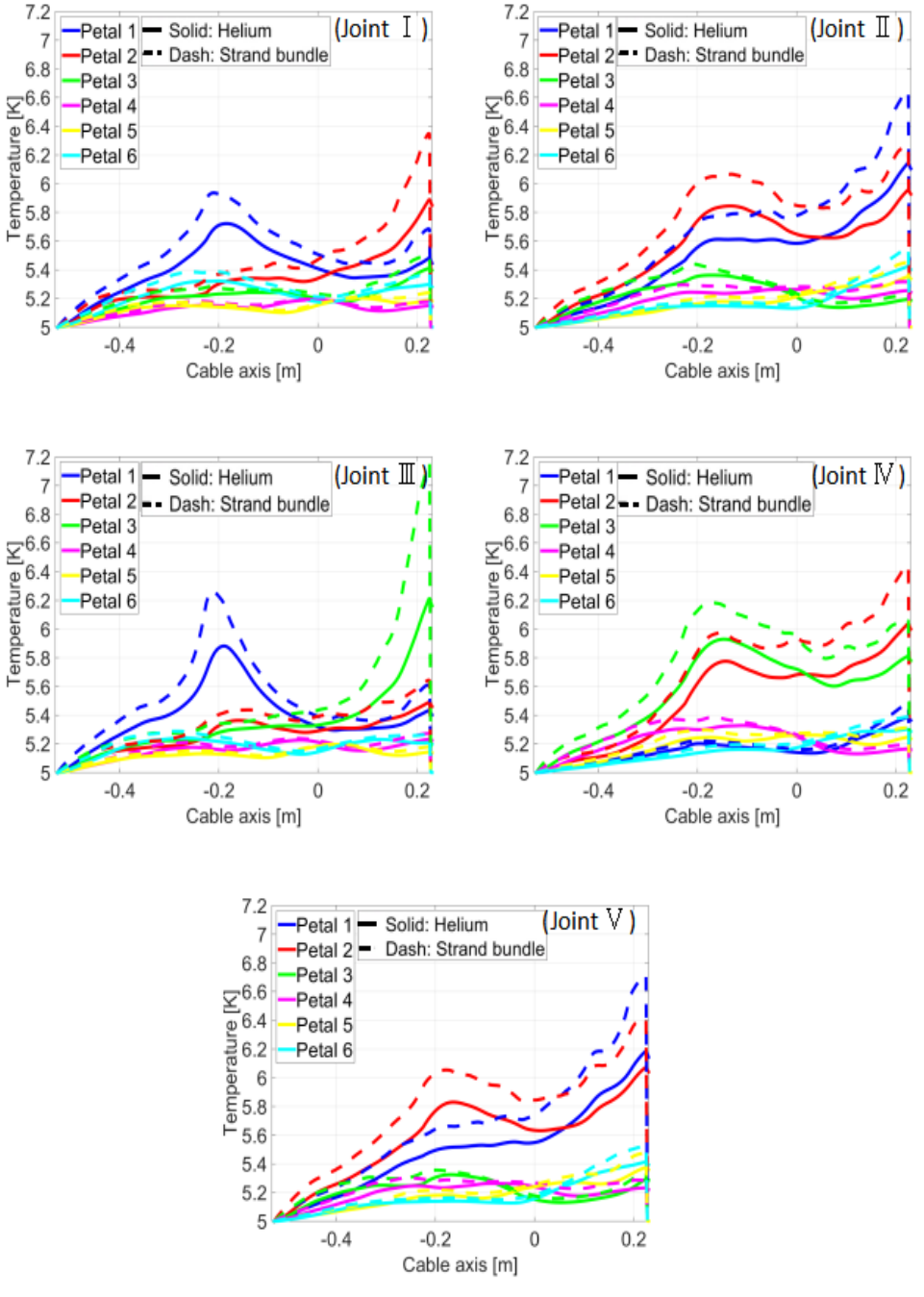


Figure 6.13: Temperature versus position along the cable axis of the strand bundle and helium in the six petals of cable A, for five joints with different configurations, with helium flowing from left to right.

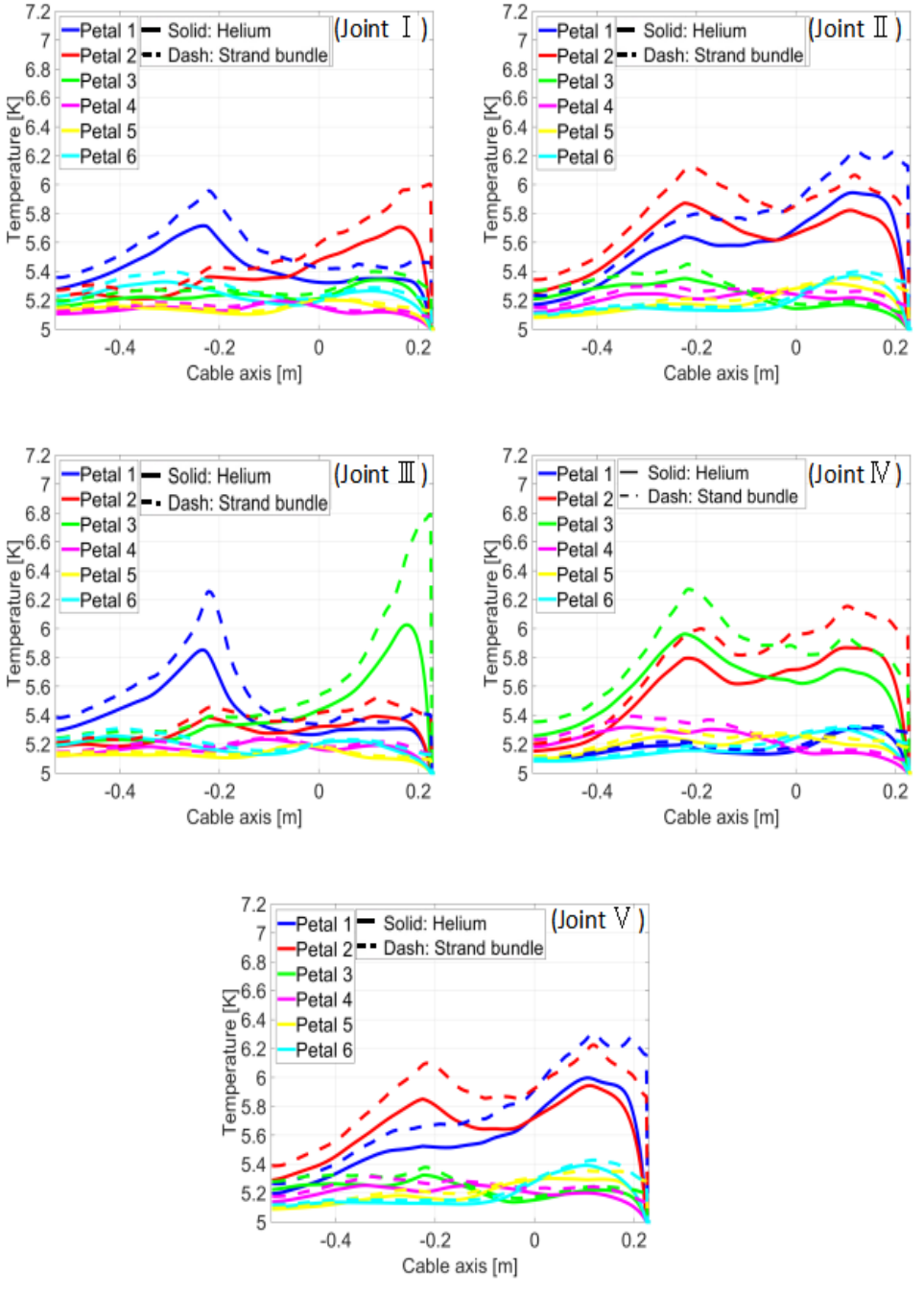


Figure 6.14: Temperature versus position along the cable axis of the strand bundle and helium in the six petals of cable A, for five joints with different configurations, with helium flowing from right to left.

temperature decreases remarkably by 0.5 to 0.8 K. This can be explained by the fact that the local coupling loss spreads along all the petal interface. Thus the power dissipation is dispersed rather than concentrated in a few strands, like in the joints without masks.

## 6.4 Conclusion

For the ITER PF type twin-box lap joints operating in pulsed mode, large coupling currents are normally induced and cause severe current non-uniformity and potentially instability. An adjusted design of ITER PF joints was proposed by introducing highly resistive polyimide layers named masks to interrupt the large induced current loops. The functionality of the masks has been systematically evaluated using the JackPot-AC/DC code, regarding aspects of current distribution, power distribution and temperature evolution.

The implementation of the masks in all considered joint configurations helps to reduce the global induced loop currents in the conductor petals down to allowable values defined by the enthalpy of the helium and desired temperature margin. It also reduces the number of strands with currents approaching or exceeding the critical current, and thereby reduces the risk of a quench in the joint.

Though, the implementation of masks does increase the local heat dissipation in some petals, but makes the heat distribution more uniform along the joint when compared to the concentrated heat in the joints without masks. This has a positive effect on the temperature profiles along the joint box, by smoothing the peaks of temperature in the petals.

Overall, the application of masks to the CICC lap-type joints will improve their stability and the working condition of the final coils. In order to further reduce the induced currents bypassing the masks, it is suggested to increase the inter-petal resistance together with decreasing the RRR of copper.

# Chapter 7

# Stability analysis of the ITER PF joint

The content of this chapter is mainly based on the following publications:

- J Huang, Y Ilyin, H H J ten Kate and A Nijhuis, ”Electro-thermal performance analysis of ITER PF joints in SULTAN and ITER operating conditions” (submitted to *Supercond. Sci. Technol.*);
- J Huang, Y Ilyin, H H J ten Kate and A Nijhuis, ”An effective electro-thermal analysis method for evaluating transient stability of ITER PF joints” (submitted to *Supercond. Sci. Technol.*).

## 7.1 Introduction

In chapter 6, electromagnetic and thermal behavior of the ITER PF joint under ramping up condition of the magnetic field was introduced, emphasizing the effect of using a mask. In the present chapter, a more comprehensive analysis of the joint's stability in steady and transient states is presented. This includes the assessment of the current carrying temperature $T_{cs}$ in stationary current condition, varying magnetic field losses, and minimum quench energy (MQE) in time dependent conditions.

Various experimental and numerical analyses were performed to investigate the joint properties and then relieve the risk of joint instability [172], [182], [192]–[194]. A comprehensive campaign assessing PF joints at SULTAN from 2016 to 2021 exemplifies the commitment to quality, covering pre-qualification, qualification, and production phases. This campaign, through rigorous evaluation of DC, AC, and stability properties, significantly advances the understanding of technological intricacies and ensures product qualification [195].

As introduced in section 1.3, an ideal superconductor becomes resistive if one of the three parameters, current density, temperature or magnetic field, exceeds the boundary of the critical surface $J_c(B,T)$. The temperature at which the operating current is equal to the critical current is named as current sharing temperature $T_{cs}$. Exceeding the $T_{cs}$ by a few mK, NbTi may turn from superconducting to normal state through an avalanche like process, which can lead to a quench of the whole cable [102]. This rather sharp transition can be explained by the steepness of the transition from superconducting to normal state [196]. During the transition, the local electric field associated with the $T_{cs}$ is expressed as [32]

$$E = E_c(\frac{I}{I_c})^n, \tag{7.1}$$

where $E_c$ is defined as the critical electrical field, usually $E_c = 10\,\mu\mathrm{V/m}$, $I_c$ is the critical current [197], $I$ is the strand transport current and $n$ defines the steepness of the voltage-current curve showing the transition, which is mostly about 30 for ITER NbTi CICCs.

The difference between the current sharing temperature and the operating temperature is referred to as the temperature margin $\Delta T$. Above $T_{cs}$, the superconductor develops a normal resistance, which enables a current sharing process and the current flow is associated with Joule heating [196]. The $T_{cs}$ characterizes the stability of a superconductor, and is essential for the performance evaluation [118]. The $T_{cs}$ test first has the background magnetic field set to a value to match the target peak magnetic field in the conductor. Then the current is ramped up to the operational current $I_{op}$, followed by a temperature ramp up.

Besides the stability related to the quasi-stationary current and changing temperature, also time-varying currents and/or magnetic fields generate loss due to the movement of flux lines. When a superconductor carries a stationary current and is simultaneously exposed to varying magnetic field, dynamic resistance occurs and leads to dynamic loss [198], [199]. The varying magnetic field and the corresponding multiple heat sources can largely affect the conductor's performance and its stability.

As regards the stability analysis, in addition to the analysis earlier introduced in chapters 4 and 6, here a more comprehensive and systematic analysis is proposed.

## 7.2 Joint quench temperature and thermal behavior

### 7.2.1 $T_q$ measurement in the SULTAN facility

As mentioned in section 1.3.1, technical superconductors typically exhibit elevated resistivity in the normal state. To mitigate heat accumulation and enhance stability during a transition from superconducting to normal state, a normal conducting stabilizer material with low resistivity is commonly applied as a low resistance shunt. The critical temperature at which the current initiates a transfer in the stabilizer is defined as the current sharing temperature $T_{cs}$, a parameter influenced by the electrical properties of both the superconductor in the normal state and the stabilizer.

The current sharing process and quench evolution as temperature increases, are evaluated in experimental tests and by simulations [45], [84], [200], [201]. In some NbTi samples, $T_{cs}$ tests reveal a sudden voltage take-off at an electric field below the conventional threshold ranges of 10 to 100 $\mu V/m$, resulting in an indeterminate transition index ($n$ value). Consequently, these data are conventionally denoted as the quench temperature $I_q$ instead of $T_{cs}$ [118].

In the scrutiny of ITER joint samples in the SULTAN facility, a pivotal qualification test involves the investigation of the current sharing temperature by observing a sudden quench temperature transition [164], [175]. In the meticulous preparation of joint samples, two sets of voltage taps and temperature sensors are positioned at distances of 490 mm and 40 mm from the joint copper sole's end, denoted as the top and bottom sensors, respectively, as illustrated in Figure 2.2. Tests are conducted with a background magnetic field of 3 T, supplying a current of 55 kA from cable B to cable A, and employing forced liquid helium at mass flow rates of 3 or 10 g/s. Additionally, heaters on the helium inlet induce incremental temperature changes of 0.5 or 0.2 K until a quench event is observed [164].

SULTAN measurements with helium mass flow rates of $10\ g/s$ exhibit a maximum temperature of approximately 6.7 K with no observed quench at full heater power. Conversely, at $3\ g/s$, a quench transpires at the bottom sensor position of cable B when the temperature reaches 7.12 K [164].

### 7.2.2 $T_q$ simulation for the SULTAN test configuration

The assessment of the current sharing and quench process is performed using the JackPot-AC/DC model by incorporating SULTAN-like boundary conditions. The schematic of the joint sample is depicted in Figure 7.1. Key geometric and material parameters are listed in Table 4.4. The cable length $L_{cable}$ is extended to $1200$ mm. The crucial input parameters of inter-strand, inter-petal and strand-to-copper sole contact resistivities were detailed in Table 4.8, which were derived from the measurements of the PFJEU6 joint sample and the associated parameterization procedures, as shown in chapter 4 [172], [202].

For better convergence of the numerical calculation, the nominal transport current of 55 kA is not applied immediately, but is ramped up from zero (at $t$ = zero) to the nominal value with a rate of $1\ kA/s$, and maintained constant until $t$ = 200 s, as shown in Figure 7.2. The steady state current plateau is the condition for the $T_{cs}$ simulations.

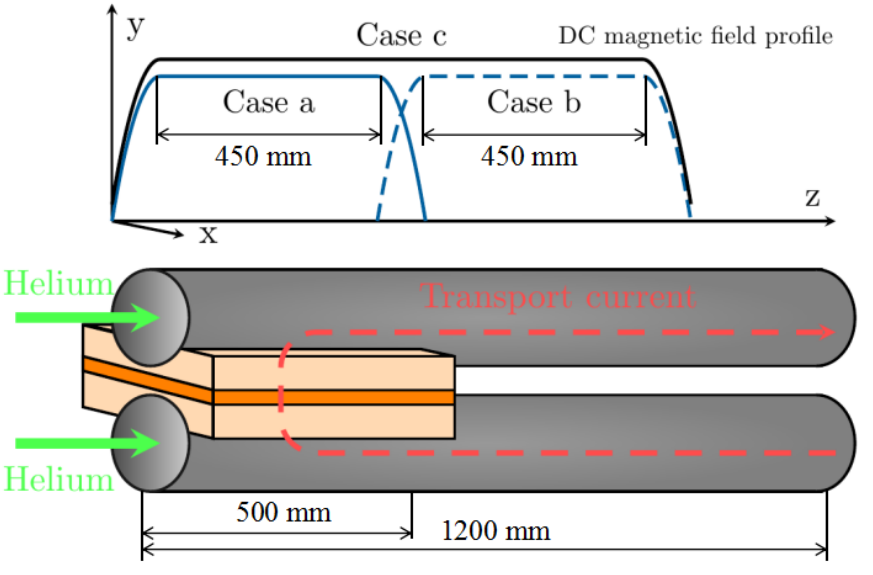


Figure 7.1: Schematic of a Poloidal Field joint, accompanied by profiles illustrating the DC magnetic field along the joint sample in the context of $T_{cs}$ simulations. Case a signifies the standard SULTAN DC magnetic field, predominantly influencing the joint box section. Case b accentuates the high field zone on the cable section, while case c employs a uniform magnetic field across the entire sample section.

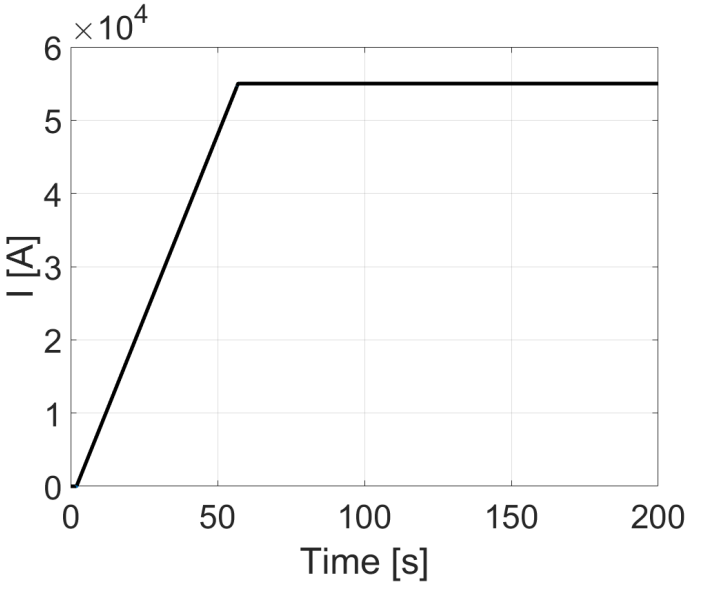


Figure 7.2: Transport current applied in the poloidal field coil joint simulation.

In consideration of the measurements with different helium mass flow rates, simulations exclusively evaluate the more demanding condition of 3 g/s flow rate. Gradually increasing helium inlet temperatures from 4.5 K to 7.2 K are simulated through a series of runs, demonstrating the evolution of helium temperature and its impact on the electric and thermal behaviors of the joint.

As introduced in chapter 2, the SULTAN magnet system, generating the DC and AC magnetic fields applied to the joint, comprises two coils. The DC magnetic field is predominantly applied in the x-direction, while the AC magnetic field operates in the y-direction, with effective high field zone (HFZ) lengths of 450 mm and 390 mm, respectively. For the measurement of the current sharing temperature, the DC coil predominantly acts on the joint box section (referred to as case a). Additionally, two modified DC magnetic field configurations, case b and case c, are simulated, with case b emphasizing the HFZ on the cable section, and case c employing a uniform magnetic field across the entire sample section. These magnetic field configurations with respect to the joint are illustrated in Figure 7.1.

### 7.2.3 Power dissipation

Current sharing and quench phenomena represent an inherent warm-up process initiated by losses, commencing locally within specific superconducting strands and potentially propagating to trigger an avalanche effect throughout the entire superconductor. Consequently, the current sharing process is inherently characterized by the progressive development of losses. To examine the impact of distinct magnetic field configurations and helium inlet temperatures on the joint performance, the comprehensive evaluation of the total power dissipation is presented in Figure 7.3. Remarkably similar power dissipation trends are discerned for helium inlet temperatures below 7.0 K. Accordingly, representative temperatures of 4.5, 7.0, 7.1, and 7.2 K are highlighted to elucidate the evolution of power dissipation.

In the context of case a, representing the standard SULTAN magnetic field configuration, no discernible escalation in power dissipation is evident for helium inlet temperatures up to 7.0 K. A subtle increment is noted as the temperature rises to 7.1 K, signifying the initiation of the current sharing process. Notably, when the temperature reaches 7.2 K, a substantial surge in power dissipation is observed. This augmentation is attributed to the progression of the current sharing and quench processes, with the eruption commencing at the helium temperature of 7.1 K, which is coincident with the quench temperature observed in the SULTAN measurement.

Contrastingly, for cases b and c, an earlier upswing in power dissipation occurs just after 7.0 K, suggesting that current sharing potentially initiates in the cable section outside the joint box. This observation implies a larger temperature margin of the conductor section within the joint box. As illustrated in Figure 7.1, case c essentially amalgamates features of both cases a and b, featuring a uniform magnetic field covering the entire joint length, akin to the actual ITER magnetic field configuration. Consequently, this underscores that the anticipated quench temperature of the ITER joint is approximately 0.2 K lower than the value derived from the SULTAN test.

The cumulative power dissipation within the joint manifests as a composite of three distinct components, distributed across the two cables, two cable-to-sole contacts, and the

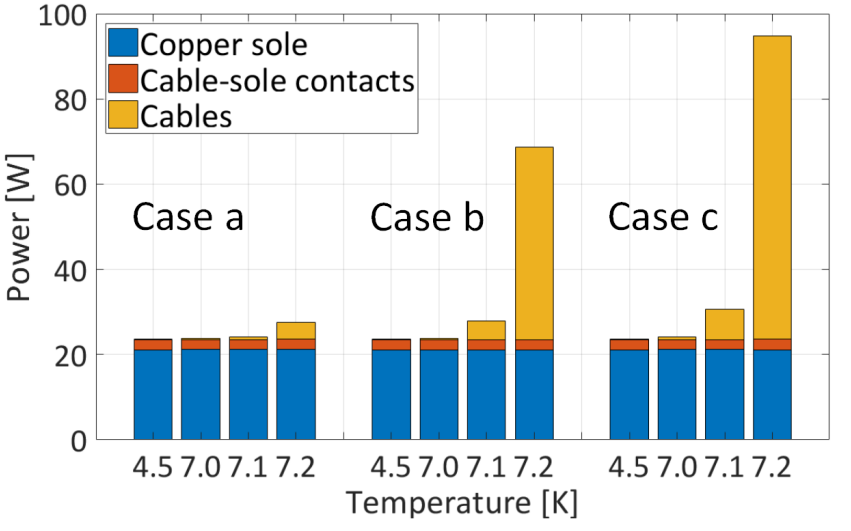


Figure 7.3: Total power dissipation and corresponding distribution across three distinct joint components, for different helium inlet temperatures and exposed to different magnetic field configurations.

copper sole itself. An examination of the joints subjected to three varying magnetic field configurations reveals a nuanced breakdown of specific power dissipation in each component, as delineated in the bar plot of Figure 7.3. Notably, a substantial proportion of power is ascribed to the copper sole through ohmic heating, remaining relatively consistent across different temperatures. During stable operation, ohmic heating in the copper sole emerges as the predominant contributor to total power dissipation. However, upon surpassing the critical temperature, a notable surge in power dissipation occurs in the cables due to inter-filament and inter-strand losses associated with the shared current traversing the copper matrix of the strand and the inter-strand contacts.

A more granular understanding of power distribution across distinct components is elucidated through the power density along the cable axis of the joint. This analysis specifically focuses on the standard SULTAN (case a) and uniform (case c) magnetic field configurations, as shown in Figures 7.4 and 7.5 respectively, at critical temperatures of 4.5, 7.0, 7.1, and 7.2 K, within the joint box section located between -0.225 and +0.275 m.

While observing a uniform distribution of power generation in the copper sole along the axis, apart from marginal decreases at the two ends, it is evident that power generation in the two cables gradually intensifies with temperature, predominantly concentrated in proximity to one end of the copper sole ($\sim 0.250$ m) in the case of the SULTAN magnetic field.

Given that ITER joints are positioned at the outer coil conductor turns, experiencing a relatively uniform magnetic field along the turn, the magnetic field configuration of case c emerges as more realistic and representative when compared to case a, where a limited uniform field length is applied. Notably, at a helium temperature of 7.1 K, wherein no explicit power increase is discerned with the magnetic field of case a, a substantial power

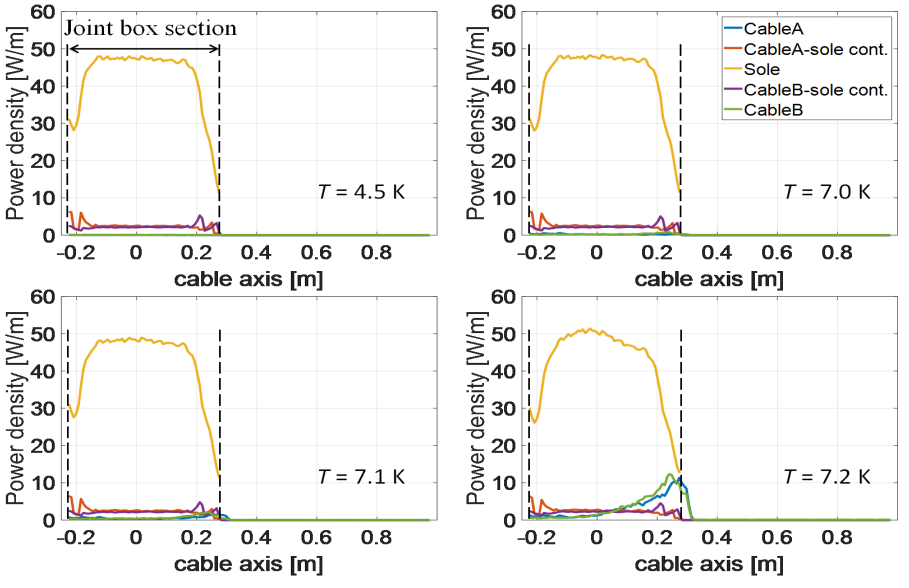


Figure 7.4: Calculated power density distribution in the joint components along the cable axis, for different helium inlet temperatures, at time instant $t = 150$ s and exposed to the SULTAN magnetic field configuration (case a).

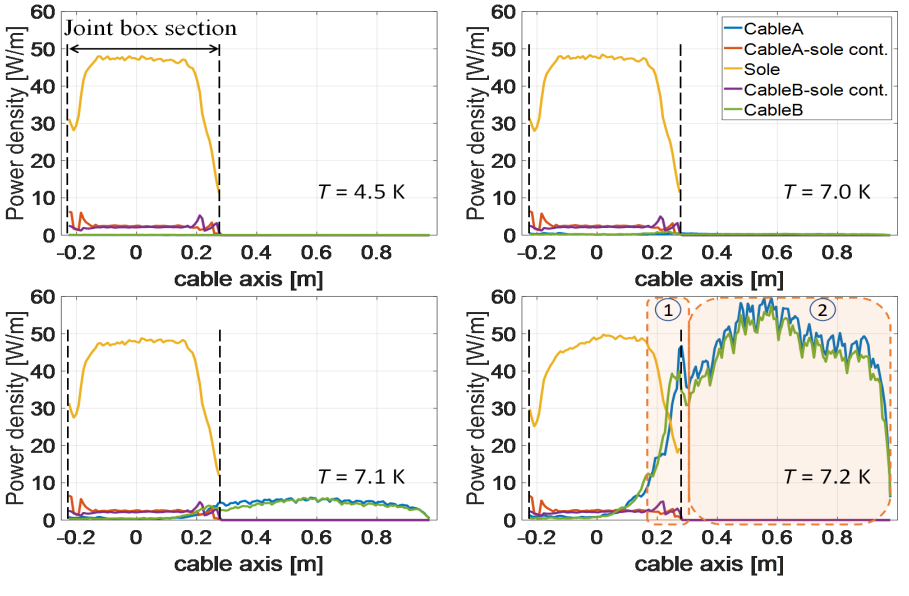


Figure 7.5: Calculated power density distribution in the joint components along the cable axis, for different helium inlet temperatures, at time instant $t = 150$ s and exposed to a uniform magnetic field configuration (case c).

generation occurs in the cable sections outside the joint box in the case of magnetic field case c. As the helium temperature escalates further to 7.2 K, in addition to an increase in power dissipation at the copper sole end (region 1), resembling the SULTAN magnetic field scenario, a pronounced surge in power is observed in region 2, specifically in the cables outside the joint box section.

Distinct 3D representations elucidating the power distribution of joints subjected to a uniform magnetic field (case c) at helium inlet temperatures of 7.0, 7.1, and 7.2 K are delineated in Figure 7.6. The three labelled regions within the figures demarcate the primary power sources. Additionally, to enhance the visualization of the cable-to-copper sole interface, the copper sole of the joint is presented as a contour frame.

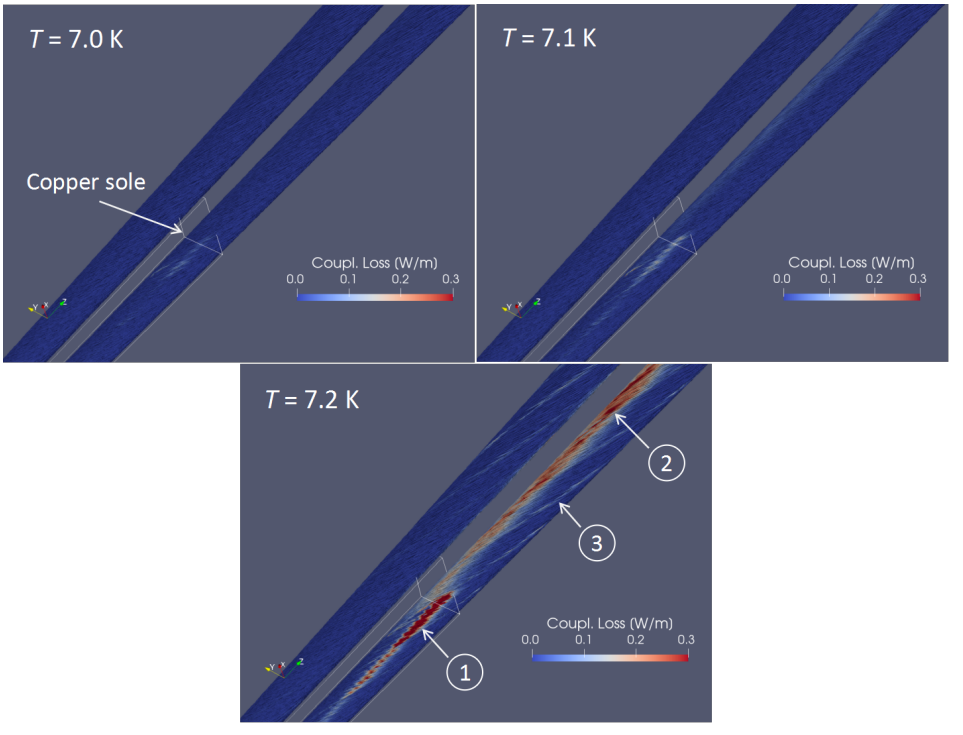


Figure 7.6: Three-dimensional visualization of power density distribution within the cables of the joint, for different inlet helium temperatures and exposure to a uniform magnetic field (case c); labelled regions highlight key sources contributing to power generation.

At helium temperatures of 7.0 and 7.1 K, the magnitude of power dissipation remains negligible. However, upon elevating the helium temperature to 7.2 K, conspicuous losses emanate from the three principal sources, denoted as 1, 2, and 3. Notably, the highest losses materialize in region 1, situated at the initial contact region between the copper sole and petals, aligning with the specific cable twisting pattern. While the maximum value approaches nearly 0.6 W/m, the display limit of power density is conservatively set to 0.3 W/m to facilitate the nuanced examination of the majority of strands.

The application of a transport current from cable B to cable A introduces a significant

self-field in the cable cross-section that is superimposed on the background magnetic field thereby intensifying the magnetic field in the innermost region 2. Consequently, a relatively elevated power dissipation emerges in region 2, primarily located in the innermost regions relative to the two cables. Notably, as the transport current gradually transfers to the copper sole in the joint box section, non-uniformly distributed power dissipation is predominantly generated outside the joint box section. The power density, as depicted in Figures 7.4 and 7.5, is computed concerning all strands in the cable cross-section, revealing that the power density in region 2 surpasses that in region 1. However, the concentration of power in the smaller region 1 results in even higher power dissipation, heightening the likelihood of triggering a quench in this specific zone. Lastly, for the source region 3, coupling losses are induced along the interfaces between neighboring petals, particularly pronounced during pulsed operating conditions, as explained in chapter 6.

### 7.2.4 Current distribution

The generation and distribution of power are intricately linked to the distribution of current, particularly during the current sharing process. For joints subjected to the four representative helium temperatures and exposed to both the standard SULTAN and uniform magnetic field profiles, the strand current distributions are delineated in Figures 7.7 and 7.8, respectively. Note the distinct position of the end of the joint box at $x$ = 0.275 m, clearly observable difference emerge between the sections inside and outside the joint box. The more diffuse current distribution within the joint box is attributable to the transfer of current between the cable and copper sole. Generally, the dispersion in superconducting strand currents, diminishes with escalating helium temperatures since the local strand critical currents undergo reduction. In a uniform magnetic field, the current distribution widens in the cable section outside the joint box. The extent of strand current dispersion essentially mirrors the severity of current sharing or even quench process. Significantly, the inset in Figure 7.8 depicts the current distribution in the six copper strands, with relatively high currents signifying a substantial transfer of current to the copper strands, culminating in the instability of the joint.

Considering the multitude of strands in a single cable, discerning the individual current evolution of the majority of strands can be challenging. Consequently, for joints subjected to magnetic field cases a and c, along with varying helium inlet temperatures, the average and standard deviation of all strand currents were computed and presented in Figure 7.9. The average currents are nearly the same for different configurations of magnetic fields and helium temperatures, that is attributed to the constant transport current, while explicit differences are observed between currents in standard deviations, reflecting the spread of strand currents. Furthermore, a notable deviation is observed in the joint box section, where substantial current exchange occurs between the cable and copper sole, with the maximum deviation occurring in the middle of the copper sole along the joint axis. Simultaneously, the gradually decreasing average current mitigates the risk of instability. Conversely, in the case of a uniform magnetic field, the standard deviation of strand current in cables outside the joint box significantly increases, and the average strand current maintains maximum values, indicating a heightened probability of excessive currents and quench in this region.

As depicted in Figures 7.5 and 7.6, the power dissipation exhibits a non-uniform distri-

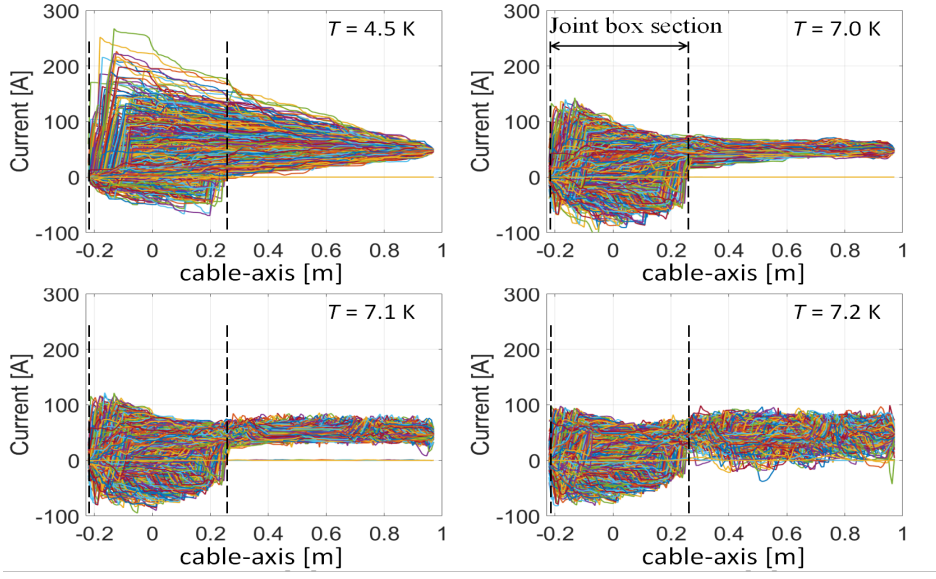


Figure 7.7: Calculated currents in all cable strands showing the distribution along the cable axis (cable A), for different helium inlet temperatures and exposed to the SULTAN magnetic field configuration (case a).

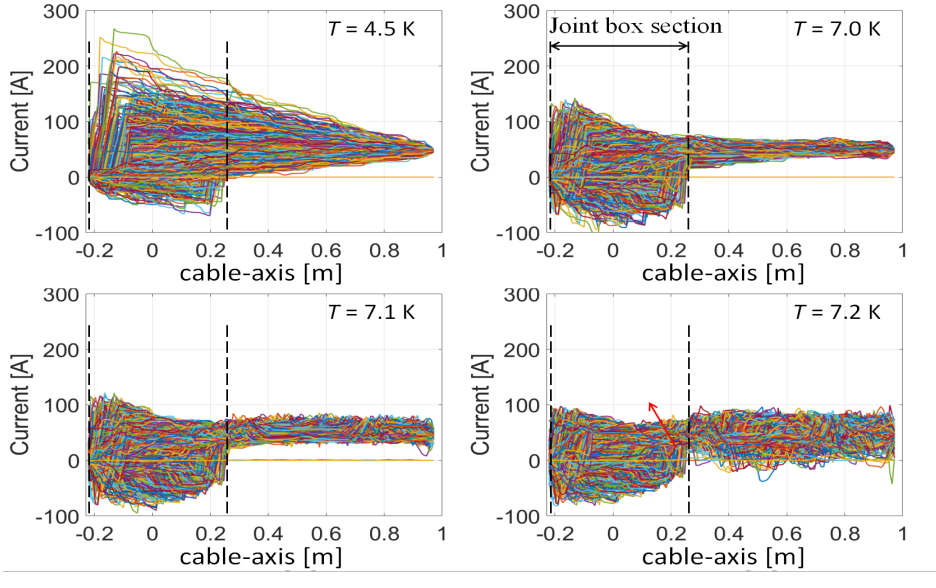


Figure 7.8: Calculated currents in all cable strands showing the distribution along the cable axis (cable A), for different helium inlet temperatures and exposed to a uniform magnetic field configuration (case c).

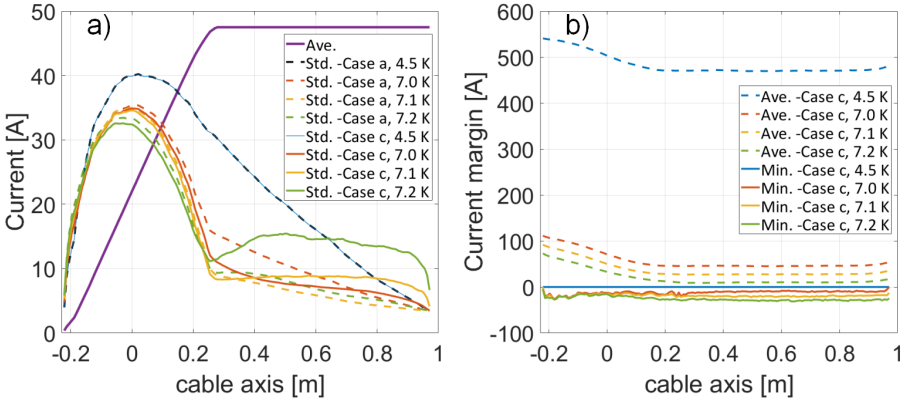


Figure 7.9: a) Average and standard deviation of strand currents along the cable; b) Average and minimum values of strand current margins along the cable axis (cable A) of the joint, considering four different helium inlet temperatures and two magnetic field configurations (cases a and c).

bution as well, showing high levels in specific regions that can potentially cause instability in certain strands. Although this tendency is not explicitly revealed by the average and deviation of strand currents in Figure 7.9, it is elucidated by evaluating the current margin of strands, defined as $I_{margin} = I_c - |I_s|$, where $I_s$ and $I_c$ are the transport current and critical current of a particular strand. Plot b of Figure 7.9 illustrates the average and minimum current margin among all strands in cable A. The gradual decrease in average current margin with increasing helium inlet temperature underscores the influence of temperature change on strand current evolution. Particularly, in proximity to the quench temperature, the minimum current margin provides profound insights into the current evolution.

After the quench transient, the resistivity of the superconducting material in normal state gradually rises, surpassing that of the surrounding stabilizer matrix. The quench back effect accelerates the propagation of current sharing significantly, leading to increased inter-filament and inter-strand coupling losses causing approximately double the change rate of current change [203]. Additionally, the relatively low critical temperature of NbTi, coupled with the low take-off voltage resulting from the large self-field gradient in the cable cross-section, leads to an earlier quench before sufficient inter-strand current redistribution can occur, without a measurable resistive transition development [88].

### 7.2.5 Electric field

The distribution of current affected by helium inlet temperatures reveals a distinct behavior. Below the critical current sharing temperature $T_{cs}$, the joint resistance predominantly influences the current distribution, with the copper sole playing a pivotal role. Conversely, above $T_{cs}$, the redistribution of current among strands significantly influences the progression of current sharing or quench. Consequently, a voltage drop emerges during the quench transient and propagates along the normal zone. In an ideal superconducting transition within technical superconductors, a smooth buildup of electric field characterizes the current sharing region, occurring with increasing current or temperature.

In the SULTAN facility, the voltage drop across the joint sample is measured using two sets of voltage taps positioned at the top and bottom locations, as depicted in Figure 2.2. In simulations, the reference zero potential point is established at the left interface between cable B and the copper sole. The potential of an individual strand and the average value at a specific position are then determined. The latter is calculated by considering all the strands in the same cable cross-section. Given that the transport current is supplied from cable B to cable A, the average voltage is generally negative in cable A and positive in cable B. The electric field is defined as the potential difference per meter along the conductor.

Considering the influence of magnetic field on the current distribution and power generation, the simulations prioritize the use of a more realistic uniform magnetic field (case c) to evaluate the electric field distribution in the joint. For helium inlet temperatures of 4.5, 7.0, 7.1, and 7.2 K, the electric field for all strands in cable A are shown in Figure 7.10.

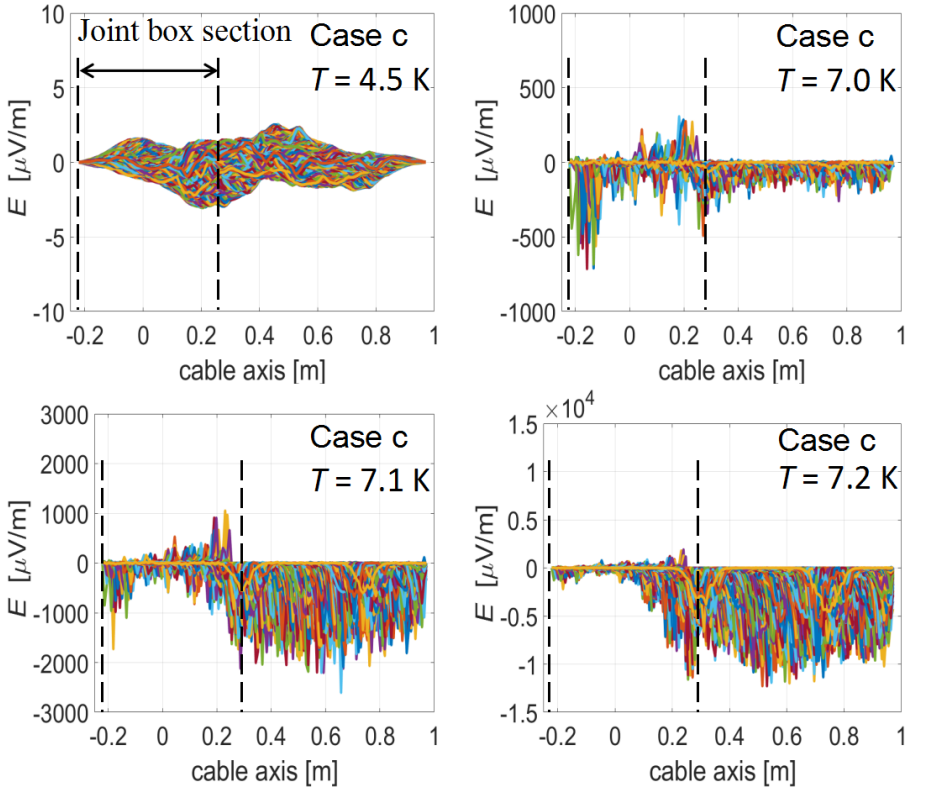


Figure 7.10: Calculated electric field distribution of strands in cable A along the cable axis, for different helium inlet temperatures.

At 4.5 K, all strands exhibit negligible electric field, each below the usual criterion of 10 μV/m. Close to the critical current sharing temperature at 7.0 K, the local peak electric field in most strands remain in the range of 100 μV/m, even with higher values near the ends of the copper sole. The average electric field remains sufficiently low though,

ensuring joint stability. A notable increase occurs at 7.1 K, particularly in strands outside the joint box, with maximum values approaching $2,000\ \mu V/m$. Such elevated local peak values raise concerns regarding stable operation. Further increase of the helium inlet temperature to 7.2 K results in a fivefold growth in maximum electric field, reaching values of $10,000\ \mu V/m$, predominantly in conductors outside the joint box region, where current transfer to the copper sole is absent.

Comparatively, the average electric field distribution as shown in Figure 7.11, emphasizes the evolving trend, albeit overlooking the diversity associated with current non-uniformity to some extent. The comparison of the four different temperature cases reveals that, for joints below quenching temperature (4.5 and 7.0 K), the average electric field remains below $10\ \mu V/m$ in the joint and cable sections. However, at 7.1 and 7.2 K, a noticeable transition occurs, with the average electric field in cable sections becoming 10 and 100 times larger than the criterion, respectively. This aligns with SULTAN test results, where a quench was observed at 7.12 K, corresponding to an average electric field of approximately $100\ \mu V/m$ and a power density of $5\ W/m$ in the cable section outside the joint box. The rapid change in electric field, especially the average value across the entire cable, provides a quantitative assessment of current sharing and the avalanche-like process during the superconducting-to-normal state transition.

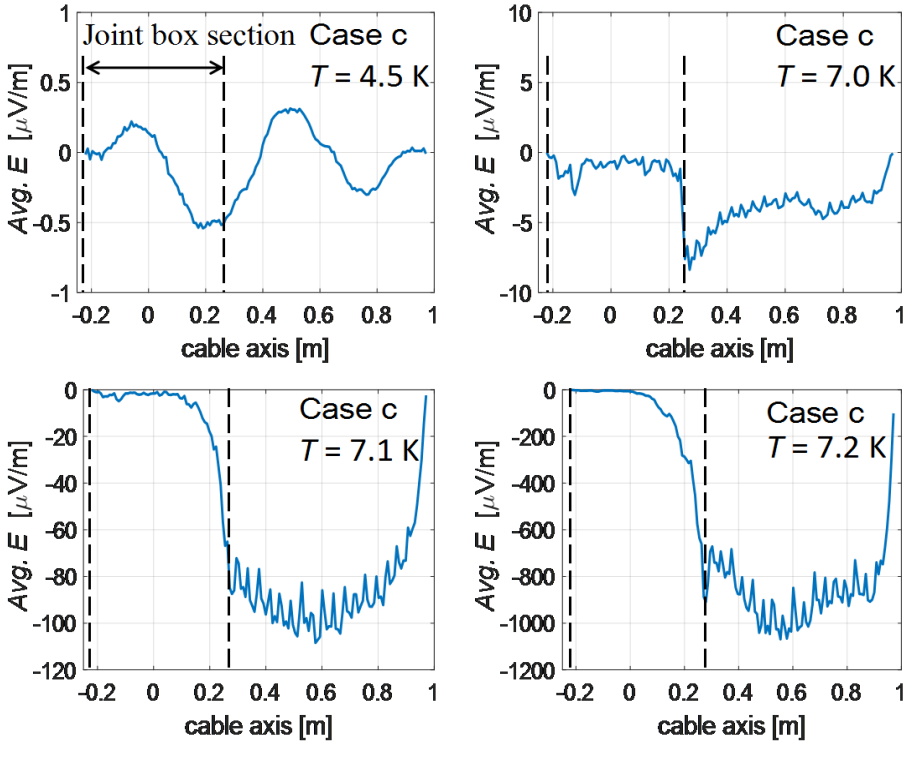


Figure 7.11: Calculated average electric field distribution of strands in cable A along the cable axis, for different helium inlet temperatures.

### 7.2.6 Thermal propagation

The quench process manifests as a coupled electro-thermal phenomenon, where the initiation of the quench and the subsequent rapid propagation of a normal zone occur when the deposited energy surpasses the heat removal capacity of the cooling system. In the case of the PF joint cooled by a forced supercritical helium flow, three distinct channels: central pipe, cable bundle, and lateral channels, operate in parallel and determine the helium flow distribution [47], as delineated in the cross-sectional view in Figure 5.1. Despite the inherently transient and three-dimensional nature of the quench process [203], [204], the thermal propagation in ITER CICCs and joints is predominantly longitudinal. This dominance allows for the application of a 1D thermal model with acceptable computational accuracy and efficiency [111].

As delineated in sections 2.3.7 and 6.3.4, the 1D thermal model stands as an integral constituent within the JackPot-AC/DC code. The thermal parameters essential for the PFJEU6 joint are meticulously obtained through dedicated measurements [166], and a comprehensive summary of the parameters is presented in Table 7.1. For each half joint, the average temperatures of strand bundle and helium in each petal, were simulated but similar behaviors are observed. Thus, only the elements pertaining to strand bundles are shown in Figures 7.12 and 7.13, corresponding to different helium inlet temperatures and exposed to the SULTAN and uniform magnetic field configurations, respectively.

Table 7.1: Summary of the main thermal parameters of the PFJEU6 joint used for the $T_{cs}$ simulations.

| **Parameter** | **Unit** | **Value** |
|---|---|---|
| Total helium mass flow rate | $\mathrm{g/s}$ | 3 |
| Heat conductivity of copper sole/shim | $\mathrm{W/m \cdot K}$ | 24/220 |
| Heat conductivity of NbTi | $\mathrm{W/m \cdot K}$ | 0.135 |
| Heat conductivity of helium | $\mathrm{W/m \cdot K}$ | 0.02 |
| Petal-He in petal, heat transfer coefficient | $\mathrm{W/m^2 \cdot K}$ | 500 |
| Sole-He in petal, heat transfer coefficient | $\mathrm{W/m^2 \cdot K}$ | 500 |
| Sole-petal strands in petal, heat transfer coefficient | $\mathrm{W/m^2 \cdot K}$ | 10 |
| Petal-petal, heat transfer coefficient | $\mathrm{W/m^2 \cdot K}$ | 23 |
| Sole-sole halves, heat transfer coefficient | $\mathrm{W/m^2 \cdot K}$ | 1600 |

In the case of the joint exposed to the standard SULTAN magnetic field profile (case a), a deficiency in heat generation outside the high-field zone results in a relatively stable evolution of petal temperatures along the cable axis. Particularly, at a helium inlet temperature of 4.5 K, significantly below the critical value, power generation causes a temperature increase of approximately 1.1 K. As the inlet helium temperature approaches the critical temperature, the temperature rise moderates to about 0.6 K. However, at 7.2 K, a strand temperature in one petal reaches 7.9 K, marking the initiation of a quench in the joint sample during the SULTAN test.

Conversely, for the joint subjected to a uniform magnetic field of 3 T along its entire length, additional power is generated in the conductors outside the joint box. When the inlet helium temperature equals or exceeds 7.1 K, inadequate heat removal leads to

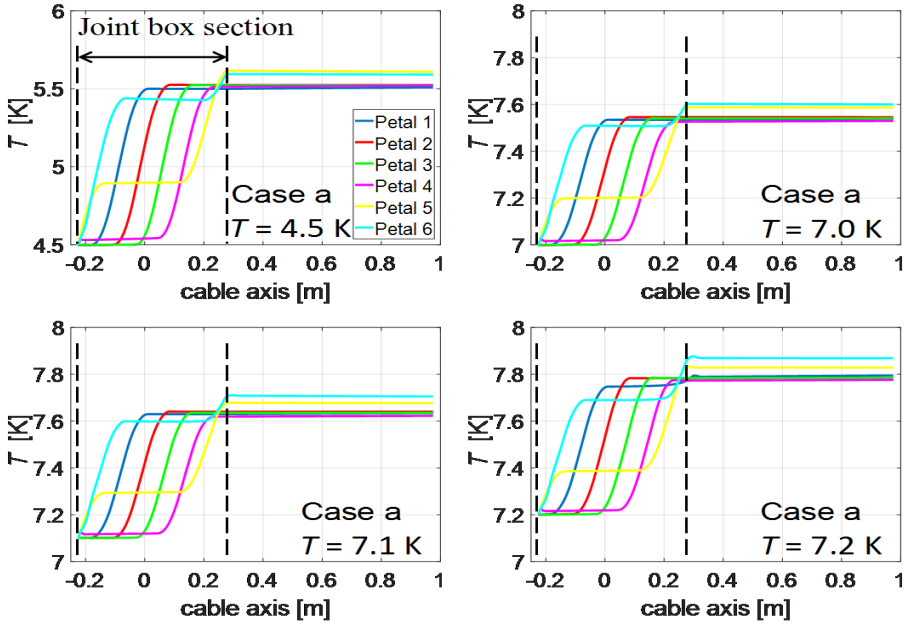


Figure 7.12: Calculated evolution of the temperature along the axis in petals of cable A, for different helium inlet temperatures and exposed to the SULTAN magnetic field profile profile (case a).

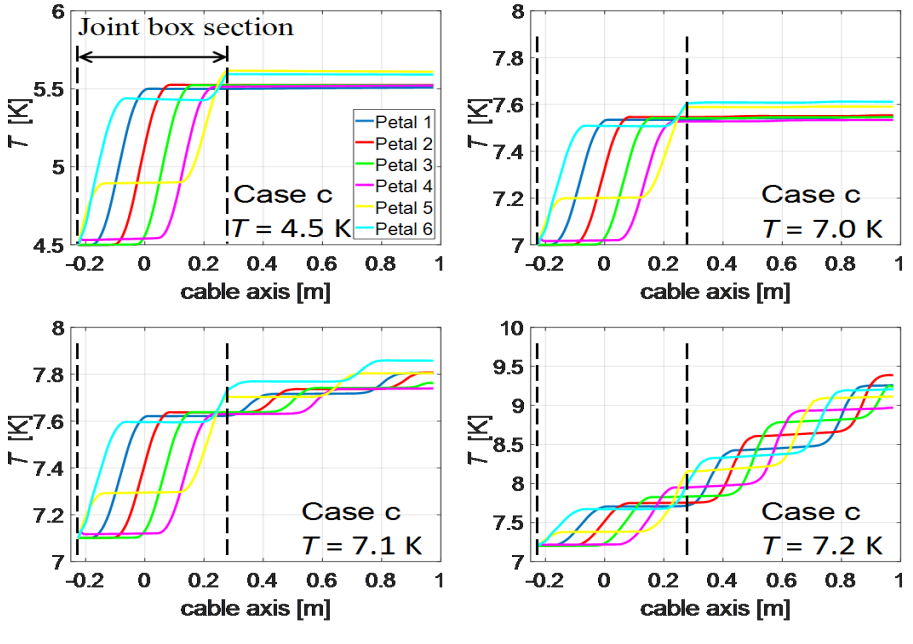


Figure 7.13: Calculated evolution of the temperature along the axis in petals of cable A, for different helium inlet temperatures and exposed to a uniform magnetic field (case c).

a continuous increase in average petal and helium temperatures along the flow direction, ultimately surpassing 9 K. Simulation results indicate that, under ITER operating conditions, there exists a minimum temperature margin of 0.6 K (7.0 to 7.6 K) necessary for recovery from DC heating. As heat accumulates further, particularly in the conductors outside the joint box, strands and helium experience elevated temperatures.

It is noteworthy that while discussing power dissipation, current, and electrical field distributions in sections 7.2.3 to 7.2.5, helium inlet temperatures are utilized to elucidate the impact of temperature on stability analysis. However, as disclosed in section 7.2.6, the helium temperature in a conductor gradually increases along the flowing direction rather than maintaining a constant value. Consequently, the actual in-situ helium temperature at a specific position must be correspondingly corrected with respect to the inlet value.

## 7.3 Transient stability

In chapters 4 and 6, the initial test and analyses of the pulsed field stability and AC loss of the joint have been presented. However, due to the limitation of the experimental facility, the applied testing conditions did not satisfy the fast changing currents and magnetic fields of the plasma operating scenario. In order to obtain more accurate transient stability predictions of the PF joint, a more comprehensive evaluation is performed based on more realistic conditions.

In terms of stability analysis, a pragmatic method is to analyze three models in combination to predict quench propagation under plasma scenario conditions [102]. The combined use of JackPot-AC/DC, multi-constant-model MCM [64], [205], and THEA code [206] is promising in assessing the stability of superconductors, with a particular focus on instantaneously and deposited energy during minimum quench energy (MQE) tests. This study introduces an effective method to evaluate joint stability, considering the generation, distribution, and deposition of energy. Furthermore, a comprehensive experimental and numerical analysis of transient stability is presented based on the representative ITER PF joint sample PFJEU6.

### 7.3.1 Test conditions

The stability (quench or recovery) test is conventionally conducted using either a fast-varying magnetic field or sinusoidal excitation at various frequencies to induce heat generation until a quench occurs upon surpassing a critical energy level. In the SULTAN facility, pivotal for assessing the stability of superconducting joints, the magnet system exerts influence through the application of both DC and AC magnetic fields. The DC magnetic field primarily operates in the $B_{dc}$ direction, while the AC magnetic field is oriented in the $B_{ac}$ direction, featuring effective high-field zone (HFZ) lengths of 450 mm and 390 mm, respectively, as indicated in Figure 2.1. For stability tests on ITER PF joints, the DC background magnetic field is maintained at 3 T, and the AC magnetic field features a trapezoidal waveform with gradually increasing gradients for both rise and fall fronts by which a quench occurrence may be detected when $\mathrm{d}B/\mathrm{d}t$ reaches 0.2, 0.4 or 0.8 T/s. The amplitude and plateau duration of the trapezoidal field remain constant at 0.4 T and 10 s, respectively. The stability tests is carried out with a transport current of 55 kA and a

carefully chosen helium mass flow rate and inlet temperature. The testing conditions are summarized in Table 7.2. It is noteworthy that quench observations are notable in case b with a trapezoidal field gradient of 0.4 T/s. A reduced helium inlet temperature of 6.0 K is used during tests with a magnetic field gradient of 0.8 T/s [164].

Table 7.2: Testing conditions of ITER PF joint transient stability in the SULTAN facility.

| **Case** | **a** | **b** | **c** |
|---|---|---|---|
| Background magnetic field [T] | 3 | 3 | 3 |
| Trapezoidal magnetic field gradient [T/s] | 0.2 | 0.4 | 0.8 |
| Trapezoidal magnetic field amplitude [T] | 0.4 | 0.4 | 0.4 |
| Trapezoidal magnetic field duration [s] | 10 | 10 | 10 |
| Transport current [kA] | 55 | 55 | 55 |
| Helium inlet temperature [K] | 6.5 | 6.5 | 6.0 |
| Helium mass flow rate [g/s] | 10 | 10 | 10 |

The numerical stability test of ITER PF joints is initially conducted under conditions mirroring those applied in SULTAN measurements, as delineated in Table 7.2. Subsequently, the test conditions were expanded to facilitate a comprehensive performance assessment, primarily achieved by adjusting the inlet temperature and mass flow rate of liquid helium. It is pertinent to highlight that, for enhanced calculation convergence, the constant transport current of 55 kA is not directly applied but is incrementally increased from zero to 55 kA with a ramp rate of 1 kA/s. Following this gradual increment, the current is maintained at a constant plateau for a duration exceeding 40 s. Concurrently, the trapezoidal magnetic field is implemented during this period of constant current plateau. The temporal evolution of the transport current and the applied magnetic field is graphically presented in Figure 7.14.

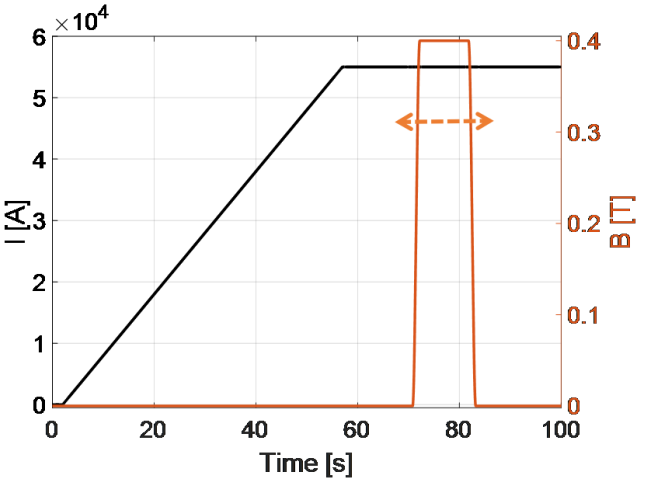


Figure 7.14: Applied transport current and trapezoidal magnetic field versus time in the numerical stability tests, with the arrow indicating the adjustable gradients of the rise and fall fronts.

Notably, to account for the variation in magnetic field gradients leading to time shifts between successive magnetic field pulses (having a consistent amplitude of $0.4$ T and a duration of 10 s), certain electromagnetic behaviors discussed in subsequent sections have been examined at different time instants accordingly.

### 7.3.2 Energy generation

In response to the influence of a large transport current and varying magnetic fields, detailed in Table 7.2, the total energy generated in the joint is a summation of ohmic heating, coupling loss, and eddy current loss. This energy is distributed among the three main components: two cable ends, copper sole, and cable-to-sole contacts. The power dissipation $P$ for the three types of trapezoidal magnetic field applied is meticulously calculated and presented in Figure 7.15.

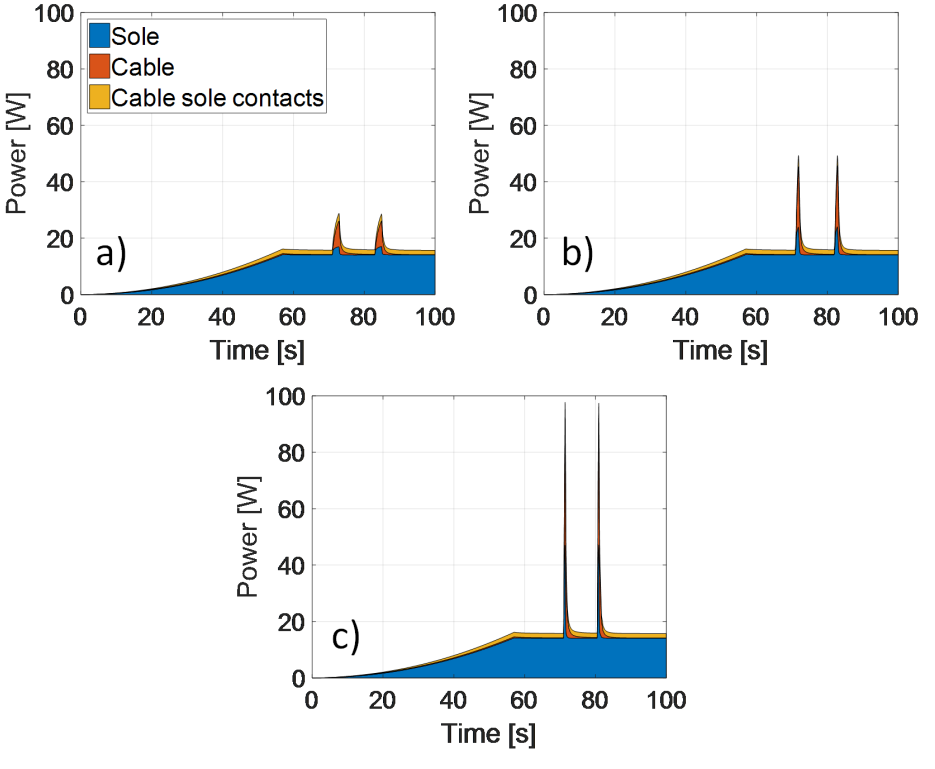


Figure 7.15: Calculated power dissipation in the PF joint simulated for a 55 kA transport current and various trapezoidal magnetic field rates: a) $\mathrm{d}B/\mathrm{d}t = 0.2$ T/s, b) $\mathrm{d}B/\mathrm{d}t = 0.4$ T/s and c) $\mathrm{d}B/\mathrm{d}t = 0.8$ T/s.

The analysis reveals a positive correlation between deposited energy and magnetic field pulse intensity. The highest dissipation occurs in the copper sole, primarily attributed to the transport current of 55 kA and manifested as ohmic heating. Introducing the trapezoidal magnetic field transient causes two power peaks corresponding to the rise and fall

fronts. By considering different time ranges, the total energy and contributions from distinct transients can be calculated using Equation 7.2

$$Q_{gen} = \int_{t_{a1}}^{t_{b1}} P dt + \int_{t_{a2}}^{t_{b2}} P dt, \tag{7.2}$$

where $t_{a1}$, $t_{b1}$, $t_{a2}$ and $t_{b2}$ represent the time instants corresponding to the start and end of two power peaks, respectively.

Compared to the nearly constant power dissipation by the transport current, the portion induced by the magnetic field transient assumes greater significance for joint stability.To precisely assess the influence of the trapezoidal magnetic field, a series of simulations with identical magnetic field configurations, but zero transport current, were conducted. It is important to note that the absence of transport current leads to an increase in critical current and the corresponding current margin. Specifically, for the three types of trapezoidal magnetic fields, the corresponding power distribution in the three individual components is distinctly presented in Figure 7.16 a. The time instant $t$ = 1 s aligns with the commencement of the rise front of the magnetic field pulse.

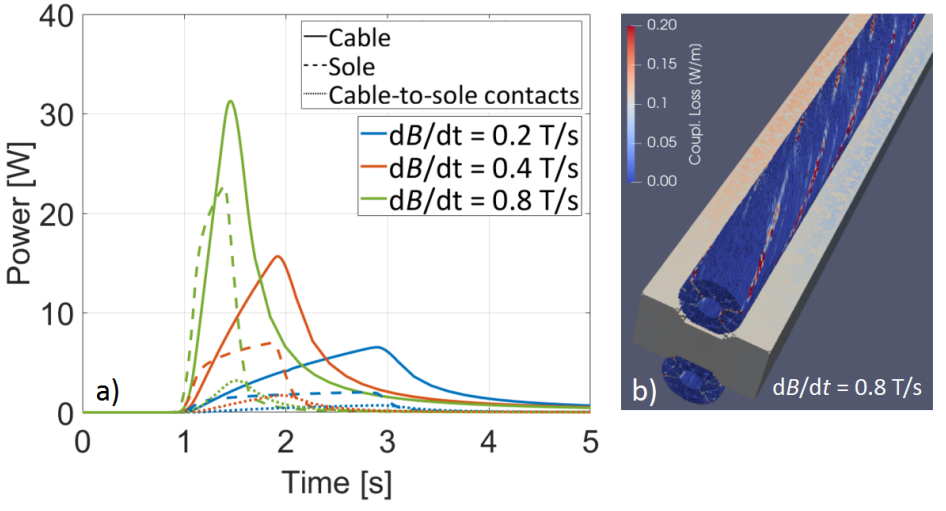


Figure 7.16: a) Calculated power distribution versus time in PFJEU6 joint components: two cables, copper sole, and cable-to-sole contacts. The power distribution is exclusively generated by the rise front of a trapezoidal magnetic field with d$B$/d$t$ = 0.2, 0.4, and 0.8 T/s, respectively, while maintaining a background magnetic field of 3 T and zero transport current. b) Detailed 3D visualization of power distribution induced by the trapezoidal magnetic field with a gradient of 0.8 T/s at the time instant of maximum power dissipation. High losses are observed along the petal-to-petal interfaces (resistive barriers). The color map of the copper sole represents the induced currents and not the AC losses.

The comparative analysis underscores that the predominant share of power dissipation occurs in the two cable ends, mainly in the form of coupling current loss. A detailed 3D visualization, depicted in Figure 7.16 b, elucidates that specific coupling current loss in

the two cables are primarily generated by local current loops and distributed along the interfaces between each pair of petals. Furthermore, this loss exhibits a positive correlation with the magnetic field transient. The generated power $P_{cpl}$ is directly proportional to the square of the time derivative of the internal magnetic field $\dot{B}_i$, as expressed in Equation 7.3 [207]

$$P_{cpl} = \frac{n\tau}{\mu_0} \cdot \dot{B_i}^2 \cdot A_{st} \cdot L, \tag{7.3}$$

with $B_i$ the internal magnetic field, depends on the external magnetic field $B_e$, defined as

$$B_i = B_e - \frac{n\tau}{2}\dot{B}_i, \tag{7.4}$$

$$B_e = \dot{B}_i \cdot t. \tag{7.5}$$

Here $\dot{B}$ represents the linear magnetic field ramp rate, with values of 0.2, 0.4 and 0.8 T/s, $\mu_0$ [H/m] denotes the magnetic permeability of vacuum, $A_{st}$ [m$^2$] signifies the total cross-sectional area of the composite strands and $L$ = 0.39 m corresponds to the effective exposure length of the SULTAN AC magnetic field. The average coupling loss time constant $n\tau$ for each single conductor is calculated to be $65 \pm 3$ ms.

### 7.3.3 Current distribution and margin

The analysis of the local power dissipation, particularly the specific distribution of coupling loss depicted in Figure 7.16, underscores the substantial dependence of joint stability on current redistribution. This redistribution primarily stems from two sources: the transport current and the coupling current induced by a varying magnetic field. Considering a joint subjected to a magnetic field gradient of $0.8$ T/s and two transport current configurations (zero and 55 kA), the evaluation of cable and petal current distributions along the joint is presented in Figure 7.17. This assessment corresponds to the time instant of maximum power dissipation, with the copper sole positioned in the region from -0.225 mm to +0.275 mm, nearly coinciding with the high-field zone of the SULTAN AC magnetic field.

In Figure 7.17 a, the cable current of 55 kA gradually transfers into the copper sole. Conversely, the induced cable current in Figure 7.17 b is approximately 50 times lower. Regarding petal currents, illustrated in Figures 7.17 c and d, they exhibit almost a symmetrical distribution with respect to the joint's center plane, with Figure 7.17 c detailing the process of petal current transfer to the copper sole stage by stage, following the specific cabling pattern and contact configurations. In the absence of transport current, the maximum amplitude of the induced petal current in Figure 7.17 d is approximately five times less than the petal current in Figure 7.17 c. Given that both cable and petal currents are sums of strand-carrying currents, the quite different ratios of 50 and 5, for two levels of currents, respectively, quantitatively indicate a significant amount of coupling current loops induced between petals. These locally induced currents manifest as positive and negative currents in neighboring petals, thereby increasing or decreasing individual petal currents accordingly. The opposing petal currents offset each other, contributing to a neutral behavior when calculating the cable current as a whole.

While the overall coupling current loss exhibits a positive correlation with magnetic field gradient, the local influence of the varying magnetic field on the coupling current

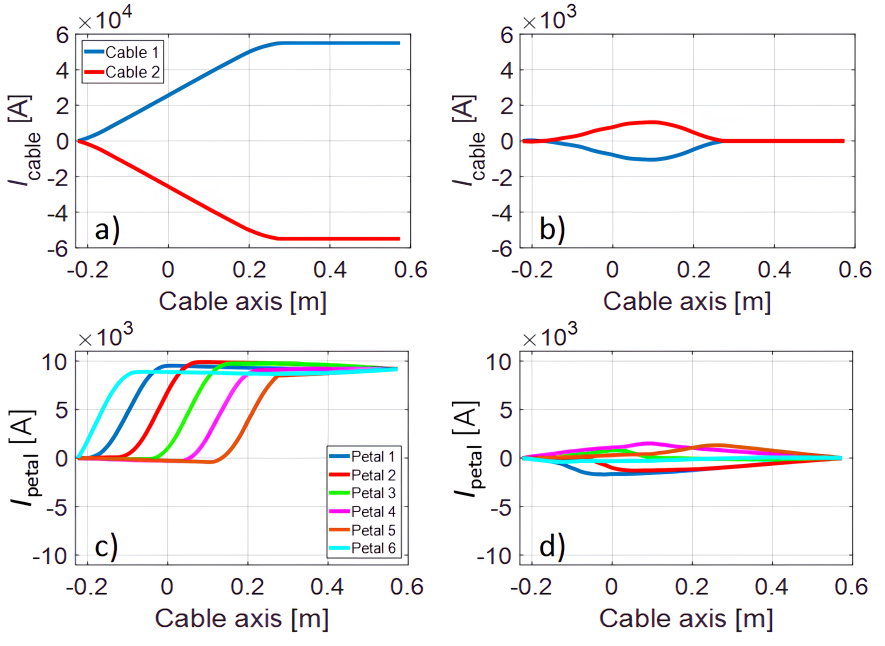


Figure 7.17: Calculated cable and petal current versus cable axis. Distribution analysis of PFJEU6 joint under trapezoidal magnetic field with gradient d$B$/d$t$ = 0.8 T/s. Cable currents depicted with a) 55 kA transport current and b) zero transport current. Petal currents distributed in one cable illustrated with c) 55 kA transport current and d) zero transport current, respectively. These analyses provide a detailed insight in current dynamics in the superconducting joint.

distribution, rather than a global influence, results in no significant differences observed in both cable and petal currents for the three types of magnetic field configurations. In other words, to some extent, cable and petal currents prove to globally determine the stability of CICCs or joints. This limitation is also a notable factor in experimental stability tests, such as those conducted in the SULTAN facility.

In addressing the potential initiation of instability by exceeding currents in specific strands, it becomes imperative to comprehend the strand-level current distribution and identify overloaded strands through the assessment of current margin. This is achieved by defining $I_{margin} = I_c - |I_s|$, where $I_c$ represents the local critical current and $|I_s|$ denotes the absolute value of the carrying current, encompassing both the transport current and induced coupling currents. The influence of locally induced coupling currents on stability, typically leading to increased currents in neighboring strands, can be discerned through the examination of the minimum current margins for each individual strand. These minimum current margins serve as indicators of the most critical elements of each segment along the cable axis. Additionally, considering the current non-uniformity in a conductor carrying a substantial transport current of 55 kA, an average current margin of all strands provides insight into the overall current distribution, serving as a corresponding reference.

For the simulated joints under the specified conditions outlined in Table 7.2, the dis-

tributions of both minimum and average current margins are calculated and presented in Figure 7.18. Similar behaviors are observed in the cases with magnetic field gradients of 0.2 and 0.4 T/s. However, in the scenario with a magnetic field gradient of 0.8 T/s and helium inlet temperature of 6.0 K, the average current margin increases due to the higher critical current at the lower inlet temperature. Conversely, the minimum current margin experiences a significant decrease owing to the faster transient magnetic field, which intensifies local coupling and carrying currents. Additionally, a negative current margin indicates current saturation and redistribution. The sharp transition and the widened disparity between average and minimum current margins suggest a pronounced current non-uniformity and redistribution from overloaded strands to others. While this phenomenon may exacerbate transient instability, it remains insufficient to conclusively determine quench initiation.

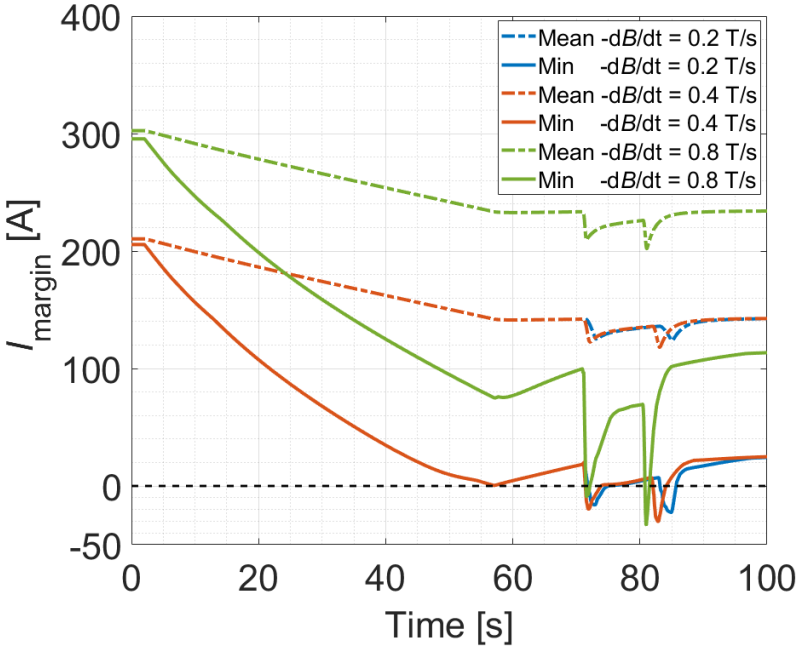


Figure 7.18: Calculated average and minimum strand current margins in a PF joint exposed to different trapezoidal magnetic fields.

### 7.3.4 Energy deposition

The stability of a superconductor hinges on maintaining a dynamic equilibrium between energy generation and heat removal, emphasizing the necessity of a sufficient energy margin for reliable operation. While sections 7.3.2 and 7.3.3 illustrate energy generation and distribution, offering insights into the potential quench process, a comprehensive understanding requires consideration of heat removal. For instance, in SULTAN stability tests,

a quench occurred in case b (Table 7.2) with a magnetic field gradient of 0.4 T/s and helium inlet temperature of 6.5 K. Conversely, in case c with a magnetic field gradient of 0.8 T/s and helium inlet temperature of 6.0 K, a higher coupling loss was observed (Figure 7.15). However, the lower temperature facilitated a higher current margin for most strands (Figure 7.18), allowing for more heat deposition without triggering a quench.

For joints exposed to various trapezoidal magnetic field rates and varying helium flow rates, the temperature differences $\Delta T$ along the copper sole, coinciding with the distance between the upstream and downstream temperature sensors, are meticulously calculated and presented in Figure 7.19, relative to corresponding inlet temperatures.

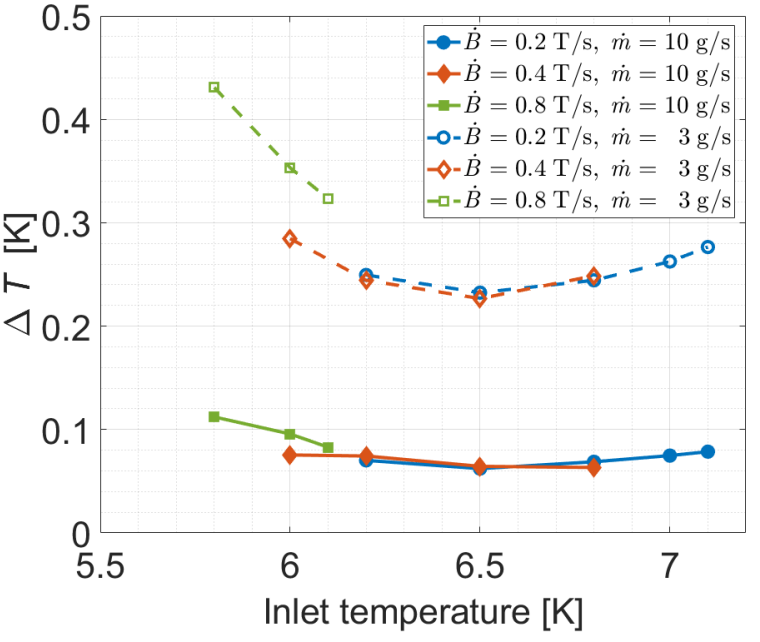


Figure 7.19: Calculated helium temperature difference across the upstream and downstream sensors for various trapezoidal magnetic field rates and liquid helium flow rate conditions.

The outcomes reveal that temperature evolution is predominantly influenced by the mass flow rate $\dot{m}$. In instances with a helium flow rate of 10 g/s, the average temperature difference remains approximately 0.1 K. However, it escalates rapidly to a range approaching 0.3 K for cases with a helium flow rate of 3 g/s, indicating the challenge of promptly removing energy deposition. In contrast, the influence of the magnetic field is comparatively minor in cases with low varying rates such as 0.2 and 0.4 T/s, but becomes more pronounced upon surpassing a specific threshold, as exemplified in the case of 0.8 T/s.

Illustratively, considering a magnetic field gradient of 0.4 T/s and helium inlet temperature of 6.5 K, the associated temperature evolution over time at the upstream $T_{up}$ and downstream $T_{down}$ sensors relative to the high-field zone of the AC magnet, is calculated and depicted in Figure 7.20. The inset plot provides insight into the corresponding temperature difference $\Delta T = T_{down} - T_{up}$.

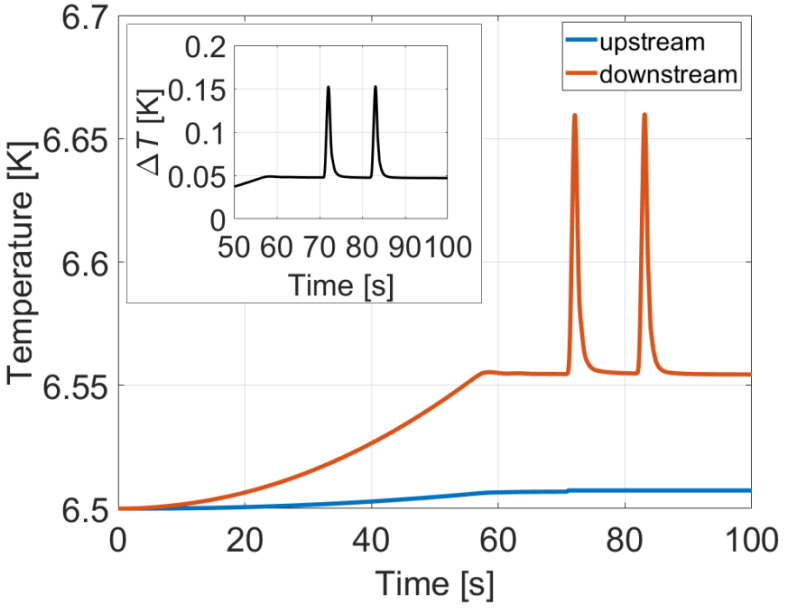


Figure 7.20: Evolution of helium temperature at upstream and downstream sensors relative to the high field zone of AC magnet. The insert delineates the temperature difference between the upstream and downstream measurements.

Similar to the calculation of energy generation $Q_{gen}$, as detailed in section 7.3.2 and represented by Equation 7.2, the energy deposition in the helium is estimated as follows [208]

$$E_{dep} = C_{He}\dot{m}\left(\int_{t'_{a1}}^{t'_{b1}} (T_{down}(t) - T_{up})\, dt + \int_{t'_{a2}}^{t'_{b2}} (T_{down}(t) - T_{up})\, dt\right), \tag{7.6}$$

where $C_{He}$ is the specific heat of helium at a constant pressure of 10 bar, $t'_{a1}$, $t'_{b1}$, $t'_{a2}$ and $t'_{b2}$ represent the time instants corresponding to the start and end of two temperature peaks, respectively.

Specifications of the cooling system, as well as heat conductivity and transfer coefficients used for the thermal stability tests of the ITER PF joint are summarized in Table 7.1. In addition, two helium mass flow rates, $\dot{m} = 3$ and 10 g/s, and incrementally increasing inlet temperatures from 5.8 to 7.1 K are used to create the stability variations.

### 7.3.5 Electro-thermal stability analysis method

The analyses presented in Figure 7.15 and Figure 7.20 demonstrate the notable influence of transient magnetic field and transport current on power dissipation and temperature evolution. However, the contribution of transport current remains relatively constant when compared to the dynamically changing peaks induced by magnetic field transients.

The generated energy progressively influences thermal disturbance along the flow direction by heating the liquid helium. The specific thermal model in the JackPot-AC/DC code operates on a petal level, treating the strands and helium flow in each individual petal as a uniformly distributed medium, as well as the temperature. For the sake of simplicity in the thermal stability analysis, especially considering the relatively small sole-petal and petal-petal heat transfer coefficients as listed in Table 7.1, a simplified model is proposed to demonstrate heat transfer and balance, by neglecting the relatively low heat transfer between strands and copper sole and petal to petal accordingly. The strands in the cable are treated as a circular entity surround by helium and do not directly contact the copper sole, as demonstrated in Figure 7.21.

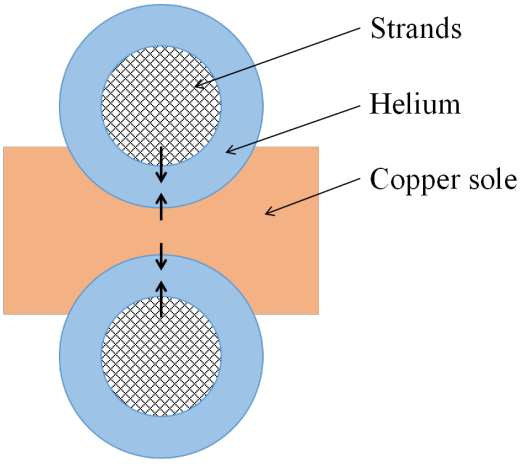


Figure 7.21: Schematic of the simplified thermal model for demonstration of the heat balance between the main three components of joints, the arrows indicate the probable heat transfer flows.

For the main three components of strands, helium and copper sole, the individual power balance equations are seen in Equations 7.7, 7.8 and 7.9, respectively, considering the influences of heat conduction, convection and deposition, while the relationship between three components is shown in Equation 7.10, with the relevant symbols are explained in Table 7.3.

As known from Figure 7.15, the total power generated in the joint nearly equals $P_{st}(x,t) + P_{sole}(x,t)$, if neglecting the minor contribution from the cable-to-sole contacts. Therefore, the left-hand side of Equation 7.10 represents the difference between the power deposited in the helium and the power generation, while the right-hand side includes the main three items enclosed in brackets. The first item denotes the heat transfer within the three components due to the temperature gradient, which is a sum of input energy with respect to the helium, the second item represents the power deposited in the strands and copper sole, while the last item is the amount of power removed by the helium, dependent on the helium mass flow rate $v_{He}$. The sum of these three items represents the heat perturbation and equilibrium in the helium, except for the influence from the sources of $P_{st}(x,t)$ and $P_{sole}(x,t)$. Therefore, based on the calculations of energy generation and deposition, as described in sections 7.3.2 and 7.3.4, respectively, a straightforward yet ef-

$$A_{st}\rho_{st}\frac{\partial C_{st}(T)T_{st}}{\partial t} = P_{st}(x,t) + A_{st}k_{st}\frac{\partial^2 T_{st}}{\partial x^2} - \varepsilon_{st}h_{st-He}(T_{st} - T_{He}) \tag{7.7}$$

$$\begin{aligned} A_{He}\rho_{He}\frac{\partial C_{He}(T)T_{He}}{\partial t} &= A_{He}k_{He}\frac{\partial^2 T_{He}}{\partial x^2} + \varepsilon_{st}h_{st-He}(T_{st} - T_{He}) \\ &+ \varepsilon_{sole}h_{sole-He}(T_{sole} - T_{He}) - v_{He}A_{He}\rho_{He}\frac{\partial C_{He}(T)T_{He}}{\partial x} \end{aligned} \tag{7.8}$$

$$\begin{aligned} A_{sole}\rho_{sole}\frac{\partial C_{sole}(T)T_{sole}}{\partial t} &= P_{sole}(x,t) + A_{sole}k_{sole}\frac{\partial^2 T_{sole}}{\partial x^2} \\ &- \varepsilon_{sole}h_{sole-He}(T_{sole} - T_{He}) \end{aligned} \tag{7.9}$$

$$\begin{aligned} A_{He}\rho_{He}\frac{\partial C_{He}(T)T_{He}}{\partial t} &- P_{st}(x,t) - P_{sole}(x,t) = \\ &+ (A_{st}k_{st}\frac{\partial^2 T_{st}}{\partial x^2} + A_{He}k_{He}\frac{\partial^2 T_{He}}{\partial x^2} + A_{sole}k_{sole}\frac{\partial^2 T_{sole}}{\partial x^2}) \\ &- (A_{st}\rho_{st}\frac{\partial C_{st}(T)T_{st}}{\partial t} + A_{sole}\rho_{sole}\frac{\partial C_{sole}(T)T_{sole}}{\partial t}) \\ &- (v_{He}A_{He}\rho_{He}\frac{\partial C_{He}(T)T_{He}}{\partial x}) \end{aligned} \tag{7.10}$$

Table 7.3: Summary of the symbols used in the thermal model analyses of the PFJEU6 joint.

| **Parameter** | **Unit** |
|---|---|
| Heat dissipation in strands $P_{st}$ | W |
| Heat dissipation in sole $P_{sole}$ | W |
| Cross-sectional area of strands $A_{st}$ | $m^2$ |
| Cross-sectional area of helium $A_{He}$ | $m^2$ |
| Cross-sectional area of copper sole $A_{sole}$ | $m^2$ |
| Strand-helium wetted perieter $\varepsilon_{st}$ | m |
| Helium-sole wetted perimeter $\varepsilon_{sole}$ | m |
| Strand heat capacity at constant pressure $C_{st}$ | m |
| Helium heat capacity at constant pressure $C_{He}$ | $J/(kg \cdot K)$ |
| Sole heat capacity at constant pressure $C_{sole}$ | $J/(kg \cdot K)$ |
| Velocity of helium flow $v_{He}$ | m/s |
| Density of strands $\rho_{st}$ | $kg/m^3$ |
| Density of helium $\rho_{He}$ | $kg/m^3$ |
| Density of copper sole $\rho_{sole}$ | $kg/m^3$ |
| Temperature of strands $T_{st}$ | K |
| Temperature of helium $T_{He}$ | K |
| Temperature of sole $T_{sole}$ | K |

fective method is proposed using the difference as a criterion and dynamically evaluating the equilibrium between energy generation and removal.

For the three trapezoidal magnetic field cases a, b, and c in Table 7.2, the transient change instead of the constant plateau dominates the evolution of power and temperature as shown in Figure 7.15 and Figure 7.20, respectively. Furthermore, the same amplitudes but different gradients mean distinct ramping times, consequently affecting the amounts of power and temperature generations in the form of peaks. Considering the constant time duration of 10 second is sufficiently long to neglect potential explicit interference between the rise and fall magnetic field fronts, the sum of time periods corresponding to the two magnetic field ramping fronts, $\Delta t_1 = 4$, $\Delta t_2 = 2$, and $\Delta t_3 = 1$ second, are adopted in the calculations of generated energy $Q_{gen}$ (Equation 7.2) and deposited energy $E_{dep}$ (Equation 7.6).

Additionally, according to the thermal model expressed in Equation 7.10, both energies are converted to power by dividing the individual time periods to appropriately assess and compare the influence of different magnetic field variations on thermal stability. The calculated results, corresponding to three values of magnetic field rates and different helium inlet temperatures and mass flow rates, are depicted in Figure 7.22.

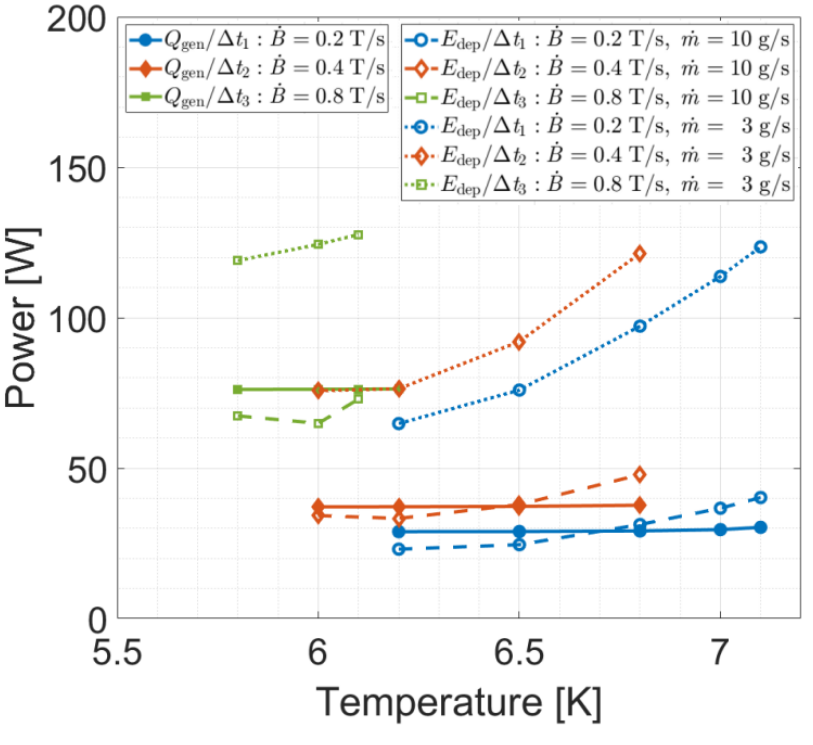


Figure 7.22: Calculated power generation versus helium temperature for assessment of transient stability in PF joints by analyzing the equilibrium between normalized energy generation and deposition. Explored under diverse conditions, including different trapezoidal magnetic field rates (0.2, 0.4, 0.8 T/s) and two helium mass flow rates (3 and 10 g/s).

The helium flow rate appears to have minimal direct impact on the electromagnetic property in the form of power generation $Q_{gen}/\Delta t$, but a pronounced effect on the deposited power $E_{dep}/\Delta t$ in helium. For joints cooled with a helium mass flow rate of 10 g/s, at a sufficiently low inlet temperature, the deposited power is lower than the generated power, signifying effective removal of generated energy and a relatively stable joint. However, as the inlet temperature increases, the deposited power gradually surpasses the generated power, leading to a quench occurrence at a certain temperature $T_q$. For magnetic field gradients of 0.2, 0.4, and 0.8 T/s, the critical quench temperatures are 6.8, 6.5, and 6.1 K, respectively. This observation aligns with the SULTAN measurements for the case of a 0.4 T/s gradient [164].

In the case of a helium flow rate of 3 g/s, the joint is no longer effectively cooled, meaning a deposited power significantly exceeding the cooling capability, leading to quench occurrence. This scenario is observed in the SULTAN stability test with 3 g/s helium flow, by which a lower transport current of 20 kA instead of 55 kA is applied.

Based on the quantitatively assessments of power generation and deposition, a criterion of is derived to estimate the thermal equilibrium, as shown in Equation 7.11

$$\begin{cases} E_{dep}/\Delta t - Q_{gen}/\Delta t < 0, & \Rightarrow \text{ Stable state,} \\ E_{dep}/\Delta t - Q_{gen}/\Delta t = 0, & \Rightarrow \text{ Critical state,} \\ E_{dep}/\Delta t - Q_{gen}/\Delta t > 0, & \Rightarrow \text{ Instable state.} \end{cases} \tag{7.11}$$

When this criterion is negative, the helium is capable of removing the generated power in time, keeping the system in stable. Otherwise, the gradually accumulated power triggers instability eventually. This method of judging the criterion indirectly reflects current and temperature margins, providing insights into the quench process. It is validated against simulations and SULTAN measurements, proving to be an effective and accurate approach for estimating quench initiation and propagation.

## 7.4 Conclusion

ITER magnet system coils are operating in severe electro-magnetic conditions with a high transport current and fast changing magnetic field. Especially for the PF coils made with NbTi superconductors, the relatively low temperature margin emphasizes the importance of sufficient thermal stability of the conductors in coil windings and joints.

The stability of the PF type of joint with stationary transport current was investigated through current sharing temperature tests first. Second, the stability under ITER operating conditions was analysed with the simulation model based on the JackPot-AC/DC code. The development of the power dissipation, current sharing, electric field distribution and thermal properties were analysed by simulation for different helium inlet temperatures. It is shown that due to the current and heat transfer properties of the copper sole in the joint, instability under ITER operating conditions occurs first in the conductor section just outside the joint box. The expected quench temperature is 0.2 K lower than the value found during the test in the SULTAN facility.

Furthermore, the stability of the joint with applied alternating field pulses was simulated. The investigation of quench occurrence and transient stability is of paramount

importance and intricacy, influenced by various electromagnetic, thermal, and hydraulic characteristics. This chapter addressed the comprehensive analysis of electromagnetic and thermal stability for ITER PF joints exposed to a transport current of 55 kA, different trapezoidal magnetic field rates, and various cooling conditions in terms of helium mass flow rates.

A novel and effective method was introduced, involving the assessment of equilibrium between energy generation and deposition, as well as the determination of current and temperature margins. This approach proved to be relatively efficient and accurate in studying the electromagnetic stability and thermal stability of the PF joint when compared to the combined models method. Significantly, it enables the determination of quench initiation and propagation on a macroscopic scale. The proposed numerical method is well-validated against SULTAN stability tests, contributing substantively to the research and development of the ITER magnet system.

Following simulations of both stationary and alternating magnetic field conditions, a systematic analysis of the joint stability has been obtained, which uniquely provides a much better understanding and guidance for safe operation of the PF coils. Moreover it benefits joint design and performance optimization of next generation ITER-like Cable-In-Conduit Conductors.

# Chapter 8

# Conclusion and outlook

The performance of the electrical joint, as a transition point between two superconducting cables or a cable and a copper terminal is critical for the reliable operation of the ITER magnet. Consequently thorough understanding and qualification tests are compulsory parts of the ITER magnet R&D program. Here we primarily focus on the so-called PF joints in the Poloidal Field coils.

The electro-magnetic and thermal performances are tested in the reference laboratories like the SULTAN facility. However, the physical testing conditions may still significantly differ from real operating ones due to the limitations imposed by the experimental facility, in terms of magnetic field values, magnetic field variation rates, sample exposure length and temperature conditions.

Therefore, in order to assess the relevance of the specific test configuration as well as to systematically study and optimize the joints for real operating conditions, precise numerical simulations are mandatory. The numerical code JackPot-AC/DC, featuring the description and simulation of CIC conductors with strand-level details, is used to analyze the performance of cables and joints.

Thorough understanding of the strand properties is fundamental for the experimental and numerical analysis of the CICCs and joints. For the ITER $Nb_3Sn$ strands that normally operate in relatively low magnetic field region ($\leq 4$ T), practical scaling laws are obtained, by performing a series of magnetization and transport current measurements for various magnetic field values. Since the transport current density is proportional to the magnetization, it is possible to combine these two series of data through a common magnetic field region, in order to obtain a unified scaling law for the whole magnetic field range that covers the ITER magnet operating condition.

The hysteresis loss of the joint is estimated using measured single strand data, taking into account the angular dependence of hysteresis loss on the applied magnetic field. By accumulating the data of hundreds of twisted strands, the hysteresis loss of CICCs and joints that operate under various magnetic field conditions are calculated. As an important fraction of the total AC loss, the accurate calculation of hysteresis loss helps to improve the stability of conductor or joint significantly.

Since inter-strand, inter-petal and strand-to-sole contact resistances determine to a high degree the performance of cables and their lap-type joints, precise knowledge of the various resistance and resistivity parameters turns out to be the key factor when quantitative predictions are required.

The various contact resistances present within a PF joint were extensively investigated at the University of Twente. The inter-strand resistances (first to fourth stage) are in the range of 2 to 4 nΩm and increase slightly with subsequent cabling stages. The inter-petal resistance (fifth stage) is in the range of 6 to 12 nΩm, which is about 2.5 to 4.5 times higher than the inter-strand resistances. The inter-strand and inter-petal contact resistances of the joint are, respectively, 30 and 300 times smaller than for regular not-compacted ITER PF conductors. Furthermore, the inter-petal to interstrand ratio is decreased from 40 to 4.5 because the conductor in the joint is compressed to a void fraction of 19%.

The strand to copper sole resistivity was evaluated by measuring the resistance between single strand pairs, each selected from different cables. The results show an average resistance of 16 nΩ and a minimal resistance of 7 nΩ, while the overall joint resistance

was measured as 5 nΩ. Besides the contact resistances, the AC loss of a PF joint was also measured by magnetization and calorimetric methods showing fairly good agreement.

For the first time, contact resistances and AC loss of a full-size ITER PF joint were measured. The relevant contact resistivity parameters are derived using JackPot-AC/DC simulations, by fitting a combination of constraints comprising various contact resistances and AC loss.

A rather good agreement has been observed between simulated and measured AC loss data, except for some unexplained discrepancy at the saturation transition region. This may be related to the specific distribution of some contact resistances, which was not further investigated within this work.

The overall comparison provides sufficient validation of the derived contact resistivities and solder parameters. In addition, a parametric sensitivity analysis of contact resistivity, solder parameters, impact of void fraction and external field configurations, was performed.

The measurements on the ITER pre-qualification PF joint samples (PFJEU2 and PFJEU3) were performed in the SULTAN facility. Unexpected nonlinear voltage-current characteristics were observed during the DC tests. The resistance increases from 5.0 to 8.5 nΩ as transport current and background magnetic field increase.

The simulations based on the JackPot-AC/DC model show that the joint resistance is expected to be nearly independent of transport current and background magnetic field. Only a small effect of some 0.5 nΩ from the magneto-resistance of copper sole and shim is anticipated. The model was adjusted to include possible electrical features related to the interfaces between cable, sole and shim.

The simulations reveal that the strong nonlinear voltage-current characteristic observed is most likely caused by a defective connection between copper sole and shim, affected by the electromagnetic force. The mechanically weakly connected parts generate a separating or compressing force under a varying electromagnetic force by transport current or background magnetic field, causing a varying resistance correspondingly.

Further a detailed analysis of the local power dissipation and current distribution in the joint and its strands is presented, allowing a quantitative assessment of the joint stability in AC operating conditions. The model outcome was validated by an experiment on a similar sample PFJEU3 and a post-mortem examination of the PFJEU2 sample.

For the ITER type twin-box lap joints operating in pulsed magnetic field mode, large coupling currents are normally induced and cause severe current non-uniformity and potentially instability. A design modification of ITER PF joints was proposed by introducing polyimide layers named masks to block the large induced current loops. The functionality of the masks was systematically simulated using the JackPot-AC/DC model, with respect to the aspects of current distribution, power distribution and temperature evolution.

The implementation of masks in all considered joint configurations helps to reduce the globally induced loop currents in the conductor petals down to allowable values mainly determined by the enthalpy of the helium and desired temperature margin. It also reduces the number of strands with currents approaching or exceeding the critical current, and thereby it reduces the risk of a quench in the joint. It was found that the implementation of masks does increase the total heat dissipation in some petals, but makes the heat dis-

tribution more uniform along the joint, compared to the concentrated heat in the joints without masks. This has obviously a positive effect on the temperature profiles along the joint box, by smoothing the peaks of temperature in the petals.

Overall, the application of masks in the CICC lap-type joints will improve the joint's thermal stability and thus give margin on the working condition of the final coils. In order to reduce further the induced currents bypassing the masks, it is suggested to increase the inter-petal resistivity in combination with somewhat decreasing the RRR of copper, to be investigated in more details.

Based on the contact resistivities derived from the measurements and the design proposal with mask implemented, joints were manufactured and underwent the strict qualification tests in the SULTAN facility. Since the ITER coils are operating in very severe electro-magnetic conditions, including the high transport current and fast changing magnetic field, especially for the PF coils wound with the NbTi superconductors, the relatively low temperature margin makes that stability becomes the priority for the design and manufacture of the conductor and joint.

The SULTAN qualification tests consist of a series of DC, AC and stability tests, however, limited by facility specific constraints. Further investigations to extend predictions to true operational ITER conditions were performed through simulations using the JackPot-AC/DC model.

The stability of the joint with transport current is evaluated with the $T_{cs}$ tests firstly. Both cases, the SULTAN-like and ITER-like DC magnetic field configurations, were analysed. With respect to the stepwise increasing helium inlet temperature, particularly at the critical state around quench, the corresponding developments of the power dissipation, current, electrical field and thermal properties were analysed quantitatively and provide a thorough understanding of the stability under DC condition.

It is found that, due to the current and heat transfer function of the copper sole in the joint, under ITER operating conditions, the instability most likely occurs first in the conductor section outside the joint box. Furthermore, the quench temperature is lower than the value tested in the SULTAN facility to a degree of about 0.2 K.

Next the stability of the joint with AC magnetic field imposed was evaluated. A novel and effective method was introduced, involving the assessment of equilibrium between energy generation and deposition, as well as the determination of current and temperature margins. This approach proved to be relatively efficient and accurate in studying the electromagnetic stability and thermal stability of the PF joint when compared to the conventional combined models method. Significantly, it enables the determination of quench initiation and propagation on a global scale.

The proposed numerical method was well-validated against SULTAN stability tests, contributing substantively to the research and development of the ITER magnet system. By means of both, experimental and numerical methods, the electro-magnetic and thermal behaviors of the ITER full-size PF lap-type joint were analysed systematically.

The ITER magnet system comprises different types of coils that work collaboratively to restrain the motion of charged plasma particles and control the shape and position equilibrium. The PF coils operates in the pulsed mode, making them more susceptible to AC loss and thermal disturbance. Particularly, the twin-box lap-type joint is critical for the

stability of the entire coil as it experiences the superconducting and non-superconducting state transition. This thesis highlights the importance of strand-level analyses of PF joints for evaluating the performance of ITER magnets, in terms of electromagnetic and thermal stability. The DC and AC results provide guidance for the safe and reliable operation of the PF coils during ITER's operation.

For the next generation fusion machines such as DEMO in Europe and CFETR in China, the CICC concept remains widely adopted due to its high current capacity, effective cooling, mechanical stability and effective quench protection [55], [209], [210]. To achieve higher magnetic fields and, or, reduced size, promising advancements in magnet technology have emerged, including use of high-$J_c$ $Nb_3Sn$ in combination with react-and-wind and grading technologies, which allow for flexible adjustment of superconducting and mechanical materials in response to local magnetic field demands. In addition, high-temperature superconducting $Re$BCO tapes, manufactured in Roebel, CORC, or TSTC type of cables [211]–[213], as well as $MgB_2$ strands in CICCs applicable for low-field coils [214], open up new possibilities in coil design, manufacturing and reliability of operation.

In general, advancements in magnet technology are aimed in two main directions [55]. In one direction the focus is on jointless coils, which would allow to reduce or even eliminate instability stemming from vulnerable joints. The use of react-and-wind type of $Nb_3Sn$ superconductor can significantly reduce effects of compressive strain, and the conductor may be jacketed by longitudinally welding of two steel half-profiles. The freedom in choosing the jacket thickness and shape implies virtually unlimited conductor manufacturing length, making it possible to manufacture an entire coil in one go provided quality control can be performed in-situ as well.

The second direction is focused on using segmented coils [54]–[57]. Due to current challenges in manufacturing $Re$BCO tape conductor of sufficient length, segmented or demountable coil technologies enable the use of high-performance $Re$BCO superconductor while allowing for flexible design, manufacturing, and maintenance procedures. However, the extensive use of joints raises the risk of degraded performance concerning control of joint resistance, current sharing, power dissipation, and thermal stability. Significant challenges remain, regarding this thesis, they include joint concepts like bridge and lap type joints [215], and designs adapted to various types of cables such as Roebel, CORC, or TSTC; as well as the effects of twisting, bending, and transposition on the electrical and mechanical behavior of joints [216], [217]. In addition, the development of technology for robotic assembly of multiple joints is needed [55].

Substantial study in joint technology is crucial for the stability and reliability of magnet systems, including the development of proper numerical models able to predict joint behavior in detail. Joint design essentially depends on specific cable configurations based on certain shape of the strands that compose them. Although the JackPot-AC/DC model has shown promise in simulating the electromagnetic and thermal performance of cable-in-conduit cables and Rutherford cables comprising round strands, certainly adjustments in the network based model are needed to accommodate non-isotropic and high aspect ratio $Re$BCO coated conductors in the form of tapes.

# Bibliography


[1] L. Rutherford *et al.*, "Transmutation effects observed with heavy hydrogen", *Proc.R.Soc.A*, vol. 144, no. 692, 1934.

[2] J. Jacquinot, "Fifty years in fusion and the way forward", *Nucl. Fusion*, vol. 50, p. 014 001, 2010.

[3] T. Donne *et al.*, "European research roadmap to the realization of fusion energy", *EUROfusion scientific publication*, 2018.

[4] J. D. Lawson, "Some criteria for a power producing thermonuclear reactor", *Proc. Phys. Soc. B*, vol. 70, pp. 6–10, 1957.

[5] W. M. Stacey, *Fusion - An Introduction to the Physics and Technology of Magnetic confinement Fusion*. WILEY-VCH, 2008.

[6] F. Romanelli *et al.*, "A roadmap to the realisation of fusion energy", *EFDA scientific publication*, 2012.

[7] M. Kikuchi *et al.*, *FUSION PHYSICS*. IAEA, 2012.

[8] B. Bigot, "Progress toward ITER's first plasma", *Nucl. Fusion*, vol. 59, p. 1120 01, 2019.

[9] N. Mitchell *et al.*, "The ITER magnet system", *IEEE Trans. Appl. Supercond.*, vol. 18, pp. 435–440, 2008.

[10] C. Sborchia *et al.*, "Design and specifications of the ITER TF coils", *IEEE Trans. Appl. Supercond.*, vol. 18, no. 2, pp. 463–466, 2008.

[11] F. Savary *et al.*, "The toroidal field coils for the ITER project", *IEEE Trans. Appl. Supercond.*, vol. 22, no. 3, p. 4 200 904, 2012.

[12] N. Mitchell *et al.*, "The ITER magnets: Design and construction status", *IEEE Trans. Appl. Supercond.*, vol. 22, no. 3, p. 4 200 809, 2012.

[13] P. Libeyre *et al.*, "An optimized central solenoid for ITER", *IEEE Trans. Appl. Supercond.*, vol. 20, no. 3, pp. 398–401, 2010.

[14] P. Libeyre *et al.*, "Addressing the technical challenges for the construction of the ITER central solenoid", *IEEE Trans. Appl. Supercond.*, vol. 22, no. 3, p. 4 201 104, 2012.

[15] B. S. Lim *et al.*, "Development of the ITER PF coils", *IEEE Trans. Appl. Supercond.*, vol. 22, no. 3, p. 4 201 404, 2012.

[16] F. Simon *et al.*, "Design of the ITER PF coil joints", *IEEE Trans. Appl. Supercond.*, vol. 22, no. 3, p. 4 804 104, 2012.

[17] A. Foussa *et al.*, "The ITER correction coils design", *IEEE Trans. Appl. Supercond.*, vol. 20, no. 3, pp. 402–406, 2010.

[18] A. Foussa *et al.*, "From design to development phase of the ITER correction coils", *IEEE Trans. Appl. Supercond.*, vol. 21, no. 3, pp. 1960–1963, 2011.

[19] ITER, "Design description document: Magnet", ITER DDD 11 ITER_D_22H-V5L v2.2, 2006.

[20] Y. Iwasa, *Case Studies in Superconducting Magnets*. New York: Springer, 2009.

[21] National High Magnetic Field Laboratory - Applied Superconductivity Center. (2018), [Online]. Available: {<url=https://nationalmaglab.org/magnet-development/applied-superconductivity-center/plots/>}.

[22] A. Godeke, "A review of the properties of $Nb_3Sn$ andtheir variation with A15 composition, morphology and strain state", *Supercond. Sci. Technol.*, vol. 19, R68–R80, 2006.

[23] L. Bottura, "A practical fit for the critical surface of NbTi", *IEEE Trans. Appl. Supercond.*, vol. 10, pp. 1054–1057, 2000.

[24] L. Muzzi *et al.*, "Test results of a NbTi wire for the ITER poloidal field magnets: A validation of the 2-pinning components model", *IEEE Trans. Appl. Supercond.*, vol. 21, pp. 3132–3137, 2011.

[25] A. Godeke *et al.*, "Scaling of the critical current in ITER type niobium-tin superconductors in relation to the applied field, temperature and uni-axial applied strain", *IEEE Trans. Appl. Supercond.*, vol. 9, no. 2, pp. 161–164, 1999.

[26] A. Godeke *et al.*, "A general scaling relation for the criticalcurrent density in $Nb_3Sn$", *Supercond. Sci. Technol.*, vol. 19, R100–R116, 2006.

[27] M. N. Wilson, *Superconducting magnets*. Oxford: Clarendon Press, 1983.

[28] T. Akachi *et al.*, "Magnetic instabilities in high field superconductors", *Jpn. J. Appl. Phys.*, vol. 20, no. 8, pp. 1559–1571, 1981.

[29] Z. Charifoulline, "Residual Resistivity Ratio (RRR) measurements of LHC superconducting NbTi cable strands", *IEEE Trans. Appl. Supercond.*, vol. 16, no. 2, pp. 1188–1191, 2006.

[30] M. C. Jewell *et al.*, "World-wide benchmarking of ITER $Nb_3Sn$ strand test facilities", *IEEE Trans. Appl. Supercond.*, vol. 20, no. 3, pp. 1500–1503, 2010.

[31] A. K. Ghosh, "*V-I* transition and n-value of multifilamentary LTS and HTS wires and cables", *Physica C*, vol. 401, pp. 15–21, 2004.

[32] D. Taylor *et al.*, "Relationship between the n-value and critical current in $Nb_3Sn$ superconducting wires exhibiting intrinsic and extrinsic behaviour", *Supercond. Sci. Technol.*, vol. 18, S297–S302, 2005.

[33] X. Xu, "A review and prospects for $Nb_3Sn$ superconductor development", *Supercond. Sci. Technol.*, vol. 30, p. 093 001, 2017.

[34] A. Devred *et al.*, “Status of ITER conductor development and production”, *IEEE Trans. Appl. Supercond.*, vol. 22, no. 3, p. 4 804 909, 2012.

[35] J. F. Li *et al.*, “New progress of ITER PF strand production in WST”, *Journal of Physics: Conference Series*, vol. 507, p. 022 014, 2014.

[36] L. Muzzi, “Cable-in-conduit conductors: Lessons from the recent past for future developments with low and high temperature superconductors”, *Supercond. Sci. Technol.*, vol. 28, p. 053 001, 2015.

[37] National High Magnetic Field Laboratory - Applied Superconductivity Center. (2013), [Online]. Available: <url=https://nationalmaglab.org/magnet-development/applied-superconductivity-center/asc-image-gallery/Nb3Sn-image-gallery>.

[38] R. Zanino *et al.*, “A review of thermal-hydraulic issues in ITER cable-in-conduit conductors”, *Cryogenics*, vol. 46, pp. 541–555, 2006.

[39] R. Zanino *et al.*, “CFD model of ITER CICC. Part VI: Heat and mass transfer between cable region and central channel”, *Cryogenics*, vol. 50, pp. 158–166, 2010.

[40] ITER, “Design description document: Conductors”, 2NBKXY v1.2, 2009.

[41] H. Kajitani *et al.*, “Development of cable-in-conduit conductor for ITER CS in Japan”, *SN Appl. Sci.*, vol. 1, no. 182, 2019.

[42] A. Nijhuis *et al.*, “Optimization of ITER $Nb_3Sn$ CICCs for coupling loss, transverse electromagnetic load and axial thermal contraction”, *Supercond. Sci. Technol.*, vol. 25, p. 015 007, 2012.

[43] Y. Wu *et al.*, “Status of the ITER conductors in China”, *IEEE Trans. Appl. Supercond.*, vol. 26, no. 4, p. 6 000 405, 2016.

[44] P. Decool *et al.*, “Joints for large superconducting conductors”, *Fusion Eng. Des.*, vol. 58-59, pp. 123–127, 2001.

[45] Y. Ilyin *et al.*, “Qualification program of lap joints for ITER coils”, *IEEE Trans. Appl. Supercond.*, vol. 28, no. 3, p. 4 201 306, 2018.

[46] Y. Ilyin *et al.*, “Design and qualification of joints for ITER magnet busbar system”, *IEEE Trans. Appl. Supercond.*, vol. 26, no. 4, p. 4 800 905, 2016.

[47] P. Decool *et al.*, “Hydraulic characterization of twin-box joints for ITER magnets”, *Fusion Eng. Des.*, vol. 146, pp. 543–546, 2019.

[48] Y. Ilyin *et al.*, “Results of all ITER TF full-size joint sample tests in Japan”, *IEEE Trans. Appl. Supercond.*, vol. 31, no. 5, p. 4 201 905, 2021.

[49] N. N. Martovetsky *et al.*, “Development of the butt joint for the ITER central solenoid”, *IEEE Trans. Appl. Supercond.*, vol. 17, no. 2, pp. 1358–1361, 2007.

[50] N. N. Martovetsky *et al.*, “Development of the joints for ITER central solenoid”, *IEEE Trans. Appl. Supercond.*, vol. 21, no. 3, pp. 1922–1925, 2011.

[51] N. N. Martovetsky *et al.*, “Development of the bus joint for the ITER central solenoid”, *Fusion Eng. Des.*, vol. 88, pp. 1601–1604, 2013.

[52] C. N. T. Dao *et al.*, "Development of coax compacted joint assemblyprocess for the ITER central solenoid", *IEEE Trans. Appl. Supercond.*, vol. 31, no. 5, p. 4 202 405, 2021.

[53] J. Rong *et al.*, "Development of superconducting joint for tokamak feeder busbar", *Fusion Eng. Des.*, vol. 138, pp. 41–47, 2019.

[54] F. J. Mangiarotti, "Design of demountable toroidal field coils with REBCO superconductors for a fusion reactor", Ph.D. dissertation, Massachusetts Institute of Technology, 2016.

[55] N. Mitchell *et al.*, "Superconductors for fusion: A roadmap", *Supercond. Sci. Technol.*, vol. 30, p. 103 001, 2021.

[56] N. Yanagi *et al.*, "Design and development of high-temperature superconducting magnet system with joint-winding for the helical fusion reactor", *Nucl. Fusion*, vol. 55, p. 053 021, 2015.

[57] B. N. Sorbom *et al.*, "ARC: A compact, high-field, fusion nuclear science facility and demonstration power plant with demountable magnets", *Fusion Eng. Des.*, vol. 100, pp. 378–405, 2015.

[58] A. M. Campbell, "A general treatment of losses in multifilamentary superconductors", *Cryogenics*, vol. 22, no. 1, pp. 3–16, 1982.

[59] W. L. Carr Jr, "AC loss in a twisted filamentary superconducting wire", *J. Appl. Phys.*, vol. 45, no. 2, pp. 929–938, 1974.

[60] W. L. Carr Jr, "Alternating field losses in a multifilamentary superconducting wire for weak AC fields superimposed on a constant bias", *J. Appl. Phys.*, vol. 46, no. 9, pp. 4048–4052, 1975.

[61] G. H. Morgan, "Theoretical behavior of twisted multi-core superconducting wire in a time varying uniform magnetic field", *Cryogenics*, vol. 41, pp. 3673–3679, 1970.

[62] G. H. Morgan, "Eddy currents in flat metal-filled superconducting braids", *Cryogenics*, vol. 44, pp. 3319–3322, 1973.

[63] G. Ries, "AC-losses in multifilamentary superconductors at technical frequencies", *IEEE Trans. Magn.*, vol. 13, no. 1, pp. 524–526, 1977.

[64] A. Nijhuis *et al.*, "Study on the coupling loss time constants in full size $Nb_3Sn$ cic model conductors for fusion magnets", *Adv. Cryog. Eng.*, vol. 42, no. B, pp. 1281–1288, 1995.

[65] D. Ciazynski *et al.*, "Electrical and thermal designs and analyses of joints for the ITER PF coils", *IEEE Trans. Appl. Supercond.*, vol. 12, no. 1, pp. 538–542, 2002.

[66] L. Bottura, "Stability and protection of CICCs: An updated designer's view", *Cryogenics*, vol. 38, no. 5, pp. 491–502, 1998.

[67] A. Nijhuis, "Mechanical and eletro-magnetic performance of $Nb_3Sn$ superconductors for fusion", Ph.D. dissertation, University of Twente, 2016.

[68] E. van Lanen and A. Nijhuis, "JackPot: A novel model to study the influence of current non-uniformityand cabling patterns in cable-in-conduit conductors", *Cryogenics*, vol. 50, pp. 139–148, 2010.

[69] P. Bruzzone *et al.*, "Upgrade of operating range for SULTAN test facility", *IEEE Trans. Appl. Supercond.*, vol. 12, no. 1, pp. 520–523, 2002.

[70] P. Bruzzone *et al.*, "Qualification tests and facilities for the ITER superconductors", *Nucl. Fusion*, vol. 49, p. 065 034, 2009.

[71] I. Pong *et al.*, "Worldwide benchmarking of ITER internal tin $Nb_3Sn$ and NbTi strands test facilities", *IEEE Trans. Appl. Supercond.*, vol. 22, no. 3, p. 4 802 606, 2012.

[72] E. P. A. van Lanen and A. Nijhuis, "Simulation of interstrand coupling loss in cable-in-conduit conductors with JackPot-AC", *IEEE Trans. Appl. Supercond.*, vol. 21, no. 3, pp. 1926–1929, 2011.

[73] M. Breschi *et al.*, "Results of the TF conductor performance qualification samples for the ITER project", *Supercond. Sci. Technol.*, vol. 25, p. 095 004, 2012.

[74] L. Reccia *et al.*, "Preparation of PF1/6 and PF2 conductor performance qualification sample", *IEEE Trans. Appl. Supercond.*, vol. 21, no. 3, pp. 1930–1933, 2011.

[75] K. Sedlak *et al.*, "DC performance results versus assessment of ITER main busbar NbTi conductors", *IEEE Trans. Appl. Supercond.*, vol. 25, no. 3, p. 4 801 204, 2015.

[76] B. Stepanov *et al.*, "Impact of sample preparation procedure on the test results of four US ITER TF conductors", *IEEE Trans. Appl. Supercond.*, vol. 20, no. 3, pp. 508–511, 2010.

[77] C. Calzolaio *et al.*, "In situ $T_c$ measurements of $Nb_3Sn$ cable in conduitconductors via an inductive method", *IEEE Trans. Appl. Supercond.*, vol. 22, no. 3, p. 9 002 604, 2012.

[78] P. Bruzzone *et al.*, "Test results of the ITER PF insert conductor short sample in SULTAN", *IEEE Trans. Appl. Supercond.*, vol. 15, no. 2, pp. 1351–1354, 2005.

[79] Y. Nunoya *et al.*, "Test result of a full-size conductor developed for the ITER TF coils", *IEEE Trans. Appl. Supercond.*, vol. 21, no. 3, pp. 1982–1986, 2011.

[80] P. Bruzzone *et al.*, "Methods, accuracy and reliability of ITER conductor tests in SULTAN", *IEEE Trans. Appl. Supercond.*, vol. 19, no. 3, pp. 1508–1511, 2009.

[81] R. J. Thome *et al.*, "Pool-cooled superconducting coils: Past, present and future", *Adv. Cryog. Eng.*, vol. 31, pp. 341–354, 1986.

[82] A. Nijhuis *et al.*, "Performance of an ITER CS1 model coil conductor under transverse cyclic loading up to 40,000 cycles", *IEEE Trans. Appl. Supercond.*, vol. 14, no. 2, pp. 1489–1494, 2004.

[83] A. Nijhuis *et al.*, "The effect of axial and transverse loading on the transport properties of ITER $Nb_3Sn$ strands", *Supercond. Sci. Technol.*, vol. 26, p. 084 004, 2013.

[84] P. Bruzzone *et al.*, "Test of ITER conductors in SULTAN: An update", *Fusion Eng. Des.*, vol. 86, pp. 1406–1409, 2011.

[85] M. Breschi *et al.*, "Performance analysis of the NbTi conductor qualification samples for the ITER project", *Supercond. Sci. Technol.*, vol. 28, p. 115 001, 2015.

[86] F. Cau *et al.*, "Inter-strand resistance in the termination of ITER conductors", *IEEE Trans. Appl. Supercond.*, vol. 18, no. 2, pp. 1101–1104, 2008.

[87] F Cau and P Bruzzone, "Inter-strand resistance measurements in the termination of the ITER SULTAN samples", *Supercond. Sci. Technol.*, vol. 22, p. 045 012, 2009.

[88] R. Wesche *et al.*, "Sudden take-off in large NbTi conductors: Not a stability issue", *Adv. Cryog. Eng. Mat.*, vol. 50, pp. 820–827, 2004.

[89] P. Bruzzone *et al.*, "Results of contact resistance distribution in NbTi and $Nb_3Sn$ ITER conductor termination", *IEEE Trans. Appl. Supercond.*, vol. 17, no. 2, pp. 1378–1381, 2007.

[90] A. Nijhuis *et al.*, "Change of interstrand contact resistance and coupling loss in various prototype ITER NbTi conductors with transverse loading in the Twente Cryogenic Cable Press up to 40,000 cycles", *Cryogenics*, vol. 44, pp. 319–339, 2004.

[91] E. P. A. van Lanen *et al.*, "Interstrand resistance measurements on the conductor terminations of TFPRO2 and JATF3 SULTAN samples", *IEEE Trans. Appl. Supercond.*, vol. 20, no. 3, pp. 474–477, 2010.

[92] Y. Wang *et al.*, "Review of AC loss measuring methods for HTS tape and unit", *IEEE Trans. Appl. Supercond.*, vol. 24, no. 5, p. 9 002 306, 2014.

[93] M. P. Oomen, "AC loss in superconducting tapes and cables", Ph.D. dissertation, University of Twente, 2000.

[94] S. Foner, "Versatile and sensitive vibrating-sample magnetometer", *Rev. Sci. Instrum.*, vol. 30, pp. 548–557, 1959.

[95] S. Foner, "The vibrating sample magnetometer: Experiences of a volunteer (invited)", *J. Appl. Phys.*, vol. 79, pp. 4740–4745, 1996.

[96] E. P. A. van Lanen *et al.*, "Full-scale calculation of the coupling losses in ITER size cable-in-conduit conductors", *Supercond. Sci. Technol.*, vol. 25, p. 025 012, 2012.

[97] E. P. A. van Lanen *et al.*, "Validation of a strand-level CICC-joint coupling loss model", *Supercond. Sci. Technol.*, vol. 25, p. 025 013, 2012.

[98] G. Rolando *et al.*, "Experimental validation of a lap-type joint AC loss model with an ITER correction coil conductor joint", *Fusion Eng. Des.*, vol. 89, pp. 867–870, 2014.

[99] G. Rolando *et al.*, "Performance assessment and optimization of the ITER toroidal field coil joints", *Supercond. Sci. Technol.*, vol. 26, p. 085 004, 2013.

[100] G. Rolando *et al.*, "Analysis of heat load, current margin and current nonuniformity in ITER PF coil joints", *IEEE Trans. Appl. Supercond.*, vol. 23, no. 3, p. 4 201 405, 2013.

[101] T. Bagni *et al.*, "Electromagnetic and thermal stability of the ITER central solenoid during a 15 MA plasma scenario", *Supercond. Sci. Technol.*, vol. 32, p. 085 002, 2019.

[102] T. Bagni *et al.*, "Analysis of ITER NbTi and $Nb_3Sn$ CICCs experimental minimum quench energy with JackPot, MCM and THEA models", *Supercond. Sci. Technol.*, vol. 30, p. 095 003, 2017.

[103] N. A. Gumerov *et al.*, *Fast Multipole Methods for the Helmholz Equation in Three Dimensions*. Oxford: Elsevier, 2005.

[104] E. P. A. van Lanen and A. Nijhuis, "Numerical analysis of the DC performance of ITER TF samples with different cabling pattern based on resistance measurements on terminations", *Supercond. Sci. Technol.*, vol. 24, p. 085 010, 2011.

[105] A. Nijhuis and H. H. J. ten Kate, "Parametric study on coupling loss in subsize ITER $Nb_3Sn$ cabled specimen", *IEEE Trans. Magn.*, vol. 32, no. 4, pp. 2743–2746, 1996.

[106] G. Rolando *et al.*, "Minimizing coupling loss by selection of twist pitch lengths in multi-stage cable-in-conduit conductors", *Supercond. Sci. Technol.*, vol. 27, p. 015 006, 2014.

[107] A. E. Ruehli, "Equivalent circuit models for three-dimensional multiconductor systems", *IEEE Trans. Microw. Theory Techn.*, vol. 3, pp. 216–221, 1974.

[108] F. W. Grover, *Inductance calculations: working formulas and tables*. New York: Dover Punlication, Inc, 1946.

[109] B. van de Wiele *et al.*, "Application of the fast multipole method for the evaluation of magnetostatic fields in micromagnetic computations", *J. Comput. Phys.*, vol. 227, pp. 9913–9932, 2008.

[110] W. Offringa, "Thermal-hydraulic joint model with typical pf joint parameters as exemplary input (test-joint)", ITER report, 4BZB5N v1.4, 2011.

[111] G. Rolando *et al.*, "Temperature and current margin of ITER central solenoid conductor designs during a 15 MA plasma scenario", *Supercond. Sci. Technol.*, vol. 27, p. 025 010, 2014.

[112] L. Bottura *et al.*, "Analysis of transverse heat transfer coefficient in CICC's with central cooling channel", *Cryogenics*, vol. 46, pp. 597–605, 2006.

[113] C. Marinucci *et al.*, "Analysis of the transverse heat transfer coefficients in a dual channel ITER-type cable-in-conduit conductor", *Cryogenics*, vol. 47, pp. 563–576, 2007.

[114] Kitware Inc. "Paraview, software code available on website:" (), [Online]. Available: `<https://www.paraview.org/>`.

[115] A. Vostner *et al.*, "Statistical analysis of the $Nb_3Sn$ strand production for the ITER toroidal field coils", *Supercond. Sci. Technol.*, vol. 30, p. 045 004, 2017.

[116] A. Devred *et al.*, "Challenges and status of ITER conductor production", *Supercond. Sci. Technol.*, vol. 27, p. 044 001, 2014.

[117] C. Zhou *et al.*, "The scaling parameterization of ITER superconducting Nb-Ti strands throughout worldwide production", *IEEE Trans. Appl. Supercond.*, vol. 26, pp. 1–4, 2016.

[118] I. Pong *et al.*, "Current sharing temperature of NbTi SULTAN samples compared to prediction using a single pinning mechanism parametrization for NbTi strand", *Supercond. Sci. Technol.*, vol. 25, p. 054 011, 2012.

[119] L. Bottura and B. Bordini, "$Jc(B,T,\varepsilon)$ Parameterization for the ITER $Nb_3Sn$ production", *IEEE Trans. Appl. Supercond.*, vol. 19, pp. 1521–1524, 2009.

[120] J. W. Ekin, "Unified scaling law for flux pinning in practical superconductors: I. separability postulate, raw scaling data and parameterization at moderate strains", *Supercond. Sci. Technol.*, vol. 23, p. 083 001, 2010.

[121] J. W. Ekin *et al.*, "Unified scaling law for flux pinning in practical superconductors: II. parameter testing, scaling constants, and the extrapolative scaling expression", *Supercond. Sci. Technol.*, vol. 29, p. 123 002, 2016.

[122] J. W. Ekin *et al.*, "Unified scaling law for flux pinning in practical superconductors: III. minimum datasets, core parameters, and application of the extrapolative scaling expression", *Supercond. Sci. Technol.*, vol. 30, p. 033 005, 2017.

[123] A. Torre *et al.*, "Review of experimental results and models for AC losses in the ITER PF and CS conductors", *IEEE Trans. Appl. Supercond.*, vol. 32, no. 6, p. 4 700 605, 2022.

[124] E. Seiler *et al.*, "Hysteresis losses and effective $J_c(B)$ scaling law for ITER $Nb_3Sn$ strands", *IEEE Trans. Appl. Supercond.*, vol. 26, p. 8 200 307, 2016.

[125] T. Boutboul *et al.*, "European $Nb_3Sn$ superconducting strand production and characterization for ITER TF coil conductor", *IEEE Trans. Appl. Supercond.*, vol. 26, no. 4, p. 6 000 604, 2016.

[126] K. Tachikawa and P. J. Lee, "History of $Nb_3Sn$ and related A15 wires", *in 100 Years of Superconductivity*, vol. 11.3, 2012.

[127] P. Bruzzone *et al.*, "Bench mark testing of $Nb_3Sn$ strands for the ITER model coil", *Adv. Cryog. Eng. Mat.*, vol. 42, pp. 1351–1358, 1995.

[128] A. Nijhuis *et al.*, "Critical current measurement with spatial periodic bending imposed by electromagnetic force on a standard test barrel with slots", *Rev. Sci. Instrum.*, vol. 77, p. 054 701, 2006.

[129] A. Godeke *et al.*, "Fundamental origin of the large impact of strain on superconducting $Nb_3Sn$", *Supercond. Sci. Technol.*, vol. 31, p. 105 011, 2018.

[130] B. Bordini *et al.*, "An exponential scaling law for the strain dependence of the $Nb_3Sn$ critical current density", *Supercond. Sci. Technol.*, vol. 26, p. 075 014, 2013.

[131] A. K. Ghosh, "Effect of barrel baterial on critical current measurements of high-$J_c$ RRR $Nb_3Sn$ wires", *IEEE Trans. Appl. Supercond.*, vol. 21, no. 3, pp. 2327–2330, 2011.

[132] D. P. Boso *et al.*, "A thermo-mechanical model for $Nb_3Sn$ filaments and wires: Strain field for different strand layouts", *Supercond. Sci. Technol.*, vol. 22, p. 125 012, 2009.

[133] B. Ghosh *et al.*, "Thermally conductive poly(ether ether ketone)/boron nitride composites with low coefficient of thermal expansion", *J. Mater. Sci.*, vol. 56, pp. 10326–10337, 2021.

[134] R. David *et al.*, *CRC Handbook of Chemistry and Physics*. NIST, 2005.

[135] R. M. Bozorth, *Ferromagnetism*. Wiley-IEEE Press, 1978.

[136] A. Godeke *et al.*, "A review of conductor performance for the LARP high-gradient quadrupole magnets", *Supercond. Sci. Technol.*, vol. 26, p. 095 015, 2013.

[137] B. Bordini, "Self-field correction in critical current measurements of superconducting wires tested on ITER VAMAS barrels", CERN-ITER Collaboration Report EDMS No.1105765, 2010.

[138] M. Sumption *et al.*, "Analysis of magnetization, AC loss, and $d_{eff}$ for various internal-Sn based $Nb_3Sn$ multifilamentary strands with and without subelement splitting", *Cryogenics*, vol. 44, no. 10, pp. 711–725, 2004.

[139] E. J. Kramer, "Scaling laws for flux pinning in hard superconductors", *J. Appl. Phys.*, vol. 44, pp. 1360–1370, 1973.

[140] W. A. Fietz and W. W. Webb, "Hysteresis in superconducting alloys – temperature and field dependence of dislocation pinning in niobium alloys", *Phys. Rev.*, vol. 178, pp. 657–667, 1969.

[141] L. D. Cooley *et al.*, "Changes in flux pinning curve shape for flux-line separations comparable to grain size in $Nb_3Sn$ wires", *Adv. Cryog. Eng. Mat.*, vol. 48, pp. 925–932, 2002.

[142] A. Godeke *et al.*, "The upper critical field of filamentary $Nb_3Sn$ conductors", *J. Appl. Phys.*, vol. 97, p. 093 909, 2005.

[143] D. M. J. Taylor *et al.*, "The scaling law for the strain dependence of the critical current density in $Nb_3Sn$ superconducting wires", *Supercond. Sci. Technol.*, vol. 18, S241–S252, 2005.

[144] K. T. Hartwig *et al.*, "Design aspects of dual nb-ta sheet diffusion barriers for $Nb_3Sn$ conductors", *IEEE Trans. Appl. Supercond.*, vol. 21, pp. 2563–2566, 2011.

[145] J. C. McKinnell *et al.*, "Tantalum-niobium alloy diffusion barriers for superconducting $Nb_3Sn$ wires in fusion applications", *Adv. Cryog. Eng. Mat.*, vol. 42, pp. 2563–2566, 1996.

[146] D. Finnemore *et al.*, "Superconducting properties of high-purity niobium", *Phys. Rev.*, vol. 149, pp. 231–243, 1966.

[147] R. Shaw *et al.*, "Critical fields of superconducting tin, indium and tantalum", *Phys. Rev.*, vol. 120, pp. 88–91, 1960.

[148] A. Godeke *et al.*, "Toward an accurate scaling relation for the critical current in niobium–tin conductors", *IEEE Trans. Appl. Supercond.*, vol. 12, pp. 1029–1032, 2002.

[149] Y. Ilyin *et al.*, "Scaling law for the strain dependence of the critical current in an advanced ITER $Nb_3Sn$ strand", *Supercond. Sci. Technol.*, vol. 20, pp. 186–191, 2007.

[150] A. Godeke *et al.*, "Inconsistencies between extrapolated and actual critical fields in $Nb_3Sn$ wires as demonstrated by direct measurements of $H_{c2}$, $H^*$ and $T_c$", *Supercond. Sci. Technol.*, vol. 16, pp. 1019–1025, 2003.

[151] L. D. Cooley *et al.*, "Simulations of the effects of tin composition gradients on the superconducting properties of $Nb_3Sn$ conductors", *Jpn. J. Appl. Phys.*, vol. 96, no. 4, pp. 2122–2130, 2004.

[152] T. Baumgartner *et al.*, "Effects of inhomogeneities on pinning force scaling in $Nb_3Sn$ wires", *Supercond. Sci. Technol.*, vol. 31, p. 084 002, 2018.

[153] D. Uglietti *et al.*, "Correlation between the overall $T_c$ distribution in bronze route $Nb_3Sn$ wires and the sn gradient in the filaments", *IEEE Trans. Appl. Supercond.*, vol. 18, no. 2, pp. 1010–1013, 2008.

[154] Y. Nabara *et al.*, "Optimization of heat treatment of Japanese $Nb_3Sn$ conductors for toroidal field coils in ITER", *IEEE Trans. Appl. Supercond.*, vol. 24, no. 3, p. 6 000 605, 2014.

[155] V. Pantsyrny *et al.*, "$Nb_3Sn$ material development in Russia", *Cryogenics*, vol. 48, pp. 354–370, 2008.

[156] E. Popova *et al.*, "The $Nb_3Sn$ layers formation at diffusion annealing of Ti-doped multifilamentary Nb/Cu–Sn composites", *Cryogenics*, vol. 63, pp. 63–68, 2014.

[157] A. Nijhuis *et al.*, "The influence of the diffusion barrier on the AC loss of $Nb_3Sn$ superconductors", *Cryogenics ICEC 15 Proceedings*, vol. 34, pp. 547–550, 1994.

[158] M. Takayasu *et al.*, "Effect of magnetic field direction on the critical current of twisted multifilamentary superconducting wires", *Adv. Cryog. Eng. Mat.*, vol. 44, pp. 1035–1042, 1998.

[159] T. Schild and H. Cloez, "Magnetic field orientation dependence of critical current in industrial $Nb_3Sn$ strands", *Cryogenics*, vol. 38, pp. 1251–1257, 1998.

[160] W. T. Liu *et al.*, "Development of fine filament NbTi superconducting strands for ITER", *IEEE Trans. Appl. Supercond.*, vol. 20, no. 3, pp. 1504–1506, 2010.

[161] A. K. Panda *et al.*, "Demagnetisation effect and its correction on the measurement of magnetic hysteresis loop of melt-spun ribbons", *J. Magn. Magn. Mater.*, vol. 261, pp. 190–195, 2003.

[162] Quantum Design Company, "Accuracy of the reported moment: Sample shape effects", SQUID VSM Application Note 1500-015, 2010.

[163] A. Bergen, "Influence of sample length and orientation on vsm experiments", University of Twente, 2012.

[164] SWISS PLASMA CENTER, "PFJEU6 SULTAN sample, test report", 2017.

[165] A. Nijhuis, H. H. ten Kate, J.-L. Duchateau, and P. Decool, "Control of contact resistance by strand surface coating in 36-strand NbTi CICCs", *Cryogenics*, vol. 41, pp. 1–7, 2001.

[166] Y. Ilyin *et al.*, "Analysis of ITER PF coil joint design underreference operating scenario", *IEEE Trans. Appl. Supercond.*, vol. 26, no. 4, p. 4 201 305, 2016.

[167] A. Nijhuis *et al.*, "Impact of void fraction on mechanical properties and evolution of coupling loss in ITER $Nb_3Sn$ conductors under cyclic loading", *IEEE Trans. Appl. Supercond.*, vol. 15, no. 2, pp. 1633–1636, 2005.

[168] Y. Ilyin *et al.*, "Effect of cyclic loading and conductorlayout on contact resistance of full-size ITER PFCI conductors", *IEEE Trans. Appl. Supercond.*, vol. 15, no. 2, pp. 1359–1362, 2005.

[169] Y. Ilyin *et al.*, "Electromagnetic performance of sub-size NbTi CICC's subjected to transverse cyclic loading", *IEEE Trans. Appl. Supercond.*, vol. 14, no. 2, pp. 1503–1506, 2004.

[170] Quantum Design Company, "Accuracy of the reported moment: Axial and radial sample positioning error", SQUID VSM Application Note 1500-010, 2010.

[171] S. Langeslag, "Internal soldering assessment of the PFJS PF SULTAN sample (PFJEU2) produced by ASG", CERN, 2016.

[172] J. Huang *et al.*, "Contact resistance, coupling and hysteresis loss measurements of ITER poloidal field joint in parallel applied magnetic field", *Supercond. Sci. Technol.*, vol. 35, p. 025 016, 2022.

[173] SWISS PLASMA CENTER, "PFEU3 SULTAN sample, test report", 2015.

[174] K. A. Yagotintsev *et al.*, "Overview of verification tests on AC loss, contact resistance and mechanical properties of ITER conductors with transverse loading up to 30 000 cycles", *Supercond. Sci. Technol.*, vol. 32, p. 105 015, 2019.

[175] M. Breschi *et al.*, "Analysis of the electrical resistances, thermal resistances, and AC losses of the ITER PF superconducting joints", University of Bologna, 2019.

[176] D. Ciazynski and B. Turck, "Theoretical and experimental study of the saturation of a superconducting composite under fast changing magnetic field", *Cryogenics*, vol. 24, no. 10, pp. 507–514, 1984.

[177] SWISS PLASMA CENTER, "PFJEU2 SULTAN sample, test report", 2016.

[178] S. March *et al.*, "Applicability of non-destructive examination to ITER TF joints", *IEEE Trans. Appl. Supercond.*, vol. 25, no. 3, p. 4 200 505, 2015.

[179] B. Stepanov *et al.*, "Twin-box ITER joints under electromagnetic transient loads", *Fusion Eng. Des.*, vol. 98-99, pp. 1158–1162, 2015.

[180] N. Bagrets *et al.*, "Low temperature thermal and thermo-mechanical properties of soft solders for superconducting applications", *IEEE Trans. Appl. Supercond.*, vol. 24, no. 3, p. 7 800 203, 2014.

[181] A. Dimitrijevic and Y. Ilyin, "Additional soldering assessment and estimation of percentage of bonding of the PFJS PF SULTAN sample (PFJEU2) produced by ASG", Technical Report EDMS NO. 1702063 CERN, 2016.

[182] J. Huang *et al.*, "Pulsed field stability and AC loss of ITER NbTi PF joints by detailed quantitative modelling", *IEEE Trans. Appl. Supercond.*, vol. 33, no. 8, p. 4 201 711, 2023.

[183] I. Aviles and A. Dimitrijevic, "Void fraction analysis of a PF SULTAN sample produced by ASG", Technical Report EDMS NO. 1702063 CERN, 2016.

[184] Y. Ilyin *et al.*, "Simulations of twin-box joints for ITER PF coils", *IEEE Trans. Appl. Supercond.*, vol. 24, no. 3, p. 9 001 905, 2014.

[185] S. Langeslag, "Weld and soldering assessment of the FSJS PF SULTAN sample 1 produced by ASG", CERN, 2016.

[186] G. D. Tommasi *et al.*, "Plasma magnetic control in tokamak devices", *Fusion Energy*, vol. 38, pp. 406–436, 2019.

[187] Q. Wang *et al.*, "Heating surge and temperature oscillation in KSTAR PF and TF coils for plasma disruption under continuous plasma discharging conditions", *IEEE Trans. Appl. Supercond.*, vol. 14, no. 2, pp. 1451–1454, 2004.

[188] H. Kajitani *et al.*, "Numerical simulation of current distribution in cable-in-conduit conductor for ITER TF coil", *IEEE Trans. Appl. Supercond.*, vol. 21, no. 3, pp. 1964–1968, 2011.

[189] A. Nijhuis *et al.*, "Analysis of the current distribution in the ITER CS-insert model coil conductor by self field measurements", *IEEE Trans. Appl. Supercond.*, vol. 12, no. 1, pp. 1675–1679, 2002.

[190] T. Casper, "Development of the ITER baseline inductive scenario", *Nucl. Fusion*, vol. 54, p. 013 005, 2014.

[191] ITER, "Magnet superconducting and electrical design criteria", ITER N 11 FDR 4 01-07-13 R1.0, 2009.

[192] P. Bauer *et al.*, "AC losses calculations for the ITER CS and PF magnet systems during plasma operation", *IEEE Trans. Appl. Supercond.*, vol. 33, no. 5, p. 4 602 405, 2023.

[193] P. F. Pison *et al.*, "The effect of specific manufacturing characteristics on PF ITER full-size joint performance", *IEEE Trans. Appl. Supercond.*, vol. 29, no. 5, p. 4 200 706, 2019.

[194] M. Breschi *et al.*, "Electrodynamic losses of the ITER PF joints during the dynamic plasma scenario", *IEEE Trans. Appl. Supercond.*, vol. 33, no. 5, p. 4 200 705, 2023.

[195] M. Breschi *et al.*, "Performance review of the joints for the iter poloidal field coils", *Supercond. Sci. Technol.*, vol. 36, p. 075 009, 2023.

[196] L. Bottura. "Cable stability". (2014), [Online]. Available: <https://doi.org/10.5170/CERN-2014-005.401>.

[197] M. Bagnasco, "Calorimetric method for current sharing temperature measurements in ITER conductor samples in SULTAN", *Fusion Eng. Des.*, vol. 84, pp. 423–426, 2009.

[198] M. Oomen *et al.*, "Dynamic resistance in a slab-like superconductor with $J_c(B)$ dependence", *Supercond. Sci. Technol.*, vol. 12, pp. 382–387, 1999.

[199] H. Zhang *et al.*, "Dynamic resistance and dynamic loss in a rebco superconductor", *Supercond. Sci. Technol.*, vol. 35, p. 113 001, 2022.

[200] B. Liu *et al.*, "The performance test and analysis of the third and fourth China PF conductor for ITER", *Physica C*, vol. 499, pp. 9–14, 2014.

[201] M. Breschi *et al.*, "Performance analysis of the toroidal field ITER production conductors", *Supercond. Sci. Technol.*, vol. 30, p. 055 007, 2017.

[202] J. Huang *et al.*, "Quantitative analysis of ITER poloidal field joints through rigorous resistivity parameterization", *accepted by Supercond. Sci. Technol.*,

[203] E. Ravaioli *et al.*, "Quench transient simulation in a self-protected magnet with a 3-D finite-difference scheme", *IEEE Trans. Appl. Supercond.*, vol. 32, no. 6, p. 4 005 205, 2022.

[204] M. Janitschke *et al.*, "A simplified approach to simulate quench development in a superconducting magnet", *IEEE Trans. Appl. Supercond.*, vol. 31, no. 5, p. 4 000 905, 2021.

[205] B. Turck and L. Zani, "A macroscopic model for coupling current losses in cables made of multistages of superconducting strands and its experimental validation", *Cryogenics*, vol. 50, pp. 443–449, 2010.

[206] L. Bottura and M. Marinucci. "Cryosoft". (), [Online]. Available: `<http://htess.com/cryosoft>`.

[207] R. Bonifetto *et al.*, "Modeling the ITER CS AC losses based on the CS insert analysis", *IEEE Trans. Appl. Supercond.*, vol. 29, no. 5, p. 4 200 907, 2019.

[208] P. Bruzzone *et al.*, "Transient stability results for $Nb_3Sn$ cable-in-conduit conductors", *IEEE Trans. Appl. Supercond.*, vol. 12, no. 1, pp. 512–515, 2002.

[209] V. Corato *et al.*, "The DEMO magnet system – status and future challenges", *Fusion Eng. Des.*, vol. 174, p. 112 971, 2022.

[210] Q. Hao *et al.*, "Conductor design and performance analysis for CFETR magnet", *Fusion Eng. Des.*, vol. 182, p. 113 224, 2022.

[211] W. Goldacker *et al.*, "Roebel cables from ReBCO coated conductors: A one-century-old concept for the superconductivity of the future", *Supercond. Sci. Technol.*, vol. 27, p. 093 001, 2014.

[212] D. C. van der laan *et al.*, "Status of CORC cables and wires for use in high-field magnets and power systems a decade after their introductions", *Supercond. Sci. Technol.*, vol. 32, p. 033 001, 2019.

[213] M. Paidpilli *et al.*, "Development of RE-Ba-Cu-O superconductors in the U.S. for ultra-high field magnets", *Supercond. Sci. Technol.*, vol. 35, p. 043 001, 2022.

[214] P. Gao *et al.*, "DC performance and AC loss of sub-size $MgB_2$ CICC conductor for fusion magnet application", *Nucl. Fusion*, vol. 62, p. 056 014, 2022.

[215] S. Ito *et al.*, "Low-resistance joint development for segment-fabrication of high-temperature superconducting fusion magnets", *Nucl. Fusion*, vol. 61, p. 115 002, 2021.

[216] M. Takayasu *et al.*, "HTS twisted stacked-tape cable conductor", *Supercond. Sci. Technol.*, vol. 25, p. 014 011, 2012.

[217] Q. Zhang *et al.*, "Bending and twisting characteristics of REBCO lap joint with indium", *IEEE Trans. Appl. Supercond.*, vol. 33, no. 5, p. 4 201 305, 2023.

# Nomenclature

## List of abbreviations

| | |
|---|---|
| AC | Alternating Current. |
| Ag | Silver, see section 1.3.1 on page 13. |
| BR | Bronze Route, see section 3.2 on page 54. |
| BSCCO | $Bi_2Sr_2Cu_nO_{2n+4+x}$, a high temperature superconducting compound, see section 1.3 on page 9. |
| CC | Correction Coil, see section 1.2.1 on page 7. |
| CEA | Atomic Energy and Alternative Energies Commission in France, see section 1.3.3 on page 17. |
| CERN | European Organization for Nuclear Research located in Geneva, Switzerland, see section 3.1 on page 54. |
| CICC | Cable-In-Conduit Conductor, a cable in jacket type conductor developed for use in nuclear fusion reactors, see section 1.3.2 on page 14. |
| CS | Central Solenoid, see section 1.2.1 on page 7. |
| CSBR | CS strand sample produced by Bronze Route process, see section 3.2 on page 54. |
| Cu | Copper. |
| CuSn | Copper Tin alloy, see section 1.3.1 on page 13. |
| D | Deuterium, see section 1.1 page 2. |
| DAs | Domestic Agencies of ITER organization, see section 1.2.1 on page 6 and section 2.1 on page 32. |
| DC | Direct Current. |
| DEMO | DEMOnstration fusion power plant, see section 1.1 page 4. |
| DP | Double Pancake, a conductor winding scheme. |
| DT | Deuterium and Tritium fusion reaction, see section 1.1 page 2. |

| | |
|---|---|
| EDX | Energy-Dispersive X-ray spectroscopy, see section 5.4 on page 124. |
| EM1, EM2 | Two prototype full-size ITER Poloidal Field NbTi conductor samples, see section 4.2.1 on page 83. |
| FFHR-d1 | Conceptual Fusion Experimental Reactor based on the Helias Line configuration (stellarator), developed by the National Institute for Fusion Science (NIFS) in Japan, see section 1.3.3 on page 21. |
| GMD | Geometric Mean Distance, see section 2.3.4 on page 44. |
| GPU | Graphics Processing Unit, see section 2.3 on page 39. |
| He, $^4$He | Helium and its isotope, see section 1.1 page 2. |
| HFZ | High Field Zone of magnetic field, see section 2.2.1 on page 33 and section 7.2.2 on page 151. |
| HTS | High Temperature Superconductor. |
| ICF | Inertial Confinement Fusion, see section 1.1 page 3. |
| IFMIF-DONES | International Fusion Material Irradiation Facility, also called DONES program, see section 1.1 page 4. |
| IT | Internal-Tin route, see section 3.2 on page 54. |
| ITER | International Thermonuclear Experimental Reactor, a tokamak nuclear fusion reactor under construction in Cadarache in France. |
| JackPot-AC/DC | A code developed at the University of Twente in order to perform transient electro-magnetic and thermal analysis on cable-in-conduit conductors and joints. |
| JET | Joint European Torus, a tokamak reactor in Culham, UK, see section 1.1 page 4. |
| JT-60 | Japanese Tokamak, see section 1.1 page 4. |
| Li, $^6$Li, $^7$Li | Lithium and its two main isotopes, see section 1.1 page 3. |
| LTS | Low Temperature Superconductor. |
| MB | Main Busbar, see section 1.3.3 page 18. |
| MLFMM | Multi-Level Fast Multipole Method, see section 2.3 on page 39. |
| MQE | Minimum Quench Energy, see section 2.2.1 on page 35 and section 7.1 on page 148. |
| $n$ | (1) neutron. see section 1.1 on pages 2 and 3,<br>(2) Quality index value characterizes the steepness of the $E$-$J$ transition, see section 1.3.1 on page 14. |
| Nb | Niobium. |

| | |
|---|---|
| NbTi | Niobium Titanium superconductor, see section 1.3 on page 9. |
| $Nb_3Sn$ | Niobium three Tin superconductor, see section 1.3 on page 9. |
| PEEC | Partial Element Equivalent Circuit, see section 2.3.2 on page 40. |
| PF | Poloidal Field, see section 1.2.1 on page 7. |
| PFISw | Poloidal Field full-size conductor Insert Sample, see section 4.2.1 on page 83. |
| PFJEU | Poloidal Field coil Joint made by EUrope. |
| $Re$BCO | Rare Earth (commonly Ytrium or Gadelinium) Barium Copper Oxide, a high temperature superconducting compound with chemical composition like $ReBa_2Cu_3O_{7-x}$, see section 1.3 on page 9 and section 1.3.3 on page 20, 21. |
| RRR | Residual Resistivity Ratio, see section 1.3.1 on page 13 and section 3.2 on page 55. |
| SC | SuperConductor. |
| SEM | Scanning Electron Microscope, see section 5.4 on page 124. |
| Sn | Tin. |
| SPC | Swiss Plasma Center at EPFL, Switzerland, see section 2.1 on page 32. |
| SQUID | Superconducting Quantum Interference Device, a highly sensitive magnetometer used to measure extremely subtle magnetic fields, see section 2.2.2 on page 37. |
| SULTAN | SUpraLeiter TestANlage, test facility of the Swiss Plasma Center at EPFL, Switzerland, see section 2.1 on page 32. |
| T | Tritium, see section 1.1 on page 2. |
| TBMs | Test Blanket Modules of ITER, see section 1.1 on page 4. |
| TF | Toroidal Field, see section 1.2.1 on page 7. |
| TFBR | TF strand sample produced by Bronze Route process, see section 3.2 on page 54. |
| TFIT | TF strand sample produced by Internal-Tin route process, see section 3.2 on page 54. |
| TFTR | Tokamak Fusion Test Reactor in Princeton, USA, see section 1.1 on page 4. |
| UT | University of Twente, the Netherlands. |
| VAMAS | Versailles Project on Advanced Materials and Standards, see section 3.2.1 on page 55. |
| VSM | Vibrating Sample Magnetometer, see section 2.2.2 on page 38. |

| | |
|---|---|
| WST | Western Superconducting Technologies Co., Ltd., see section 1.4.1 on page 24. |
| WUCD | Warming-Up and Cooling-Down process, see section 2.2.1 on page 36. |

## List of Symbols

| | |
|---|---|
| $\alpha$, $\alpha_1$, $\alpha_2$ | (1) Fitting parameters of scaling law, see section 1.3 on page 10 and section 3.1 on page 53, |
| | (2) Slope of the initial linear section of AC loss versus frequency curve, see section 1.4.3 on page 26 and section 4.2.2 on page 100. |
| $\beta$, $\beta_1$, $\beta_2$ | Fitting parameters of scaling law, see section 1.3 on page 10 and section 3.1 on page 53. |
| $\gamma$, $\gamma_1$, $\gamma_2$ | Fitting parameters of scaling law, see section 1.3 on page 10, section 3.1 on page 53 and section 3.3.3 on page 62. |
| $\epsilon$ | Strain, see section 1.3 on page 11. |
| $\epsilon_{axial}$ | Axial strain (sum of applied and pre-compression strains), see section 1.3 on page 12. |
| $\epsilon_{0,a}$ | Remaining strain component when $\epsilon_{axial} = 0$, see section 1.3 on page 12. |
| $\epsilon_{shift}$ | Strain related item, see section 1.3 on page 12. |
| $\theta$ | (1) Angle between applied magnetic field and strand direction during VSM measurements, see section 3.4 on page 69, |
| | (2) Angle between two cable-sole contacting edges, see section 6.2 on page 131. |
| $\kappa_1$ | Parameter related to the thermodynamic critical field, see section 3.3.3 on page 62. |
| $\mu_0$ | Magnetic permeability in vacuum, see section 1.4.1 on page 23, section 2.2.1 on page 36 and section 7.3.2 on page 166. |
| $\nu$ | Free parameter affecting the temperature dependence on pinning force during determination of scaling law, see section 3.3.3 on page 62. |
| $\rho'$ | Contact resistivity, see section 2.3.3 on page 41. |
| $\rho_t$ | Transverse inter-filamentary resistivity, see section 1.4.2 on page 25. |
| $\rho_{sole}$ | Resistivity of copper sole, see section 4.2.2 on page 91 and section 6.2 on page 131. |
| $\rho_{shim}$ | Resistivity of copper shim, see section 4.2.2 on page 91. |
| $\rho_{mask}$ | Resistivity of mask, see section 4.2.2 on page 91. |
| $\rho_{equ}$ | Equivalent copper resistivity of joint taking into account both copper sole and shim, see section 5.3.1 on page 114. |
| $\rho_{ss}$ | Interstrand resistivity, see section 4.2.2 on page 91, 93, 95, and section 6.2 on page 131. |

| | |
|---|---|
| $\rho_{ip}$ | Interpetal resistivity, see section 4.2.2 on page 91, 93, 95, and section 6.2 on page 131. |
| $\rho_{sj}$ | Strand-to-copper sole resistivity, see section 4.2.2 on page 91, 93, 95, and section 6.2 on page 131. |
| $\sigma$ | Density of strand, see section 3.2.1 on page 56. |
| $\tau$, $\tau_i$ | Time constant of system, see section 1.4.2 on page 25. |
| $\tau_{eff}$ | Effective time constant, see section 1.4.3 on page 25. |
| $\Phi$ | (1) Magnetic flux, see section 2.3.5 on page 47, |
| | (2) Cable diameter, see section 4.2.2 on page 91, and section 6.2 on page 131. |
| $A$ | (1) Contact area, see section 2.3.3 on page 41, |
| | (2) Magnetic vector potential, see section 2.3.5 on page 46. |
| $a$ | (1) Distance between the centres of both legs of tested SULTAN sample, see section 2.2.1 on page 36, |
| | (2) Fitting parameter of scaling law that related to internal magnetic field, see section 3.3.3 on page 62. |
| $A_{st}$ | Total cross-sectional area of the composited strands, see section 7.3.2 on page 166. |
| $B$ | Magnetic field. |
| $b$ | Reduced magnetic field, see section 1.3 on page 10, 11. |
| $B_a$ | Applied magnetic field, see section 1.4.2 on page 25. |
| $B_{ac}$ | Background AC magnetic field, see section 2.2.1 on page 33. |
| $B_{c2}$ | Upper critical magnetic field, see section 1.3 on page 9 and section 3.3.3 on page 62. |
| $B_{c20}$ | Upper critical magnetic field at 0 K, see section 1.3 on page 11 and section 3.1 on page 52. |
| $B^*_{c2m}$ | Inhomogeneity average upper critical magnetic field, see section 1.3 on page 12. |
| $B_{corr}$ | Corrected magnetic field, see section 3.3.2 on page 59. |
| $B_{dc}$ | Background DC magnetic field, see section 2.2.1 on page 33. |
| $B_e$ | External magnetic field, see section 1.4.2 on page 24, section 2.3.6 on page 47 and section 3.3.2 on page 59. |
| $B_i$ | Internal magnetic field, see section 1.4.2 on page 24 and section 3.3.3 on page 62. |

| | |
|---|---|
| $B_{irr}$ | Irreversibly magnetic field, see section 3.1 on page 53. |
| $B_{irr\_0}$ | Irreversibly magnetic field at zero temperature, see section 3.1 on page 53. |
| $B_m$ | Magnitude of magnetic field, see section 3.2.1 on page 56. |
| $B_p$ | Penetration field, see section 1.4.1 on page 22 and section 3.3.3 on page 62. |
| $B_{th}$ | Threshold value of applied magnetic field, see section 3.3.3 on page 63. |
| $c$ | Speed of light, see section 1.1 page 2. |
| $C_0, C_1, C_2$ | Fitting parameters of scaling law of superconductors, see section 1.3 on page 10 and section 3.1 on page 53. |
| $C_{a,1}, C_{a,2}$ | Second and third invariant of axial strain sensitivity, see section 1.3 on page 12 and section 3.1 on page 53. |
| $C^T, C^L$ | Coupling matrix in transverse or longitudinal direction, respectively, see section 2.3.6 on page 47. |
| $C_p$ | Specific heat of helium, see section 7.3.4 on page 169. |
| $D_i, D_v$ | Matrix of current and voltage elements, see section 2.3.6 on page 47. |
| $D_{coil}$ | Diameter of mini-coil sample, see section 3.2.1 on page 56. |
| $d_{eff}$ | Effective filament diameter of strand, see section 3.3.2 on page 60. |
| $d_f$ | Filament diameter, see section 1.4.1 on page 23 and section 3.3.4 on page 68. |
| $d_{rc}$ | Parameter used for adjusting inner radius of cable, see section 2.3.3 on page 42. |
| $d_{sj}$ | Contact width between strand and copper sole, see section 2.3.3 on page 43. |
| $d_{sol}$ | Solder thickness, see section 2.3.3 on page 43. |
| $d_{ss}$ | Distance between strands, see section 2.3.3 on page 42. |
| $d$ | Diameter of strand, see section 2.3.3 on page 42, section 3.2.1 on page 56, section 3.4 on page 69 and section 4.2.2 on page 91. |
| $E$ | (1) Energy conversed from mass-energy conversion, see section 1.1 on page 2,<br>(2) Electric field, see section 1.3.1 on page 14. |
| $E_c$ | Electric field criterion, see section 1.3.1 on page 14 and section 7.1 on page 148. |
| $E_{gen}$ | Energy deposition, see section 7.3.4 on page 169. |

| | |
|---|---|
| $F$ | Electro-magnetic force, see section 5.4 on page 124. |
| $f$ | Frequency, see section 1.4.3 on page 26. |
| $F_p$, $F_p^1$, $F_p^2$ | Pinning force and components, see section 3.1 on page 53 and section 3.3.3 on page 62. |
| $G$ | Transverse conductance matrix, see section 2.3.6 on page 47. |
| $H$ | Height of copper sole of joint, see section 4.2.2 on page 91 and section 6.2 on page 131. |
| $H_{shim}$ | Thickness of copper shim of joint, see section 4.2.2 on page 91 and section 6.2 on page 131. |
| $H_{cable}$ | Cable offset to middle plane of joint, see section 4.2.2 on page 91 and section 6.2 on page 131. |
| $I$ | Current. |
| $I_c$ | (1) Critical current, see section 1.3.1 on page 14,<br>(2) Measured current, see section 3.3.2 on page 59. |
| $I_{coil}$ | Current in coil, see section 1.4.4 on page 26. |
| $I_{margin}$ | Current margin, see section 5.3.2 on page 122, section 6.2.2 on page 138, section 7.2.4 on page 157 and section 7.3.2 on page 167. |
| $I_s$ | Strand carrying current, see section 5.3.2 on page 122, section 6.2.2 on page 138 and section 7.2.4 on page 157. |
| $I_{op}$ | Operating current, see section 1.3 on page 12. |
| $I_t$ | Transport current, see section 1.4.1 on page 23. |
| $J$ | Current density. |
| $J_c$ | Critical current density, see section 1.3 on page 9 and section 1.4.1 on page 22. |
| $J_{ce}$ | Engineering critical current density, see section 3.3.2 on page 59. |
| $k$ | Multiplying factor with respect to the strand diameter, for adjustment of solder thickness, see section 2.3.3 on page 43 and section 4.2.2 on page 91. |
| $L$ | (1) Twist pitch, see section 1.4.2 on page 25,<br>(2) Self-inductance of strand element, see section 2.3.4 on page 44,<br>(3) Length of strand sample for VSM measurement, see section 3.4 on page 69,<br>(4) Length of copper sole of joint, see section 4.2.2 on page 91 and section 6.2 on page 131. |

| | |
|---|---|
| $l$ | (1) Length of the conductor section during contact resistance measurement, see section 2.2.2 on page 37,<br>(2) Length of the strand segment during calculation of mutual- and self-inductances, see section 2.3.4 on page 44. |
| $L_{cable}$ | Length of cable of joint, see section 4.2.2 on page 91 and section 6.2 on page 131. |
| $L_i$, $L_j$ | Current carrying elements in calculation of mutual inductance, see section 2.3.4 on page 44. |
| $M$ | (1) Magnetization, defined as magnetic moment per unit volume, see section 1.4.1 on page 23 and section 3.3.1 on page 57,<br>(2) Number of high resistivity regions in the non-homogeneous contact resistance model, see section 5.3 on page 114 and section 5.3.2 on page 119. |
| $m$ | Mass of mini-coil strand sample, see section 3.2.1 on page 56. |
| $M^+$, $M^-$ | Upper and lower branches of a magnetization loop, respectively, see section 3.3.1 on page 58. |
| $M_{ij}$ | Mutual inductance between two elements of $i$ and $j$, see section 2.3.4 on page 44. |
| $N$ | Number of normal or low resistivity regions in the non-homogeneous contact resistance model, see section 5.3 on page 114 and section 5.3.2 on page 119. |
| $n$ | Quality index value characterizes the steepness of the $E$-$J$ transition, see section 1.3.1 on page 14. |
| $N_f$ | Number of filaments in a strand, see section 3.3.4 on page 68. |
| $n_s$, $n_i$ | Shape factor of the filamentary core or $i$th cabling stage, $n_s = 2$ for a wire with circular cross section, see section 1.4.2 on page 25 and section 1.4.3 on page 26. |
| $p$ | Fitting parameter of scaling law of superconductors, see section 3.1 on page 53 and section 3.3.3 on page 62. |
| $P_{cpl}$ | Generated coupling loss power, see section 7.3.2 on page 166. |
| $P_{Joule}$ | Joule heating power, see section 1.4.4 on page 26. |
| $P_{ratio}$ | Patch ratio, see section 5.3.2 on page 119, 121, 123. |
| $Q$ | (1) Amount of energy released or absorbed,<br>(2) Ratio of energy output to input, see section 1.2.1 on page 7. |
| $q$ | Fitting parameter of scaling law of superconductors, see section 3.1 on page 53 and section 3.3.3 on page 62. |

| | |
|---|---|
| $Q_{exp}$ | Measured AC loss of joint, see section 4.2.2 on page 97. |
| $Q_{gen}$ | Energy generation, see section 7.3.2 on page 164. |
| $Q_{hys}$ | Hysteresis loss, see section 1.4.1 on page 23, section 3.3.1 on page 58 and section 4.2.1 on page 89. |
| $Q_{sim}$ | Simulated AC loss of joint, see section 4.2.2 on page 97. |
| $Q_{vsm}$ | Hysteresis loss derived from VSM measurements, see section 4.2.1 on page 89. |
| $R$ | (1) Resistance of joint, see section 2.2.1 on page 34 and section 1.4.4 on page 26,<br>(2) Radius of $Nb_3Sn$ filamentary area in the strand cross section, in unit [mm], see section 3.3.2 on page 59. |
| $r$ | (1) Conductor bundle radius, see section 2.2.1 on page 36,<br>(2) Radial position of the strand within a cable, see section 2.3.3 on page 42,<br>(3) Ramp rate of sweeping magnetic field in VSM measurements, see section 3.2.1 on page 56. |
| $R_c$ | Contact resistance, see section 2.2.2 on page 37 and section 4.2.1 on page 81. |
| $\Delta r_s$ | Thickness of solder layer in joint, see section 4.2.2 on page 91, 93, 95. |
| $r_{out}$ | Outer radius of the cable, see section 2.3.3 on page 42. |
| $S$ | Strain dependent term of scaling law of $Nb_3Sn$ material, see section 1.3 on page 12. |
| $S_i, S_j$ | Areas perpendicular to current flow in the calculation of mutual inductance, see section 2.3.4 on page 45. |
| $S_{total}$ | Total area of the strand cross section taking into account the non-superconductor materials, see section 3.3.2 on page 59. |
| $T$ | Temperature. |
| $t$ | (1) Reduced temperature see section 1.3 on page 10, 11,<br>(2) Time instant. |
| $\Delta T$ | Temperature margin, see section 1.3 on page 12 and section 7.3.4 on page 169, 170. |
| $T_c$ | Critical temperature. |
| $T_{c0}$ | Critical temperature with zero magnetic field, see section 3.1 on page 52. |
| $T_c^*$ | Critical temperature affected by strain, see section 1.3 on page 11. |

| | |
|---|---|
| $T^*_{cm}$ | Inhomogeneity averaged critical temperature, see section 1.3 on page 11. |
| $T_{cs}$ | Current sharing temperature, see section 7.3 on page 12 and section 7.2.1 on page 149. |
| $T_{He}$, $T_{He,1:i}$ | Helium temperature in the central channel or $i$th petal in the thermal model, see section 2.3.7 on page 48. |
| $T_{in}$ | Inlet temperature of helium flow, see section 7.3.4 on page 169. |
| $T_{op}$ | Operating temperature, see section 1.3 on page 12. |
| $T_q$ | Quench temperature, see section 2.2.1 on page 34 and section 7.2.1 on page 149. |
| $T_{st,1:i}$ | Temperature of the $i$th petal in the thermal model, see section 2.3.7 on page 48. |
| $V$ | (1) Voltage or voltage difference, see section 2.2.1 on page 35, |
| | (2) Voltage matrix, see section 2.3.6 on page 47, |
| | (3) Volume of mini-coil strand sample, see section 3.2.1 on page 56. |
| $V_i$, $V_j$ | Volumes of blocks, see section 2.3.4 on page 45. |
| $W$ | (1) Width of copper sole of joint, see section 4.2.2 on page 90 and section 6.2 on page 131, |
| | (2) Width of solder layer, see section 4.2.2 on page 91, 93, 95. |
| $w_{ss}$ | Contact width between strands, see section 2.3.3 on page 42. |
| $x_{sj}$ | Strand-to-sole distance, see section 2.3.3 on page 43. |